A Case Study of the Galactic H ii Region M17 and Environs: Implications for the Galactic Star Formation Rate

by

Matthew Samuel Povich

A dissertation submitted in partial fulfillment of the
requirements for the degree of

Doctor of Philosophy
(Astronomy)

at the

University of Wisconsin – Madison

2009

Abstract

Determinations of star formation rates (SFRs) in the Milky Way and other galaxies are fundamentally based on diffuse emission tracers of ionized gas, such as optical/near-infrared recombination lines, far-infrared continuum, and thermal radio continuum, that are sensitive only to massive OB stars. OB stars dominate the ionization of H II regions, yet they make up <1% of young stellar populations. SFRs therefore depend upon large extrapolations over the stellar initial mass function (IMF). The primary goal of this Thesis is to obtain a detailed census of the young stellar population associated with a bright Galactic H II region and to compare the resulting star formation history with global SFR tracers. The main SFR tracer considered is infrared continuum, since it can be used to derive SFRs in both the Galactic and extragalactic cases. I focus this study on M17, one of the nearest giant H II regions to the Sun ($d = 2.1$ kpc), for two reasons: (1) M17 is bright enough to serve as an analog of observable extragalactic star formation regions, and (2) M17 is associated with a giant molecular cloud complex, ~100 pc in extent. The M17 complex is a significant star-forming structure on the Galactic scale, with a complicated star formation history.

This study is multiwavelength in nature, but it is based upon broadband mid-infrared images from the *Spitzer*/GLIMPSE survey and complementary infrared Galactic plane surveys. I begin by measuring the global spectral energy distribution from the integrated infrared–radio emission of the M17 H II region and photodissociation region (PDR). The morphology of the infrared emission is consistent with a wind-blown bubble model for the H II region, with a large, central cavity surrounded by ionized gas. I report the discovery of 6 stellar-wind bow shocks driven by O stars in M17 and in (or near) the even larger H II region RCW 49. The bow shocks graphically illustrate the important role played by stellar winds in shaping the structure and dynamics of H II regions and lead to the identification of 4 new candidate O stars.

A dramatic, new view of the M17 environs is provided by the high-resolution, wide-area coverage of GLIMPSE. I report the discovery that the M17 H II region itself is located on the rim of a 20-pc diameter bubble outlining the PDR of a ~5 Myr old H II region. This configuration raises the tantalizing possibility that the formation of M17 ionizing cluster was triggered by the expansion of the bubble. Several dozen intermediate-mass ($\gtrsim 3\ M_\odot$) young stellar objects (YSOs) are distributed around the rim of the bubble, indicating even more recent triggered star formation. I estimate the star formation rate in the extended M17 environment from the YSO mass function (YMF), and compare this to the star formation rate in the central ionizing cluster, $\mathrm{SFR}_X \sim 0.01\ M_\odot\ \mathrm{yr}^{-1}$, derived from the observed X-ray luminosity function

(XLF) of the young stellar population. The XLF and the YMF both show great promise for establishing new calibrations of star formation rates the Galaxy, since both trace the intermediate-mass range of the IMF rather than the extreme high-mass tail.

I conclude with comparisons between SFR_X and the SFRs predicted for M17 by widely-used calibrations based on IR and radio continuum emission. The results imply that current SFR determinations based on ionized gas tracers are uncertain by factors of $\sim$2–3, due chiefly to large uncertainties in the masses and ionizing photon production rates of O stars and the need to correct for the high binary fractions observed among massive stars.

To Kerean —
The scope of space and time is vast beyond comprehension,
and yet, against all odds, we found each other.

and

To Jim —
I will "keep looking up," and when I do,
I will be thinking of you.

Acknowledgments

It seems to me that the process of working toward a Ph.D. needs to be its own reward; if the end goal is all that is desired, the experience of several years of post-graduate study may devolve into an odyssey of frustration and suffering. My education has become my career, and my dissertation now seems more like a conjunction than an exclamation point. My task would have been made much more difficult, and my journey far less pleasant, if not for the people who have influenced my life and my path during these past five years.

I have been extremely fortunate to work with an advisor, Ed Churchwell, who is more than a great scientist; he is a first-rate human being in all respects. I thank Ed for his friendship and his tutelage, his gentle encouragement and steady supply of ideas, and his refraining from vanishing following his retirement a few years back. I have also benefited immensely from my interactions with my unofficial "lieutenant advisor," Barbara Whitney, who typifies the smart, savvy, and grounded astronomer I have always admired. I am grateful to all of my coauthors on the papers that constitute Chapters 2, 3, and 4, the backbone of this thesis, and especially Marilyn Meade, Brian Babler, Thomas Robitaille, and Robert Benjamin—they will know why they have been singled out here. I thank Debra Shepherd and Christer Watson for bringing me on board papers they lead and then allowing me free reign to develop and test new analysis techniques that became central to this Thesis. Conversations with Leisa Townsley and Jay Gallagher were helpful not just for their scientific content, but for keeping me excited about my own science as well. John Raymond, my undergraduate mentor, was instrumental in setting me on my professional trajectory and equipping me to succeed as a graduate student. Kenny Wood also made an enormous imprint on my early experiences in astronomical research, and as Madison's chief cheerleader, Kenny strongly influenced my choice of graduate school. It turns out to have been an excellent choice.

I acknowledge the *Spitzer* telescope and instrument teams, and the staff at the *Spitzer* Science Center, for producing and operating one of the greatest observatories in the known universe, without which this thesis certainly would not have been possible. I am also grateful to the National Science Foundation for the award of an Astronomy & Astrophysics Postdoctoral Fellowship, the vehicle for the next stage of my professional development.

The graduate students in the Astronomy Department are a remarkably intelligent, gifted, active, funny, and tight-knit group of people. I have greatly enjoyed spending time in their company, and someday

I might even forgive them for electing me Student Czar. I give special thanks to my fellow inmates of Sterling 5533, who put up with much nonsense from me over the years: Aaron Geller, Laura Trouille, Ryan Keenan, Tommy Nelson, and Ella Braden. I will also always carry around fond memories those nights spent sitting at the City Bar (or occasionally in my living room) playing euchre with Kyle Westfall, Nathaniel Doane, and Aaron.

I dedicate this Thesis to two of the most important people in my life: my wife, Kerean Grant Povich, and my late, dear friend James Clark. I am forever grateful to Kerean for agreeing to spend three years in the frozen tundra of Wisconsin for the love of a humble graduate student—if not for Kerean, this Thesis almost certainly would have been longer in the making. She is, quite simply, the most amazing woman I have ever met. I believe Jim thought so too. I had known Jim all of my life and hardly ever had I seen him make a new friend as quickly as he adopted Kerean. The two of them should enjoy sharing the dedication page. Jim was the world's most gentle soul, always quick to laugh, devoted friend, avid stargazer. He and I taught ourselves the constellations together using H. A. Rey's book, a red-filtered flashlight, and the dark skies of Downeast Maine.

I mention last the two people who have given me their unconditional love and support from the very beginning, my parents, Judith and Michael Povich. The knowledge that they were always behind me has given me the confidence to pursue my dreams and to choose the more difficult, risky path, when it mattered most.

Contents

List of Tables

List of Figures

Chapter 1

Introduction

> *"White!" [Saruman] sneered. "It serves as a beginning.*
> *White cloth may be dyed. The white page can be overwritten;*
> *and the white light can be broken."*
>
> *"In which case it is no longer white," said [Gandalf].*
> *"And he that breaks a thing to find out what it is has left the path of wisdom."*
>
> — The Lord of the Rings, Book II, Chapter 2
> *by J. R. R. Tolkien*

1.1 H II Regions and Star Formation Rates

Hot, massive stars produce copious far-ultraviolet radiation, photoionizing the interstellar medium (ISM) and producing H II regions. H II regions are strong emitters of thermal radio continuum, recombination lines, forbidden lines, and infrared (IR) continuum from dust. Ionizing stars tend not to move far from their natal clusters during their relatively short lifetimes of $\lesssim$10 Myr. Hence, H II regions are bright beacons marking active sites of star formation throughout the Milky Way and other galaxies.

Only the most massive <1% of stars are responsible for ionizing H II regions. Due to the observational difficulties of resolving individual stars in external galaxies beyond the Magellanic clouds, the stellar initial mass function (IMF)[1] is one of the master keys to astronomy. Star formation rate (SFR) diagnostics employed in extragalactic studies (Kennicutt 1998a) rely fundamentally upon extrapolation over an IMF to quantify the entire young stellar population based upon observational tracers, like optical/near-IR recombination lines and far-IR continuum, that are sensitive only to a handful of the most massive stars (O and early B types). The relative rarity of high-mass stars makes this extrapolation enormous.

Measuring the SFR of a galaxy is like taking its pulse. Massive stars account for most of the luminosity in star-forming galaxies while pumping energy and heavy elements into the interstellar medium (ISM) through "feedback" processes, specifically radiation, stellar winds, and supernovae. Galaxy evolution models require the SFR as a fundamental input parameter (Larson 1974; Chiappini, Matteucci, & Gratton 1997; Kaufmann & Haehnelt 2000; de Rossi et al. 2009), primarily because massive star feedback sets the composition and energetics of the ISM. But evolved, low- and intermediate-mass stars manufacture large quantities of interstellar dust and are responsible for much of the chemical enrichment of abundant elements like carbon. Since low-mass stars also contain the bulk of the stellar mass and remain on the main sequence much longer, they dominate galactic dynamics and structure. To confidently predict the evolution of a galaxy, it is necessary to quantify the contribution of low- and intermediate-mass star formation to the star formation efficiency of molecular clouds and the total SFR.

In contrast to "global" extragalactic star formation studies, "local" Galactic observations have long been able to resolve individual young stars and young stellar objects (YSOs). One of the greatest successes of modern observational astrophysics has been the description of the pre-main-sequence (PMS) evolution

---

[1] The IMF is defined as the relative fraction of stars formed as a function of stellar mass.

of low-mass stars, from cold, collapsing molecular cloud cores to accreting protostars to PMS stars with circumstellar disks (Shu, Adams, & Lizano 1987). This picture provides a compelling explanation for the origin of the Solar System itself, and yet it was pieced together primarily from the study of a few dozen objects in two nearby, low-mass star formation regions, the Taurus-Auriga and Ophiucus molecular clouds (Adams, Lada, & Shu 1987; Kenyon & Hartmann 1987). Most stars are thought to form in massive clusters containing hundreds or thousands of stars (Lada & Lada 2003). The Sun itself likely formed in a dense, cluster environment (Hester & Desch 2005). High spatial resolution observations of star formation have historically been restricted to molecular clouds within ∼1 kpc of the Sun, a volume containing only one bona fide OB cluster, the Trapezium cluster ionizing the Orion H II region (Hillenbrand 1997). As a consequence, our understanding of the process through which massive (>8 $M_{\odot}$) stars form in spite of strong feedback is incomplete, as is our understanding of the effect of the harsh cluster environment on the formation of lower-mass stars.

On a galactic scale, Taurus-Auriga is invisible, and Orion is barely a run-of-the-mill H II region, ionized by a single O6 star (Genzel & Stutzki 1989). Thanks to advances in the capabilities of multiwavelength observational facilities, particularly the high-resolution IR surveys produced with the *Spitzer Space Telescope*, it is now possible to extend detailed investigations of the stellar populations in young massive clusters out to distances of several kpc, including major sites of Galactic star formation in the nearest spiral arms. This thesis is about the interrelationships between recent star formation and molecular cloud environments. I focus primarily on M17, a Galactic H II region that is sufficiently luminous to serve as an analog of observable extragalactic star formation regions. From the global emission properties of a giant H II region, to the shaping of the ISM by massive star feedback, to a census of individual stars and YSOs in an extended molecular cloud complex, this research reveals the potential for connecting our locally-derived knowledge of star formation to a global picture of the Milky Way as a star-forming galaxy.

1.1.1 Extragalactic Star Formation Parameterizations

In the seminal work quantifying the relation between star formation and global galactic ISM, Schmidt (1959) postulated that the SFR surface density $\Sigma_{\rm SFR}$ ($M_{\odot}$ yr^{-1} kpc^{-2}) varies as a power-law N of the ISM gas surface density $\Sigma_{\rm gas}$ ($M_{\odot}$ pc^{-2}), such that

$$\Sigma_{\rm SFR} \propto \Sigma_{\rm gas}^{N}. \tag{1.1}$$

Based upon the luminosity function of Galactic disk stars within 500 pc of the Sun and a model of the local ISM gas density, Schmidt (1959) concluded that the value of N was around 2.

This original formulation of the "Schmidt Law" painted galactic star formation with a very broad brush, averaging over several Gyr of star formation history. But SFRs vary over time. Recent and ongoing star formation have an immediate impact on galaxy morphology, providing one of the basic discriminators used in the Hubble classification of galaxies (Hubble 1926). Hence a great deal of effort has been expended on cultivating observational tracers sensitive to star formation that has occurred within the past ~10 Myr.

Kennicutt (1998a) presented an overview of the various diagnostic methods used to measure extragalactic SFRs. All such methods are based on stellar population synthesis models. Synthesis models generate integrated spectra of stellar populations as functions of mass and age, which can then be compared either to observed spectra or to broadband colors. The IMF is at the core of such models, as it provides the weighting used in the selection of stars from grids of stellar evolutionary tracks. In the standard form of the IMF, first identified by Salpeter (1955), the frequency of stars at a given mass is given by

$$\xi(M_\star) \propto M_\star^{\gamma}, \tag{1.2}$$

where $\xi(M_\star)dm$ is the number of stars in the mass interval $m, m+dm$ and $\gamma \approx -1.35$ for $M_\star > 0.5$ $\mathrm{M}_\odot$ (Kroupa 2001). The very steep mass-luminosity relation of main-sequence stars, $L \propto M_\star^{3.5}$, rises faster toward higher stellar masses than the IMF falls, and so the integrated light from young stellar populations is completely dominated by the OB stars in H II regions.

Optical and near-IR recombination lines provide a straightforward means of counting the Lyman continuum photons responsible for ionizing H II regions. The Hα line is the most commonly used, thanks to its brightness and easy accessibility to ground-based observations (Kennicutt 1998a). The principal drawback of Hα as an SFR tracer is extinction of line photons, especially in the case of young H II regions surrounded by large amounts of obscuring dust. Near-IR recombination lines such as Pα have been gaining popularity as observational facilities have continued to improve (e.g. Calzetti et al. 2007). When ionizing photons are absorbed by dust, their energy is reradiated in the thermal IR, making IR continuum luminosity a highly promising SFR diagnostic, at least in the case of individual H II regions or circumnuclear starbursts where the stellar radiation field is dominated by young stars. Applying the population synthesis model of Leitherer & Heckman (1995) to a continuous burst of star formation lasting 10–100 Myr and assuming solar metallicity, Kennicutt (1998b) derived the following relation:

$$\text{SFR } (\text{M}_\odot \text{ yr}^{-1}) = 4.5 \times 10^{-44} L_{\text{FIR}} \text{ (erg s}^{-1}) = 1.7 \times 10^{-10} L_{\text{FIR}} \text{ (L}_\odot). \tag{1.3}$$

Using this calibration requires that L_{FIR} be measurable (or at least estimable) over the entire far-IR wavelength range carrying the bolometric luminosity of the starburst, generally 10–100 μm. The *Infrared Astronomy Satellite (IRAS)* survey provided the requisite far-IR fluxes for 30,000 galaxies (Moshir et al. 1992). Calzetti et al. (2007) used individual star-forming regions in 33 galaxies observed by the *Spitzer* Infrared Nearby Galaxies Survey Kennicutt et al. (SINGS; 2003) to cross-calibrate the emission in the Multiband Imaging Photometer for *Spitzer* (MIPS) 24 μm band with Lyman continuum photon flux traced by the Pα line. They found, for high-metallicity environments dominated by star formation, that

$$\text{SFR } (\text{M}_\odot \text{ yr}^{-1}) = 1.27 \times 10^{-38} [L_{24} \text{ (erg s}^{-1})]^{0.8850} = 6.64 \times 10^{-9} [L_{24} \text{ (L}_\odot)]^{0.8850}, \tag{1.4}$$

where L_{24} is the luminosity emitted in the 24 μm MIPS band. The relation is nonlinear because L_{24} depends upon the shape of the spectrum emitted by the dust, a function of the dust temperature. The Calzetti et al. (2007) calibration is useful because it removes the need to observe the entire far-IR spectrum, instead using a single mid-IR band. A giant leap forward from *IRAS*, *Spitzer* provided resolution and sensitivity sufficient to detect individual star-forming complexes in nearby galaxies, as well as to extend the detection of star-forming galaxies to higher and higher redshifts (e.g. Mobasher et al. 2005; Wiklind et al. 2008).

Kennicutt (1998b) compiled a sample of 61 normal disk and 36 IR-selected starburst galaxies spanning 5 orders of magnitude in gas surface density and over 6 orders of magnitude in SFR surface density. The galaxies in the Kennicutt (1998b) sample, reproduced in Figure 1.1, follow a Schmidt Law (Equation 1.1) with $N = 1.4 \pm 0.15$. This result has come to be known as the “Schmidt–Kennicutt Law.” The simplest physical explanation for this rather remarkable correspondence is one in which the global SFR is set by the rate of self-gravitational collapse driven by large-scale perturbations within the disk, for example star formation triggered by spiral density waves. In this case, the timescale for perturbations is set by the local dynamical timescale, τ_d, and

$$\rho_{\text{SFR}} \propto \frac{\rho_{\text{gas}}}{\tau_d} \propto \frac{\rho_{\text{gas}}}{(G\rho_{\text{gas}})^{-0.5}} \propto \rho_{\text{gas}}^{1.5}. \tag{1.5}$$

For a galactic disk with near-constant scaleheight, the volume densities in the above equation can be replaced with surface densities, retrieving the Schmidt–Kennicutt Law. The dynamical timescale τ_d is often tied to the orbital timescale in the disk (Silk 1997).

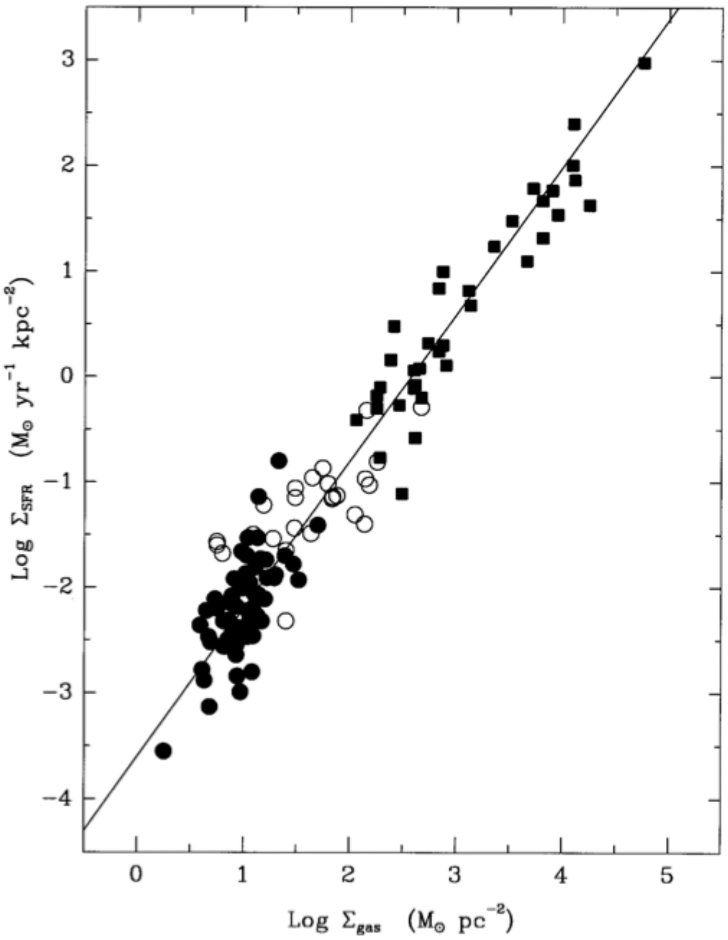

Fig. 1.1.— Composite Schmidt-Kennicutt Law, reproduced from Kennicutt (1998b). SFR surface density is plotted versus gas surface density for normal disk galaxies (*filled circles*), starburst galaxies (*squares*) and the centers of the normal disk galaxies (*open circles*). The line is a least-squares fit with power-law index $N = 1.40$.

All of the parameterizations of extragalactic star formation outlined above are empirical by nature; it is still not well understood *why* they work. The Schmidt–Kennicutt Law appears to hold over a wide range of galaxy conditions and types, but it is an inherently unreliable predictor of the SFR in any given galaxy. There is a large amount of scatter about the trend plotted in Figure 1.1; the scatter approaches 2 dex at $\Sigma_{\rm gas} = 10$ M$_\odot$ pc^{-1}, which happens to be the mean gas surface density at the Solar circle in the Milky Way (see Figure 1.2). The best-fit slope to the normal disk galaxies alone is $N = 2.47 \pm 0.39$ (Kennicutt 1998b), a significant departure from the best-fit slope when starburst galaxies are included (Figure 1.1). Hence, normal galaxies are *not* consistent with the slope of $N = 1.5$ predicted by the perturbational origin of the Schmidt Law (Equation 1.5). This is puzzling, because in normal spiral galaxies large-scale perturbations tied to the orbital timescale might be expected to play a dominant role in driving star formation, while starbursts are more likely to have an external trigger, such as an interaction or merger event (Bushouse 1986; Kennicutt et al. 1987).

1.1.2 The Milky Way As a Star-Forming Galaxy

Smith, Biermann, & Mezger (1978; hereafter SBM78) established the $\sim$5 $\mathrm{M}_\odot$ yr^{-1} "canonical" value for the Galactic SFR by calculating the number of O stars required to ionize all of the Galactic H II regions then known from radio continuum surveys. Calibrating the total stellar mass, $\langle M \rangle$, to the Lyman continuum photon emission rate, $\langle N_c \rangle$, SBM78 derived

$$\langle M \rangle / \langle N_c \rangle = 4.6 \times 10^{-47}\ \mathrm{M}_\odot / (\mathrm{phot\ s}^{-1}), \tag{1.6}$$

assuming a Salpeter (1955) IMF and using the models of Panagia (1973) to relate ionizing photon fluxes emitted to the stellar masses of OB stars. For Galactic H II regions, SBM78 calculated $\langle N_c \rangle$ from the thermal (free-free) radio continuum flux emitted by Galactic H II regions, using Equation 2 of Mezger, Smith, & Churchwell (1974) and correcting for a factor of $\sim$2 internal absorption of ionizing photons by dust associated with the ionized gas. Equation 1.6 is converted into a rate by dividing by $t(\mathrm{H\ II}) = 5 \times 10^5$ yr, the adopted average age of Galactic radio H II regions (SBM78):

$$\mathrm{SFR}\ (\mathrm{M}_\odot\ \mathrm{yr}^{-1}) = 9.2 \times 10^{-53} \langle N_c \rangle\ (\mathrm{phot\ s}^{-1}). \tag{1.7}$$

Thermal radio continuum is a poor diagnostic of extragalactic SFRs because the radio emission from ionized gas is relatively faint, and the emission measure is a strong function of gas density, making older, less dense H II regions undetectable. Actively star-forming galaxies tend to be dominated by non-thermal emission from supernovae at radio wavelengths.

Building upon the work of SBM78, Güsten & Mezger (1982) made a new estimate of the Galactic SFR from radio H II regions, taking into account the thermal radio emission from "extended low-density" H II regions, including ionizing photons escaping from giant H II regions. Güsten & Mezger (1982) reported a Galactic SFR of 13 $\mathrm{M}_\odot$ yr^{-1}. This higher SFR was due neither to a more thorough accounting of Galactic star formation nor to a significant fraction of ionizing photons escaping from giant H II regions. Instead, the departure from SBM78 is explained almost entirely by the adoption of the lognormal IMF of Miller & Scalo (1979), which, compared to a Salpeter power-law IMF, predicts fewer high-mass stars relative to solar-mass stars.[2] This increases $\langle M\rangle/\langle N_c\rangle$ from Equation 1.6 by a factor of ~2. In addition, Güsten & Mezger (1982) assumed a maximum stellar mass of 60 $M_\odot$ for the most luminous O stars, while SMB78 assumed 100 $M_\odot$, and decreasing the maximum stellar mass also tends to increase $\langle M\rangle/\langle N_c\rangle$, since, very approximately, $N_c(M) \propto L(M) \propto M^{3.5}$. Such discrepancies illustrate vividly that the reported values of the Galactic SFR are subject to large systematic uncertainties. These systematics are largely due to the fact that, just as in external galaxies, to date no measurement of the Galactic SFR has involved the *direct* detection of stars.

More recent estimates of the Galactic SFR using independent methods have yielded values similar to the SBM78 result. In one of the more innovative measurements, Diehl et al. (2006) used the *INTEGRAL* spacecraft to observe gamma-ray line emission from radioactive ^{26}Al and calculated a rate of 1.9 ± 1.1 core-collapse supernovae per century in the Galaxy, corresponding to a reported SFR of ~4 $M_\odot$ yr^{-1}. Misiriotis et al. (2006) constructed a model of the spatial distribution of stars, gas, and dust in the Galaxy constrained by *COBE* satellite observations of the Galactic IR emission. The best model gave a Galactic SFR of 2.7 $M_\odot$ yr^{-1}. Because they essentially used a population synthesis model tied to far-IR observations, Misiriotis et al. (2006) were able to derive an "internal" Schmidt Law for the Milky Way that showed good agreement with the extragalactic Schmidt-Kennicutt Law (Figure 1.2).

The Milky Way is generally excluded from comparative studies of star-forming galaxies because we lack a unified, global picture of its structure and star formation activity. The location of the Solar System inside the Galactic disk gives us a disadvantaged perspective when attempting to study the Milky Way as a whole. Sightlines through the disk suffer very high extinction due to the dusty ISM, hence SFR diagnostics depending upon optical/UV observational tracers such as Hα, widely viewed as among the most reliable diagnostics of extragalactic SFRs (Kennicutt 1998a,b; Calzetti et al. 2007), cannot be applied to the Milky Way (just as they cannot be applied to external disk galaxies viewed nearly edge-on). Radio and far-IR observations are unaffected by extinction and thus far have provided most of the Galactic SFR estimates (SMB78; Miller & Scalo 1979; Güsten & Mezger 1982; Misiriotis et al. 2006). The IR shows the greatest promise for providing convergence between extragalactic and Galactic SFR measurements, because there is

---

[2] Scalo (1998) writes: "It has been a source of consternation for me that many authors, especially in the areas of PMS stars and galaxy evolution, continue to use the lognormal IMF advocated by [Miller & Scalo (1979)]. There is no longer any evidence I know of for a lognormal IMF." In this thesis, I will generally employ a modified version of the Salpeter IMF that allows the power-law slope to change, or "break," at several distinct mass values, with the first and most significant break occurring near 0.5 $M_\odot$ (Kroupa 2001). Such is the form of the IMF in the Orion Nebula Cluster, to date the only massive cluster to have its IMF measured over a mass range spanning O stars to brown dwarfs (Muench et al. 2002).

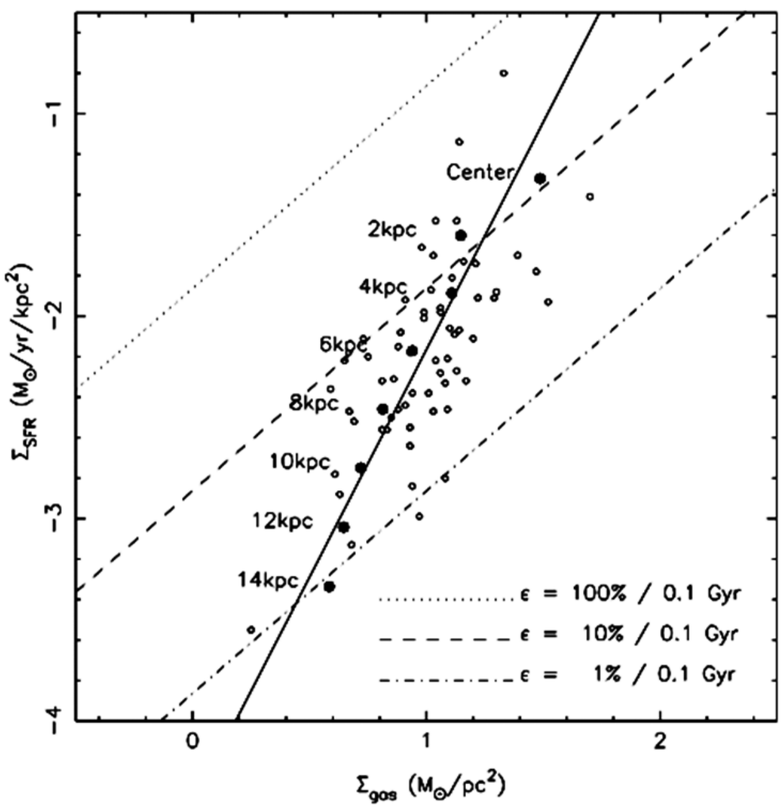

Fig. 1.2.— Schmidt-Kennicutt Law for the Milky Way disk, reproduced from Misiriotis et al. (2006). Values for $\log \Sigma_{\rm SFR}$ versus $\log \Sigma_{\rm gas}$ in successive annuli about the Galactic center are plotted as *filled circles* with the annular radius labeled. The solid line represents a best-fit power-law index $N = 2.18$. The normal disk galaxies from Kennicutt (1998b) are plotted as *open circles*. Three parallel *dotted*, *dashed*, and *dash-dotted* lines correspond to star formation efficiencies of 100%, 10%, and 1% per Gyr, respectively.

no reason why a calibration similar to the Calzetti et al. (2007) 24 μm diagnostic (Equation 1.4) could not be developed for the Galactic case. There remain, however, significant challenges stemming from uncertain distances to Galactic H II regions and confusion of multiple star-formation regions overlapping along a given line of sight.

In spite of the observational challenges created by extinction, uncertain distances, and confusion, the Milky Way *should* be the ultimate SFR calibrator. The Galaxy offers the overwhelming advantage of high resolution. Instrumentation technology has advanced to the point that it is now routine to resolve individual stars in young embedded clusters several kpc distant. This makes it possible to directly probe the young stellar populations in massive clusters ionizing Galactic H II regions, constraining the IMF and stellar ages and investigating the detailed physical processes governing star formation. The resulting detailed star formation histories of Galactic H II regions and the associated molecular clouds could then be calibrated against diffuse emission tracers, like integrated IR luminosity, that are used to study star formation in external galaxies.

And yet, as I will demonstrate in this Thesis, the details are messy. Star formation is a highly complex, non-equilibrium process, and it is somewhat surprising that any relation as simple as a Schmidt Law holds at all. Of particular concern is the role played by feedback from massive stars. The parameterizations of Equations 1.1 and 1.5 tacitly assume that the large-scale star formation efficiency[3] is a well-behaved, monotonically increasing function of gas density only (Figure 1.2). It is far from clear why this should be the case. Ionization by massive stars heats the ISM, which would seem to suppress further star formation, but given that the ISM is inhomogeneous, the resulting overpressurization may trigger subsequent star formation by compression of cool gas clumps embedded in the warm, ionized medium ("radiative implosion"; Stutzki et al. 1988). Driven by thermal pressure and winds from massive stars (Weaver et al. 1977), H II regions expand and erode their natal molecular clouds, hence suppressing further star formation, but molecular gas is swept up in advance of the ionization front, and the resulting compression may trigger subsequent star formation ("collect-and-collapse"; Whitworth et al. 1994; Dale et al. 2007). Finally, massive star clusters produce multiple supernova explosions that almost certainly destroy the remnants of the original molecular cloud during their initial, violent adiabatic expansion phase, halting star formation, but numerical simulations predict that more evolved supernova remnants expanding isothermally can trigger star formation in neighboring molecular clouds $\gtrsim$14 pc away (Foster & Boss 1996).

1.2 The Galactic Plane in the Age of IR Surveys

Thanks to a wealth of new observational data, much of it originating from unbiased surveys with images and source catalogs compiled in publicly-available archives, sites of active star formation in the Galactic plane have been revealed in unprecedented detail. The sheer volume of data presents an embarrassment of riches, and nowadays the pace of new discoveries seems to be limited primarily by a shortage of manpower. In particular, the capabilities of IR observatories have increased by orders of magnitude in resolution and sensitivity over the past 30 years, since the original radio measurement of the Galactic SFR was made (SBM78). The IR is the best part of the spectrum for the direct observational study of individual stars in young, embedded clusters. All stellar photospheres emit IR photons, which efficiently pass through

---

[3] In contrast to the "local" star formation efficiency commonly defined in Galactic studies of individual molecular clouds as $M_{\rm stars}/(M_{\rm stars} + M_{\rm gas})$, the large-scale star formation efficiency is the fraction of gas in a galactic system consumed by star formation per unit time.

obscuring dust. YSOs are particularly good targets for IR surveys because they exhibit excess IR emission over their photospheres due to the presence of dusty circumstellar disks and infalling envelopes.

1.2.1 IR Surveys Before *Spitzer*

The groundbreaking *IRAS* survey (Neugebauer et al. 1984) mapped 95% of the sky at 12, 25, 60, and 100 μm, including the entire Galactic plane. As mentioned above, *IRAS* led to the adoption of far-IR diagnostics of extragalactic SFRs (Equation 1.3), and it spurred forward Galactic star formation research as well. *IRAS* revealed major sites of ongoing massive star formation throughout the Galaxy, including numerous previously undiscovered ultracompact (UC) H II regions ionized by O stars (Wood & Churchwell 1989).[4] The main drawback of *IRAS* was its low (several arcmin) resolution. While numerous low-mass YSOs in nearby regions like Taurus-Auriga were observed, *IRAS* could not resolve individual sources in more distant, massive clusters. Still, *IRAS* remains a valuable resource, especially for obtaining far-IR luminosities of large Galactic clouds and H II regions (see Chapter 2).

The Air Force *Midcourse Space Experiment (MSX)* surveyed the Galactic plane in four mid-IR bands from 8 to 21 μm (Price et al. 2001). The $\sim 18''$ spatial resolution of *MSX* provided a dramatic improvement over *IRAS*, and the absolute photometric calibration of *MSX* remains the gold standard among IR surveys (see Chapter 2). *MSX* is useful for obtaining mid-IR fluxes of high-mass YSOs (generally corresponding to early B stars on the main sequence) that are bright enough to saturate the *Spitzer* survey images (Chapter 4). *MSX* also revealed thousands of IR dark clouds, seen in silhouette against the 8 μm Galactic background emission, that trace the cores of dense molecular clouds (Simon et al. 2006). IR dark clouds often host massive YSOs in the earliest stages of formation (see Shepherd et al. 2007, for example).

The Two-Micron All-Sky Survey (2MASS; Skrutskie et al. 2006) was the seminal near-IR (JHK_S) survey of the entire sky. Although still affected by high extinction through the Galaxy, 2MASS provided an unprecedented view of the Galactic disk and bulge stellar populations. The 2MASS astrometric and magnitude systems rapidly became standards for multiwavelength studies.

1.2.2 The *Spitzer* Galactic Plane Surveys

Spitzer was launched into an Earth-trailing orbit on 25 August 2003, the fourth and final of the NASA Great Observatories. In spite of its relatively small, 0.85-m aperture, *Spitzer* boasted unprecedented

---

[4] UC H II regions are an early stage of massive stellar evolution, during which the star is still deeply embedded in the dense molecular cloud core and the radius of the ionized region is small.

resolution and sensitivity in the mid-IR (3.6–70 μm) and the capacity to scan large areas of the sky relatively quickly. Thus *Spitzer* was one of the greatest survey telescopes ever put into space, although it was not used exclusively for that purpose.

The Galactic Legacy Infrared Mid-Plane Survey Extraordinaire (GLIMPSE; Benjamin et al. 2003; Churchwell et al. 2009) comprised a series of 3 surveys with *Spitzer*, utilizing the Infrared Array Camera (IRAC) to image the innermost 130° of the Galactic plane at 3.6, 4.5, 5.8, and 8.0 μm.[5] The $\sim 2''$ spatial resolution of IRAC was well-matched to that of 2MASS while the longer wavelengths were even less affected by extinction. GLIMPSE star counts quickly began to revolutionize our understanding of Galactic structure, confirming that the Milky Way is a strongly barred galaxy (Benjamin et al. 2005) and that the disk is likely dominated by 2 major spiral arms, detected as overdensities in the evolved stellar population of the disk (Churchwell et al. 2009). The MIPS Galactic Plane Survey (MIPSGAL; Carey et al. 2009) imaged the area covered by the first 2 GLIMPSE surveys with the *Spitzer*/MIPS instrument at 24 and 70 μm. The GLIMPSE and MIPSGAL survey areas include nearly all of the Galactic plane inside the Solar circle, the regions containing the highest gas density and hence the greatest star formation activity in the Galaxy (Figure 1.2).

As I will show in Chapter 4, GLIMPSE and MIPSGAL are highly sensitive to YSOs in the intermediate mass range (3 $\mathrm{M}_\odot \leq M_\star \leq 10\ \mathrm{M}_\odot$), where determinations of the IMF are the most reliable (Scalo 1998). Because intermediate-mass stars lose detectable circumstellar disks very quickly ($\lesssim$1 Myr; Haisch, Lada, & Lada 2001a), *Spitzer* reveals the youngest stellar populations in the Galaxy. Star formation is distributed widely throughout giant molecular clouds (GMCs) associated with prominent Galactic H II regions (Whitney et al. 2004; Megeath et al. 2005; Indebetouw et al. 2007). Many YSOs in the earliest stages of formation are found in the photodissociation regions (PDRs) around H II regions (Deharveng, Zavagno, & Caplan 2005; Koenig et al. 2008; and see Chapter 4), suggesting that the expansion of H II regions often triggers subsequent bursts of star formation. These recent results have sparked renewed interest in the idea, first proposed by (Elmegreen & Lada 1977), that massive star formation propagates in successive generations throughout GMC complexes.

Spitzer has proven to be a highly effective tool for detecting Galactic H II regions. Churchwell et

---

[5] A fourth survey, GLIMPSE 360, is planned for the post-cryogenic *Spitzer* "warm" mission, beginning in mid-2009. Due to drastically increased temperatures, the MIPS, IRS, and 2 of the IRAC detectors will no longer function. Only the IRAC 3.6 and 4.5 μm bands will be available. Using these 2 bands, GLIMPSE 360 will image the outer Galactic plane areas not included in previous *Spitzer* surveys.

al. (2006, 2007) compiled (very incomplete) catalogs containing nearly 600 IR "bubbles" (apparent shell structures). The vast majority of these bubbles are thought to be PDRs outlining H II regions, although only ∼30% correspond to known radio H II regions. H II regions ionized by stars hotter than O6 likely produce wind-driven bubbles (Watson et al. 2008). In this thesis I will treat the subjects of H II regions, wind-blown bubbles, and triggered star formation in detail (Chapters 2–4).

1.3 Thesis Goals and Outline

This Thesis lays the foundations for a multi-year research program to investigate the global distribution of star formation in the Galaxy and make a new determination of the Galactic SFR. The primary goal is to obtain a detailed census of the young stellar population associated with a bright Galactic H II region and to compare the resulting star formation history with global SFR tracers. Other important goals include:

- Measure the IR–radio spectral energy distribution (SED) of a giant H II region for comparison with extragalactic SFR diagnostics.
- Relate IR emission morphology to the underlying structure of Galactic H II regions and molecular clouds. Identify easily recognizable observable properties of H II regions in IR surveys.
- Investigate the role of winds from massive stars in shaping H II region structure. Is star formation triggered by expanding H II regions an important component of the overall SFR?
- Develop diagnostics for the mass and age distributions of YSOs detected in GLIMPSE and MIPSGAL using SED models, and in the process test the applicability of YSO models to the observations.
- Demonstrate that IR survey data, in combination with radio and X-ray observations, can be used to obtain a relatively complete census of current star formation activity in Galactic GMC complexes.

In Chapter 2, I present the global SED of the M17 H II region and PDR, assembled from various IR and radio surveys. The SED is used to calculate the energy balance of the nebula, leading to new constraints on the nebular geometry and the distance to the region. I introduce IRAC band-ratio images to locate the interface between the ionized gas and PDR. Mid-IR spectroscopy confirms that emission features from polycyclic aromatic hydrocarbons (PAHs) are bright in the PDR but disappear within the H II region. The interpretation that PAH molecules are destroyed by far-ultraviolet photons provides a physical explanation for the morphology of the IR dust bubbles identified in GLIMPSE and supports their identification as H II regions (Churchwell et al. 2006, 2007). I discuss the structure of M17 in terms of a wind-blown bubble model, which is supported by the detection of diffuse, soft X-ray emission from wind-shocked, 10 MK plasma filling the interior of the H II region (Townsley et al. 2003).

In Chapter 3, I report the discovery of 6 stellar-wind bow shocks driven by O stars in the M17 and RCW 49 H II regions. The bow shocks illustrate vividly the importance of stellar winds in setting H II region dynamics and structure. Both M17 and RCW 49 are broken bubbles; they vent wind-shocked plasma into the diffuse ISM through breaches in their PDRs. The most spectacular of the bow shocks in RCW 49 provides indirect evidence for a flow of hot plasma escaping the H II region at a velocity of several hundred km s^{-1}.

In Chapter 4, I analyze star formation activity in the extended molecular cloud structures associated with M17. I compare various methods for identifying YSOs from their broadband IR colors or SEDs and discuss the selection biases inherent in each method. Contamination from unassociated sources with similar IR colors to young stars and YSOs is a significant problem that any census of the stellar content of star-formation regions in the inner Galaxy based on IR observations must overcome. I develop a method for removing contaminants statistically, producing a highly-reliable catalog of YSOs with high probability of association with the M17 complex. I compute a lower limit on the SFR in the extended environment around M17 and find it to be >16% of the SFR in the central regions of M17. The M17 H II region itself lies on the rim of an extended bubble, 20 pc in diameter, outlining an H II region several Myr old. I identify a group of candidate ionizing stars inside the bubble and examine the possibility that the expansion of this bubble triggered the majority of current star formation in the M17 region. If this is the case, then sequential triggering by massive star feedback is a fundamental mode of star formation in GMC complexes.

In Chapter 5, I calculate the SFR of M17 predicted from the global IR and radio emission (Chapter 2), using SFR diagnostics from both Galactic and extragalactic studies (§1.1). I compare these predictions with the SFR of M17 derived from detailed analysis of the stellar population (Chapter 4), and discuss the resulting discrepancies in terms of the systematic errors involved in SFR determinations. I conclude Chapter 5 with a discussion of the difficulty of interpreting the Schmidt Law in light of the complicated, multi-generational nature of star formation in GMC complexes.

In Chapter 6, I summarize my conclusions and suggest directions for future work.

References

Adams, F. C., Lada, C. J., & Shu, F. H. 1987, ApJ, 312, 788

Benjamin, R. A. et al. 2003, PASP, 115, 953

Benjamin, R. A. et al. 2005, ApJ, 630, L149

Broos, P. S. et al. 2007, ApJS, 169, 353

Bushouse, H. A. 1986, AJ, 91, 255

Calzetti, D. et al. 2007, ApJ, 666, 870

Carey, S. J. et al. 2009, PASP, 121, 76

Chiappini, C., Matteucci, F., & Gratton, R. 1997, ApJ, 477, 765

Churchwell, E., Povich, M. S., et al. 2006, ApJ, 649, 759

Churchwell, E., Watson, D. F., Povich, M. S., et al. 2007, ApJ, 670, 428

Churchwell, E. et al. 2009, PASP, 121, 213

Dale, J. E., Bonnell, I. A., & Whitworth, A. P. 2007, MNRAS, 375, 1291

de Rossi, M. E., tissera, P. B., de Lucia, G., & Kaufmann, G. 2009, MNRAS, 395, 210

Deharveng, L., Zavagno, A., & Caplan, J. 2005, A&A, 433, 565

Diehl, R. et al. 2006, Nature, 439, 45

Elmegreen, B. G. & Lada, C. J. 1977, ApJ, 214, 725

Foster, P. N. & Boss, A. P. 1996, ApJ, 468, 784

Genzel, R. & Stutzki, J. 1989, ARA&A, 27, 41

Güsten, R. & Mezger, P. G. 1982, Vistas in Astronomy, 26, 159

Haisch, K. E., Lada, E. A., & Lada, C. J. 2001a, AJ, 121, 2065

Hester, J. J. & Desch, S. J. 2005, ASPC, 341, 107

Hillenbrand, L. A. 1997, AJ, 113, 1733

Hubble, E. P. 1926, ApJ, 64, 321

Indebetouw, R., Robitaille, T. P., Whitney, B. A., Churchwell, E., Babler, B., Meade, M., Watson, C., & Wolfire, M. 2007, ApJ, 666, 321

Kaufmann, G. & Haehnelt, M. 2000, MNRAS, 311, 576

Kennicutt, R. C., Jr., Roettiger, K. A, Keel, W. C., van der Hulst, J. M., & Hummel, E. 1987, AJ, 93, 1011

Kennicutt, R. C., Jr. 1998, ARA&A, 36, 189

Kennicutt, R. C., Jr. 1998, ApJ, 498, 541

Kennicutt, R. C., Jr. et al. 2003, PASP, 115, 928

Kenyon, S. J. & Hartmann, L. 1987, ApJ, 323, 714

Koenig, X. P., Allen, L. E., Gutermuth, R. A., Hora, J. L., Brunt, C. M., & Muzerolle, J. 2008, ApJ, 688, 1142

Kroupa, P. 2001, MNRAS, 322, 231

Lada, C. J. & Lada, E. 2003, ARA&A, 41, 57

Larson, R. B. 1974, MNRAS, 166, 585

Leitherer, C. & Heckman, T. M. 1995, ApJS, 96, 9

Megeath, S. T. et al. 2005, in IAU Symp. 227: Massive Star Birth: A Crossroads of Astrophysics, eds. R. Cesaroni, M. Felli, E. Churchwell, & C. M. Walmsley, 383

Mezger, P. G., Smith, L. F., & Churchwell, E. 1974, A&A, 32, 269

Miller, G. E. & Scalo, J. M. 1979, ApJS, 41, 513

Misiriotis, A., Xilouris, E. M., Papamastorakis, J., Boumis, P. & Goudis, C. D. 2006, A&A, 459, 113

Mobasher, B. et al. 2005, ApJ, 635, 832

Moshir, M. et al. 1992, Explanatory Supplement to the IRAS Faint Source Survey, Version 2, JPL, D-10015 8/92. Pasadena, California

Muench, A. A., Lada, E. A., Lada, C. J. & Alves, J. 2002, ApJ, 573, 366

Neugebauer, G. et al. 1984, ApJ, 278, L1

Panagia, N. 1973, AJ, 78, 929

Price, S. D., Egan, M. P., Carey, S. J., Mizuno, D. R., and Kuchar, T. A. 2001, AJ, 121, 2842

Scalo, J. 1998, ASPC, 142, 201

Schmidt, M. 1959, ApJ, 129, 243

Salpeter, E. E. 1955, ApJ, 121, 161

Shepherd, D. S., Povich, M. S. et al. 2007, ApJ, 669, 464

Shu, F. H., Adams, F. C. & Lizano, S. 1987, ARA&A, 25, 23

Silk, J. 1997, ApJ, 481, 702

Simon, R., Jackson, J. M., Rathborne, J. M., & Chambers, E. T. 2006, ApJ, 639, 227

Skrutskie, M. F. et al. 2006, AJ, 131, 1163

Smith, L. F., Biermann, P., & Mezger, P. G. 1978, A&A, 66, 655 (SMB78)

Stutzki, J., Stacey, G. J., Genzel, R., Harris, A. I., Jaffe, D. T., & Lugten, J. B. 1988, ApJ, 332, 379

Townsley, L. K., Feigelson, E. D., Montmerle, T., Broos, P. S., Chu, Y.-H., & Garmire, G. P. 2003, ApJ, 593, 874

Watson, C., Povich, M. S., Churchwell, E. B., Babler, B. L., Chunev, G., Hoare, M., Indebetouw, R., Meade, M. R., Robitaille, T. P. & Whitney, B. A. 2008, ApJ, 681, 1341

Weaver, R., McCray, R., Castor, J., Shapiro, P., & Moore, R. 1977, ApJ, 218, 377

Whitney, B. A., Indebetouw, R., Bjorkman, J. E., & Wood, K. 2004, ApJ, 617, 1177

Whitworth, A. P., Bhattal, A. S., Chapman, S. J., Disney, M. J., & Turner, J. A. 1994, MNRAS, 268, 291

Wikland, T., Dickinson, M., Gerguson, H. C., Giavalisco, M., Mobasher, B., Grogin, N. A., & Panagia, N. 2008, ApJ, 676, 781

Wood, D. O. S. & Churchwell, E. 1989, ApJ, 340, 265

Chapter 2

A Multiwavelength Study of M17: The Spectral Energy Distribution and PAH Emission Morphology of a Massive Star-Formation Region

Originally published by M. S. Povich, J. M. Stone, E. Churchwell, E. G. Zweibel, M. G. Wolfire, B. L. Babler, R. Indebetouw, M. R. Meade, & B. A. Whitney in The Astrophysical Journal, Volume 660, Issue 1, pp. 346–362 (May 2007)

Abstract

We combine diffuse emission photometry from GLIMPSE and several other Galactic plane surveys covering near-IR through radio wavelengths to synthesize a global spectral energy distribution (SED) for the M17 complex. By balancing the integrated flux in the SED with the total bolometric luminosity of all known O and early B stars in the ionizing cluster, we estimate a distance to M17 of $1.6^{+0.3}_{-0.1}$ kpc. At this distance, the observed total flux in the SED corresponds to a luminosity of $2.4 \pm 0.3 \times 10^6$ $L_\odot$. We find that the SED from the H II region peaks at shorter wavelengths and has a qualitatively different shape than the SED from the photodissociation region (PDR). We find that polycyclic aromatic hydrocarbons (PAHs) are destroyed over a short distance or edge at the boundary of the H II region. We demonstrate that this PAH destruction edge can be located easily using GLIMPSE band-ratio images and confirm this using *Spitzer*/IRS spectra. We investigate the relative roles of extreme ultraviolet (EUV) and X-ray photons in the destruction of PAHs, concluding that X-rays are not an important PAH destruction mechanism in M17 or, by extension, in any other Galactic H II region. Our results support the hypothesis that PAHs are destroyed by EUV photons within H II regions. PAHs dominate the mid-IR emission in the neutral PDR beyond the ionized gas.

2.1 Introduction

M17, the Omega Nebula [W38 at $(l, b) = (15^\circ.1, -0^\circ.7)$], is a premier example of a young, massive star-formation region in the Galaxy. It has a rich observational literature that spans nearly two centuries. Felli, Churchwell, & Massi (1984; hereafter FCM84) summarized the infrared (IR) and radio observations of M17 up to 1984. A more recent review of the M17 literature and discussion of its properties is given by Townsley et al. (2003; hereafter T03). Although not the most luminous H II region in the Galaxy, M17 is one of the brightest IR and thermal radio sources in the sky, comparable to the nearby Orion Nebula (Orion A). M17 is four times more distant from the Sun than Orion and considerably more energetic. The M17 H II region is ionized by the open cluster NGC 6618, which contains over 100 OB stars (Lada et al. 1991) and has an age of less than 3 Myr (Jiang et al. 2002). The center of the cluster is dominated by a ring of 7 O stars $1'$ in diameter (Hanson, Howarth, & Conti 1997). NGC 6618 contains at least 4 O stars earlier than O6 V, the spectral type of θ^1 Ori C, the most luminous star in the Trapezium cluster in Orion.

The stars in the central part of the NGC 6618 cluster lie behind an average extinction of $A_V = 8$, but in many parts of M17 the extinction is considerably higher, with $A_V > 20$ (Hanson, Howarth, & Conti 1997). Because its complex extinction varies with both position and wavelength, M17 is optically bright but much more brilliant in the IR, and the morphology of the extended emission is highly dependent upon the wavelength observed. The underlying structure of the radio H II region is divided into two parts, usually called the northern and southern bars, lying on either side of the star cluster (see Figure 2.1 for a large-scale view of M17). The two bars with their respective photodissociation regions (PDRs) meet each other at an apparent angle of about 45°, forming an inverted "V" shape as viewed in Galactic co-ordinates, with the "V" opening away from the Galactic midplane. Although only the northern bar is observable at optical wavelengths (in Hα, for example), the southern bar contains the majority of the mass and current star formation activity, including the ultracompact (UC) H II region M17-UC1 (FCM84), the bright IR source M17 SW-IRS (also called the "Kleinmann-Wright Object", Kleinmann & Wright 1973), and numerous young stellar objects (YSOs) (Nielbock et al. 2001). Hence the southern bar and PDR are considerably brighter than the northern bar at mid-IR to radio wavelengths.

The M17 H II region is erupting from the side of the giant molecular cloud M17 SW, and the southern bar marks the primary interface between the ionization edge (I-front) of the H II region and the molecular gas (Lada 1976; FCM84). The entire H II region is expanding, with the southern bar gradually eating into the side of the molecular cloud while the northern bar is pushed outward in the opposite direction (Tsivilev & Krasnov 1999; Pellegrini et al. 2007). The physical processes shaping M17 are analogous to those operating in the Orion Nebula, but the nearly edge-on orientation of the I-front in the southern bar of M17 facilitates the detailed study of the interaction between the H II region, PDR, and molecular cloud (FCM84; Meixner et al. 1992; Chrysostomou et al. 1992; Crété et al. 1999). The entire M17 H II region can be regarded as an energetic interstellar bubble blown into the surrounding interstellar medium (ISM) by the action of the combined winds of the OB stars (Weaver et al. 1977; Koo & McKee 1992; Capriotti & Kozminski 2001) . The region between the two bars has been almost completely evacuated; T03 observed that superheated ($T \sim 10^7$ K) X-ray-emitting plasma fills the cavity and exits at the eastern opening (toward negative Galactic latitudes) as a "champagne flow" energized by multiple shocks from colliding OB winds. Hence, M17 is an extremely energetic example of the class of interstellar bubbles associated with massive star-formation regions catalogued in the Galactic Legacy Infrared Mid-Plane Survey Extraordinaire (GLIMPSE) by Churchwell et al. (2006), although M17 was not selected for the GLIMPSE bubbles catalogue due to its peculiar, "V"-shaped morphology. M17 is also considered a prime candidate site for sequential or stimulated star-formation (Elmegreen & Lada 1976). The NGC 6618 cluster members appear to be recently emerged from their natal dust envelopes while the bars contain populations of heavily embedded YSOs (Lada et al. 1991; Hanson, Howarth, & Conti 1997; Jiang et al. 2002), suggesting a differentiation in age across the complex. Following the initial wave of star formation that produced the ionizing cluster, the expansion of the H II region drives the southern bar into M17 SW, compressing it and possibly inducing marginally stable protostellar cores to collapse.

M17 has been studied extensively over a wide range of wavelengths, and due to its location near the Galactic midplane it has been observed as part of multiple Galactic plane surveys from the near-IR to radio. We have made use of new and archival image mosaics of M17 from GLIMPSE, the Two-Micron All-Sky Survey (2MASS; Skrutskie et al. 2006), the *Midcourse Space Experiment* (*MSX*; Price et al. 2001) Galactic Plane Survey, the *IRAS* Sky Survey Atlas (ISSA[1]), and the Multi-Array Galactic Plane Imaging Survey (MAGPIS; Helfand et al. 2006) to synthesize a multiwavelength picture of the global

---

[1] Go to http://irsa.ipac.caltech.edu/IRASdocs/issa.exp.sup/

diffuse emission characteristics of M17. The high mid-IR resolution and sensitivity provided by the Infrared Array Camera (IRAC) on the *Spitzer Space Telescope* allow us to map the structures of the H II region and PDRs in unprecedented detail using image mosaics from GLIMPSE. In particular, we can trace the transition between the I-front and the PDR that is outlined by emission generally attributed to polycyclic aromatic hydrocarbon (PAH) molecules. Complementary spectra from the *Spitzer* Infrared Spectrograph (IRS) provide evidence of the changing ionization state of the gas and the emergence of PAH emission features, supporting our interpretation of the GLIMPSE images. We summarize the various datasets used in this study in §2.2, and we discuss our aperture photometry and construction of a global spectral energy distribution (SED) for M17 in §2.3. Analysis of the PAH emission morphology and the role of extreme ultraviolet (EUV) photons and possibly X-rays in destroying PAH molecules are presented in §2. 4. Our conclusions are summarized in §2.5.

2.2 The Data

2.2.1 GLIMPSE and 2MASS

M17 is the brightest large ($> 10'$ in extent) source of diffuse mid-IR emission in the entire GLIMPSE survey area ($|l| = 10°$–$65°$, $|b| \leq 1°$; Benjamin et al. 2003). This survey imaged the Galaxy using the four bands of *Spitzer*/IRAC, centered at 3.6, 4.5, 5.8, and 8.0 μm with corresponding bandwidths of 0.75, 1.0, 1.4, and 2.9 μm (Fazio et al. 2004). High-resolution ($1.2''$ pixels) image mosaics were created by the GLIMPSE pipeline[2] from Basic Calibrated Data (BCD) image frames processed by the *Spitzer* Science Center (SSC). The GLIMPSE pipeline removes artifacts such as stray light (all bands), muxbleed ([3.6] and [4.5] bands), and banding ([5.8] and [8.0] bands).[3] The SSC Mopex package was used to mask image artifacts (primarily cosmic rays) and the IPAC Montage package was used to mosaic the images. Mosaics produced from 2MASS (Skrutskie et al. 2006) data provide complementary images to GLIMPSE in the near-IR JHK_S bands.

A modified version of Daophot (Stetson 1987) was used to extract point sources detected at greater than the 2σ level from the GLIMPSE and 2MASS image frames. Daophot creates residual images of the GLIMPSE images with the point sources removed. These residual frames were mosaicked in Montage to

---

[2] Details of the data processing can be found at http://www.astro.wisc.edu/glimpse/docs.html

[3] See the *Spitzer* Observer's Manual at http://ssc.spitzer.caltech.edu/documents/som/ for definitions of the various IRAC image artifacts.

produce large-area residual image mosaics. The residuals, intended for photometry of diffuse or extended emission, are the GLIMPSE image mosaics with the point sources removed and saturated pixels masked out. The positions and fluxes of extracted point sources detected at greater than 3σ in any of the 4 GLIMPSE bands are entered into the GLIMPSE Full List of point sources, of which the Point Source Archive (sources detected at greater than 5σ in any two GLIMPSE bands) and the 99.5%-reliable GLIMPSE Point Source Catalog are subsets. For the purposes of this study, we utilize both the GLIMPSE and 2MASS mosaics and GLIMPSE residual image mosaics of M17, supplemented by GLIMPSE and 2MASS point-source fluxes from the Full List.

2.2.2 *MSX*

The Spirit III instrument on board the *MSX* satellite surveyed the Galactic plane in four IR bands (Price et al. 2001): A (isophotal wavelength 8.28 μm, $\gtrsim$50% peak intensity 6.8–10.8 μm), C (12.13 μm, 11.1–13.2 μm), D (14.65 μm, 13.5–15.9 μm), and E (21.3 μm, 18.2–25.1 μm). The spatial resolution of this instrument was $\sim$18.3$''$, and we use cutout images of M17 from the NASA/IPAC Infrared Science Archive (IRSA)[4] that have 6$''$ pixels. Although its resolution and sensitivity are inferior to that of *Spitzer*, the absolute flux calibration of *MSX*, determined in-flight by measuring the fluxes from projectiles fired away from the spacecraft, is reliable to $\sim$1% (Price et al. 2004). Hence *MSX* mid-IR fluxes are the most accurate currently available, providing the benchmark against which IRAC [8.0] fluxes can be compared (Cohen et al. 2007). The lower sensitivity of *MSX* is advantageous in studying M17, because this region is extremely bright in diffuse IR emission. The *MSX* images do not saturate in any of the 4 bands, while the IRAC [8.0] image is saturated in the brightest part of the SW bar, and the 24 μm image from the Multiband Imaging Photometer for *Spitzer* Galactic Plane Survey (MIPSGAL; Carey et al. 2006) is completely saturated over the entire M17 H II region.

2.2.3 *IRAS*

From January to November 1983 the *Infrared Astronomy Satellite (IRAS)* mapped 98% of the sky in four broad IR bands. These bands have effective wavelengths of 12, 25, 60, and 100 μm with bandwidths of 6.5, 11, 40, and 37 μm, respectively (Beichman et al. 1988). Although the sensitivity of *IRAS* was

---

[4] See http://irsa.ipac.caltech.edu/Missions/msx.html

comparable to that of *MSX*, its resolution was much lower, and the ISSA cutout images[5] have 1.5′ pixels.

2.2.4 MAGPIS Radio Continuum

The MAGPIS project, described by Helfand et al. (2006), is a compilation of high-resolution images spanning the Galactic plane from the Very Large Array (VLA) and complementary IR surveys. Cutouts from available images can be downloaded from the MAGPIS website.[6] M17 is included in the VLA New Galactic Plane Survey (New GPS) at 20 cm and the GPS at 90 cm. The 20-cm images combine data from the B, C, and D configurations of the VLA with data from the Effelsberg 100-m telescope, resulting in high-resolution images (2″ pixel sizes, with 6.2″ × 5.4″ half-power restoring beamwidth) that do not suffer from the usual interferometric loss in flux. The 90-cm images were produced from VLA maps in the B and C configurations.

2.2.5 *Spitzer*/IRS Spectra

Spitzer/IRS observations were obtained as part of program ID 3697, PI Wolfire, to map the PDR in M17 SW in the IRS SH (Short-High) and LH (Long-High) modules (Houck et al. 2004). In this work, we make use of the SH pointings, covering the wavelength range of 9.9–19.6 μm with a spectral resolution of ∼600. The observations consist of 11 sets of SH astronomical observation requests (AORs), each with 12 one-half slit steps (5.6″) in the slit-parallel direction and 4 full slit steps (4.7″) in the slit-perpendicular direction. The integration time was 6 seconds per position. The first AOR was carried out in October 2004 and the remaining 10 in April 2005. The BCDs have been processed with the SSC pipeline IRS 13.2.

2.3 SED and Energy Balance

2.3.1 Aperture Photometry

To construct multiwavelength SEDs of M17, we performed aperture photometry on images from each of the near- through mid-IR bands, using point-source subtracted images where appropriate. We extracted sub-mosaics from each of the apertures shown superimposed upon a 3-color (*red*=5.8 μm, *green*=4.5 μm, and *blue*=3.6 μm) GLIMPSE mosaic of the M17 region in Figure 2.1. The diffuse emission morphology of M17 is very complex, yet we chose mainly box-shaped apertures for ease of extraction. We are able to use

---

[5] See http://irsa.ipac.caltech.edu/Missions/iras.html

[6] See http://third.ucllnl.org/gps/

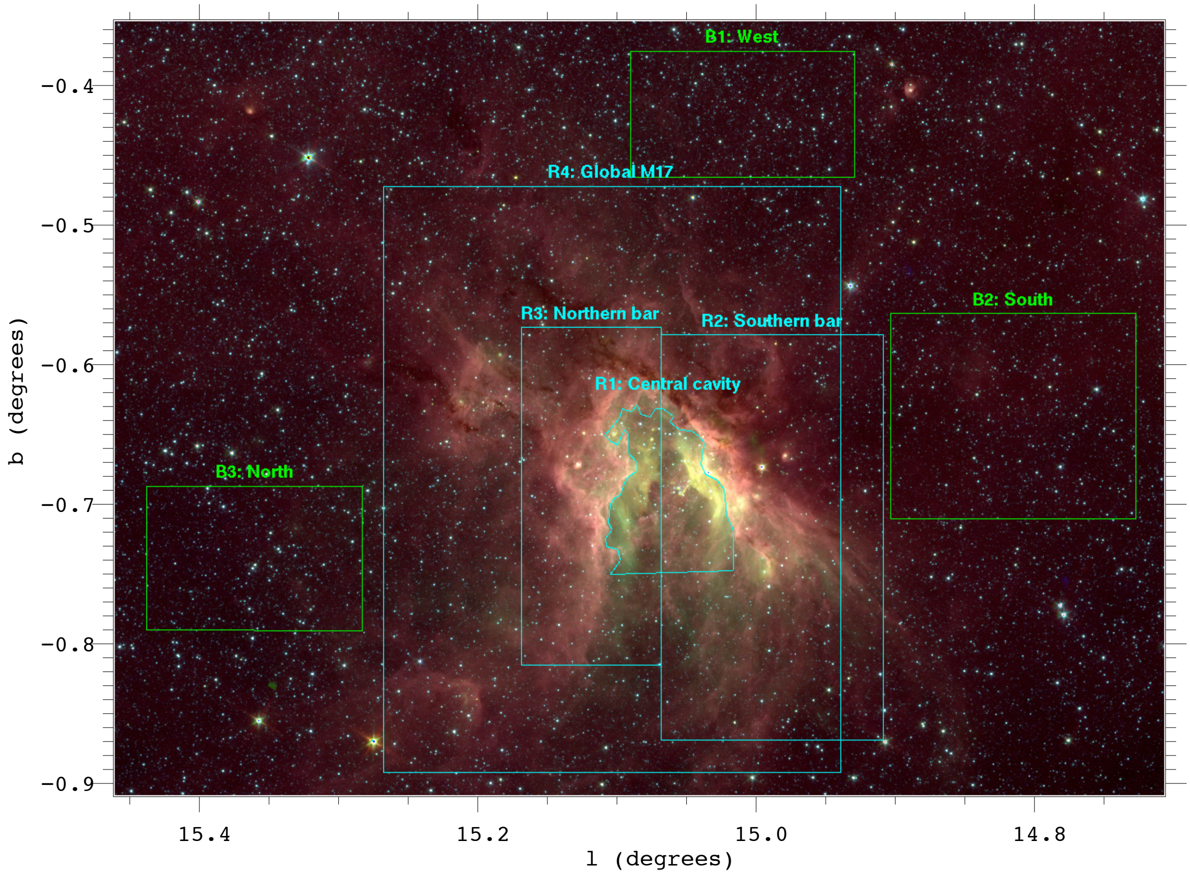

Fig. 2.1.— Apertures (*cyan*) used to extract diffuse fluxes overplotted on a 3-color (*red*=5.8 μm, *green*=4.5 μm, *blue*=3.6 μm) GLIMPSE image mosaic of the M17 region. The *green* boxes enclose areas used to determine the background levels. Point-source subtracted residual images were used for the GLIMPSE diffuse photometry. The Northern and Southern bars are named after their orientation with respect to equatorial coordinates; this image is displayed in Galactic coordinates.

this simple scheme because M17 is extremely bright relative to the IR background in the Galactic plane, and we are interested only in large-scale integrations of the flux from different parts of the nebula, as well as the "global" flux from the entire nebula. Aperture R1 was chosen to extract emission dominated by the H II region. Our target apertures range in size from $\sim 4' \times \sim 6'$ (R1) to $16.4' \times 21.1'$ (box R4). We measured the flux in each of the background apertures (B1, B2, and B3) and used a weighted average of the measured fluxes to compute a background level, B (Jy/pix), for each IR band. We integrated the intensity images (MJy/sr) over each target aperture (R1, R2, R3, and R4) and converted these values to flux F_0 (Jy). The background-subtracted fluxes were then calculated for each aperture as

$$F = F_0 - B n_{\rm pix}, \tag{2.1}$$

where n_{pix} is the number of pixels contained within the aperture.

The above procedure was carried out on the GLIMPSE residual images for IRAC [3.6], [4.5], and [5.8] that are free of the pollution of point sources and on the *MSX* and *IRAS* images. The lower resolution and sensitivity of *MSX* and *IRAS* precludes the removal of the majority of the point sources detected by GLIMPSE. Fortunately, in a region like M17 the brightness of diffuse IR emission increases sharply with wavelength, while the total flux in stars (the majority of which are field stars, not YSOs) decreases. In IRAC [5.8], the total flux of all point sources included in the Full List (see §2.2.1) from the M17 bars is less than 1% of the diffuse flux measured from the residual image. When treating the *MSX* and *IRAS* bands it is therefore safe to neglect the contribution of point sources.

The 2MASS near-IR bands are stellar-dominated over most of the GLIMPSE survey area, and therefore no residual images are made of the 2MASS mosaics. A portion of the southern bar of M17 near M17-UC1 is bright enough in diffuse emission to reach the non-linear saturation limit of 4.0 mag[7] for IRAC [8.0], and this part of the residual image is heavily masked as a result. We therefore use a modified version of our aperture photometry scheme to obtain the diffuse fluxes in the JHK_S and [8.0] bands. We measure fluxes in each aperture directly from the mosaics, which include stars, and then determine the diffuse flux values for F_0 and B used in Equation (2.1) by subtracting the total flux from all point sources in the corresponding aperture area of the Full List from the total flux (diffuse and stellar) in the mosaic. Because both the mosaics and residual images have the same flux calibration, for a given aperture the flux in the mosaic image should agree with the flux in the residual image plus the total flux of all extracted point sources. Although the [8.0] flux will still be underestimated using this procedure, for the construction of a global SED it is preferable to include flux from saturated pixels than to exclude these pixels completely. There is a possible disparity between these two procedures due to the small gap between the 2σ detection level of sources extracted from the residual image and the 3σ minimum level of sources included in the Full List. As a check, comparison of these two methods, carried out for the same set of apertures in IRAC [3.6], [4.5], and [5.8] (for which we have both mosaics and good residual images of M17), shows that the results agree to within a few percent. All of our diffuse fluxes are formally upper limits because there is an irreducible contribution from unresolved or otherwise unextracted point sources in all of the bands. In practice, however, the background subtraction partially offsets the potential systematic contribution

---

[7] Go to: http://www.astro.wisc.edu/glimpse/GQA-master.pdf

of unextracted point sources, and our conservative estimates of the uncertainties on our measured fluxes accounts for any remaining effect.

We estimate the uncertainties on our measured IR fluxes primarily from the background levels, incorporating the total fluxes of point sources, $F_\star$, subtracted from the mosaic fluxes in JHK_S and [8.0]. Hence our fractional uncertainties are given by

$$\frac{\delta F}{F} = \left[\left(\frac{Bn_{\rm pix}}{F_0}\right)^2 + \left(0.2\frac{F_\star}{F_0}\right)^2\right]^{\frac{1}{2}}, \tag{2.2}$$

which becomes simply

$$\frac{\delta F}{F} = \frac{Bn_{\rm pix}}{F_0}$$

when point source fluxes are not used ($F_\star = 0$). We made every attempt to be conservative with these uncertainty estimates. Typical percentage uncertainties on our global fluxes (aperture R4) for M17 are 50% at K_S (where background levels are high and unresolved stellar emission is a significant source of contamination to the diffuse emission), <30% for the GLIMPSE bands, ∼5% for *MSX*, and 5–27% for IRAS 12–100 μm. For the other, smaller apertures where the diffuse emission is brighter on average, the uncertainties are lower.

Additional sources of systematic error affect the absolute diffuse flux calibrations of IRAC images. Cohen et al. (2007) compared the fluxes measured by IRAC at 8.0 μm and *MSX* at 8.3 μm for a sample of 43 Galactic H II regions and found, correcting for the difference in the bandpasses, that the present calibration of IRAC [8.0] tends to overestimate diffuse fluxes by 36%. This problem is believed to be due to scattered light inside the camera and therefore should similarly affect IRAC [5.8]. Because there are no *MSX* bands lying close to the 3 lower-wavelength IRAC bands, aperture correction factors have been estimated for all four bands using extragalactic SED templates. The two approaches agree well for IRAC [8.0]. We therefore adopt the SSC "infinite-aperture" correction factors determined by Jarrett[8] and multiply our flux values at 3.6, 4.5, 5.8, and 8.0 μm by factors of 0.91, 0.94, 0.73, and 0.74, respectively. There is an additional source of systematic error caused by "full-frame pull-up," also called "droop," whereby the flux of a bright source can be redistributed across the IRAC detector, raising the diffuse emission everywhere within the affected image frame. Droop is evident in many GLIMPSE mosaics, especially at 8.0 μm, where a frame containing a bright compact source appears brighter than adjacent frames. The causes of droop are not

---

[8] Go to http://ssc.spitzer.caltech.edu/irac/calib/extcal

well-understood, and at present there is no way to fully correct for this effect, but since M17 extends over a large area containing many individual IRAC frames, any redistributed diffuse flux is likely to be counted as part of the global SED.

The *IRAS* flux calibration has been checked against *COBE*/DIRBE (Hauser et al. 1991) and a linear transformation of the form

$$F_{\rm cor} = {\rm Gain} \times F + {\rm Offset} \tag{2.3}$$

to correct the *IRAS* fluxes has been derived.[9] We apply these transformations to our measured *IRAS* fluxes, with the caveat that the correction is most valid at angular scales comparable to the 1-degree resolution of DIRBE. The uncertainties on the correction constants (Gain and Offset) are propagated into our final uncertainty estimates. Finally, the breadth of the *IRAS* bands necessitates the application of color-corrections to the isophotal fluxes (Beichman et al. 1988). We chose color-correction factors based on a blackbody SED model determined from the observed ratio of 60 to 100 μm fluxes. For M17, the color-corrections primarily affect the 12 and 25 μm fluxes; the 60 and 100 μm fluxes are largely unchanged. The combined effect of the *IRAS* flux transformations and color-corrections is to decrease the flux values at 12, 60, and 100 μm by $\sim$5%, $\sim$20%, and $\sim$35%, respectively, while increasing the flux at 25 μm by $\sim$17%.

We use the same apertures to extract the integrated radio continuum fluxes from the VLA MAGPIS images at 20 cm and 90 cm. In this case, background subtraction is inappropriate, and the images, while probably not missing significant flux, were not intended for photometric applications. In addition, part of the M17 H II region extends beyond the edge of the New GPS survey, and consequently the 20-cm image of M17 is slightly cropped in our largest apertures. We estimate this causes a loss of not more than 5% of the continuum flux, based on the very low extrapolated brightness of the missing portions compared with the peak brightness observed. Hence we use the MAGPIS data with caution, assigning error bars of 30%, but it is possible to check our results. The thermal radio continuum of M17 has been measured previously using single-dish radio observations. Schraml & Mezger (1969) give 609 Jy at 1.95 cm and Goss & Shaver (1970) give 794 Jy at 6 cm. Our value of 687 Jy for the MAGPIS 20 cm is consistent with these older measurements. No uncertainty estimates are given for these published fluxes, so we also assign them 30% error bars. Several other continuum flux measurements for M17 are quoted in the literature. The fluxes measured by Altenhoff et al. (1970) at 2, 6, and 20 cm, all under 600 Jy, appear to be systematically

---

[9] See http://irsa.ipac.caltech.edu/IRASdocs/issa.exp.sup/ch4/D.html

underestimated. Downes et al. (1980) give a flux of 844.5 Jy at 6 cm, but this is a rough estimate derived from the peak flux assuming that the source is Gaussian, a poor assumption for a region as complex as M17. The radio continuum fluxes that we use for this work have been independently determined at 3 different frequencies, and all are in good relative agreement.

2.3.2 The Shapes of the SEDs

The measured integrated IR fluxes with their uncertainties for our 4 apertures on M17 are given in Table 2.1. Conti & Crowther (2004) measured the diffuse IR fluxes for M17 in the *MSX* C and E bands and in all the *IRAS* bands except 12 μm. Their values of 22,400 and 89,100 Jy at 12.13 and 21.30 μm, respectively, agree well with our determinations of *MSX* fluxes, adjusting for the smaller size of their $9'$ circular aperture relative to our most comparable combination of apertures, R2+R3. Their *IRAS* fluxes of 83,200, 214,000, and 224,000 Jy at 25, 60, and 100 μm resemble our uncorrected *IRAS* fluxes but differ significantly from our final values, after the cross-calibration with DIRBE and color corrections are performed. Conti & Crowther (2004) do not report applying any calibration or color corrections to their *IRAS* fluxes.

Table 2.1. M17 Integrated Diffuse Infrared Fluxes (Jy)

Band	λ	Bandwidth	Aperture R1		Aperture R2		Aperture R3		Aperture R4	
	(μm)	(μm)	F_1	δF_1	F_2	δF_2	F_3	δF_3	F_4	δF_4
2MASS J	1.25	0.16	37	3	28	10	29	6	46	23
2MASS H	1.65	0.25	45	5	30	15	32	10	31	23
2MASS K_S	2.17	0.26	80	6	79	25	66	14	113	56
IRAC 1	3.6	0.75	110	10	240	50	200	30	540	210
IRAC 2	4.5	1.0	170	10	290	40	220	20	620	140
IRAC 3	5.8	1.4	500	60	1,300	300	1,100	200	2,900	1,100
IRAC 4 obs.[a]	8.0	2.9	3,000	200	5,000	1,000	4,200	550	11,000	3,800
IRAC 4 pred.[b]	8.0	2.9	4,480	170	5,600	500	4,480	360	11,500	600
MSX A	8.28	4.0	4,000	100	5,000	400	4,000	300	10,300	500
IRAS	12	5.5	6,300[c]	200	5,700	400	5,000	300	11,000	1,200
MSX C	12.13	2.1	13,500	200	14,600	1,000	10,700	600	27,500	1,400
MSX D	14.65	2.4	22,100	100	21,300	600	14,500	300	37,700	1,900
MSX E	21.30	6.9	52,400	200	59,700	1,000	39,000	500	105,000	5,000
IRAS	25	11	48,100[c]	1,000	60,300	1,900	37,100	1,000	110,000	4,800
IRAS	60	40	49,000[c]	3,700	98,000	11,000	75,000	6,400	230,000	30,000
IRAS	100	37	39,800[c]	6,300	86,000	20,000	59,000	11,000	195,000	53,000

[a] Because IRAC [8.0] saturates in the brightest parts of M17, the observed fluxes given here are underestimates of the actual emission, particularly for apertures R1 and R2.

[b] IRAC [8.0] fluxes predicted using the ratio of IRAC [8.0]/*MSX* A $= 1.12 \pm 0.03$ derived by Cohen et al. (2007) for a typical bright H II region SED.

[c] The resolution of *IRAS* ($\sim 0.5'$ at 12 μm to $\sim 2'$ at 100 μm; Beichman et al. 1988) is too coarse to allow a precise extraction of flux from R1, therefore the *IRAS* fluxes for this aperture are only in approximate spatial correspondence with the other fluxes listed.

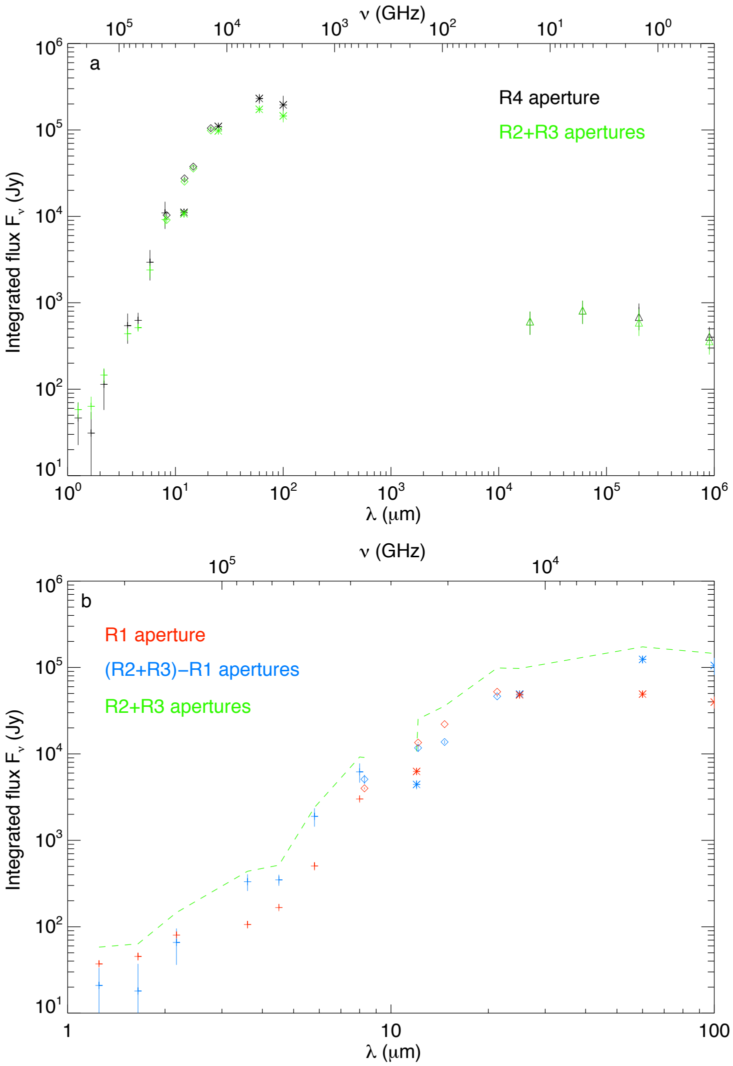

Fig. 2.2.— Integrated diffuse SEDs for M17. Infrared fluxes and error bars from Table 2.1 are plotted: 2MASS+GLIMPSE (plus signs), *MSX* (diamonds), and *IRAS* (asterisks). Radio continuum points from Goss & Shaver (1970), Schraml & Mezger (1969), and MAGPIS are plotted as triangles. (*a*) The fluxes from the largest-area aperture, R4 (*black*), represents the "global" SED of M17, while the sum of the fluxes from apertures R2+R3 (*green*) captures the total emission from the two bars and central cavity. The underlying shape of the IR SED is thermal (blackbody) emission from dust. The thermal (free-free) radio continuum is approximately flat from 2–20 cm, falling off by 90 cm. (*b*) Comparison of the IR-only SED from the H II region (*red*) with the PDR (*blue*) shows that the IR emission peaks at shorter wavelengths for dust that lies closer to the ionizing cluster. The *red* and *blue* points sum to the SED of the R2+R3 apertures, reproduced from (*a*) as a *green* dashed line. The break in the line spans the silicate absorption feature near 10 μm, for which we have no data.

We constructed SEDs using the IR flux values of Table 2.1 along with the radio continuum fluxes at 1.95 cm (Schraml & Mezger 1969), 6 cm (Goss & Shaver 1970), 20 cm, and 90 cm. The SEDs from different combinations of apertures are presented in Figures 2.2. Figure 2.2*a* illustrates the shape of the global SED. It is qualitatively similar to the SED of a dust cocoon surrounding a single newly-formed early-type star (Churchwell, Wolfire, & Wood 1990; Vig et al. 2006). The underlying shape of the global IR SED resembles a blackbody curve that peaks near 60 μm. This is a "greybody" composite of many underlying dust blackbodies, representing a large range of grain temperatures and sizes found throughout the M17 region. The radio emission from 1.95–20 cm is the approximately flat, thermal Bremsstrahlung (free-free) continuum from electrons in the H II region, and it is optically thick at longer wavelengths, as evidenced by the lower flux at 90 cm. The dust continuum rises steeply from near-IR through mid-IR wavelengths. Figure 2.2*b* compares the IR SED of the H II region surrounding NGC 6618 (aperture R1; *red*), with that of the two PDR bars excluding the H II region (apertures R2+R3 - R1; *blue*). The total SED of R2+R3 is reproduced for reference (*green* dashed line); the break in the line spans the silicate feature at 9.7 μm for which we have no observational coverage. The SED from the H II region has a steeper mid-IR continuum and peaks at a shorter wavelength ($\lambda_{\rm peak} \sim 24$ μm) than the SED from the PDRs ($\lambda_{\rm peak} \sim 60$ μm). This is an indication that the grain population inside the H II region is at higher temperatures and probably has a smaller size distribution (Giard, Bernard, & Dennefield 1992) compared to the dust in the PDRs. Figure 2.2*b* also illustrates the relative contributions of the PAH emission features to the IRAC and *MSX* bands both within the H II region and the PDRs. IRAC [3.6], [5.8], and [8.0] all contain strong PAH emission features and, in the PDR SED, show marked flux excesses relative to IRAC [4.5], which does not include any PAH emission feature. These excesses largely disappear in the H II region SED, although there is some PAH emission in aperture R1, primarily coming from the front and back walls of the cavity. The 2MASS JHK_S fluxes are much higher from inside the H II region than outside. The diffuse near-IR emission is probably dominated by scattered starlight, augmented by free-bound emission from the Paschen and Brackett ionization edges that fall within the J and K_s bands, respectively.

The IRAC [4.5] band, while free of PAH emission, contains one potentially strong emission feature from H II regions, the H I Brα recombination line at 4.05 μm. The emissivity of the Brα line is related to the specific free-free emissivity by

$$\frac{j(\mathrm{Br}\alpha)}{j_\nu(ff)} = 3.058 \times 10^{12} \left(\frac{T_e}{10^4\ \mathrm{K}}\right)^{0.35} \left(\frac{\nu}{15\ \mathrm{GHz}}\right)^{0.1} \qquad [\mathrm{Hz}]. \tag{2.4}$$

We evaluate this ratio using an electron temperature $T_e = 8000$ K (Subrahmanyan & Goss 1996). We then calculate the specific flux level of the Brα emission line distributed across the broad IRAC [4.5] band as

$$F_\nu(\mathrm{Br}\alpha) = \frac{j(\mathrm{Br}\alpha)}{j_\nu(ff)} \frac{F_\nu(\nu)}{\Delta\nu}, \tag{2.5}$$

where $F_\nu(\nu)$ is the free-free continuum flux measured at radio frequency ν and $\Delta\nu = 1.5 \times 10^{13}$ Hz is the IRAC [4.5] bandwidth. The results of these calculations using the radio continuum fluxes at 1.95, 6, and 20 cm are given in Table 2.2. Comparison of $F_\nu(\mathrm{Br}\alpha)$ with the fluxes in the IRAC [4.5] band, $F_\nu(4.5\ \mu\mathrm{m})$, for various apertures from Table 2.1, reveals that, on average, the Brα emission line contributes ~20% of the flux at 4.5 μm. It is reasonable to hypothesize a higher fractional contribution of Brα if we examine only the emission from the heart of the H II region compared to the emission from the PDRs largely excluding the H II region. Table 2.2 includes estimates of $F_\nu(\mathrm{Br}\alpha)$ based on the 20 cm flux from aperture R1 alone and the combination of apertures R2+R3−R1 (see Figure 2.2*b*). The contribution of Brα to the 4.5 μm flux in aperture R1 is 22%. This value is not significantly higher than the estimates for the entire R4 aperture, but the percentage Brα contribution in R2+R3−R4, calculated from the 20-cm data, is only 15%. We could be underestimating the Brα emissivity if the the free-free emission becomes optically thick at 20 cm. The free-free emissivity is not precisely flat; it rises toward lower frequencies as $j_\nu(ff) \propto \nu^{-0.1}$, yet the measured flux at 20 cm falls slightly below the flux at 6 cm. This optical depth effect is unlikely to be large on the whole, but it could manifest itself most noticeably in the brightest part of the H II region, causing us to underestimate the degree of enhancement to the Brα line emission there. Taken together,

Table 2.2. Brα Line Emission from Free-Free Radio Continuum

	ν (GHz)	$F(ff)$ (Jy)	$F(4.5)$ (Jy)	$F(\mathrm{Br}\alpha)$ (Jy)	% Brα
(R4)	15	609	620	115	19
	5	784	620	133	21
	1.5[a]	687	620	103	17
(R1)	1.5[a]	257	170	38	22
(R2+R3-R1)	1.5[a]	334	340	50	15

[a] The MAGPIS 20-cm fluxes are slightly underestimated for apertures R2, R3, and R4 because the image is clipped. It is also possible that the free-free emission is optically thick at 20 cm. For these reasons, the continuum fluxes at 1.5 GHz and the Brα line fluxes derived from them are lower limits.

these results indicate that the Brα line emission appears to have a similar spatial distribution to that of the dust greybody continuum, but there is a marginally significant strengthening of the Brα line relative to the dust continuum in the central parts of the H II region. The globally-integrated [4.5] diffuse emission is dominated by the central part of the H II region.

2.3.3 The Luminosity Distance to M17

Another view of the global SED of M17 is presented in Figure 2.3. Plotting the fluxes in λF_λ space shows that the energy radiated in the IR is the dominant source of luminosity, far more important than the energy radiated at sub-mm to radio wavelengths. In fact, over 90% of the emergent luminosity of M17 is carried by photons with $\lambda \lesssim 100$ μm. We perform a spline interpolation (heavy line in Figure 2.3) to the

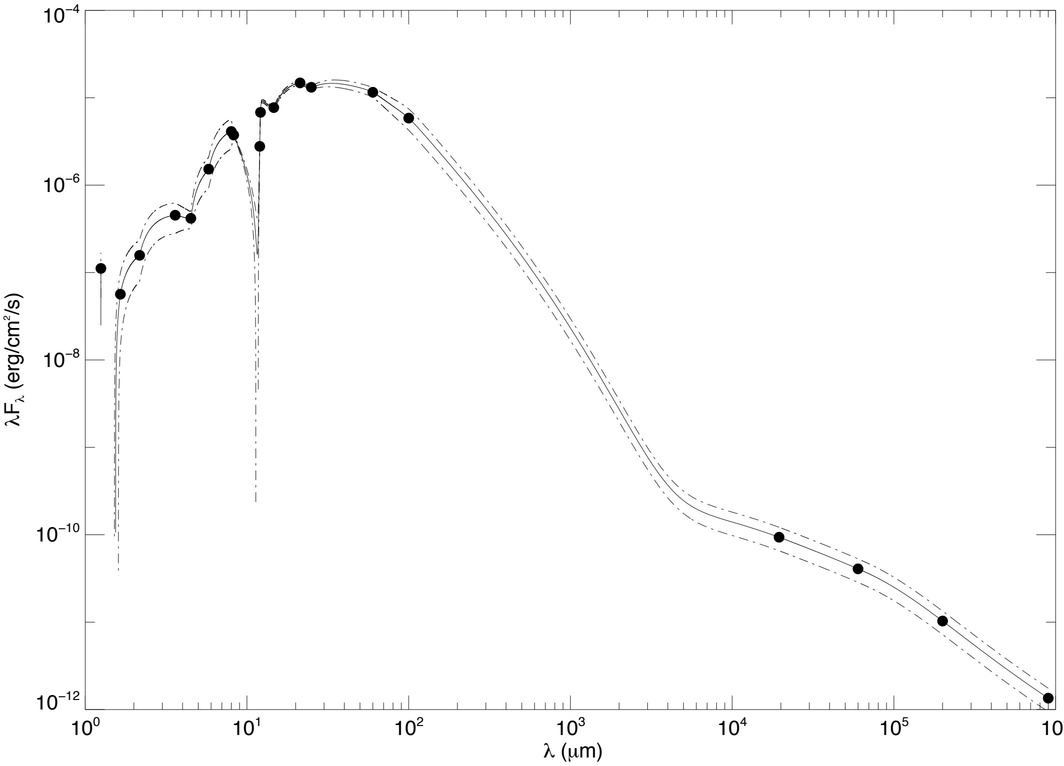

Fig. 2.3.— Global SED of M17 (aperture R4) plotted in λF_λ space. Over 90% of the emergent energy is carried by photons with $\lambda \lesssim 100$ μm. The solid curve is the spline interpolation of the SED that was integrated to obtain the total luminosity of M17, and the dash-dotted curves are the upper and lower uncertainty envelopes. The apparent deep absorption feature near 10 μm is an artifact of the spline interpolation. The large uncertainties on the JHK_S flux values cause the interpolation to fail at the extreme short-wavelength end of this plot, but because the near-IR contributes a negligible amount of energy to the overall SED, this does not significantly impact the result of the integration.

SED and integrate the result over all near-IR through radio wavelengths to obtain the total luminosity of the M17 complex,

$$L_{\mathrm{SED}}(d) = 4\pi d^2 \int F_\lambda d\lambda. \tag{2.6}$$

We determine the uncertainty on $L_{\mathrm{SED}}(d)$ by deriving maximum and minimum values using spline interpolations to the upper and lower error envelopes of F_λ shown in Figure 2.3 (dash-dotted lines). The often-cited (*eg.* Chini, Elsässer, & Neckel 1980) kinematic distance to M17 is 2.2 kpc, which gives L_{SED}(2.2 kpc)= $4.5 \pm 0.6 \times 10^6$ $L_\odot$. More recent photometric distance estimates place M17 closer to the Sun, at 1.3 kpc (Hanson, Howarth, & Conti 1997) or 1.6 kpc (Nielbock et al. 2001). Our derived luminosity is significantly reduced using a nearer distance estimate; L_{SED}(1.6 kpc)= $2.4 \pm 0.3 \times 10^6$ $L_\odot$.

We compare the observed total luminosity of M17 to the combined bolometric luminosity of all the known ionizing stars in the NGC 6618 cluster. A similar analysis of the energetics of M17 was attempted by Harper et al. (1976), who derived a luminosity of 5.6×10^6 $L_\odot$ and concluded that the region must contain the equivalent of 5–10 O5 stars. Currently there are 13 known O stars in NGC 6618. These are listed in order of decreasing mass in Table 2.3, along with their bolometric luminosities estimated from the calibrations of bolometric luminosity with spectral type of Martins, Schaerer, & Hillier (2005). The cluster also contains at least 35 B stars earlier than B3 (see Appendix A of T03), and we include these in our energy calculations using the bolometric luminosities of de Jager & Nieuwenhuijzen (1987) but do not list them in Table 2.3 to save space. Because the spectral types of several of the O stars are poorly constrained, we are able only to give maximum and minimum possible values for the total bolometric luminosity of the ionizing stars, obtaining L_{OB}(max)= 3.58×10^6 $L_\odot$ and L_{OB}(min)= 2.72×10^6 $L_\odot$ for the combinations of all earliest and all latest possible spectral types, respectively. We assume that all of the stars are dwarfs on the zero-age main sequence (ZAMS); this is reasonable given the youth of the cluster (Jiang et al. 2002). Over 96% of the luminosity is produced by the 13 O stars alone, and virtually all of the remainder is accounted for by the early B stars. This is consistent with the ZAMS luminosity function of a cluster that obeys a Salpeter-type initial mass function; less than 1% of the total bolometric luminosity will come from stars later than B3.

Our analysis of the energetics of M17 is summarized in Table 2.4. Energy is input to the nebula largely by UV radiation from the ionizing stars, and this radiation is reprocessed by dust grains and re-emitted as IR photons. If the nebular geometry were spherical (in other words, a completely embedded

Table 2.3. Luminosities of O Stars in NGC 6618

Name[a]	RA (J2000)	Dec (J2000)	Spectral Type	$\log L_{\rm bol}$ ($L_\odot$)[b]
CEN 1	18 20 29.92	−16 10 45.5	O4+O4	5.68+5.68[c]
CEN 43	18 20 33.14	−16 11 21.6	O3–O4	5.83–5.68
CEN 2	18 20 34.55	−16 10 12.1	O5	5.51
CEN 37	18 20 30.54	−16 10 53.3	O3–O6	5.83–5.30
OI 345	18 20 27.52	−16 13 31.8	O6	5.30
CEN 18	18 20 25.94	−16 08 32.3	O7–O8	5.10–4.90
CEN 25	18 20 30.92	−16 10 08.0	O7–O8	5.10–4.90
OI 352	18 20 35.86	−16 15 43.1	O8	4.90
CEN 16	18 20 22.76	−16 08 34.3	O9–B2	4.72–3.5
CEN 61	18 20 30.30	−16 10 35.2	O9–B2	4.72–3.5
CEN 3	18 20 35.47	−16 10 48.9	O9	4.72
CEN 31	18 20 24.45	−16 08 43.3	O9.5	4.62

[a] This list is adapted from Appendix A of T03 and Table 9 of Broos et al. (2006). Identifications are from the catalogs of CEN = Chini, Elsässer, & Neckel (1980) and OI = Ogura & Ishida (1976). Two sources from the T03 list, CEN 34 and CEN 102, have been dropped. These were not detected in X-rays, and their mid-IR colors suggest that they are either red giants not associated with M17 or YSOs, but not O stars.

[b] Bolometric luminosities are taken from Martins, Schaerer, & Hillier (2005) for O stars and from de Jager & Nieuwenhuijzen (1987) for B stars.

[c] This source, Kleinmann's Anonymous star, is a binary whose components are partially resolved by GLIMPSE.

Table 2.4. Energy Budget of M17

	Stellar luminosity intercepted by nebula		
3-dimensional nebular geometry	fraction of flux intercepted, f	$fL_{\rm OB}$(max) (10^6 $L_\odot$)	$fL_{\rm OB}$(min) (10^6 $L_\odot$)
spherical	1	3.58	2.72
conical	0.96	3.44	2.61
clamshell (45°)	0.875	3.13	2.38
clamshell (90°)	0.75	2.68	2.04
	Emergent luminosity observed in SED		
	d (kpc)	$L_{\rm SED}(d)$ (10^6 $L_\odot$)	
	2.2	4.5 ± 0.6	
	1.6	2.4 ± 0.3	

cluster), all of the stellar flux would be intercepted and the emergent luminosity, $L_{\rm SED}$, would be equal to the stellar luminosity, $L_{\rm OB}$ (first row of Table 2.4). The IR morphology of M17 shows that this is clearly not the case. The dominant morphological features of M17 are the two emission bars that meet each other at an apparent angle of 45°. Although the ionizing stars lie behind an average of $A_V = 8$ mag of optical extinction along the line of sight, the extinction in the direction of the opening angle between the bars is likely to be negligible. Several possible 3-dimensional geometries are suggested by this morphology, and each would allow the nebula to intercept a fraction $f = 1 - \Omega/4\pi$ of the stellar flux, where Ω is the solid angle of the opening as measured from the cluster. In the most heavily embedded geometry, the bars are simply the cross-section of a cone that we view from the side. About 4% of the stellar flux escapes through the base of the cone, and the remaining $0.96L_{\rm OB}$ is intercepted by the nebula and reprocessed to emerge in the SED. Alternatively, the geometry could take more of a "clamshell" form, where the two halves meet at an angle ranging from 45° ($f = 0.875$) if oriented edge-on to the line of sight, to perhaps 90° ($f = 0.75$) if inclined. This last configuration is the least embedded geometry that we can reasonably postulate for M17.

A balancing of the possible combinations of input and the emergent energies compared in Table 2.4 reveals that M17 must lie at less than the kinematic distance of 2.2 kpc, because the maximum intercepted stellar luminosity falls below the minimum luminosity required to produce the observed SED at $d = 2.2$ kpc. We can place an upper limit on the distance to M17 by scaling the maximum stellar luminosity to the appropriate distance,

$$\frac{fL_{\rm OB}({\rm max})}{2.4\times10^6\ {\rm L}_\odot} = \left(\frac{d({\rm max})}{1.6\ {\rm kpc}}\right)^2 .$$

This gives d(max)= 1.9 kpc for the conical geometry, $f = 0.96$. A similar argument yields a minimum distance d(min)= 1.5 kpc. We therefore adopt the distance estimate of 1.6 kpc given by Nielbock et al. (2001). At this distance, the luminosity in the SED makes it unlikely that M17 contains any stars earlier than O4, although a spectral type of O3 for CEN 43 (see Table 2.3) is not ruled out.

We can constrain the most probable nebular geometry to some form between a cone and a clamshell with an opening angle of ~45°. This interpretation agrees qualitatively with the structural model of Pellegrini et al. (2007), who deduce a similarly heavily-embedded geometry for the M17 complex.

2.4 PAH Emission

The hypothesis that PAHs are responsible for a number of strong IR emission features was first proposed by Léger & Puget (1984) and has gained increasing support over the last 15 years (see Allamandola, Tielens, & Barker 1989; Hudgins & Allamandola 1999; van Kerckhoven et al. 2000; Peeters et al. 2004). PAHs are large organic molecules incorporating tens or hundreds of C atoms. The C skeletal structure consists of linear chains or planar tessellations of multiple benzene rings with H atoms attached on the periphery (see Draine 2003 for a review). Exposure to UV radiation excites various vibrational modes in this class of molecules, causing them to radiate strongly as emission features in the IR. The major known emission features of PAHs are summarized in Table 2.5, along with the observational coverages of these features provided by the IRAC, *MSX*, and IRS SH data presented in this work.

While UV photons of sufficiently low energy excite PAH emission features, EUV and harder photons instead destroy the molecules (Voit 1992). Hard radiation fields are produced by OB stars, and the GLIMPSE images reveal that the mid-IR Galaxy is lit up by PAH emission that is particularly strong near H II regions like M17. The morphology of this emission often assumes ringlike “bubble” shapes, with

Table 2.5. Infrared emission features from PAH molecules

Vibrational mode[a]	λ (μm)	Obs. coverage
C-H stretching	3.3	IRAC 1
C-C stretching	6.2	IRAC 3
C-C stretching	7.7	IRAC 4, *MSX* A
C-H in-plane bending	8.6	IRAC 4, *MSX* A
C-H solo out-of-plane bending (PAH$^+$)[b]	11.0	*MSX* C, IRS SH
C-H solo out-of-plane bending	11.3	*MSX* C, IRS SH
C-H duo out-of-plane bending	12.0	*MSX* C, IRS SH
C-H trio out-of-plane bending	12.7	*MSX* C, IRS SH
C-H quartet out-of-plane bending	13.55	*MSX* D, IRS SH
C-C-C skeletal out-of-plane bending[d,]	16.5, 17.4	IRS SH

[a] Except where noted otherwise, this list is based upon Allamandola, Tielens, & Barker (1989). *Solo, duo*, etc. refer to the number of H atoms contiguous with the H atom involved in the vibration.

[b] From Hudgins & Allamandola (1999)

[c] From van Kerckhoven et al. (2000)

[d] From Peeters et al. (2004)

sharp emission cutoffs surrounding cavities of little or no diffuse emission (Churchwell et al. 2006). The most likely explanation for the abrupt disappearance of PAH emission within H II regions is that the PAH molecules themselves are destroyed over a small distance scale or "edge" that lies near the I-front. The PAH molecules near this destruction edge are highly excited and emit strongly, and while this emission falls off rapidly with increasing distance beyond the I-front, it remains highly extended, stimulated by softer UV photons permeating the PDR.

2.4.1 GLIMPSE Band-Ratio Images

The GLIMPSE broadband mid-IR images of M17 do not show PAH emission alone, but rather a composite of emission features and dust continuum. It is possible, however, to locate the PAH destruction edge in the GLIMPSE images and thus to separate those areas of M17 that are PAH-dominated from those that are continuum-dominated. Because the IRAC [4.5] band does not contain any PAH feature, taking the ratio of this band with any of the other three bands largely divides out the continuum contribution, and the resultant band-ratio images trace primarily PAH emission. We produce these ratio images using background-subtracted GLIMPSE residual images from IRAC [3.6], [4.5], and [5.8]. We do not use IRAC [8.0] because it is saturated in much of the southern bar. We apply a median filter of width 7 pixels to the residual images to remove any remaining emission spikes from imperfectly extracted PSF wings of bright stars, and then smooth the result over 3 neighboring pixels using a boxcar algorithm.

Figure 2.4*a* shows the ratio image of IRAC [5.8]/[4.5] that traces the 6.2 μm PAH feature. The PAH-destruction zone, where the emission is continuum-dominated, appears as a prominent, dark Ω-shaped region. The outer boundary of this zone is the PAH destruction edge, and this can be traced by overlaying a single fiducial contour (*white* in Figure 2.4*a*) representing $[5.8]/[4.5] = 4.5$. The outer boundary appears as a sharp dropoff, almost a step function, in 3 cuts taken through the ratio image (Figure 2.4*b*), and this dropoff everywhere spans the fiducial contour value of 4.5. The inner boundary traced by this contour is more ragged, and the climb back above the fiducial contour is more gradual in the image cuts. The physical origin for this inner transition back to PAH-dominated emission is quite different from that of the PAH destruction edge. PAHs cannot survive at the heart of the M17 H II region, rather, the combined winds of the OB stars in the cluster have evacuated the central cavity of virtually all dust (T03; Pellegrini et al. 2007), thereby clearing out the source of the bright mid-IR continuum and leaving only the relatively faint signatures of the PAH-dominated front and back walls of the cavity. Figures 2.5*ab* tell a similar story using the ratio image of IRAC [4.5]/[3.6] tracing the 3.3 μm PAH feature. Here the PAH-bearing band is divided into the PAH-free band, so the PAH destruction zone appears as a bright Ω instead of a dark one. The fiducial contour (*yellow* in Figure 2.5*a*) has a value of [4.5]/[3.6] = 1.25 and traces almost the same path as the fiducial contour in Figure 2.4*a*.[10] In this combination of bands, the continuum-dominated region exhibits more structure. In particular, 3 probable stellar-wind bowshocks stand out in the northern bar. Two of these are associated with the late O stars CEN 16 and CEN 18 listed in Table 2.3, while the third is associated with an unidentified star in the northern bar. All of the bowshocks are oriented toward the central ring of O stars in NGC 6618. Among the bowshocks is one obvious dark pillar, or "elephant trunk," that also points toward the center of the ionizing cluster. These features provide further evidence for the importance of stellar winds in dynamically shaping the M17 complex (see T03).

As a control, we present the ratio image and corresponding cuts for IRAC [5.8]/[3.6], two PAH-bearing bands, in Figures 2.6*ab*. The PAH destruction zone is less distinct in this ratio image and practically invisible in the 1-dimensional cuts. The PAH destruction edge can be located as a thin, dark band in Figure 2.6*a*, highlighted by the overplotted fiducial contours from Figures 2.4*a* and 2.5*a* (*white* and *yellow*, respectively). The morphology of this ratio image may be attributed, in part, to the variation in the strength of the 3.3 μm and 6.2 μm PAH features relative to the respective continuum strengths in bands [3.6] and [5.8] along the PAH destruction edge. This interpretation implies that the 6.2 μm feature has a greater fractional contribution to the [5.8] band than the 3.3 μm to the [3.6] band. The appearance of the PAH destruction edge in this ratio image could also be influenced by differential extinction that affects the shorter-wavelength IRAC bands more than the longer-wavelength bands. The ratio of [5.8]/[3.6] increases with extinction because 3.6 μm photons are significantly more affected by extinction than 5.8 μm photons. If the extinction drops sharply just interior to the PAH destruction edge, the observed emission at 3.6 μm will recover more dramatically than the emission at 5.8 μm, suddenly suppressing the ratio. Conversely, the brightest area of this ratio image occurs in the upper-right of Figure 2.6*a*. This is the location of the molecular cloud M17 SW, where we would expect the highest extinction in this image.

We can apply the fiducial contours derived from the ratio images to the interpretation of the GLIMPSE mosaics. Single-band mosaics of M17 for each of the 4 IRAC bands are shown in Figure 2.7.

---

[10] We are primarily concerned here with the locations of these fiducial ratio contours, rather than the values of the fiducial ratios. Note that the ratios quoted in the text were derived from IRAC images without first applying the flux calibration correction factors described in §2.3.1. With the correction applied, these ratios become [5.8]/[4.5] = 3.6 and [4.5]/[3.6] = 1.37.

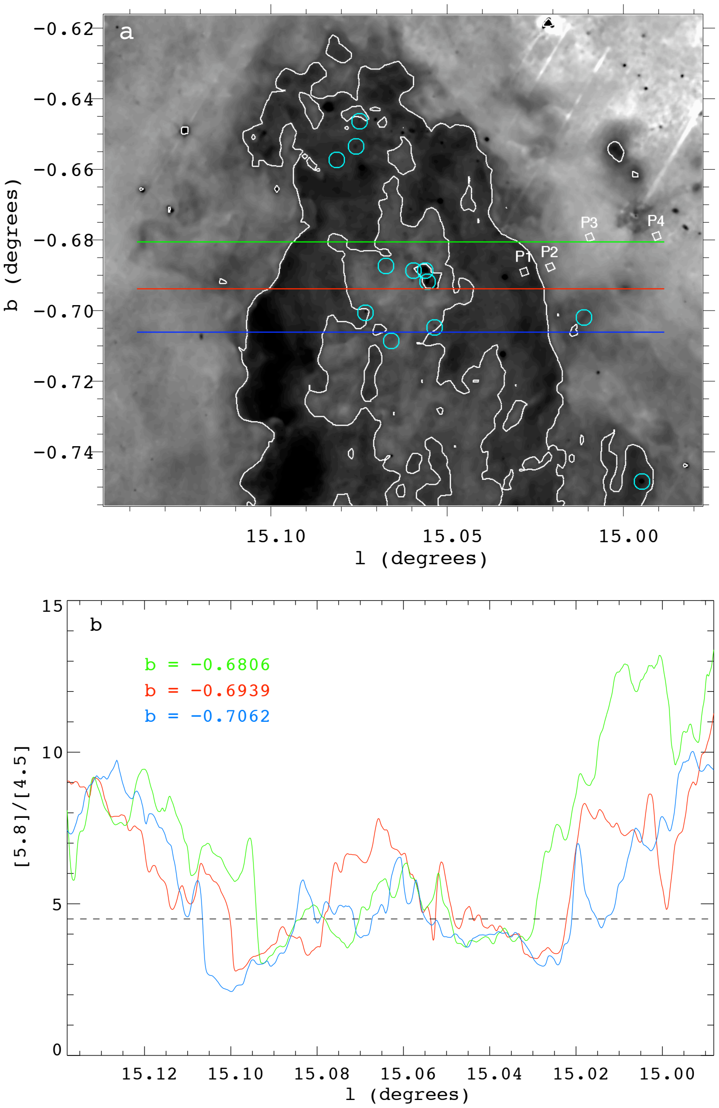

Fig. 2.4.— (*a*) Ratio image of IRAC [5.8]/[4.5]. The most prominent feature of this image is the dark region where PAH emission in IRAC [5.8] disappears. The boundary of this region can be traced by a fiducial contour (*white*) representing a ratio of [5.8]/[4.5] = 4.5. 4 IRS SH slit pointings are overplotted, and one of them, P1, falls within the no-PAH zone. The positions of the O stars listed in Table 2.3 are indicated by *cyan* circles. Taking the band ratios in areas where the absolute mid-IR intensity is low amplifies image artifacts and noise. The bright area in the upper-right corner of this image takes a sightline through the molecular cloud M17 SW, where the extinction is particularly high, and hence some streaks (known artifacts of the [5.8] band) and speckling (noise) are apparent. (*b*) Image cuts in longitude l through the ratio image, color-coded by position in latitude b. All three cuts exhibit sharp dropoffs where they cross the outer boundary of the dark zone, and these transitions all span the fiducial contour value of 4.5 (dashed line).

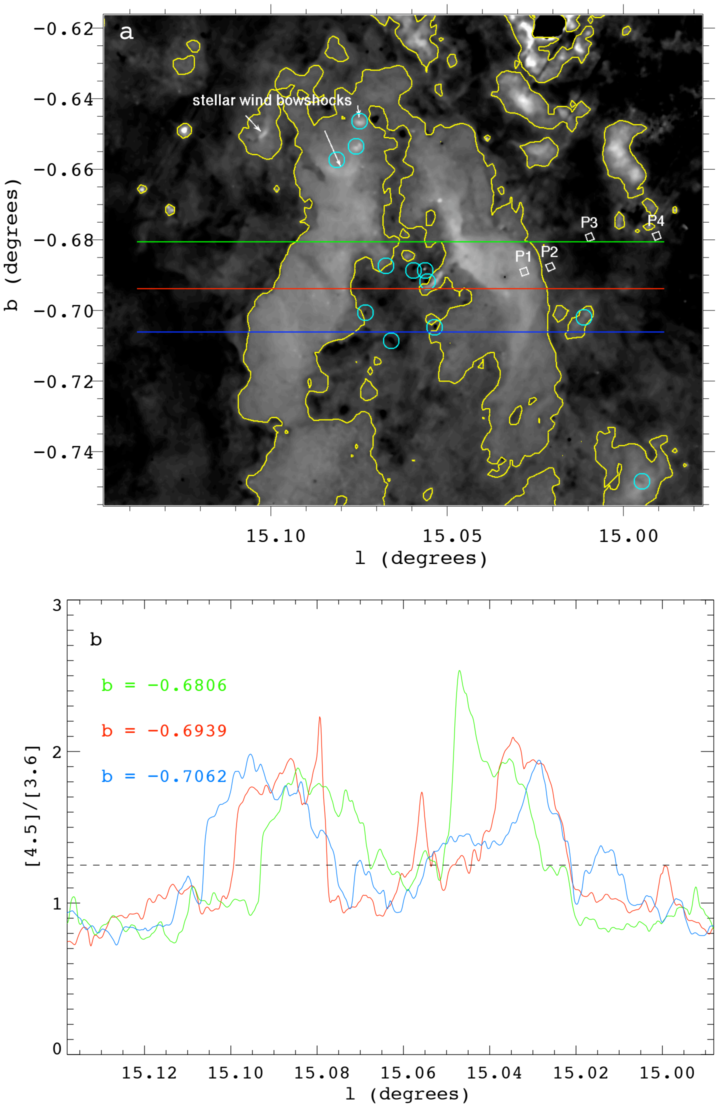

Fig. 2.5.— Same as Figure 2.4, but taking the ratio of IRAC [4.5]/[3.6]. Because the band that has no PAH emission is divided by a PAH-bearing band, the no-PAH zone here appears as a bright region in the image. This region is bounded by the fiducial contour (*yellow*) [4.5]/[3.6] = 1.25. Note that the bright region highlights some distinct structures, including 3 bright apparent bowshocks associated with OB stars and a nearby dark pillar in the northern bar. The broad, bright ridge in the southern bar with a narrow finger jutting into the central cavity coincide with the brightest radio emission from the H II region (FCM84), hence these features may be due to enhancement of the Brα recombination line contribution to the [4.5] emission. The several bright structures in the upper-right corner that lie above the fiducial contour appear to be image artifacts in the [4.5] band.

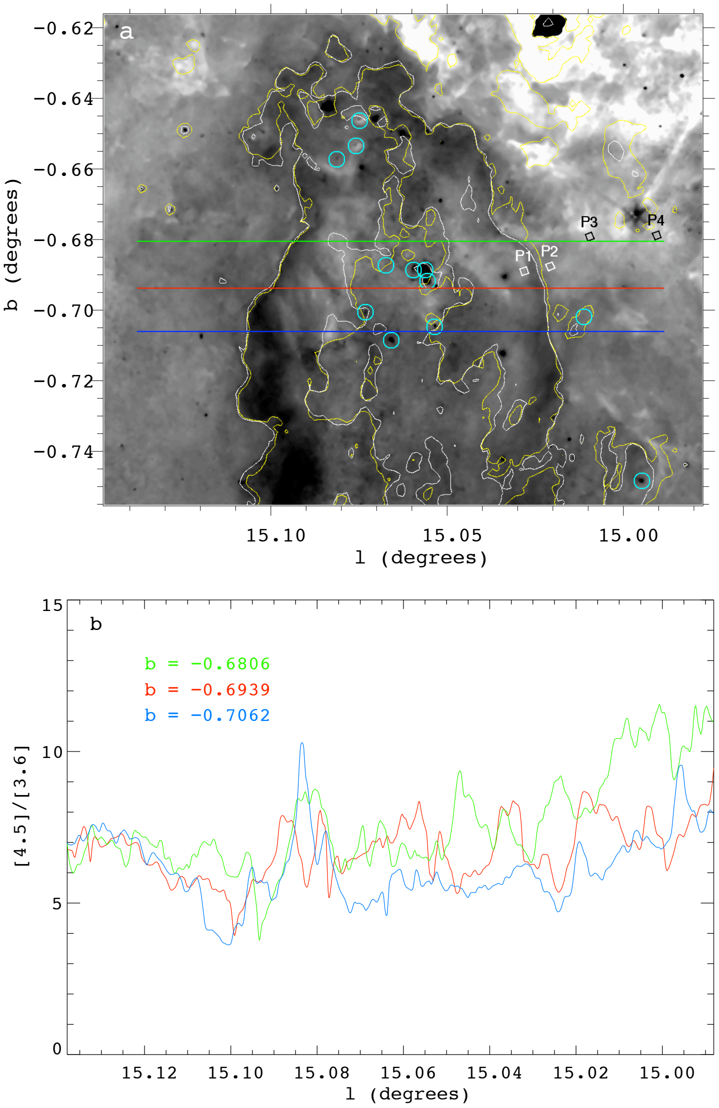

Fig. 2.6.— Same as Figure 2.4, but taking the ratio of IRAC [5.8]/[3.6]. Because both bands include PAH emission features, the PAH destruction zone is much less distinct in this ratio image and practically invisible in its corresponding cuts. It is not possible to draw a single contour around the no-PAH zone based upon the [5.8]/[3.6] ratio, however, the PAH destruction edge is visible in this image as a dark band with good spatial correspondence to the fiducial contours from Figs. 2.4*a* and 2.5*a* (*white* and *yellow*, respectively).

The fiducial contour from Figure 2.4*a* is overplotted on the [4.5] and [8.0] images. The region exterior to this contour is PAH-dominated, while the Ω-shaped area enclosed by the contour is the PAH-free zone. The emission at [3.6], [5.8], and [8.0] increases sharply at the outer contour in both the northern and southern bars, evidence of the sudden appearance of the mid-IR PAH emission features. The dust continuum is particularly bright in the [8.0] band, hence this band shows a very bright ridge of emission in the southern bar interior to the PAH destruction edge. The [4.5] emission, in contrast, maintains approximately the same brightness across the PAH destruction edge, although some of the same dust continuum morphology exhibited by the [8.0] image is also readily apparent at [4.5]. Overplotted on the [3.6] and [5.8] images are contours of the 20 cm continuum from MAGPIS. The radio continuum traces free-free emission in the H II region, and these contours closely trace the [4.5] emission. This morphological similarity is due to the fact that the primary contributors to the IRAC [4.5] band are small-grain dust continuum photons with the $\sim$20% contribution from H I Brα recombination line emission estimated in §2.3.2 above, both of which effectively trace the radio H II region. The strong PAH features in the other 3 IRAC bands contribute diffuse emission that remains relatively bright far into the PDR, yet most of the same morphological features are still faintly visible at [4.5]. This suggests that there may be some additional continuum contribution underlying all of the GLIMPSE bands, perhaps dehydrogenated PAHs as postulated by Giard, Bernard, & Dennefield (1992) or the short-wavelength tail of the dust thermal continuum.

The structure of the PAH emission and location of the PAH destruction edge in M17 has been measured previously in both the northern (Chrysostomou et al. 1992) and southern (Giard, Bernard, & Dennefield 1992; Crété et al. 1999; Kassis et al. 2002) bars. These observations were generally of lower resolution and sensitivity than the GLIMPSE data and covered only limited portions of the M17 complex, but the PAH morphologies presented agree well with our interpretation of the mid-IR morphology observed in GLIMPSE. A general picture emerges in which the PAH destruction edge occurs at or just outside the boundary of the H II region as defined by the I-front (FCM84), with the PAH emission extending far into the PDR. This is supported by the fact that the peak of the 20 cm emission is either coincident with or lies just inside the boundary of the PAH destruction zone throughout M17 (Figure 2.7). It is difficult to precisely locate the position of the I-front relative to the PAH edge, owing to the complicated 3-dimensional geometry of the region. The 20 cm emission appears to extend into the PAH-dominated PDR bars, but this is probably a projection effect.

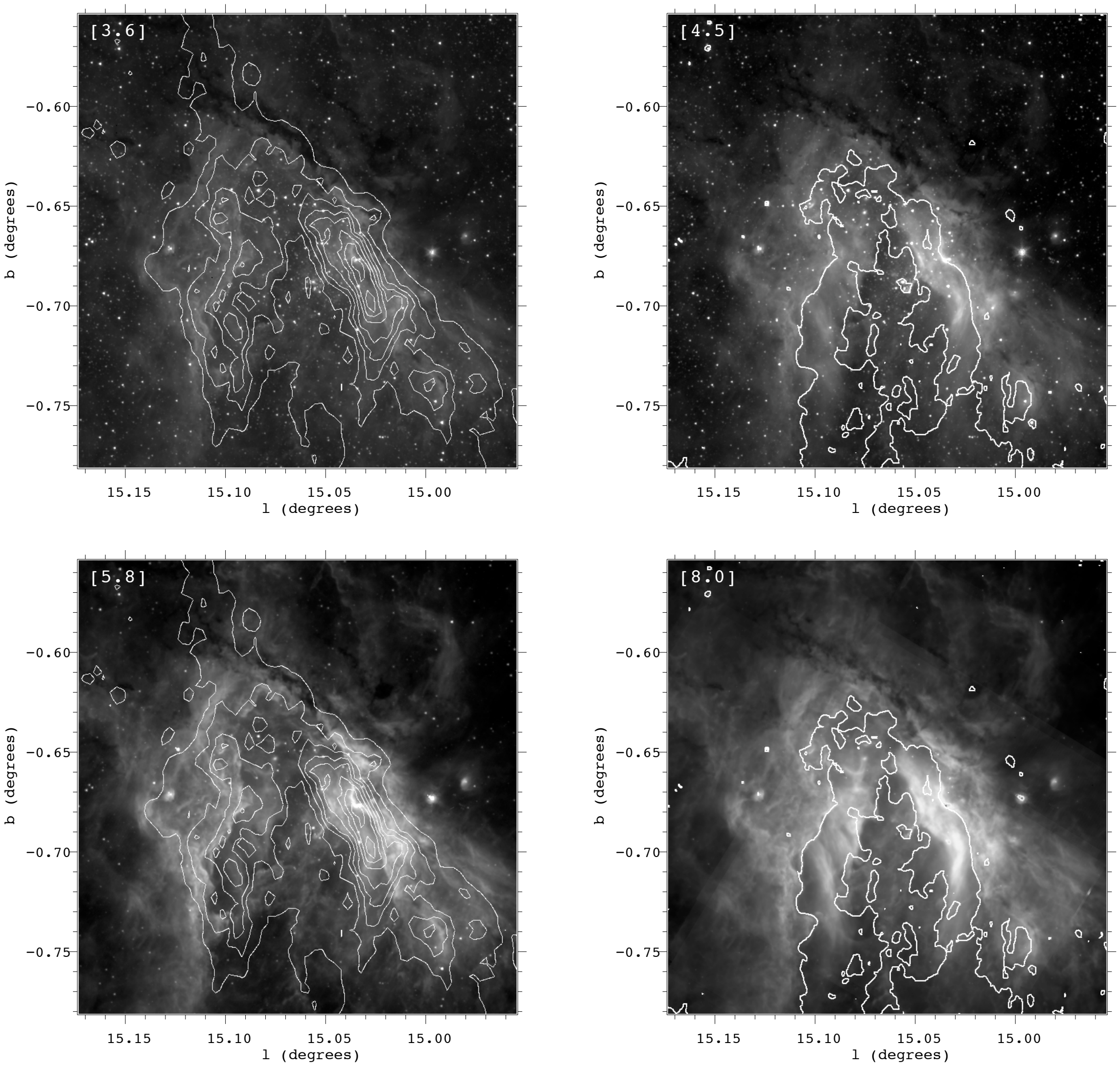

Fig. 2.7.— Comparison of the 4 GLIMPSE single-band mosaics of M17. All 4 images show the same field of view. IRAC [4.5] traces mainly dust continuum with a ∼20% contribution from the H I Brα recombination line. The other 3 IRAC bands trace the same continuum but include a strong contribution from PAH emission features in the PDR. On the [4.5] and [8.0] images, the fiducial contour from Figure 2.4 is shown tracing the PAH destruction edge and inner cavity wall. Overplotted on the [3.6] and [5.8] images are 20-cm VLA MAGPIS contours at intervals of 0.04 mJy/beam from 0.02 to 0.34 mJy/beam.

2.4.2 IRS Spectroscopy

To further test our results concerning the PAH emission, we analyzed a series of 4 spectra taken from the *Spitzer*/IRS SH observations of the M17 southern bar. These 4 spectra were extracted from the slit pointings labeled P1–P4 in Figures 2.4*a*, 2.5*a*, and 2.6*a*. Only pointing P1 falls inside the PAH-destruction zone, and the other 3 pointings sample the PDR in order of increasing distance from the PAH destruction

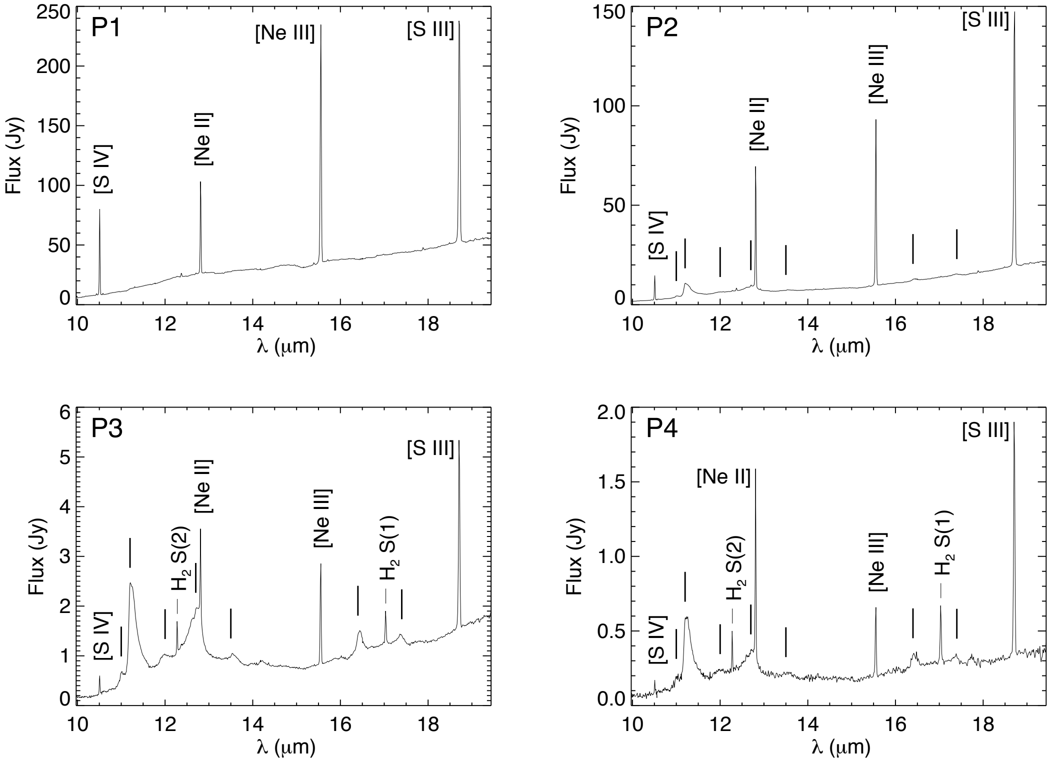

Fig. 2.8.— Four IRS SH spectra. The panels represent a series of slit pointings P1–P4 that span the H II region–PDR interface in the southern bar, in order of increasing distance from the ionizing cluster. Note the change in flux scale for each panel. The unlabeled vertical dashes mark PAH emission features listed in Table 2.5. There are no PAH features in pointing P1, the only pointing that falls inside the PAH destruction zone identified in Figs. 2.4–2.5. The changing physical conditions between the H II region and througout the PDR are marked by the variation in relative strengths of the forbidden lines of different ionization states; both [S IV]/[S III] and [Ne III]/[Ne II] decrease monotonically from P1 to P4.

edge. The spectra from these 4 extractions, covering the IRS SH wavelength range of 9.9–19.6 μm, are plotted in the 4 panels of Figure 2.8. The brightness of the spectrum drops by over 2 orders of magnitude between pointings P1 and P4, and the flux scale has been adjusted accordingly in each panel. The PAH features listed in Table 2.5 that fall within this wavelength range are apparent in all but pointing P1; these are marked by vertical dashes but not labeled in order to minimize clutter in the plots. The disappearance of the PAH features in pointing P1 is fully consistent with our interpretation of the GLIMPSE images. In terms of absolute flux, the PAH emission features are the brightest by far in pointing P2, although this is not obvious due to the the flux scaling required to display the full height of the bright fine-structure lines of [S IV] 10.510 μm, [Ne II] 12.814 μm, [Ne III] 15.555 μm, and [S III] 18.713 μm.

The fine-structure lines trace the ionization state of the gas in the PDR. Both the level of ionization in the gas and the strength of the emission lines are high near the I-front. Hence the ratio of the higher-ion lines, [S IV] and [Ne III], to their lower-ion counterparts, [S III] and [Ne II], is greatest in extraction P1, the only one of our sample spectra taken from within the H II region. The brightness of the [S IV] line drops precipitously across the I-front/PDR interface, as a comparison of the P1 and P2 spectra shows. The ratios [S IV]/[S III] and [Ne III]/[Ne II] continue to decrease with increasing distance into the PDR, with the latter ratio inverting (becoming smaller than unity) somewhere between pointings P2 and P3. The overall diminishing of the fine-structure lines with distance from the ionizing cluster is consistent with the attenuation of the radiation field.

These same 4 spectra, normalized to their respective median continuum values, are plotted on the same set of axes in Figure 2.9*a*. A relative vertical shift of +1 is applied to each successive spectrum from P1–P4 for display purposes. The color-coding of the spectra corresponds to the colors (except that *white* maps to *black*) of the slit positions overlaid on the 3-band (*red*=5.8 μm, *green*=4.5 μm, *blue*=3.6 μm) GLIMPSE mosaic image of M17 in Figure 2.9*b*. The PAH destruction edge (*white* contour from Figure 2.4) can be traced throughout this image where the [3.6] and [5.8] emission (*blue-red*) appears to give way to [4.5] emission (*green*). The O stars listed in Table 3 are identified (*cyan* circles), showing how the 4 IRS pointings together form a series of spectra sampling the southern bar at locations progressively more distant from the central ionizing cluster. Two bright infrared sources, the UC H II region M17-UC1 and the probable massive YSO M17 SW-IRS, are also labeled in Figure 2.9*b* for reference, but these sources are produced by B-type stars (FCM84), and hence are not significant contributors to the ionization of the M17 complex.

While the absolute strengths of the PAH features decrease with increasing distance into the PDR (Figure 2.8), the strengths of the PAH features relative to the continuum increase, and the strengths of the molecular hydrogen lines, H_2(0,0) S(1) at 12.279 μm and H_2(0,0) S(2) at 17.035 μm, increase relative to the PAH emission. The shapes and relative strengths of the PAH features do not appear to change much between the spectra. This is puzzling, considering that we might expect at least the 11.0 μm feature, attributed to PAH cations (PAH^+) (Hudgins & Allamandola 1999) to lose strength relative to the neighboring strong PAH neutral feature at 11.3 μm with increasing distance into the PDR, as the overall level of ionization in the gas is observed to decrease.

The PAH emission is not confined to the strong features. Clearly apparent in the P2–P4 spectra in

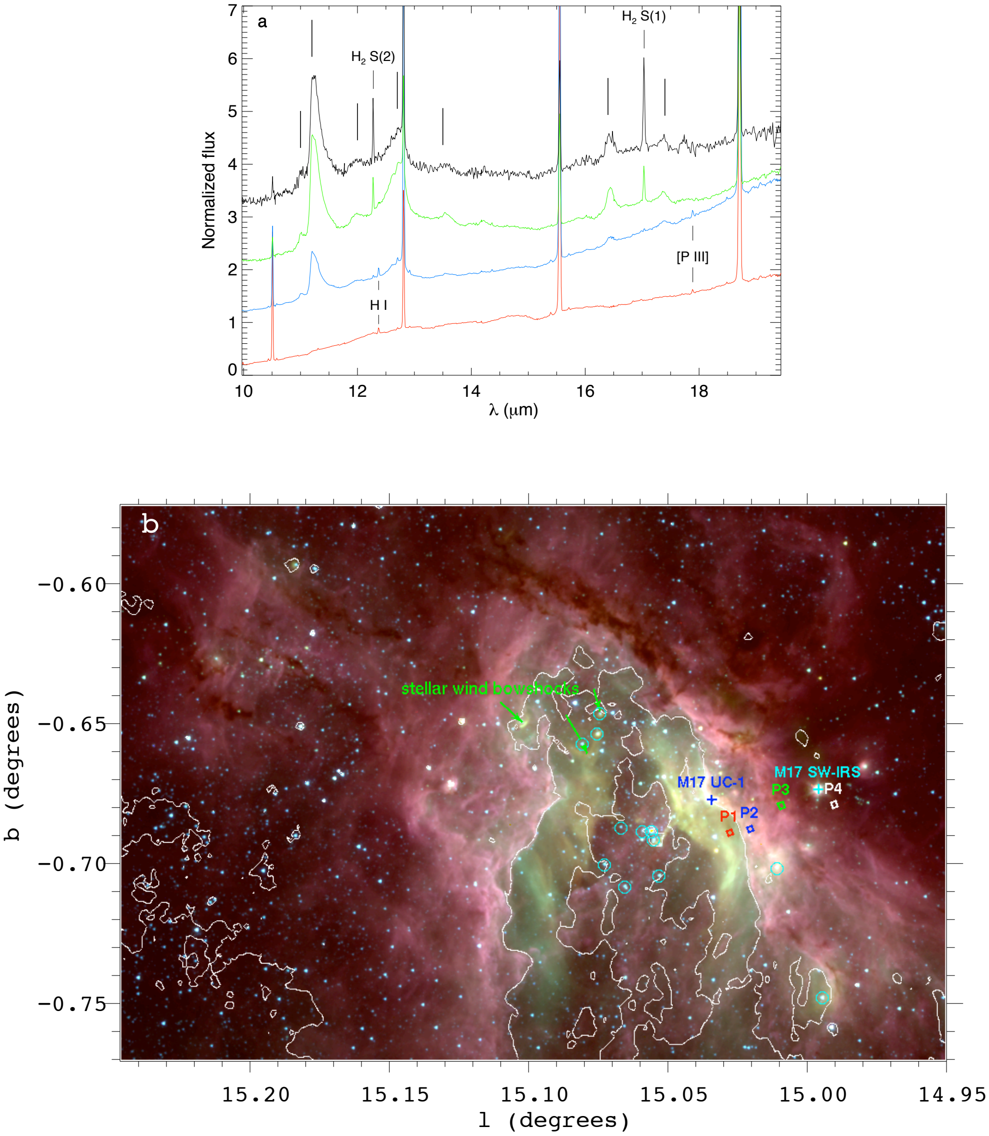

Fig. 2.9.— (*a*) Same 4 spectra as in Figure 2.8, normalized to their respective median continuum values and plotted on the same scale. An arbitrary relative vertical shift of +1 is added to each successive spectrum for display purposes. This scaling displays the strengths of the PAH (marked by unlabeled vertical dashes) and H_2 emission features relative to the continuum at each position. The color-coding corresponds to that of the slit positions overlaid on the 3-band (*red*=5.8 μm, *green*=4.5 μm, *blue*=3.6 μm) GLIMPSE mosaic (*b*). The *white* fiducial contour from Figure 2.4 is reproduced here. The O stars listed in Table 2.3 are marked by cyan circles. *Green* arrows point toward the upstream direction of the stellar-wind bowshocks. There is an elongated pillar near the largest bowshock with a bright YSO at its tip. The orientations of the arrows and the pillar converge on the central ring of O stars. Also labeled are the UC H II region M17-UC1 and the bright IR source M17 SW-IRS.

Figure 2.9*a* are broad emission plateaus extending from 11–14 μm and 16.5–17.5 μm (van Kerckhoven et al. 2000), connecting groups of PAH emission features that are related by vibrational mode (see Table 2.5). The relative strengths of the PAH emission features do not appear to vary much throughout the PDR, even as the overall brightness of the PAH emission spectrum decreases with increasing distance from the PAH destruction edge. This suggests that the PAH features in the IRAC bands, which fall shortward of the IRS SH wavelength coverage, should exhibit similar spatial morphologies. Follow-up observations of M17 using the IRS SL mode would enable an investigation of the shorter-wavelength PAH features in more detail, but we can produce a rough morphological comparison using our available data.

We used CUBISM v1.01 to produce a map of the 11.3 μm PAH feature from the IRS SH map. The extraction boxes for the spectral map are overlaid on an IRAC [8.0] image mosaic of M17 in Figure 2.10*a*, and the 11.3-μm PAH map is shown in Figure 2.10*b*. The map shows a narrow spectral window between 11.16 and 11.40 μm with adopted continuum regions at 10.80 to 10.92 μm and 11.67 to 11.80 μm. We avoid the 11.0 μm PAH emission feature for continuum subtraction. Note that CUBISM uses selected regions on either side of the feature to estimate the continuum. For broad features and a steep continuum, the subtraction is not perfect. Adopting different spectral regions for the continuum will yield minor variations in the map. Also note that the IRS SH module uses 2 pixels in the cross dispersion direction, and for our AORs (full steps perpendicular) the map necessarily contains 2 pixel spatial averages across the slit. If there are gaps in the maps, and CUBISM does not contain sufficient information to assign a value to a pixel, the software assigns a value of zero. This occurred in approximately 2% of the pixels, and to compensate we have simply interpolated a value from neighboring pixels.

Comparison of Figures 2.10*a* and 2.10*b* reveals similarities between the morphology of the 11.3-μm PAH emission feature and the IRAC [8.0] broadband emission. The brightest emission in the 11.3-μm map occurs near the arc of the PAH destruction edge, to the left of which the emission drops to virtually zero. M17 SW-IRS is also prominent. Both the PAH destruction edge and M17 SW-IRS can be identified in the [8.0] image as well, but the former is more difficult to spot because of the sharply rising brightness of the 8.0 μm continuum inside the H II region. This highlights the major difference between the PAH spectral map and the IRAC [8.0] image; the brightest region of [8.0] in the entire M17 complex is almost pure continuum emission, devoid of PAHs. *Spitzer*/IRAC images of energetic H II regions such as M17 should therefore not be interpreted solely in terms of PAH emission, because the continuum contribution can be strong, even

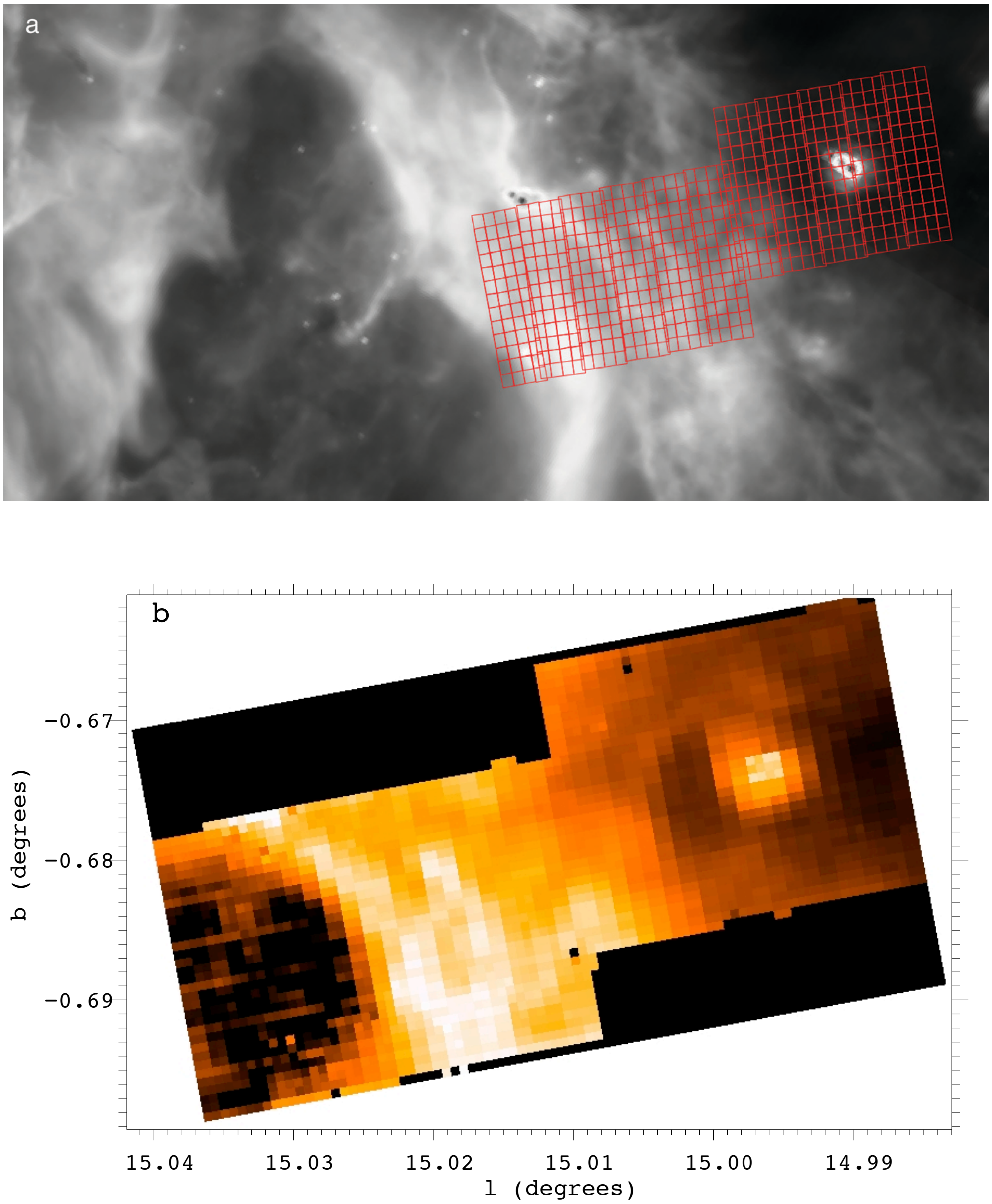

Fig. 2.10.— (*a*) Extraction boxes (*red*) used to create an IRS SH spectral map are overlaid on an IRAC [8.0] mosaic of M17. (*b*) Map of the 11.3 μm PAH feature, constructed from the IRS SH spectral map. The spatial resolution of the PAH map is lower than that of the IRAC [8.0] image by a factor of ∼10. Although the overall morphological similarities are unmistakable, there is one crucial difference between the PAH map and the [8.0] image. The PAH emission in the map disappears to the left of the bright arc of the PAH destruction edge, while bright continuum dominates the same part of the broadband image. M17 SW-IRS is visible in both panels as the bright point source at $(l, b) = (14.996, -0.673)$.

dominant, especially at 8.0 μm.

2.4.3 PAH Destruction by EUV and X-ray Photons

Figure 2.11 gives a multiwavelength view of M17. A hot plasma outflow from the cavity surrounding the ionizing star cluster glows in soft X-rays (*blue*) and the cavity walls are demarcated by 21.3 μm dust continuum emission (*red*). The entire M17 complex is surrounded by a PAH-emitting "wrapper" (*green*) that traces the boundary of the PDR. Whether the onset of PAH emission coincides precisely or only approximately with the boundary of the PDR is impossible to determine due to projection effects. In this section we show that the dearth of PAH emission inside the H II region is most likely due to destruction by stellar EUV photons. Given the X-ray content of M17 (T03) we also consider the role of X-rays in PAH destruction and in particular whether they are able to push the location of the PAH destruction edge beyond the I-front.

EUV and X-ray destruction of PAHs is governed by the processes of photo-thermo-dissociation (Léger et al. 1989) and Coulomb explosion (Leach 1987). Photo-thermodisso-ciation is a process analogous to sublimation in which transient heating vibrationally excites PAHs. Coulomb explosion involves double photoionization. The resulting dication generates a repulsive force in excess of the potential barrier, thus fragmenting the PAH. Larger PAHs are destroyed more rapidly since they present greater cross sections. The destruction rate a distance r from a source with luminosity spectrum L_E is

$$\Gamma_D = N_{\mathrm{C}} \int \frac{\sigma_E L_E}{4\pi r^2} e^{-\tau_E} \, \frac{dE}{E} \qquad [\mathrm{s}^{-1}] \tag{2.7}$$

where N_{C} is the number of carbon atoms per PAH molecule (we use $N_{\mathrm{C}} = 100$ in our calculations), σ_E is the photoionization cross-section, and τ_E is the optical depth.

PAHs are able to rebuild by accreting carbon atoms. This accretion rate is given by Voit (1992) as

$$R_{\mathrm{C}^+} n(\mathrm{C}^+) \sim (3.8 \times 10^{-11}) Y N_C^{3/2} n(\mathrm{C}^+) \qquad [\mathrm{s}^{-1}] \tag{2.8}$$

where $n(\mathrm{C}^+)$ is the number density of C^+ and Y is the sticking coefficient (assumed to be of order unity). For simplicity, we will assume that carbon is undepleted and singly ionized, and take C/H $\sim 4 \times 10^{-4}$ (Spitzer 1978). This leads to an upper limit on R_{C^+}.

We assume the UV radiation field is dominated by the central 8 O stars of NGC 6618 (Table 3) and synthesize black body curves for each star based on its radius and effective temperature (Table 1 of

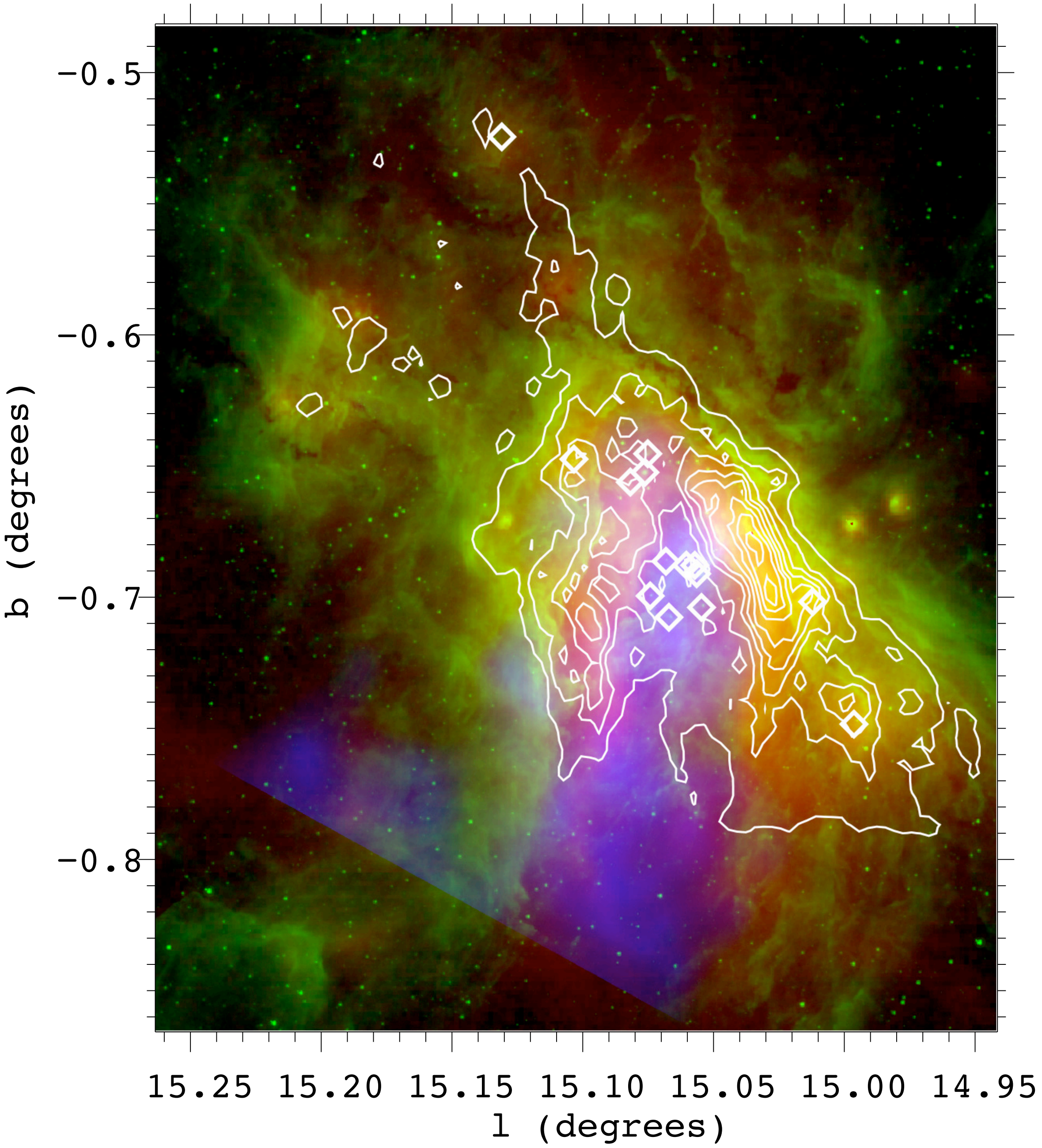

Fig. 2.11.— Multiwavelength M17. A river of MK plasma glows in soft X-rays (0.5–2.0 keV *Chandra* diffuse emission map from T03, *blue*) as it flows outward from the central cavity surrounding the O stars of NGC 6618 (*cyan* circles). The radio H II region (20 cm continuum, *white* contours) defines the cavity walls, and warm dust permeates the ionized gas, as shown by the 21.3 μm continuum emission (*MSX* E, *red*). The entire M17 complex is surrounded by a dusty wrapper (GLIMPSE [5.8], *green*) that traces the PDR in emission from PAHs.

Martins, Schaerer, & Hillier 2005) using

$$F_\lambda d\lambda = \frac{2\pi h c^2 \lambda^{-5}}{e^{\frac{hc}{\lambda kT}} - 1} \left(\frac{R}{r}\right)^2 d\lambda \tag{2.9}$$

where $(R/r)^2$ is the geometrical dilution factor. We first consider the destruction of PAHs throughout the entire H II region, assuming the (unrealistic) case of zero attenuation. Using the carbon photoionization cross-section of Verner et al. (1996), in Equation (2.7), and integrating over the range $11.26\,\mathrm{eV} < E < 291\,\mathrm{eV}$, between the energy threshold for the liberation of a carbon L-shell electron and the maximum energy for which the cross-section is valid, we find the destruction rate exceeds the accretion rate for $r < 400(10^3/n_{\mathrm{H}})^{1/2}(10^2/N_{\mathrm{C}})^{1/4}$ pc from the cluster center. This demonstrates that the O stars in M17 emit more than enough UV to destroy the PAHs in their vicinity. The fact that the observed PAH destruction edge falls near the I-front, only ∼1 pc from the ionizing stars, is evidence that the EUV radiation field is significantly attenuated in the H II region.

We then evaluated the destruction rate outside the I-front. We assumed the UV spectrum truncates abruptly at 13.6 eV, held τ_E constant at $10^{-21} N_H$ (Osterbrock & Ferland 2006), set $r = 1$ pc in Equation (2.7), and solved for the column density at which PAH creation balances destruction. The result, $N \sim 1.2 \times 10^{22}$ cm^{-2} with $n_H = 560$ cm^{-3} (Pellegrini et al. 2007), would imply that the PAH destruction edge lies several pc outside the I-front. This is inconsistent with the observations. The discrepancy could be explained by additional extinction, most likely due to dust within the H II region.

Finally, to consider the role of X-ray photons we used the X-ray photoionization cross-section of Voit (1991) in Equation (2.7). We calculated the X-ray emission (Raymond & Smith 1977) assuming a gas in coronal equilibrium at $T \sim 7 \times 10^6$ K with a total luminosity $L \sim 9.5 \times 10^{33}$ erg s^{-1} (T03). Setting r to 1 pc in Equation (2.7), we compute a maximum Γ_D (zero attenuation) of $1.1 \times 10^{-14} N_{\mathrm{C}}\ s^{-1}$. If $n_{\mathrm{H}} \sim 560$ cm^{-3} (Pellegrini et al. 2007) and $N_{\mathrm{C}} = 100$, Equation (2.8) shows that the destruction rate never exceeds the accretion rate. This suggests that X-rays are not a significant destruction mechanism of PAHs in M17 and hence do not significantly affect the location of the PAH destruction edge. Since M17 is particularly luminous in X-rays, we can extend our conclusion to suggest that X-ray destruction of PAHs is not an important mechanism in any Galactic H II region. PAH destruction is caused by the action of EUV photons.

2.5 Conclusions

We have utilized images from multiple Galactic plane surveys spanning the near-IR to radio continuum wavelengths to construct the global SED of M17. The integrated flux in this SED gives a bolometric luminosity of 2.4×10^6 $L_\odot$ at a luminosity distance of 1.6 kpc. This is consistent with the total bolometric luminosity of the known OB stellar content of NGC 6618, the ionizing cluster of the M17 H II region. Our upper limit of 1.9 kpc on the luminosity distance rules out the kinematic distance estimate of 2.2 kpc. Accepting the distance estimate of 1.6 kpc derived by Nielbock et al. (2001) and used by T03 and others, the earliest-type star in M17 may be O3 V, but it is unlikely either that there is more than one star earlier than O4 V or that many O stars (or other high-luminosity stars) remain undiscovered in M17. We can also constrain the 3-dimensional geometry of M17 to a form between a cone and a clamshell with a 45° opening angle. The structural model of Pellegrini et al. (2007), the most detailed three-dimensional model of the M17 nebular geometry to date, is consistent with our results. The Pellegrini et al. (2007) model, however, concentrates on the line-of-sight through the southern bar, noting in particular the nearly edge-on orientation of the interface between the H II region and the PDR, but is less specific in describing the same structures in the northern bar. The GLIMPSE images show a sharp separation between the PAH-dominated PDR and the dust continuum-dominated H II region in the northern bar as well as in the southern bar. This indicates that the northern bar also presents a nearly edge-on view of the interface of the PDR with the H II region.

We have located the PAH destruction edge surrounding the M17 H II region using band-ratio images produced from the GLIMPSE residual images. We confirm the disappearance of PAHs within the destruction zone using spectroscopic data from *Spitzer*/IRS. We calculate the photo-destruction rate of PAHs by EUV photons and find that this destruction mechanism accounts for the absence of PAHs in the M17 H II region. Comparison of the GLIMPSE images with the MAGPIS 20 cm maps reveals that the PAH destruction edge lies everywhere close to the I-front. Due to the complicated 3-dimensional structure of M17, it is difficult to tell whether the edge of the H II region and the onset of PAH emission in the PDR are always spatially coincident or if there can be a significant gap between the two. We explored the possibility of an X-ray destruction mechanism for PAH molecules that could push the destruction edge beyond the I-front, but found that the diffuse X-ray flux in M17 observed by T03 is insufficient to destroy PAHs faster than they can form. This result likely applies to nearly all Galactic H II regions, the majority of which are less energetic than M17.

The anatomy of a massive star-formation region is exemplified by M17. A cluster of massive stars provides sufficient Lyman continuum radiation to ionize the surrounding gas and destroy PAH molecules. The H II region is permeated by dust, probably with small grain sizes (Giard, Bernard, & Dennefield 1992), and these warm grains produce a bright IR continuum. Although stochastic heating processes probably dominate the continuum at $\lambda \lesssim 10$ μm, the radiation field is sufficiently strong that small grains can achieve thermal equilibrium and radiate approximately as blackbodies at longer mid-IR wavelengths. This continuum peaks at wavelengths from 20–100 μm, and hence H II regions generally stand out in *MSX* and *Spitzer*/MIPS images. Helou et al. (2004) carried out a *Spitzer* study of the spiral galaxy NGC 300 and found that IRAC [8.0] emission tends to highlight the rims of star-formation regions, while MIPS 24 μm emission usually peaks interior to these rims. The view of M17 presented in Figure 2.11 tells a similar story, where the 21.3 μm dust continuum emission (*red*) highlights the H II region bars (radio contours), while the 5.8 μm PAH-dominated emission (*green*) wraps around the entire complex and defines a sharp rim at the PAH destruction edge.

In very energetic regions like M17, the dust continuum can be very bright even at IRAC wavelengths, hence care should be used in interpreting the IRAC images of bright H II regions. Because 3 of the 4 IRAC bands trace similar emission processes (dust continuum + PAH emission features), the remaining band, [4.5], tends to stand out in multi-band color composite images. This band contains several emission lines, predominantly the Brα recombination line in an H II region. It is tempting to interpret the IRAC [4.5] emission, appearing as a "green glow" interior to the bright emission rims defining the PAH destruction edge in Figure 2.9*b*, as perhaps an ionized flow that emits strongly in Brα evaporating off of the interior walls of a dust cavity. Such an evaporating flow was proposed by Weaver et al. (1977), but we have shown that the Brα line contributes only ∼20% of the broad-band IRAC [4.5] emission in M17. While the [4.5] image does trace the H II region, and there is a marginally significant enhancement of Brα interior to the PAH destruction edge, the "green glow" in M17 and IRAC color mosaics of similar H II regions is primarily an artifact of the image stretch used to create the color composites. The [4.5] band, lacking PAH emission, tends to be much fainter in diffuse emission than the [5.8] and [8.0] bands, hence the [4.5] stretch is often brightened relative to that of the other bands for display purposes. The [5.8] and especially [8.0] bands can exhibit bright continuum emission where there is no PAH contribution, hence in M17 there are two prominent diffuse emission edges, the outer edge of PAH destruction, and the inner edge closer to the ionizing cluster where the dust has been cleared away by stellar winds.

The dynamical effect of the combined OB stellar winds shapes the physical distribution of gas and dust in M17, as evidenced by the central cavity filled with shock-heated plasma and the apparent bowshocks near 4 massive stars. The PAH destruction edge has, in many places, a morphology suggestive of multiple shock fronts. The observed IR morphology of the region is further determined by the radiative effects of dust heating and PAH excitation. The results of this work provide further proof of the dominant feedback mechanisms employed by OB stars in shaping and illuminating their birthplaces.

We thank Leisa Townsley for providing us with images of the diffuse X-ray flux of M17 detected by *Chandra* and for her numerous helpful suggestions as the referee. We are grateful to Martin Cohen for his invaluable insights on diffuse flux calibrations. Discussions with Melvin Hoare provided useful ideas for improving this work. Support for this work, part of the *Spitzer Space Telescope* Legacy Science Program, was provided by NASA through contracts 1224653 (University of Wisconsin at Madison), 1224681 (University of Maryland), and 1224988 (Space Science Institute). JMS was supported by NASA ATP grant NNGO5IGO9G. Additional support for Spitzer Space Telescope GO observations was provided by NASA through an award issued by JPL/Caltech. MGW was supported in part by NASA Long Term Space Astrophysics grant NNG05GD64G.

References

Allamandola, L. J., Tielens, A. G. G. M., & Barker, J. R. 1989, ApJS, 71, 733

Altenhoff, W. J., Downes, D., Goad, L., Maxwell, A., & Rinehart, R. 1970, A&AS, 1, 319

Beichman, C. A., Neugebauer, G., Habing, H. J., Clegg, P. E., & Chester, T. J., eds. 1988, IRAS Catalogs and Atlases: Explanatory Supplement, NASA RP-1190

Benjamin, R. A. et al. 2003, PASP, 115, 953

Broos, P. S. et al. 2006, ApJ, submitted, (astro-ph/0612590)

Capriotti, E.R. & Kozminski, J. F. 2001, PASP, 113, 677

Carey, S. J. et al. 2006, AAS, 209.8801

Chini, R., Elsässer, H., & Neckel, T. 1980, A&A, 91, 186 (CEN)

Chrysostomou, A., Brand, P. W. J. L., Burton, M. G., & Moorhouse, A. 1992, MNRAS, 256, 528

Churchwell, E., Wolfire, M. G., & Wood, D. O. S. 1990, ApJ, 354, 247

Churchwell, E., Povich, M. S., et al. 2006, ApJ, 649, 759

Cohen, M. et al. 2007, MNRAS, 374, 979

Conti, P. S. & Crowther, P. A. 2004, MNRAS, 355, 899

Crété, E., Giard, M., Joblin, C., Vauglin, I., Léger, A., & Rouan, D. 1999, A&A, 352, 277

Downes, D., Wilson, T. L., Bieging, J. & Wink, J. 1980, A&AS, 40, 397

Draine, B. T. 2003, ARA&A, 41, 241

Elmegreen, B. G. & Lada, C. J. 1976, AJ, 81, 12

Fazio, G. G. et al. 2004, ApJS, 154, 10

Felli, M., Churchwell, E., & Massi, M. 1984, A&A, 136, 53 (FCM84)

Giard, M., Bernard, J. P., & Dennefield, M. 1992, A&A, 264, 610

Goss, W. M. & Shaver, P. A. 1970, AuJPA, 14, 1

Hanson, M. M., Howarth, I. D., & Conti, P. S. 1997, ApJ, 489, 698

Harper, D. A., Low, F. J., Rieke, G. H., & Thronson, H. A. 1976, ApJ, 205, 136

Hauser, M. G. et al. 1991, AIPC, 222, 161

Helfand, D. J., Becker, R. L., Fallon, A., & Tuttle, S. 2006, AJ, 131, 2525

Helou et al. 2004, ApJS, 154, 253

Houck, J. R. et al. 2004, SPIE, 5487, 62

Hudgins, D. M. & Allamandola, L. J. 1999, ApJ, 516, L41

de Jager, C. & Nieuwenhuijzen, H. 1987, A&A, 177, 217

Jiang, Z. et al. 2002, ApJ, 577, 245

Kassis, M., Deutsch, L. K., Campbell, M. F., Hora, J. L., Fazio, G. F., & Hoffman, W. F. 2002, AJ, 124, 1636

van Kerckhoven, C. et al. 2000, A&A, 357, 1013

Kleinmann, D. E. & Wright, E. L. 1973, ApJ, 185, L131

Koo, B.-C., & Mckee, C. F. 1992, ApJ, 388, 103

Lada, C. 1976, ApJS, 32, 603

Lada, C. J., DePoy, D. L., Merrill, K. M., & Gatley, I. 1991, ApJ, 374, 533

Leach, S. 1987, J. Electr. Spectrosc. 41, 427

Léger, A. & Puget, J. L. 1984, A&A, 137, L37

Léger, A., Boissel, P., Désert, F. X., & d'Hendecourt, L. 1989, A&A, 213, 351

Martins, F., Schaerer, D. & Hillier, D. J. 2005, A&A, 436, 1049

Meixner, M., Haas, M. R., Tielens, A. G. G. M., Erickson, E. F., & Werner, M. 1992, ApJ, 390, 499

Nielbock, M., Chini, R., Jütte, M., & Manthey, E. 2001, A&A, 273, 284

Ogura, K. & Ishida, K. 1976, PASJ, 28, 35 (OI)

Osterbrock, D. E. & Ferland, G. J. 2006, Astrophysics of Gaseous Nebulae and Active Galactic Nuclei, University Science Books.

Peeters, E., Mattioda, A. L., Hudgins, D. M. & Allamandola, L. J. 2004, ApJ, 617, L65

Pellegrini, E. W. et al. 2007, ApJ, in press, (astro-ph/0611808)

Price, S. D., Egan, M. P., Carey, S. J., Mizuno, D. R., and Kuchar, T. A. 2001, AJ, 121, 2842

Price, S. D., Paxson, C., Engelke, C. & Murdock, T. L. 2004, AJ, 128, 889

Raymond, J. C., & Smith, B. W. 1977, ApJS, 35, 419.

Schraml, J. & Mezger, P. G. 1969, ApJ, 156, 269

Skrutskie, M. F. et al. 2006, AJ, 131, 1163

Spitzer, L. 1978, Physical Processes in the Interstellar Medium, Wiley-Interscience.

Stetson, P. 1987, PASP, 99, 191

Subrahmanyan, R. & Goss, W. M. 1996, MNRAS, 281, 239

Townsley, L. K., Feigelson, E. D., Montmerle, T., Broos, P. S., Chu, Y.-H., & Garmire, G. P. 2003, ApJ, 593, 874 (T03)

Tsivilev, A. P. & Krasnov, V. V. 1999, Astron. Rep., 43, 511

Verner, D. A., Ferland, G. J., Korista, K. T., & Yakolev, D. G. 1996, ApJ, 465, 487

Vig, S., Ghosh, S. K., Kulkarni, V. K., Ojha, D. K., & Verma, R. P. 2006, ApJ, 637, 400

Voit, G.M. 1991, ApJ, 379, 122

Voit, G. M. 1992, MNRAS, 258, 841

Weaver, R., McCray, R., Castor, J., Shapiro, P., & Moore, R. 1977, ApJ, 218, 377

Chapter 3

Interstellar Weather Vanes: GLIMPSE Mid-Infrared Stellar-Wind Bow Shocks in M17 and RCW 49

Originally published by M. S. Povich, R. A. Benjamin, B. A. Whitney, B. L. Babler, R. Indebetouw, M. R. Meade, & E. Churchwell in The Astrophysical Journal, Volume 689, Issue 1, pp. 242–248 (December 2008)

Abstract

We report the discovery of six infrared stellar-wind bow shocks in the Galactic massive star formation regions M17 and RCW 49 from *Spitzer* GLIMPSE (Galactic Legacy Infrared Mid-Plane Survey Extraordinaire) images. The InfraRed Array Camera (IRAC) on the *Spitzer Space Telescope* clearly resolves the arc-shaped emission produced by the bow shocks. We combine Two Micron All-Sky Survey (2MASS), *Spitzer, MSX,* and *IRAS* observations to obtain the spectral energy distributions (SEDs) of the bow shocks and their individual driving stars. We use the stellar SEDs to estimate the spectral types of the three newly-identified O stars in RCW 49 and one previously undiscovered O star in M17. One of the bow shocks in RCW 49 reveals the presence of a large-scale flow of gas escaping the H II region at a few 10^2 km s^{-1}. Radiation-transfer modeling of the steep rise in the SED of this bow shock toward longer mid-infrared wavelengths indicates that the emission is coming principally from dust heated by the star driving the shock. The other 5 bow shocks occur where the stellar winds of O stars sweep up dust in the expanding H II regions.

3.1 Introduction

The Solar wind ends in a termination shock (e.g. Decker et al. 2005), where the pressure of the heliosphere balances the ram pressure of the surrounding interstellar medium (ISM). Massive stars with more energetic winds generate much stronger shocks. In cases where the relative motion between the star driving the wind and the ambient ISM is large, the shock will be bent back around the star. If the relative velocity is supersonic, the ambient ISM gas is swept into a second shock, forming an arc-shaped "bow shock" that is separated from the termination shock by a contact discontinuity. Stellar-wind bow shocks have been reported for a variety of sources, including nearby runaway O stars (van Buren & McCray 1988; van Buren, Noriega-Crespo, & Dgani 1995; Noriega-Crespo et al. 1997; Brown & Bomans 2005; Comerón & Pasquali 2007; France et al. 2007), high-mass X-ray binaries (Churchwell et al. 1992; Kaper et al. 1997; Huthoff & Kaper 2002), LL Ori-type stars (Bally et al. 2000), radio pulsars (Gaensler & Slane 2006), Galactic center O stars (Geballe et al. 2004, 2006), and mass-losing red giants (Martin et al. 2007). Recently, an infrared (IR) bow shock has been observed around the young A-type star δ Vel (Gáspár et al. 2008). Cometary H II regions also resemble bow shocks, due either to density gradients in the ambient gas or to motion of the ionizing source with respect to the interstellar surroundings (van Buren et al. 1990; Arthur & Hoare 2006). Both the direction of a bow shock and its "standoff distance" from the star generating the wind are determined by the velocity of the star with respect to the surrounding medium. In the case of runaway O stars, this is dominated by the high space motion of the star.

We report the detection of three mid-IR bow shocks in each of two massive star formation regions: M17 and RCW 49. Two of the bow shocks in M17 are around known O stars. We will demonstrate that the other bow shocks are also around likely O stars. Since these stars are in or near expanding H II regions, we find that the direction of the bow shock is determined principally by the flow of the ISM rather than the space motion of the star.

3.2 Observations and Interpretation

The Galactic Legacy Infrared Mid-Plane Survey Extraordinaire (GLIMPSE; Benjamin et al. 2003) programs have mapped the inner Galactic midplane ($|l| \leq 65^\circ$) using the IRAC instrument on the *Spitzer Space Telescope* ($2''$ resolution; Fazio et al. 2004). RCW 49, located at $(l, b) = (284.3, -0.3)$, was observed as part of the validation of the GLIMPSE observing strategy. The same area of the sky was imaged 10 times with 2-second exposures, and the combined data were mosaicked together to produce high resolution images ($0.6''$ pixels) of this region in the four IRAC bands: 3.6, 4.5, 5.8, and 8.0 μm. An overview of these observations was given by Churchwell et al. (2004). M17, at $(l, b) = (15.0, -0.7)$, was included in the GLIMPSE survey area, with two visits on the sky combined to make mosaics with $0.6''$ pixels.

3.2.1 M17

In Chapter 2, we presented the diffuse emission morphology of M17 at multiple wavelengths from IR to radio, constraining the distance to 1.4–1.9 kpc. We will assume the widely-adopted value of 1.6 kpc for the M17 distance, following Nielbock et al. (2001). The winds and radiation of the O stars in the NGC 6618 cluster have excavated a cavity in the center of the M17 H II region. The cavity is filled with hot, X-ray-emitting gas from shocked stellar winds (Townsley et al. 2003). In Chapter 2, we noted the presence of 3 apparent stellar-wind bow shocks along the northern wall of the cavity, along with a prominent "elephant trunk," or pillar, all oriented in the direction of the central ring of 7 O stars in NGC 6618. These structures are highlighted in Figure 3.1, a GLIMPSE image of M17 with an enlargement of the region containing the bow shocks. The bow shocks stand out as yellow-orange features in the image because they are faint at 3.6 μm (colored *blue*) compared to the other 3 IRAC bands.

We designate these stellar-wind bow shocks in Figure 3.1 with the name of the region followed by an identification number, in order of increasing Galactic longitude (for example, M17-S1). IR fluxes for all of the bow shock driving stars are given in Table 3.1, and background-subtracted IR fluxes from aperture photometry of the bow shocks are listed in Table 3.2. Spectral types of two of the driving stars have been determined photometrically (Bumgardner 1992) and spectroscopically (Hanson, Howarth, & Conti 1997). M17-S1 is associated with CEN 16, an O9–B2 star. The larger bow shock, M17-S2, is driven by CEN 18, an earlier-type star (O7–O8). Both bow shocks were detected at 10.5 and 20 μm by Nielbock et al. (2001). These observations did not resolve the arc shapes of the bow shocks, and Nielbock et al. (2001) attributed the excess IR emission to circumstellar disks and classified CEN 16 and IRS 9 (the star visible just to the right of the arrowhead in Figure 3.1) as massive protostars.

M17-S3 lies outside of the field analyzed by Hanson, Howarth, & Conti (1997), and the driving star does not appear in any catalog of the region. It is not found in any GLIMPSE sourcelist, because the bright, spatially variable diffuse background prevented the automatic extraction of the point source. We

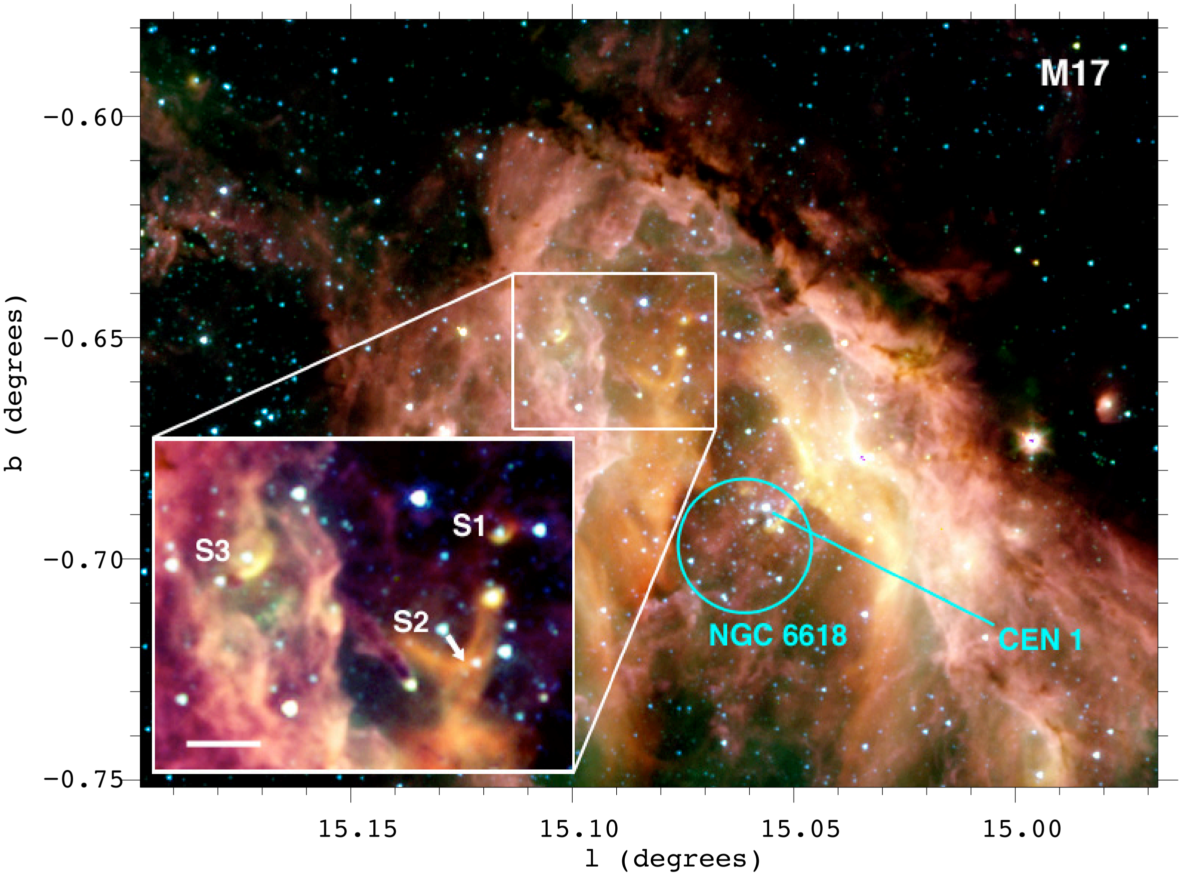

Fig. 3.1.— GLIMPSE full-color image of M17 (*blue:* 3.6 μm, *green:* 4.5 μm, *orange:* 5.8 μm, *red:* 8.0 μm). The region containing the bow shocks M17-S1, -S2, and -S3 is enlarged (scalebar shows $30'' = 0.23$ pc at 1.6 kpc). The central ring of O stars in the NGC 6618 cluster is circled. The bow shocks, along with the prominent pillar structure near M17-S2, all appear to be oriented in the general direction of CEN 1, the O4-O4 binary system in the center of the ionizing cluster.

measured the flux of this source manually using a $5''$ aperture. Using the spectral energy distribution (SED) fitting tool of Robitaille et al. (2007), we fit the IR fluxes of this star (Table 3.1) with Kurucz (1993) stellar atmosphere models. Following the method described by Watson et al. (2008), we scale the models to the 1.6-kpc distance of M17 and estimate a spectral type of O7 V for the star. Carrying out the same analysis on 7 other O stars in M17 with independently known spectral types (Chapter 3), we estimate that our spectral typing is accurate to within 2 subclasses.

3.2.2 RCW 49

RCW 49 presents a more complicated morphology than M17. Churchwell et al. (2004) discussed the structure and spectrum of the diffuse emission. Like M17, RCW 49 is filled with X-ray gas (Townsley et al. 2005). The interstellar structures are dominated by two large cavities. The first, blown out to the West, contains the massive young cluster Westerlund 2, and the second is an enclosed bubble around the Wolf-Rayet star WR 20b (Figure 3.2). The distance to RCW 49 remains disputed, with recent estimates placing the region as close as 2.8 kpc (Ascenso et al. 2007) or as far as 8.0 kpc (Rauw et al. 2007), with a kinematic distance estimate of 6 ± 1 kpc (Dame 2007). We consider distances of both 4.2 kpc (Churchwell et al. 2004) and 6 kpc in our analysis.

We have found three bow shocks associated with RCW 49, shown in three separate insets in Figure 3.2. RCW 49-S1 is unique among our sample, because it lies relatively far from the H II region, but we believe it is associated with RCW 49 for the following reasons: (1) The RCW 49 distance is consistent with the luminosity of the driving star being an O star (see below); and (2) the bow shock points (approximately) toward the central cluster, Westerlund 2. Because it is far from any other bright IR source, RCW 49-S1 appears as a point source in both the *Midcourse Space Experiment* (*MSX*; Price et al. 2001) and *Infrared Astronomical Satellite* (*IRAS*; Beichman et al. 1988) point source catalogs, and these fluxes are also given in Table 3.2.

RCW 49-S2 is oriented away from Westerlund 2 and appears to be influenced primarily by the nearby WR 20b. RCW 49-S3 is oriented in the general direction of Westerlund 2. None of the RCW 49 bow shocks

Table 3.1. 2MASS and IRAC[a] IR Fluxes for Bow Shock Driving Stars (mJy)

ID #	l	b	$F[J]$	$F[H]$	$F[K]$	$F[3.6]$	$F[4.5]$[b]	$F[5.8]$[b]
M17-S1	15.07486	-0.64607	196	214	186	96	67	···
M17-S2	15.08126	-0.65699	427	534	495	257	181	120
M17-S3[c]	15.10325	-0.64867	103	200	238	151	≤ 154	≤ 155
RCW 49-S1	284.07646	-0.43228	24	40	46	28	21	15
RCW 49-S2	284.30107	-0.37121	10	18	20	13	≤ 11	≤ 27
RCW 49-S3	284.33999	-0.28269	83	97	90	47	32	27

[a] None of these stars was detected in the IRAC [8.0] band.

[b] In cases where bow shock emission appears to cause a mid-IR excess over the stellar spectrum, the [4.5] and [5.8] fluxes are reported as upper limits. Due to suspected contamination from the bow shock or other diffuse emission, these fluxes are treated as upper limits to the stellar flux.

[c] Because the star driving SWB M17-3 is surrounded by bright, complex diffuse background emission, it was not extracted as part of the GLIMPSE point-source catalog. The fluxes reported here were measured using aperture photometry.

points directly back toward the central cluster, while all three M17 bow shocks do. Perhaps the expanding bubbles driven by Westerlund 2 and the Wolf-Rayet stars are interacting turbulently, producing non-radial components to the flows. It is also possible that the bow shock driving stars have large orbital motions relative to the dynamic interstellar medium.

The three bow shock driving stars in RCW 49 are of previously undetermined spectral type, so we again estimate the spectral type by fitting model SEDs to the broadband fluxes of Table 3.1, scaled to both the 4.2 kpc and 6 kpc distances. The results are given in Table 3.3. All three stars are plausibly O stars. Assuming 4.2 kpc, the driving star of RCW 49-S1 is fit as O6 V, RCW 49-S2 as O 9 V, and RCW 49-S3 as O5 V (or O9 III). If we increase the distance to 6 kpc, the fits become O 5 III, O6 V, and O5 V (or O6.5 III), respectively (see Watson et al. 2008, for an explanation of the degeneracy between luminosity classes). The spectral types at 6 kpc seem improbably luminous. Highly luminous and windy stars dominate the

Table 3.2. IR Fluxes for Bow Shocks (mJy)

				IRAC Fluxes[a]		
ID #	$l_{\rm apex}$	$b_{\rm apex}$	F[3.6][b]	F[4.5]	F[5.8]	F[8.0]
M17-S1	15.0744	-0.6465	≤ 34	71 ± 9	252 ± 42	1110 ± 290
M17-S2	15.0791	-0.6613	43 ± 17	245 ± 48	1240 ± 159	8700 ± 1500
M17-S3	15.1026	-0.6503	69 ± 16	240 ± 19	620 ± 100	1800 ± 320
RCW 49-S1	284.0775	-0.4305	5.7 ± 0.9	12 ± 1	33 ± 1	322 ± 5
RCW 49-S2	284.3018	-0.3712	≤ 2	9.6 ± 0.5	32 ± 3	172 ± 7
RCW 49-S3	284.3388	-0.2829	≤ 21	50 ± 7	160 ± 20	825 ± 120
				MSX Fluxes[c]		
	MSXC6 Name		F[8.3]	F[12.1]	F[14.6]	F[21.3]
RCW 49-S1	G284.0776-00.4340		627	2729	5674	1.56×10^4
				IRAS Fluxes[c]		
	IRAS Name		F[12]	F[25]	F[60]	F[100]
RCW 49-S1	IRAS 10205-5729		3810	4.21×10^4	$\leq 2.26 \times 10^5$	2.75×10^5

[a] The IRAC fluxes are background-subtracted. Fluxes were measured using irregular apertures drawn to enclose all of the visible bow shock structure. Separate apertures were used to estimate the background flux. For each bow shock, the same set of apertures was used for all IRAC wavelengths.

[b] In cases where stellar emission appears to be confused with bow shock emission, the [3.6] bow shock fluxes reported are upper limits only.

[c] RCW 49-S1 is a point source in both the *MSX* and *IRAS* catalogs. All of the other bow shocks are confused with bright diffuse background IR emission features at the resolutions of *MSX* and *IRAS*.

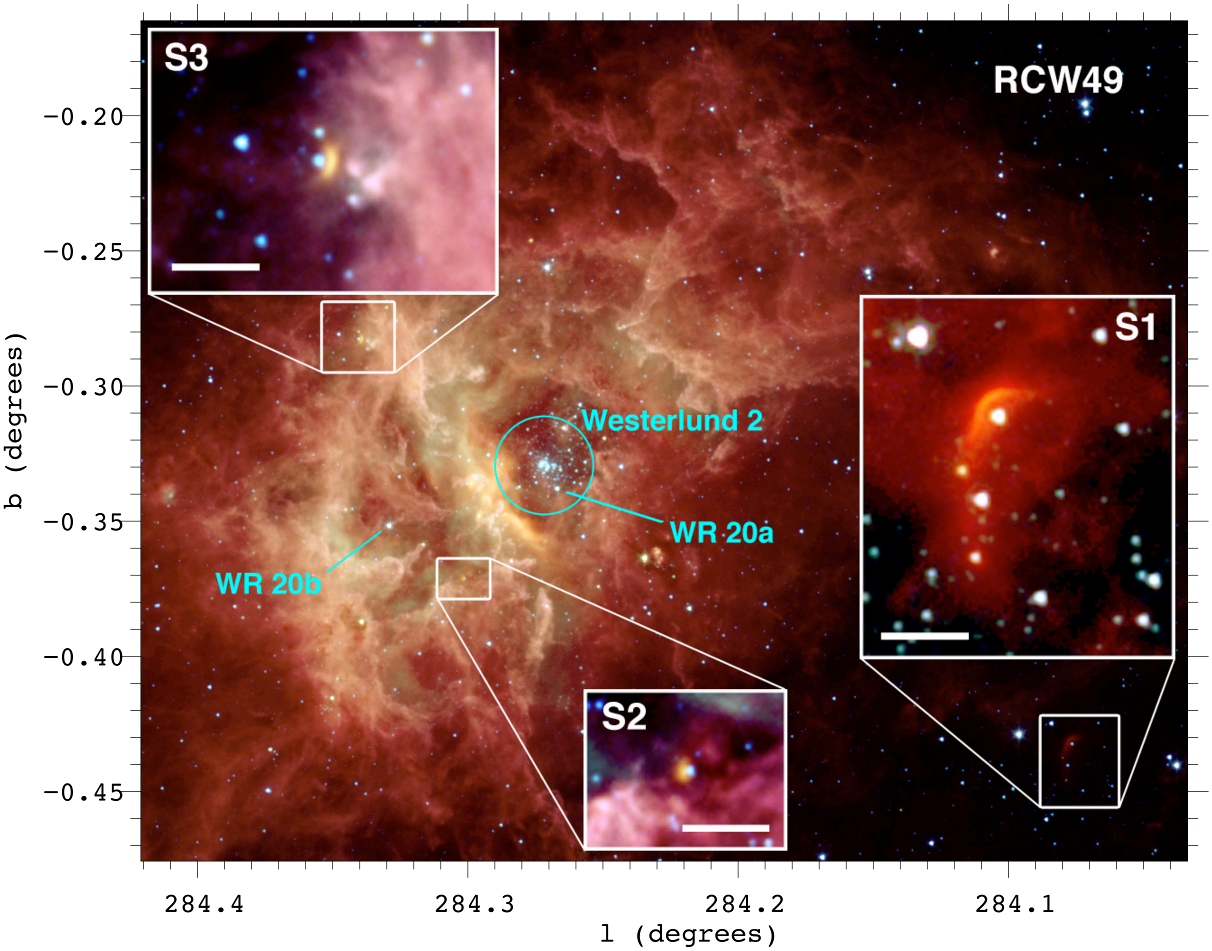

Fig. 3.2.— GLIMPSE full-color image of RCW 49 (*blue:* [3.6], *green:* [4.5], *orange:* [5.8], *red:* [8.0]). The bow shocks RCW 49-S1, -S2, and -S3, are enlarged in 3 separate insets (scalebars are $30'' \approx 0.6$ pc at 4.2 kpc). Three energy sources that could drive large-scale interstellar flows are also indicated: The Westerlund 2 cluster (circled), and the Wolf-Rayet stars WR 20a and WR 20b.

dynamics of their local ISM. We do not observe IR bow shocks around any of the earliest-type stars in either RCW 49 or M17, because they have blown large, evacuated cavities in the centers of the H II regions. Little or no ambient material remains close to the stars to produce a bow shock.

Apart from the Wolf-Rayet systems, one of the earliest stars in RCW 49 is G284.2642-00.3156. Using optical spectroscopy, Uzpen et al. (2005) classified this star as O4 V(f) and derived a spectrophotometric distance of 3.2±0.5 kpc. Using IR SED fitting, we confirm that the luminosity of this star is consistent with an O4 V star at 3.2 kpc. Yet this distance falls on the low end of the range of published distance estimates for RCW 49, and we do not adopt it here. Like CEN 1 in M17, G284.2642-00.3156 may be an unresolved, equal-mass O4–O4 binary. Doubling the luminosity moves the spectrophotometric distance from 3.2 to 4.5 kpc, in agreement with a distance of 4.2 kpc but inconsistent with 6 kpc.

3.3 Bow Shock Properties

The standoff distance d_w of a bow shock from its driving star is the point where the momentum flux of the stellar wind balances the momentum flux of the ambient medium: $n_w v_w^2 = n_0 v_0^2$. Following van Buren & McCray (1988), we normalize the stellar wind mass loss rate, $\dot{M}_{w,-6} = 10^{-6}$ M$_\odot$ yr^{-1}, stellar wind velocity $v_{w,8} = 10^8$ cm s^{-1}, ambient hydrogen particle density of $n_{0,3} = 10^3$ cm^{-3}, and use a mean ISM gas mass per hydrogen atom $\mu = 2.36 \times 10^{-24}$ g. Assuming a spherically symmetric stellar wind with a mass-loss rate given by $\dot{M} = 4\pi d_w^2 \mu n_w v_w$, the velocity of the star with respect to the ambient ISM can

Table 3.3. Bow Shock Standoff Distances and Estimated Stellar Wind Properties

ID #	Spectral type[a]	$\dot{M}_{w,-6}v_{w,8}$[b]	$d_w \cos i$ (pc)	$d_{cl} \cos i$ (pc)	$v_0 n_{0,3}^{1/2} (\cos i)^{-1}$ (km s^{-1})
M17 Distance = 1.6 kpc					
M17-S1	O9–B2 V	≤ 0.2	0.03	1.4	≤ 22
M17-S2	O7–O8 V	0.5–2.5	0.11	0.9	10–22
M17-S3	O7 V	0.5–2.5	0.05	1.7	21–47
RCW 49 Distance = 4.2 kpc					
RCW 49-S1	O6 V	~ 1.3	0.16	16.2	11
RCW 49-S2	O9 V	~ 0.2	0.04	2.46	17
RCW 49-S3	O5 V or O9 III	2.5–3.2	0.096	6.13	25–28
RCW 49 Distance = 6.1 kpc					
RCW 49-S1	O5 III	~ 16	0.23	23.2	26
RCW 49-S2	O6 V	~ 1.3	0.06	3.52	28
RCW 49-S3	O3 V or O6.5 III	> 3.2	0.14	8.8	> 19

[a] Spectral types for the stars driving M17-S1 and -S2 are taken from CEN and Hanson, Howarth, & Conti (1997). All others were estimated by fitting Kurucz (1993) stellar atmosphere models to the broadband IR fluxes (Table 3.1) and scaling to the distance of M17 or RCW 49. Spectral types given for RCW 49 are highly uncertain due to the disputed distance to that region.

[b] Estimates of stellar mass-loss rates $\dot{M}_{w,-6} = \dot{M}_w/(10^{-6}$ M$_\odot$ yr$^{-1})$ and wind velocities $v_{w,8} = v_w/(10^8$ cm s$^{-1})$ are based upon Vink, de Koter, & Lamers (2001) and Fullerton, Massa, & Prinja (2006).

be written as

$$v_0 = 1.5 \left(\frac{d_w}{\mathrm{pc}} \right)^{-1} (\dot{M}_{w,-6} v_{w,8})^{1/2} n_{0,3}^{-1/2} \; [\mathrm{km\ s^{-1}}], \tag{3.1}$$

where v_w is the terminal velocity of the stellar wind. Values of $v_0 n_{0,3}^{1/2}$ and d_w for each bow shock are presented in Table 3.3. The standoff distance can be measured only as $d_w \cos i$ on the sky, where i is the inclination (or viewing angle) made by the line connecting the star with the apex of the bow shock against the plane of the sky ($i = 0$ if the line joining the star to the bow shock apex lies in the plane of the sky). Because a bow shock oriented at high i will not produce an arc morphology, it is likely that $i \lesssim 45°$, and hence $\cos i$ will not differ greatly from unity in our measurements.[1] The distance from each bow shock to the likely source of the large-scale ISM flow, measured on the sky as $d_{cl} \cos i$, are also presented for reference in Table 3.3.

The mass-loss rates and stellar wind velocities in Equation 3.1 suffer from high dispersion as a function of spectral type (Fullerton, Massa, & Prinja 2006), a factor of 2 or even greater, and this is compounded by a comparable level of uncertainty in the spectral types. The uncertainty on our measurements of d_w ranges from ∼20% for the largest bow shocks (M17-S2 and RCW 49-S1) to ∼ 40% for the smaller bow shocks that are barely resolved by IRAC. We estimate that $v_0 n_0^{1/2}$ is uncertain by a factor of 2 in M17 and up to a factor of 3 in RCW 49, where the spectral types of the driving stars are less constrained. These uncertainties, reflected in the range of values for $v_0 n_0^{1/2}$ in Table 3.3, are dominated by the uncertainty in the stellar wind properties.

We have neglected the effects of turbulent pressure in our calculation of the momentum flux balance of the bow shocks. This is a potentially significant contributor to the total ISM pressure held off by the bow shocks. The effect of turbulent pressure would be to systematically decrease the standoff distance d_w, causing us to overestimate v_0.

In reality, for the fast winds of early-type stars, the observed bow shock is displaced from the standoff distance by a significant amount. This happens because the cooling timescale of the shocked stellar wind is very long. The result is a thick layer of hot gas intervening between the wind terminal shock at the standoff distance and the thin, dense layer of interstellar gas and dust forming the observed bow shock. The numerical simulations of Comerón & Kaper (1998) predict that the bow shock should be located at twice the standoff distance from the driving star. In this case, our derived values of $v_0 n_0^{1/2}$ in Table 3.3

---

[1] The average value of $\cos i$ for $0 \leq i \leq 45°$ is 0.9.

would be underestimated by the same factor of 2. This systematic correction is comparable to the intrinsic uncertainties in our estimates of $v_0 n_0^{1/2}$, and it partially compensates for the effects of neglecting turbulent pressure in the ambient ISM. Therefore, the assumption that the observed distance of the bow shocks from the driving stars corresponds to the standoff distance d_w should not have a large impact on our results, and we find that the cautious application of Equation 3.1 yields reasonable results.

Orbital velocities of O stars in massive clusters are typically < 10 km s^{-1}. The expansion speed of ionized gas in H II regions is generally comparable to the sound speed of $\sim$10 km s^{-1}, and this appears to be true in M17 (Pellegrini et al. 2007). Most of the bow shocks (the exception being RCW 49-S1) are apparently located within the ionized gas of the radio H II regions. The likely explanation for the bow shock emission in the IR is that dust in the H II regions (Chapter 2) is swept-up by the bow shocks. The observed average electron density in the Northern bar of the M17 H II region is $\sim$10^3 cm^{-3} (Felli, Churchwell, & Massi 1984), so the values of $v_0 n_{0,3}^{1/2}$ listed in Table 3.3 are likely to be close to the actual relative velocities of the stars and the ISM for most of the bow shocks.

The values of $v_0 n_{0,3}^{1/2}$ calculated for M17-S1 and -S2 are in good agreement. M17-S3, however, presents a different picture. M17-S3 appears to be associated with a "teardrop" structure (Figure 1) in the photodissociation region (PDR), near the ionization front. The ambient density surrounding this star could be significantly higher than the density within the H II region. If v_0 for this bow shock is comparable to that of the other 2 bow shocks in M17, then $n_{0,3} \sim 2.25$ cm^{-3} in this location. This value agrees with the measurements of electron density in the dense clumps of ionized gas in M17 (Felli, Churchwell, & Massi 1984). The unusual morphology of the diffuse IR emission associated with M17-S3 suggests that the star may have recently emerged from an evaporating globule on the edge of the PDR; a larger, more evolved analog of the nearby pillar structure seen in Figure 1.

In RCW 49, all 3 bow shocks are found in very different locations, but we note that 2 of the bow shocks appear to be similar in size, color, and ambient environment (Figure 2). The largest bow shock, RCW 49-S1, is different, since it is located relatively far (16.2 pc at 4.2 kpc) from Westerlund 2, outside the H II region. The presence of RCW 49-S1, along with its orientation, indicates that RCW 49 vents a large-scale flow of gas through the cavity opening to the West. RCW 49-S1 is located near the rim of a large radio blister associated with RCW 49, which provides additional evidence for a large-scale gas flow escaping the RCW 49 H II region (Whiteoak & Uchida 1997) This flow likely originates in the combined winds of the Westerlund 2 cluster and thus should be much more diffuse than the H II region gas (Townsley et al. 2003, 2005). Assuming a density of 1 cm^{-3} in the flow from Westerlund 2, the standoff distance of RCW 49-S1 at 4.2 kpc gives a flow velocity of $\sim$350 km s^{-1}. Such a high value of v_0 is reasonable, given that the gas must move supersonically relative to the star to produce a shock, and the sound speed in the hot, rarefied gas of the flow streaming away from the H II region is $\sim$100 km s^{-1}.

Because RCW 49-S1 was detected by *MSX* and *IRAS* in addition to GLIMPSE, we can construct the SED of the bow shock from 4.5 μm to 100 μm (Table 3.2). We computed SED models of RCW 49-S1 using a 3-D radiative equilibrium code (Whitney et al. 2003) modified to include very small grain (VSG) and PAH emission (Wood et al. 2008). We used the canonical mass fraction for VSG/PAH grains of 5% (Draine & Li 2007). We modeled the bow shock geometry as a paraboloid with the apex offset by $d_w = 0.16$ pc from the O6 V star (assuming $i = 0$ and the 4.2 kpc distance). For models that reproduced the observed images, the SED shape was insensitive both to the thickness of the shock and to the radial density profile of the dust (with the total mass scaled to match the observed SED). The black line in Figure 3.3 shows the SED for a model with a density varying as r^{-2} from the 0.16 pc standoff distance out to a radius of 1.5 pc. The observed SED shortward of 30 μm is well-matched by the model. For radial density exponents from -2 to 0, the mass of this material ranges from $\sim$0.5 M$_\odot$ to 2 M$_\odot$, respectively, assuming a dust-to-gas mass ratio of 0.01. The optical depth in all models is low, with $A_V < 0.02$ within 1 pc. To match the *IRAS* data at 60 and 100 μm requires low-density material farther from the star. The *green* line in Figure 3.3 is a model including a shell 2–3 pc from the star. This material added mid-IR PAH emission, so we lowered the VSG/PAH mass fraction to 3% to continue to match the mid-IR SED, and the image still matches the data well. The A_V through the bow shock in this model is 0.25, most of it due to the outer shell. Along the line of sight to the star, $A_V = 10$, so the bow shock and shell contribute a negligible fraction of the interstellar extinction. These models show that dust distributed in a bow shock geometry matches both the images and the SED reasonably well. The IR emission from the bow shock can be explained by reprocessed stellar radiation without any additional dust heating by the shock.

The structure of RCW-S1 is probably significantly different from that of the other 5 bow shocks in our sample, because it is located in a distinct interstellar environment. Because of the high temperature and low density in the flow outside the H II region, the shocked interstellar gas cannot cool quickly enough to form a dense layer behind the bow shock, as likely happens in the other 5 cases. The shock is approximately

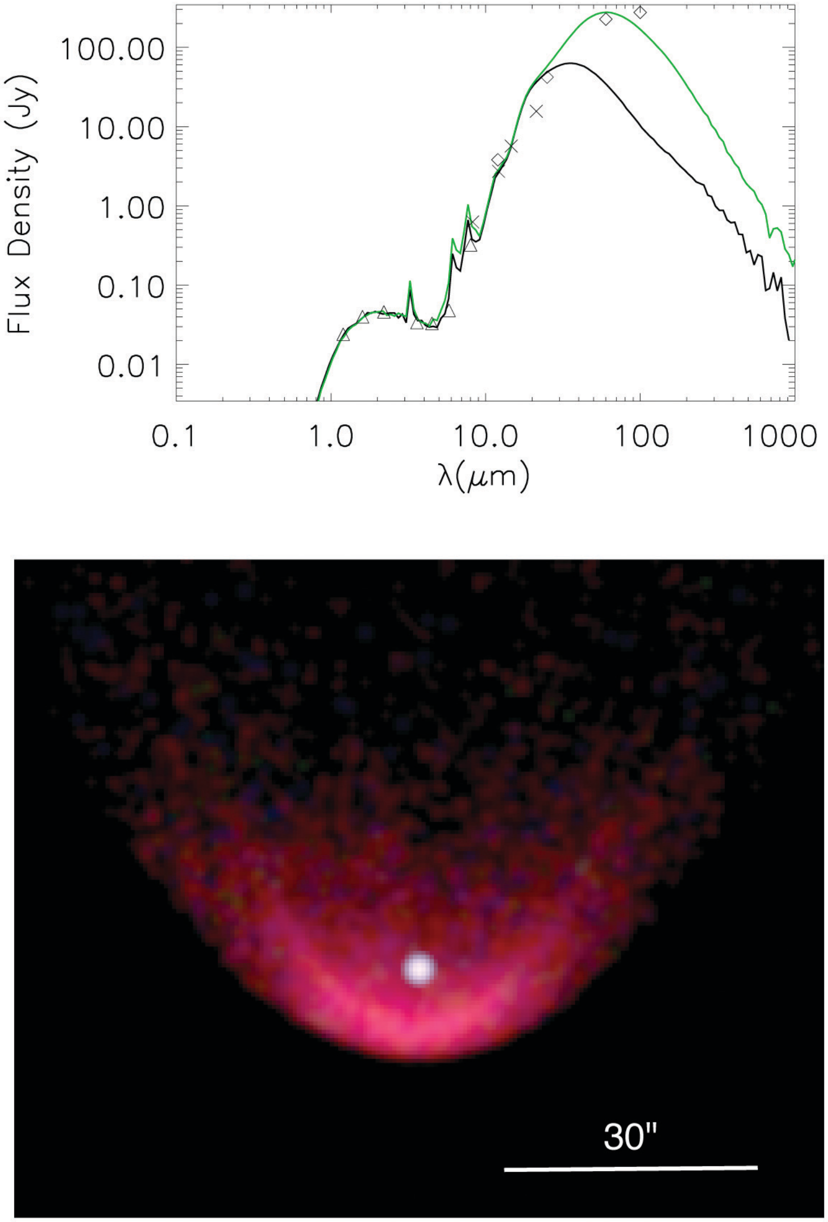

Fig. 3.3.— Radiation transfer model of RCW 49-S1. *Top:* Model SEDs plotted with the fluxes of the bow shock and driving star from Tables 1 & 2 (*triangles:* 2MASS and GLIMPSE; *crosses: MSX*; *diamonds: IRAS*). The *green* curve includes low-density material in a shell 2–3 pc from the star in order to match the *IRAS* 60 and 100 μm fluxes. *Bottom:* Image of the model bow shock at GLIMPSE wavelengths (compare to Figure 2).

adiabatic, remaining very hot and only moderately compressed (by a factor of ∼4) as it flows past the star, forming a relatively thick layer. Hence, while RCW-S1 is the only bow shock in our sample observed at enough different mid-IR wavelengths to allow us to create a meaningful model of the emission, it may not be appropriate to draw strong conclusions about the remaining bow shocks based upon this model.

3.4 Summary

We have observed 6 prominent IR bow shocks in M17 and RCW 49. These objects appear to be produced by the winds of individual O stars colliding with large-scale interstellar gas flows in the H II regions. One bow shock, M17-S3, may be the leading edge of an evaporating globule containing a newly-formed and previously undiscovered O star in the well-studied M17 region. All three bow shocks associated with RCW 49 lead us to identify new candidate O stars. Our stellar classifications also suggest that the true distance to RCW 49 is less than the kinematic distance of 6 kpc.

The bow shocks are bright at IR wavelengths due to emission from dust swept up from the ambient ISM and heated by radiation from the bow shock driving stars. As Gáspár et al. (2008) note, IR excess emission from a bow shock could be attributed to the presence of a circumstellar disk, particularly when the bow shock morphology is not spatially well-resolved. This can be a pitfall for observational studies of accreting massive protostars.

The collective winds of the most luminous stars in young, massive clusters produce overlapping large-scale flows that hollow out thermally hot cavities in the parent molecular cloud (Townsley et al. 2003). The largest bow shock presented here, RCW 49-S1, is evidence that the combined winds of the ionizing stars in Westerlund 2 have escaped the H II region, creating a flow of hot gas moving at a few 10^2 km s^{-1} that extends at least 16 pc away from RCW 49.

The driving stars of the other 5 bow shocks are surrounded by ionized gas and dust of their natal H II regions, where the density of the ambient medium ($n_0 \sim 10^3$ cm^{-3}) is sufficiently high to produce the observed bow shocks with a relative velocity of only 10–20 km s^{-1}. The winds of the bow shock driving stars do not directly encounter the >2000 km s^{-1} winds from the most massive stars in the cluster. Instead, the bow shocks are shaped by the expansion of the ionized gas in the H II regions relative to the orbital motions of the stars.

Eventually, supernova explosions will produce high velocity shock waves that heat and disperse the original gas cloud. In star forming regions like M17 and RCW 49 that have not yet been disrupted by supernovae, IR bow shocks serve as interstellar "weather vanes," indicating the speed and direction of large-scale gas flows at points within and around giant H II regions.

We thank the anonymous referee for incisive and very useful suggestions that helped us improve this work. We are grateful to Joseph Cassinelli, Eric Pellegrini, John Raymond, Ellen Zweibel, Heidi Gneiser, and Don Cox for useful conversations while preparing this paper. M. S. P. thanks the members of the "dissertator club," Kathryn Devine, K. Tabetha Hole, and Nicholas Murphy, for their helpful comments. This work was supported by NSF grant AST-030368 (E. B. C.) and NASA/JPL Contracts 1282620 and 1298148. Additional support was provided by the NASA Theory Program (NNG05GH35G; B. A. W.). R. I. acknowledges support from a Spitzer Fellowship at the time that these data were analyzed, and from JPL RSA1275467.

References

Arthur, S. J., & Hoare, M. G. 2006, ApJS, 165, 283

Ascenso, J., Alves, J., Beletsky, Y., & Lago, M. T. V. T. 2007, A&A, 466, 137

Bally, J., O'Dell, C. R., & McCaughrean, M. J. 2000, AJ, 119, 2919

Beichman, C. A., Neugebauer, G., Habing, H. J., Clegg, P. E., & Chester, T. J., eds. 1988, IRAS Catalogs and Atlases: Explanatory Supplement, NASA RP-1190

Benjamin, R.A. et al. 2003, PASP, 115, 953

Brown, D., & Bomans, D. J. 2005, A&A, 439, 183

Bumgardner, T. E. 1992, M.S. thesis, Ohio State Univ., Columbus

Chini, R., Elsässer, H., & Neckel, T. 1980, A&A, 91, 186 (CEN)

Churchwell, E., Bieging, J. H., van der Hucht, K. A., Williams, P. M., Spoelstra, T. A. Th., & Abbott, D. C. 1992, ApJ, 393, 329

Churchwell, E. et al. 2004, ApJS, 154, 322

Comerón, F. & Kaper, L. 1998, A&A, 338, 273

Comerón, F. & Pasquali, A. 2007, A&A, 467, L23

Dame, T. M. 2007, ApJ, 665, L163

Decker, R. B. et al. 2005, Science, 309, 2020

Draine, B. T. & Li, A. 2007, ApJ, 657, 810

Fazio, G. G. et al. 2004, ApJS, 154, 10

Felli, M., Churchwell, E., & Massi, M. 1984, A&A, 136, 53

France, K., McCandliss, S. R., & Lupu, R. E. 2007, ApJ, 655, 920

Fullerton, A. W., Massa, D. L., & Prinja, R. K. 2006, ApJ, 637, 1025

Gaensler, B. M., & Slane, P. O. 2006, ARA&A, 44, 17

Gáspár, A., Su, K. Y. L., Rieke, G. H., Balog, Z., Kamp, I., Martínex-Galarza, J. R., & Stapelfeldt, K. 2008, ApJ, 672, 974

Geballe, T.R., Rigaut, F., Roy, J.-R., & Draine, B.T. 2004, ApJ, 602, 77

Geballe, T. R., Najarro, F., Rigaut, F., & Roy, J.-R. 2006, ApJ, 652, 370

Hanson, M. M., Howarth, I. D., & Conti, P. S. 1997, ApJ, 489, 698

Huthoff, F., & Kaper, L. 2002, A&A, 383, 999

Kaper, L., van Loon, J. T., Augusteijn, T., Goudfrooij, P., Patat, F., Waters, L. B. F. M., & Zijlstra, A. A. 1997, ApJ, 475, L37

Kurucz, R. 1993, ATLAS9 Stellar Atmosphere Programs and 2 km/s grid. Kurucz CD-ROM No. 13. Cambridge, MA: Smithsonian Astrophysical Observatory

Martin, D, C. et al , 2007, Nature, 448, 780

Nielbock, M., Chini, R., Jütte, M., & Manthey, E. 2001, A&A, 273, 284

Noriega-Crespo, A., van Buren, D., & Dgani, R. 1997, AJ, 113, 780

Pellegrini, E. W. et al. 2007, ApJ, 658, 1119

Price, S. D., Egan, M. P., Carey, S. J., Mizuno, D. R., and Kuchar, T. A. 2001, AJ, 121, 2842

Rauw, G., Manfroid, J., Gosset, E., Nazé, Y., Sana, H., De Becker, M., Foellmi, C., & Moffat, A. F. J. 2007, A&A, 463, 981

Robitaille, T. P., Whitney, B. A., Indebetouw, R., & Wood, K. 2007, ApJS, 169, 328

Townsley, L. K., Feigelson, E. D., Montmerle, T., Broos, P. S., Chu, Y.-H., & Garmire, G. P. 2003, ApJ, 593, 874

Townsley, L., Feigelson, E., Montmerle, T., Broos, P., Chu, Y.-H. Garmire, G., & Getman, K. 2005, X-Ray and Radio Connections, eds. L.O. Sjouwerman & K.K Dyer (NRAO: Santa Fe, NM)

Uzpen, B. et al. 2005, ApJ, 629, 512

van Buren, D. & McCray, R. 1988, ApJ, 329, 93

van Buren, D., Mac Low, M. M., Wood, D. O. S., & Churchwell, E. 1990, ApJ, 353, 570

van Buren, D., Noriega-Crespo, A., & Dgani, R. 1995, AJ, 110, 2914

Vink, J. S., de Koter, A., & Lamers, H. J. G. L. M. 2001, A&A, 369, 574

Watson, C., Povich, M. S., Churchwell, E. B., Babler, B. L., Chunev, G. Hoare, M., Indebetouw, R., Meade, M. R., & Whitney, B. A. 2008, ApJ, 681, 1341 (astro-ph 0806.0609)

Whitney, B. A., Wood, K., Bjorkman, J. E., & Wolff, M. J. 2003, ApJ, 591, 1049

Whiteoak, J. B. Z. & Uchida, K. I. 1997, A&A, 317, 563

Wood, K., Whitney, B. A., Robitaille, T. P., & Draine, B. T. 2008, ApJ, in press (astro-ph 0807.2398)

Chapter 4

The Extended Environment of M17: A Star Formation History

Originally published by M. S. Povich, E. Churchwell, J. H. Bieging, M. Kang, B. A. Whitney, C. L. Brogan, C. A. Kulesa, M. Cohen, B. L. Babler, R. Indebetouw, M. R. Meade, & T. P. Robitaille in The Astrophysical Journal, Volume 696, Issue 2, pp. 1278–1306 (May 2009)

Abstract

M17 is one of the youngest and most massive nearby star-formation regions in the Galaxy. It features a bright H II region erupting as a blister from the side of a giant molecular cloud (GMC). Combining photometry from the *Spitzer* Galactic Legacy Infrared Mid-Plane Survey Extraordinaire (GLIMPSE) with complementary infrared (IR) surveys, we identify candidate young stellar objects (YSOs) throughout a $1.5^\circ \times 1^\circ$ field that includes the M17 complex. The long sightline through the Galaxy behind M17 creates significant contamination in our YSO sample from unassociated sources with similar IR colors. Removing contaminants, we produce a highly-reliable catalog of 96 candidate YSOs with a high probability of association with the M17 complex. We fit model spectral energy distributions to these sources and constrain their physical properties. Extrapolating the mass function of 62 intermediate-mass YSOs ($M_\star > 3$ $M_\odot$), we estimate that >1000 stars are in the process of forming in the extended outer regions of M17. The remaining 34 candidate YSOs are found in a 0.17 deg^2 field containing the well-studied M17 H II region and photodissociation region, where bright diffuse mid-IR emission drastically reduces the sensitivity of the GLIMPSE point-source detections.

By inspecting IR survey images from *IRAS* and GLIMPSE, we find that M17 lies on the rim of a large shell structure ~0.5° in diameter (~20 pc at 2.1 kpc). We present maps of ^{12}CO and ^{13}CO ($J = 2 \rightarrow 1$) emission observed with the Heinrich Hertz Telescope. The CO emission shows that the shell is a coherent, kinematic structure associated with M17, centered at $v = 19$ km s^{-1}. The shell is an extended bubble outlining the photodissociation region of a faint, diffuse H II region several Myr old. We identify a group of candidate ionizing stars within the bubble. YSOs in our catalog are concentrated around the bubble rim, providing evidence that massive star formation has been triggered by the expansion of the bubble. The formation of the massive cluster ionizing the M17 H II region itself may have been similarly triggered. We conclude that the star formation history in the extended environment of M17 has been punctuated by successive waves of massive star formation propagating through a GMC complex.

4.1 Introduction

Most star formation in the local universe is observed to occur in dense, massive clusters of hundreds or thousands of stars that are created by the gravitational collapse and fragmentation of massive cores within giant molecular clouds (GMCs). In the Galaxy, one of the best nearby laboratories for the study of star formation in the environment of a rich, massive cluster is M17, the Omega Nebula. Most of the observational attention given to M17 has focused on the bright "blister" H II region, $\sim 5'$ in diameter, erupting from the side of the M17 molecular cloud, a GMC at a velocity of 20 km s^{-1} with a mass $>3\times10^4$ $M_\odot$ (Lada 1976). The H II region divides the M17 molecular cloud into two components, and following the nomenclature of Wilson, Howe, & Balogh (1999) we will refer to the more massive, southern component as "M17 South" and the northern component as "M17 North" (see Figure 4.1). M17 has served both as an infrared (IR) spectral template for photodissociation regions (PDRs) surrounding bright H II regions (Cesarsky et al. 1996; Verstraete et al. 1996) and as a prototype for H II region structure (Felli, Churchwell, & Massi 1984; Brogan & Troland 2001; Pellegrini et al. 2007; Povich et al. 2007, hereafter PSC07).

The ionization of the M17 H II region is provided by the rich cluster NGC 6618, which is deeply embedded in the gas and dust of the M17 cloud. Optical and near-IR photometric and spectroscopic studies have uncovered at least 16 O stars and over 100 B stars in NGC 6618 (Ogura & Ishida 1978; Chini, Elsässer, & Neckel 1980; Lada et al. 1991; Hanson, Howarth, & Conti (1997); Hoffmeister et al. 2008, hereafter H08). Several water masers have been observed around M17 (Cesarsky et al. 1978), and a prominent hypercompact H II region, M17 UC-1, lies on the interface of the H II region with M17 South (Felli, Churchwell, & Massi 1984; Sewilo et al. 2004). M17 has been searched repeatedly for massive stars with circumstellar disks (Nielbock et al. 2001; Chini et al. 2004b), and thousands of IR-excess sources have been reported in and around the H II region (Lada et al. 1991; Jiang et al. 2002, hereafter J02; H08) High-resolution observations using the *Chandra X-ray Observatory* have provided a census of the young stellar population of M17 (Broos et al. 2007; hereafter BFT07). BFT07 found IR counterparts for 771 of the 886 X-ray sources in their sample, and they report that only ∼10% of these sources exhibit IR emission in excess of a stellar photosphere due to the presence of dust in circumstellar disks and/or infalling envelopes. Taken together, the observations suggest that, while some fraction of the NGC 6618 stellar population has

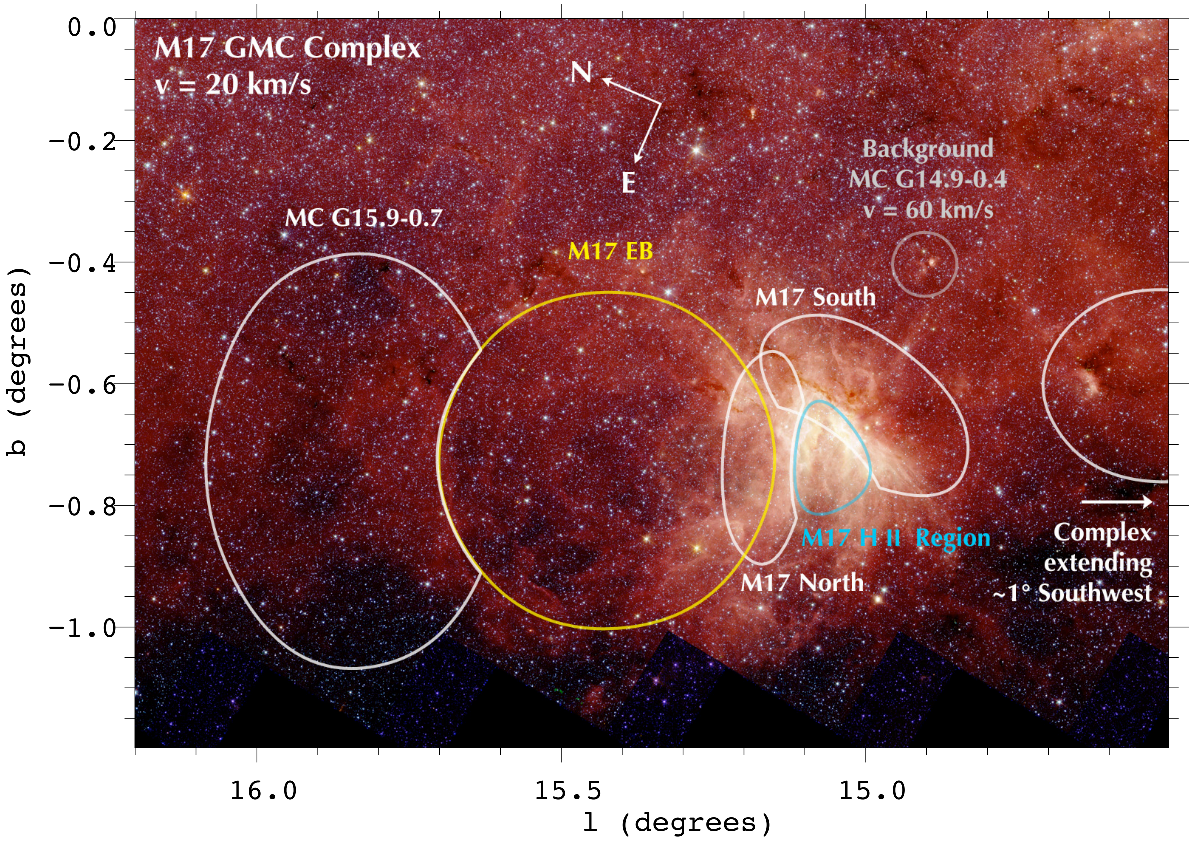

Fig. 4.1.— GLIMPSE full-color image of the M17 field (*red:* 8.0 μm, *orange:* 5.8 μm, *green:* 4.5 μm, and *blue:* 3.6 μm). A schematic diagram showing the approximate boundaries of large-scale structures mentioned in the text is overlaid. The molecular clouds shown in *white* and *gray* have been identified from the CO survey data of Sanders et al. (1986).

ceased accreting, massive star formation is ongoing in and around the M17 H II region. Many authors have suggested that the birth of a second generation of massive stars has been triggered on the periphery of the H II region by the expansion of the ionized gas into the M17 molecular cloud (Cesarsky et al. 1978; Felli, Churchwell, & Massi 1984; J02; H08).

The extended environment of M17 has often been overlooked. Elmegreen & Lada (1976) presented CO observations of a large molecular cloud complex associated with M17 at v = 20 km s^{-1} extending more than 1° to the Southwest, parallel to the Galactic mid-plane (Figure 4.1). They suggested that the entire complex is undergoing sequential star formation, beginning with the OB stars of NGC 6618 at the northeast tip. Jaffe & Fazio (1982) cast doubt on this sequential star formation scenario by presenting 13 far-infrared sources within the extended complex that did not show a progression of decreasing age with increasing distance from M17. Several high-resolution Galactic plane radio surveys in molecular or atomic line emission have included M17 (Sanders et al. 1986; Mizuno & Fukui 2004; McClure-Griffiths et al. 2005). The Massachusetts–Stony Brook Galactic Plane CO Survey (Sanders et al. 1986), which provided (b, v) maps with $45''$ resolution that include M17 and its vicinity. The Sanders et al. (1986) CO $J = 1$–0 maps clearly show both the M17 molecular cloud and the complex identified by Elmegreen & Lada (1976), and they reveal an additional molecular cloud at $v = 20$ km s^{-1}, centered at $(l, b) = (15.9^\circ, -0.7^\circ)$. We name this second cloud MC G15.9-0.7 (Figure 4.1).

Unbiased surveys of the Galactic plane reveal large structures that are missed by pointed observations with limited fields-of-view. Visual inspection of images from the *Spitzer Space Telescope* Galactic Infrared Mid-Plane Survey Extraordinaire (GLIMPSE) reveals a circular dust shell $\sim 0.5^\circ$ in diameter outlined by faint, diffuse 8 μm emission. M17 marks the Southwest rim of the shell (see Figure 4.1). This structure is also apparent in *Infrared Astronomy Satellite* (*IRAS*) images at 60 μm and 100 μm. The dust shell appears to extend from M17 to MC G15.9-0.7. Diffuse 8 μm emission is usually attributed to polycyclic aromatic hydrocarbons (PAHs) that fluoresce when illuminated by ultraviolet (UV) radiation. The shell morphology is similar to that of the IR bubbles identified in GLIMPSE by Churchwell et al. (2006). Such bubbles typically outline the PDRs of H II regions (Chapter 2, Watson et al. 2008). The dust shell near M17 was not selected for the GLIMPSE bubbles catalog because it is partially obscured by the bright diffuse emission from M17 and lacks a well-defined inner rim. Nevertheless, we will demonstrate that the shell is an extended bubble outlining the PDR of a large, faint H II region associated with M17. We call this structure the M17 extended bubble (M17 EB; Figure 4.1).

While the screen of cold, dense molecular gas in M17 South probably prevents the stellar winds and ionizing radiation from the OB stars in NGC 6618 from influencing the extended molecular cloud complex to the Southwest, on the Northeast side of M17 there is evidence that M17 EB is interacting with both MC 15.9-0.7 and M17 itself. The M17 H II region surrounds a central cavity that is filled by hot, diffuse plasma observed by *Chandra* (Townsley et al. 2003, Chapter 2). *ROSAT* observations covering a larger area show soft X-ray emission spilling out of the H II region and apparently filling part of M17 EB; this X-ray emission is spatially coincident with faint Hα emission (Dunne et al. 2003). A search for SIMBAD objects in the interior of M17 EB reveals several stars with OB spectral types. We will show that these stars represent the most massive members of the cluster ionizing M17 EB and that this cluster is both distinct from and older than NGC 6618. We refer to this progenitor cluster as NGC 6618PG.

The distance to M17 has been somewhat disputed in recent years. Most estimates have been based upon optical/near-IR photometry of the most luminous stars. Hanson, Howarth, & Conti (1997) reported a distance of $1.3^{+0.4}_{-0.2}$ kpc, a significant departure from the kinematic distance of 2.3 kpc. Nielbock et al. (2001) subsequently employed a revised extinction law (Chini & Wargau 1998) and derived a distance of 1.6 ± 0.3 kpc. The value of 1.6 kpc has since been widely adopted. PSC07 balanced the flux in the integrated IR SED of M17 with the bolometric luminosity of all known ionizing stars in NGC 6618 and reported a distance of $1.6^{+0.3}_{-0.2}$ kpc. This luminosity distance assumed both that all of the major ionizing stars in the region were known and, like the previous spectrophotometric distance estimates, that the majority of the known ionizing stars were *not* in unresolved binary or otherwise multiple systems. Recently, H08 showed that the most luminous stellar system in M17, the O4+O4 binary star called Kleinmann's Anonymous star or CEN 1 (Chini, Elsässer, & Neckel 1980), is itself composed of two spectroscopic binary systems of nearly equal-mass components. This discovery, along with new distance moduli for other massive stars in NGC 6618, lead H08 to revise the M17 distance once again, to 2.1 ± 0.2 kpc, in agreement with the kinematic distance. In this work, we will generally adopt the 2.1 kpc distance, but we will also consider 1.6 kpc where the distance uncertainty could significantly impact our results.

We take advantage of the large area surrounding M17 observed by the *Spitzer* Galactic plane surveys to investigate star formation in the extended environment of M17, emphasizing the newly-discovered structures to the Northeast. We have combined GLIMPSE with longer-wavelength IR survey data from both the Multiband Imaging Photometer for *Spitzer* (MIPS) Galactic plane survey (MIPSGAL) and the *Midcourse Space Experiment* (*MSX*). We use these datasets to investigate the population of young stellar objects (YSOs), identified by their IR excess emission, over a large ($\sim 1.5^\circ \times 1^\circ$) area surrounding M17. Our investigation includes the full spatial extent of the M17 molecular cloud, M17 EB, and MC G15.9-0.7. We have followed up the infrared survey data with high-resolution ^{12}CO and ^{13}CO $J = 2$–1 observations. In §4.2 we summarize our observations and data reduction. We describe our methods for selecting and characterizing YSO candidates in §4.3, and we discuss the extended young stellar population of M17 in relation to the molecular cloud structures in §4.4. In §4.5, we synthesize these results into a picture of propagating massive star formation in M17, and we summarize our conclusions in §4.6.

4.2 Observations and Data Processing

4.2.1 IR Galactic Plane Survey Data

4.2.1.1 GLIMPSE

As part of the *Spitzer* Legacy Science Program, GLIMPSE (Benjamin et al. 2003) imaged the Galactic plane from $|l| = 0°$–$65°$, $|b| \leq 1°$ using the four mid-IR bands (3.6, 4.5, 5.8, and 8.0 μm) of the Infrared Array Camera (IRAC) on the *Spitzer Space Telescope* (Fazio et al. 2004). High-resolution ($1.2''$ pixels) image mosaics were created by the GLIMPSE pipeline[1] from Basic Calibrated Data (BCD) image frames processed by the *Spitzer* Science Center (SSC). The GLIMPSE point-source extractor, a modified version of Daophot (Stetson 1987) was used to extract point sources from the individual image frames. The 5σ point-source detection limits of GLIMPSE are nominally 0.2, 0.2, 0.4, and 0.4 mJy for the [3.6], [4.5], [5.8], and [8.0] bands, respectively, and higher in regions of bright diffuse emission. Flux densities of sources detected at greater than 5σ at least twice in one or more of the 4 IRAC bands were included in the GLIMPSE Point Source Archive. The highly-reliable GLIMPSE Point Source Catalog is a subset of the Archive. Both the Archive and the Catalog incorporated JHK_S flux densities from the 2MASS point source catalog (Skrutskie et al. 2006) to produce final sourcelists containing flux densities from 1–8 μm in 7 near- to mid-IR bands. For this study, we use the GLIMPSE v2.0 Point Source Archive and the GLIMPSE v3.0 image mosaics. The majority of the Archive sources used in our analysis will also appear in the highly-reliable Catalog because of our additional requirement that each source must be detected in at least 4 bands (see §4.3.2). We use the Archive instead of the catalog because the Archive identifies sources with near-saturated fluxes that can later be used as lower limits and contains more sources in crowded regions. Mosaics produced from 2MASS data provide near-IR images that complement GLIMPSE.

4.2.1.2 MIPSGAL

We downloaded 24 μm and 70 μm post-BCD mosaics of the MIPSGAL survey (Carey et al. 2009) from SSC. The 24 μm mosaics have $2.4''$ pixels and the 70 μm mosaics have $4.8''$ pixels. MIPSGAL point-source catalogs were not yet available at the time of this study, so we extracted 24 μm point-source fluxes using the GLIMPSE extractor. Because the GLIMPSE pipeline software is not optimized for MIPSGAL

---

[1] Details of the data processing can be found at http://www.astro.wisc.edu/glimpse/docs.html

data, this procedure generates the following types of false source detections: noise peaks, small resolved structures, and artifacts from the point-spread function wings of bright sources. As a first cut to reduce the number of false sources in our analysis, we removed all 24 μm sources with larger than 25% error in measured flux density ($F/\delta F < 4$) from the sourcelist. We then spatially correlated (bandmerged) the 24 μm sources with the GLIMPSE Archive sources. If an Archive source was located within $2.4''$ of the central position of a 24 μm source, the source was considered to have a 24 μm detection and the [24] flux was appended to the Archive fluxes. If more than one Archive source was located within $2.4''$ of a 24 μm source, the [24] flux was appended as an upper limit for each correlated Archive source. The correlation procedure favors "true" 24 μm point sources because these are more likely to have a GLIMPSE counterpart, but occasionally a false source or false correlation makes it into the bandmerged list. The final 8-band (combined 2MASS, GLIMPSE, and MIPSGAL [24]) sourcelists were inspected by eye to reject any remaining suspicious sources (see §4.3.2).

4.2.1.3 Aperture Photometry

We did not attempt to automatically extract MIPSGAL [70] point source fluxes. Only ~10 obvious 70 μm unresolved sources are visible in the BCD mosaics within our analysis region, so we extracted the [70] fluxes of interesting sources manually, using aperture photometry. Visual inspection of the GLIMPSE mosaics revealed ~10 compact red sources that are resolved by IRAC and hence not in the Archive. Such sources may be luminous YSOs that heat ambient dust in molecular clouds out to a few pc distance. One pc corresponds to 78 $1.2''$ GLIMPSE mosaic pixels at 2.1 kpc. Our aperture photometry procedure used the Funtools[2] package with the SAOImage DS9[3] image display program to extract fluxes from apertures defined by eye. For each source extracted, we used the same target apertures for the 7 2MASS+IRAC bands and increased the aperture size as needed for the 2 MIPSGAL bands. We varied the position of the background sampling a minimum of 3 times to estimate the contribution of the background subtraction to the flux uncertainty. Although the background subtraction generally dominated the uncertainty on the extracted fluxes, our uncertainty estimates also included photon counting statistics (prior to the correction for Zodiacal emission) and the uncertainty introduced by applying the IRAC extended aperture corrections[4]

---

[2] See http://hea-www.harvard.edu/RD/funtools/ds9.html.

[3] See http://hea-www.harvard.edu/RD/ds9/ref.

[4] See http://ssc.spitzer.caltech.edu/irac/calib/extcal/.

to sources with effective radii $> 9''$.

4.2.1.4 *MSX*

The Spirit III instrument on board the *MSX* satellite surveyed the Galactic plane in four IR bands (Price et al. 2001): A (isophotal wavelength 8.28 μm), C (12.13 μm), D (14.65 μm), and E (21.3 μm). The 5σ point-source detection limits for *MSX* are 100, 1100, 900, and 200 mJy for A, C, D, and E bands, respectively. The sensitivity of the *MSX* A and E bands is just below the saturation limits of IRAC and MIPS, so these bands can be used to replace the fluxes of point sources saturated at IRAC [8.0] and MIPS [24], respectively. The spatial resolution of the *MSX* images is $\sim 18.3''$, so confusion is an issue when correlating *MSX* Catalog[5] sources with the GLIMPSE Archive. After selecting YSO candidates based on the combined GLIMPSE and MIPS [24] photometry (see §4.3.1), we correlated only the brightest saturated and near-saturated YSO candidates with the *MSX* catalog, using a $6''$ correlation radius. We did not use the *IRAS* Point-Source Catalog for this work because its low resolution causes too much confusion with multiple GLIMPSE sources.

4.2.2 CO Observations with the Heinrich Hertz Submillimeter Telescope

We mapped the M17 region in the $J = 2 \rightarrow 1$ transitions of ^{12}CO and ^{13}CO with the 10-m Heinrich Hertz Telescope (HHT) on Mt. Graham, Arizona between 2008 February and 2008 June. The receiver was a dual polarization superconductor-insulator-superconductor (SIS) mixer system employing single-sideband (SSB) mixers with outputs for both upper and lower sidebands, each with a 4–6 GHz IF band. The ^{12}CO $J = 2 \rightarrow 1$ line at 230.538 GHz was placed in the upper sideband and the ^{13}CO $J = 2 \rightarrow 1$ line at 220.399 GHz in the lower sideband, with a small offset in frequency to ensure that the two lines were adequately separated in the IF band, since the sideband rejection was typically 17–20 dB. The spectrometers, one for each of the two polarizations and the two sidebands, were filter banks with 256 channels of 1 MHz width and separation. At the observing frequencies, the spectral resolution was 1.3 km s^{-1} and the angular resolution of the telescope was $32''$ (FWHM). A set of $10' \times 10'$ fields were mapped with on-the-fly (OTF) scanning in RA at $10''$ per sec with row spacing of $10''$ in declination, over a total of 60 rows. Each field required about 2 hours of elapsed time. System temperatures were calibrated by the standard ambient temperature load method (Kutner & Ulich 1981) after every other row of the map grid. Atmospheric conditions were

---

[5] See http://irsa.ipac.caltech.edu/applications/Gator/.

generally clear and stable, and the system temperatures were usually nearly constant at $T_{\rm sys} \sim 200$ K (SSB) for each $10' \times 10'$ field.

Data for each polarization and CO isotopomer were processed with the *CLASS* reduction package (from the University of Grenoble Astrophysics Group), by removing a linear baseline and convolving the data to a square grid with $10''$ grid spacing (equal to approximately one-third the telescope beamwidth). The intensity scales for the two polarizations were determined from observations of W51D (W51-IRS2) made just before the OTF maps. The gridded spectral data cubes were processed with the *Miriad* software package (Sault et al. 1995) for further analysis. The two polarizations were averaged for each sideband, yielding images with RMS noise per pixel and per velocity channel of 0.15 K-T_A^* for both the ^{12}CO and ^{13}CO transitions.

We mapped a total of 26 $10' \times 10'$ fields, arranged in a semi-regular pattern to cover the main M17 H II region and M17 EB. These 26 fields were combined onto a common spatial grid and converted to Galactic coordinates for comparison with the GLIMPSE images.

4.3 YSO Selection and Characterization

An overview of the target field of the GLIMPSE survey searched for YSOs is presented in Figure 4.1, with the approximate boundaries of the M17 H II region, the bubble M17 EB, and the major molecular cloud structures from Sanders et al. (1986) overlaid. The top of the image is the Galactic mid-plane ($b = 0°$), and the jagged bottom edge is the boundary of the GLIMPSE survey between $b = -1°$ and $-1.2°$. Most of this image is occupied by the molecular cloud complex at $v = 20$ km s^{-1} that includes M17. A smaller cloud, MC G14.9-0.4 associated with compact, bright diffuse mid-IR emission, lies in the background at $v = 60$ km s^{-1}.

We identify candidate YSOs in this image based on their IR excess emission, with the goal of determining the YSO population associated with M17. The location of M17 near the Galactic mid-plane and only 15° from the Galactic center produces a long sightline through the Galaxy in the mid-IR that passes through multiple spiral arms; hence we expect that the GLIMPSE Archive contains many YSOs or other objects with similar IR colors that lie at different distances, unassociated with M17. The average extinction produced by the molecular clouds in the target field is too low to significantly reduce the number of background sources detected in the mid-IR (see §4.4.1.1). Because M17 is bounded in longitude by potentially star-forming molecular clouds and in latitude by the Galactic mid-plane and the survey edge, there is no portion of the GLIMPSE image in Figure 4.1 that could be used as an off-source region to estimate the contamination in our sample from foreground or background sources (see §4.3.3). Fortunately, the region symmetric to M17, reflected above the Galactic mid-plane, lacks obvious CO emission marking molecular clouds (Sanders et al. 1986; Mizuno & Fukui 2004) and is correspondingly free of the bright diffuse 8.0 μm emission in GLIMPSE that usually identifies H II regions. We selected a circular control field of 0.5° radius centered at $(l, b) = (15.08^\circ, 0.61^\circ)$. Since this region has the same Galactic longitude and absolute latitude occupied by M17 but exhibits no obvious signs of massive star formation, it can be used to address the question of what the Galactic plane would look like if M17 were not present. We analyzed the control field in parallel with the M17 target field, using the same procedure to select candidate YSOs from both fields.

4.3.1 Fitting YSO Model SEDs to Broadband IR Fluxes

Our principal tools for identifying and characterizing candidate YSOs from this rich dataset were the grid of YSO models from Robitaille et al. (2006, hereafter RW06) and the spectral energy distribution (SED) fitting tool of Robitaille et al. (2007, hereafter RW07). The model grid consists of 20,000 2-dimensional Monte Carlo radiation transfer models (Whitney et al. 2003a,b, 2004) spanning a complete range of stellar mass and evolutionary stage and output at 10 viewing angles (inclinations), so the model fitting tool actually has 200,000 SEDs to choose from. The model fitting tool uses a fast χ^2-minimization linear regression algorithm (RW07). We can robustly distinguish between YSOs and reddened photospheres of main-sequence and giant stars because YSOs require a thermal emission component from circumstellar dust to reproduce the shapes of their mid-IR excesses. The Monte Carlo radiative transfer models upon which the fitting tool relies have been tested extensively by successfully fitting the SEDs of numerous well-characterized YSOs in Taurus (RW07). The models and fitting tool have also been employed to analyze the YSO populations of the Eagle Nebula (Indebetouw et al. 2007), several other Galactic massive star formation regions observed as part of GLIMPSE (Shepherd et al. 2007; Watson et al. 2008), and the Large Magellanic Cloud (Whitney et al. 2008).

The radiation transfer technique employed in the RW06 models propagates “photons” from the central source through the circumstellar environment. The models solve for the temperature structure of the circumstellar material and include absorption and re-emission by dust along with photons produced by disk accretion and backwarming of the stellar photosphere (Whitney et al. 2003a,b, 2004). When we fit models to observed YSOs, we essentially use Monte Carlo radiation transfer to look through the veil of circumstellar dust, placing the central star on the H-R diagram by interpolating between pre-main-sequence (PMS) evolutionary tracks (Bernasconi & Maeder 1996; Siess, Dufour, & Forestini 2000). Like all complex models, the YSO models have built-in assumptions, degeneracies, and a multi-dimensional parameter space to explore. In general, fitting these models to real data results in many different sets of parameters that can describe a YSO almost equally well. Rather than attempt (futilely) to find a unique solution, we accept a range of well-fit models to investigate how well we can *constrain* the physical properties of each YSO. The distance to the modeled sources places an important external constraint on the allowable luminosities of the well-fit YSO models. For M17, we used the distance range of 1.6–2.3 kpc, effectively building the distance uncertainty into our constraints on the YSO properties from the model parameters. The number of acceptable models also decreases rapidly with increasing range of IR wavelengths from available data included in the SED.

The steps of our process for selecting candidate YSOs are outlined in Table 4.1, along with the number and density of sources in both the target and control fields at each step. We began by removing sources with SEDs that are consistent with stellar photospheres. We fit all sources that are detected in $N_{\rm data} \geq 4$ of the 8 near- through mid-IR bands in the GLIMPSE Archive combined with MIPSGAL 24 μm fluxes (126,385/352,225 sources in the target field and 71,391/191,010 sources in the control field; Table 4.1) with SEDs from 7853 model stellar atmospheres (Brott & Hauschildt 2005) included in the RW07 fitting tool. Interstellar extinction based upon the mid-IR extinction law of Indebetouw et al. (2005) was included

Table 4.1. Source Counts in the YSO Search

	M17 Target Field (1.67 deg^2)		Control Field (0.78 deg^2)	
Sources	Number	Density (deg^{-2})	Number	Density (deg^{-2})
In GLIMPSE Archive	352,225	211,000	191,010	245,000
Fit with SED models ($N_{\rm data} \geq 4$)	126,385	75,700	71,391	91,500
Well-fit by stellar photosphere SEDs ($\chi^2/N_{\rm data} \leq 5$)	124,768	74,700	70,628	90,500
Poorly-fit by stellar photosphere SEDs ($\chi^2/N_{\rm data} > 5$)	1,617	970	763	980
Well-fit by YSO SEDs ($\chi^2/N_{\rm data} \leq 5$)	979	590	370	470
In final sample of YSO candidates	406	240	106	140
In M17 YSO candidate subsample[a]/control subsample[b]	195	205	25	100

[a] Irregularly shaped region with area 0.95 deg^2 (See §4.4).

[b] Square box centered at $(l, b) = (15.1^\circ, 0.7^\circ)$ with area 0.25 deg^2.

in the model fits, so even highly reddened stars (we allow a maximum A_V of 30 mag when fitting stellar photosphere SEDs) returned good fits. We considered all sources with a best-fit χ^2, normalized by the number of flux datapoints used in the fit, satisfying $\chi^2/N_{\rm data} \leq 5$ to be well-fit by stellar photospheres. We determined this threshold value by visual inspection of the best-fit SEDs for a variety of sources. To avoid biasing the fits for sources where the flux uncertainties have been underestimated, before fitting any models we conservatively reset the uncertainties to a floor value of $\delta F/F = 10\%$ for all sources in the GLIMPSE Archive with $\delta F/F < 10\%$. For the MIPS [24] fluxes, we used an uncertainty floor of 15%.

We then took the 1,617 sources in the target field and 763 sources in the control field that were poorly fit by stellar photospheres and fit them a second time using the RW06 YSO models. Again, we considered sources with a best-fit $\chi^2/N_{\rm data} \leq 5$ to be well-fit, and these formed the basis of our YSO sample. The vast majority of sources that were well-fit neither by stellar photospheres nor YSO models are actually stars with saturated fluxes or poor photometry (often in the [24] band where our photometry is less robust) or signs of variability (a mismatch between 2MASS and GLIMPSE photometry due to the different epochs of the observations). Eleven sources in the target field appeared to be good YSO candidates with marginal fits. Several of these had saturated fluxes in one or more bands, and one (G015.6653-00.4989) exhibited excess emission in the [4.5] band similar to previously-studied sources associated with molecular outflows (Smith et al. 2006; Davis et al. 2007; Shepherd et al. 2007; Cyganowski et al. 2008). These were moved to the "well-fit" sample after the questionable flux measurements were replaced with upper or lower limits.

4.3.2 A Highly Reliable Sample of Candidate YSOs

Our primary goal was to produce a highly reliable sample of candidates YSO. As shown in Table 4.1, only 979/126,385 or 0.77% of sources fit with SED models in the M17 target field were fit well by YSO models but could not be fit well by stellar photospheres. This fraction was significantly lower for the control field, with 370/71,391 or 0.5% of sources (the counting uncertainty is 0.02%). While the model fitting process performed the service of discarding the >99% of sources that we were not interested in studying, simply being well-fit by YSO model SEDs was a necessary but insufficient criterion for a source to be included in the final sample. As a last step, we culled sources from the sample by inspecting all of the SED fits by eye, in many cases returning to the GLIMPSE and MIPSGAL images to confirm visually the existence of a valid source in each band with a reported detection. Two common reasons to reject a well-fit YSO candidate necessitated this final inspection:

1. The IR excess emission that prevented the source from being fit well by stellar photosphere models occurs only in the IRAC [8.0] band, with no detection at MIPS [24]. Such an SED can be produced by poor source extraction in regions with highly structured diffuse emission or a Malmquist bias affecting faint sources in the GLIMPSE sourcelists. The Malmquist bias occurs because when a source is selected for the Archive on the basis of a 5σ detection in any combination of bands, the fluxes of the remaining bands can be entered in the Archive even if they are at lower confidence levels. Stars are typically faint at 8 μm, and often a noise peak or a diffuse background feature can be extracted from the position of a star observed in the other bands, causing an artificially high measured [8.0] flux. While a few of the sources exhibiting this SED may actually be YSOs, we make the conservative decision to discard all questionable candidates.
2. A suspicious IR excess is observed in the MIPS [24] band only. The difference in resolution between MIPS and IRAC increases the chance of a false match when correlating sources between MIPSGAL and GLIMPSE. This often happens near bright, saturated 24 μm sources where the extended wings of the MIPS point-spread function can be extracted as individual point sources and matched with an overlapping GLIMPSE source. This creates a spurious 24 μm excess attributed to the GLIMPSE source.

Both of the above issues constitute important caveats to consider if searching for YSOs possessing "transition disks" with large inner holes that might have been cleared out by planets, since such sources exhibit IR excess emission only at longer wavelengths.

The brightest sources in our sample also appear in the *MSX* point source catalog, so we used available *MSX* fluxes to fill in the SED between IRAC and MIPS and replace saturated IRAC [8.0] and MIPS [24] fluxes, where possible. Bright sources with very red SEDs from $K-[8.0]$ that are isolated from other IR-excess sources are candidate evolved stars on the asymptotic giant branch (AGB). Carbon stars, for example, have mean absolute K-band magnitudes of $\sim$6.8 (Wallerstein & Knapp 1998) and are often enshrouded by dusty envelopes generated by strong winds (Guandalini et al. 2006); such stars have similar SEDs to YSOs from K to [8.0] and, even when located on the far side of the Galaxy, will be among the brightest sources observed in GLIMPSE. The RW07 fitting tool incorporates 75 AGB star SED templates derived from *Infrared Space Observatory* (*ISO*) spectroscopy (Sylvester et al. 1999; Hony, Waters, & Tielens 2002). After fitting bright sources with the AGB star templates, we removed 30 and 15 likely AGB stars from the

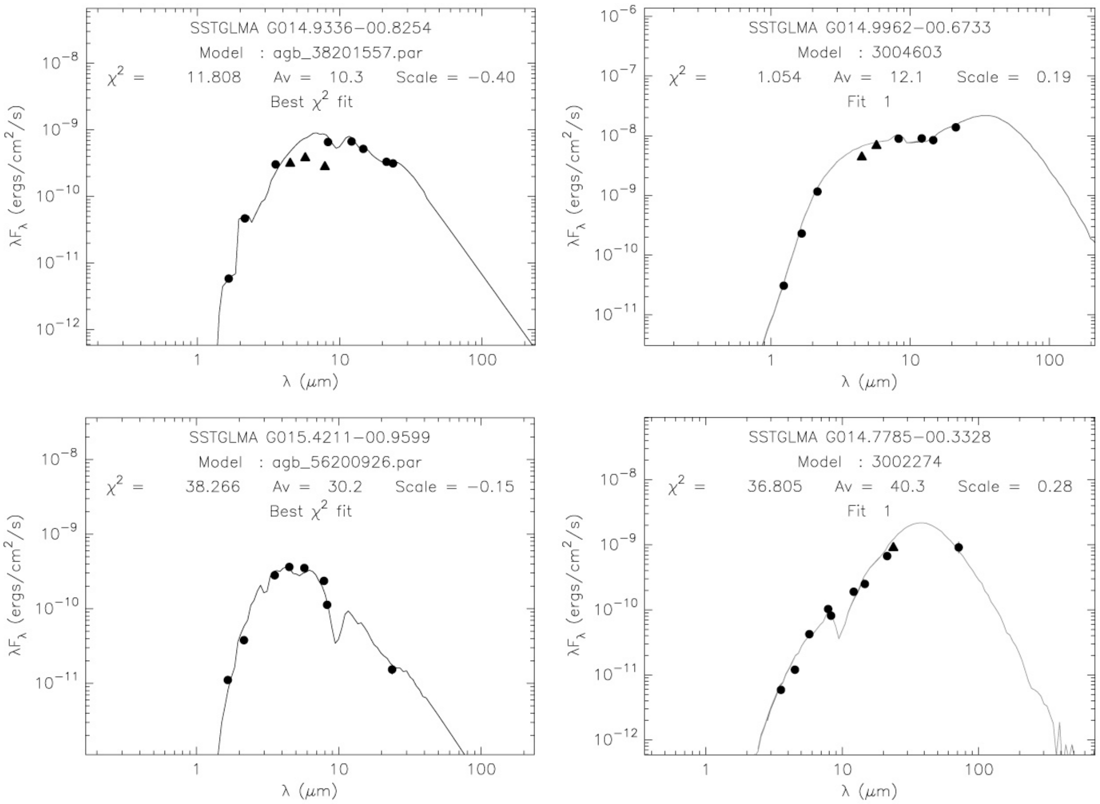

Fig. 4.2.— Example plots of best-fit model SEDs to available near- and mid-IR photometry. Two sources well-fit by AGB star spectral templates (*left* panels) are compared to two sources well-fit by YSO models (*right* panels) with similar brightnesses. Triangles denote datapoints with saturated fluxes that were used only as lower limits for the model fitting. The best-fit SED to the KW Object is plotted in the *upper-right* panel.

target and control samples, respectively.

Example SEDs of two probable AGB stars and two bright candidate YSOs from the target field are plotted in Figure 4.2. The most distinctive features of the AGB star SEDs are the precipitously red K−[8.0] spectral index and the turnover to a Rayleigh-Jeans spectrum at wavelengths longward of ∼24 μm. The YSO models that fit the SEDs of these bright sources tend to be massive stars with optically thick disks but without substantial infalling envelopes. Such objects are relatively rare, the best example in M17 being the Kleinmann-Wright (KW) Object (Kleinmann & Wright 1973), a suspected Herbig Be star (Chini et al. 2004a). The SED of the KW Object is plotted in the upper-right panel of Figure 4.2. Several candidate YSOs, including the one shown in the lower-right panel of Figure 4.2, are detected at 70 μm by MIPSGAL, but no candidate AGB stars are observed at 70 μm. Generally, YSO disks and envelopes contain cool ($T_d \sim 30$ K) dust that becomes optically thin at relatively large radii from the central star, while the dust distribution in AGB stellar winds has a much smaller effective radius, giving higher effective temperatures ($T_d \gtrsim 200$ K). It is therefore reasonable to expect that the SEDs of AGB stars will peak at shorter wavelengths than those of YSOs, but this difference cannot be observed without data at wavelengths of 24 μm or longer, and there may be exceptions to this general rule.

Visual inspection of the M17 target field revealed 6 bright, compact resolved IRAC sources that have SEDs well-fit by YSO models. These sources are noted in Tables 4.2–4.4 (see §4.4.1.2). Four of the 6 are *MSX* point sources, and their SEDs are suggestive of a PAH spectrum. The model fits to these sources were improved dramatically by assuming PAHs contributed significantly to the emission in the 4 bands with the strongest PAH features, IRAC [5.8] & [8.0] and *MSX* A & C. The RW06 YSO models did not include emission from PAHs; hence to fit sources with potentially PAH-dominated spectra we set these 4 bands as upper limits. Using the fluxes of the well-fit models to estimate the continuum levels in the bands affected by PAHs, we find that PAHs contribute anywhere from 30% to 90% of the broadband fluxes. The YSO models for 3 of these 4 sources indicate central stars with photospheric temperatures of $T_{\rm eff} \sim 2 \times 10^4$ K, hot enough to produce the UV radiation necessary to excite PAH transitions (Chapter 2 and references therein). The fourth source, F53 in Table 4.3 (at the end of this Chapter), was fit by few high-$T_{\rm eff}$ models. This object appears to be associated with the molecular cloud MC G14.9-0.4 (see Figure 4.1), giving it a near kinematic distance of 4.8 kpc at the cloud velocity of 60 km s^{-1}. This is far beyond the maximum distance of 2.3 kpc given to the model fitting tool, and at the larger distance this source is likely to be a compact H II region. This interpretation is supported by the fact that the source also appears to have associated radio emission from the 11-cm continuum survey of Reich et al. (1990). For consistency, we leave this source in the final sample of candidate YSOs, but we exclude it, along with other sources listed in Table 4.3 that are found outside the M17 subregion defined in §4.4.1, from the analysis of YSOs associated with M17.

4.3.3 YSO Evolutionary Stages

RW06 divided the YSO models into evolutionary Stages according to the envelope accretion rate $\dot{M}_{\rm env}$ and the circumstellar disk mass $M_{\rm disk}$, both normalized by the mass of the central star $M_\star$:

$$\begin{array}{lll} \text{Stage 0/I:} & \dot{M}_{\rm env}/M_\star > 10^{-6}\ {\rm yr}^{-1} & \\ \text{Stage II:} & \dot{M}_{\rm env}/M_\star < 10^{-6}\ {\rm yr}^{-1}; & M_{\rm disk}/M_\star > 10^{-6} \\ \text{Stage III:} & \dot{M}_{\rm env}/M_\star < 10^{-6}\ {\rm yr}^{-1}; & M_{\rm disk}/M_\star < 10^{-6}. \end{array}$$

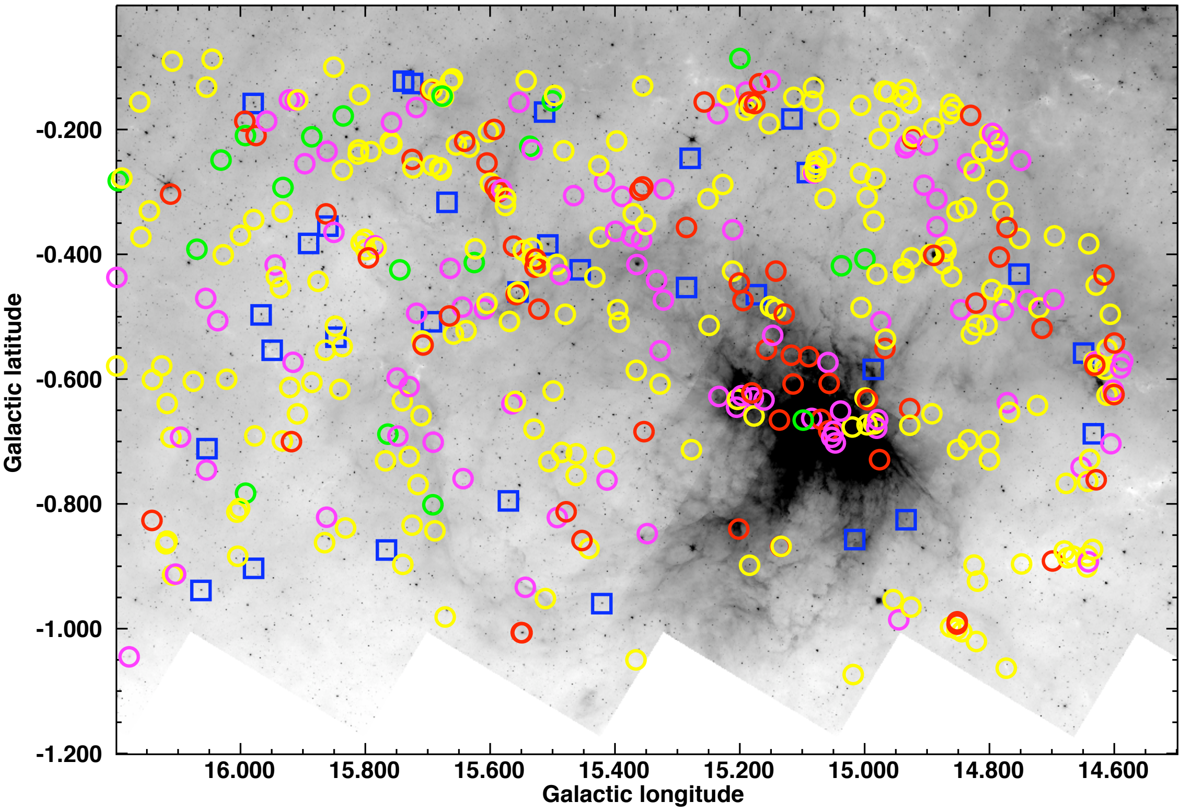

Fig. 4.3.— GLIMPSE 8.0 μm image of the M17 analysis target field (inverted logarithmic grayscale). Positions of the 406 candidate YSOs in the final sample are marked by circles color-coded according to the most probable evolutionary Stage of each source: *red* circles are Stage 0/I candidates (deeply embedded in infalling envelopes); *yellow* are Stage II (optically thick circumstellar disks); *green* are Stage III (optically thin circumstellar disks); and *magenta* are candidate YSOs for which the Stage is more ambiguous. *Blue* squares denote candidate AGB stars removed from the YSO sample. The apparent lack of candidate YSOs in the extreme top and right portions of the image reflects the boundaries of the search area.

These YSO classifications are based upon model parameters corresponding to physical properties, but they parallel the popular observational T Tauri classification system that uses IR spectral indices (Lada 1987). Stage 0/I YSOs are protostars heavily embedded in the infalling gas and dust of their natal envelopes. Stage II YSOs, like Class II T Tauri stars, have optically thick circumstellar disks that dominate their near- to mid-IR SEDs. Stage III YSOs have optically-thin remnant disks and their SEDs are dominated by photospheric emission; these objects are difficult to identify by IR excess alone (given our error bars of $\geq 10\%$–15%), hence very few examples are found in our conservative YSO sample. Because each candidate YSO was fit with multiple YSO models, we determined the evolutionary Stage of each source statistically.

We defined the set of "well-fit" models to each source as those models with fits meeting the criterion of

$$\frac{\chi^2}{N_{\rm data}} - \frac{\chi^2_{\rm min}}{N_{\rm data}} \leq 2, \tag{4.1}$$

where $\chi^2_{\rm min}$ is the goodness-of-fit parameter for the best-fit model. We estimated the *relative* probability of each model in the set according to

$$P(\chi^2) = e^{-(\chi^2 - \chi^2_{\rm min})/2} \tag{4.2}$$

and normalized such that $\Sigma P = 1$. This allowed us to construct a probability distribution for the evolutionary Stage of each source from the Stages of all the well-fit models. The most probable Stage of each source was defined by $\Sigma P(\text{Stage}) \geq 0.67$; if this condition could not be met, then the Stage of the source was considered to be ambiguous.

The 406 candidate YSOs in the final sample of the M17 target field are overplotted as circles on a GLIMPSE [8.0] image in Figure 4.3. The color-coding of the circles corresponds to the most probable evolutionary Stage of each source. Candidate YSOs are distributed throughout the image (the absence of sources from the top and right margins of the image is due simply to the boundaries of our search area). Numerous small "clusters" of 5–10 YSOs are apparent, and larger groups are associated with the M17 molecular cloud and the rim of M17 EB. Candidate YSOs associated with the M17 molecular cloud would dominate the sample if not for the strong masking effect of the bright diffuse mid-IR emission from the H II region and PDR. The point-source detection limit rises dramatically near the M17 H II region, and only the most luminous YSOs are detectable within the area where the 8.0 μm image in Figure 4.3 appears black. The MIPSGAL 24 μm image is completely saturated within the H II region, and a relatively high fraction of candidate YSOs near the H II region have ambiguous Stage (*magenta* circles) because 24 μm fluxes are an important discriminator between disk- and envelope-dominated sources (RW06).

4.3.4 Mid-IR Color-Color Plots

In Figures 4.4 and 4.5 we compare our model-based classifications of all stars and YSOs in the M17 target field with classification systems derived from IRAC mid-IR colors (Allen et al. 2004, hereafter A04; Gutermuth et al. 2008, hereafter G08). A04 showed, through a study of several nearby young clusters, that a box-shaped region in the IRAC [3.6] – [4.5] versus [5.8] – [8.0] color-color diagram (shown in Figs. 4.4) contains primarily Class II YSOs with disks. A04 found that protostars were located in the redward extension of this "disk domain" along both color axes. G08 built upon the work of A04 to devise a more

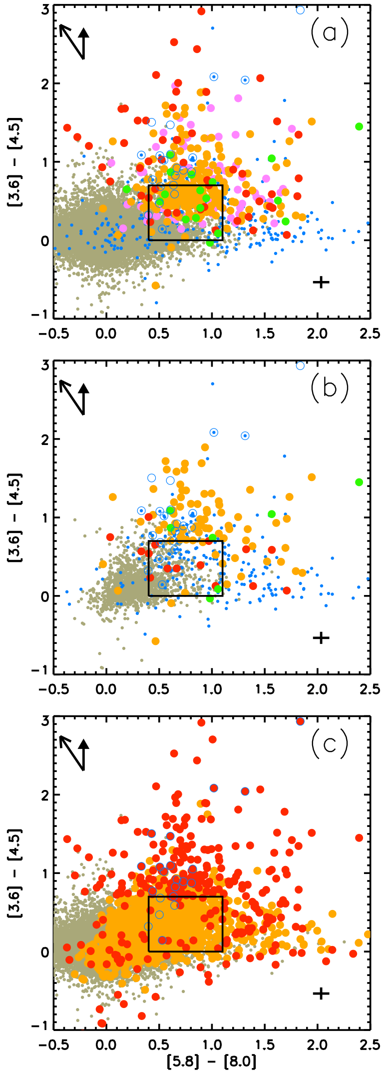

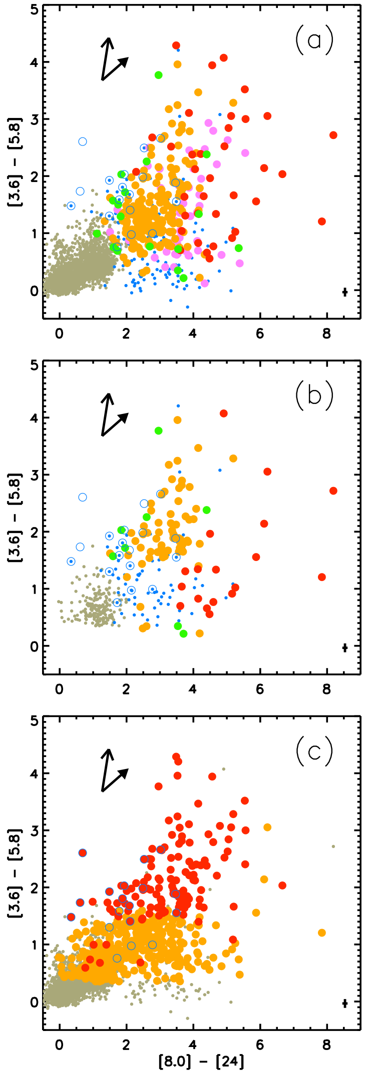

Fig. 4.4.— (*Left column*) Mid-IR color-color space showing sources in the target field that were detected in all 4 IRAC bands. The "disk domain" of A04 is contained within the black box. (*a*) Candidate YSO selection and classification from model fitting. Small *gray* dots are sources well-fit by stellar photosphere SEDs. Large dots are sources in the final YSO sample (*red:* Stage 0/I; *orange:* Stage II; *green:* Stage III; and *lavender:* ambiguous). (*b*) Sources for which our model-based classification differs from the IRAC color-color classification of G08. Sources discarded from the final YSO sample (small *blue* dots) remain in this plot if they have IRAC colors consistent with YSOs according to G08. (*c*) G08 YSO selection and classification (*gray:* stellar photospheres; *red:* protostars; and *orange:* Class II). In all plots, *blue* circles are candidate AGB stars, reddening vectors for $A_V = 30$ mag based on the extinction laws of Weingartner & Draine (2001) and Indebetouw et al. (2005) are shown as open and filled arrows, respectively, and black crosses give typical photometric errors.

Fig. 4.5.— (*Right column*) Same as Figure 4.4, except a color space combining IRAC with MIPS [24] photometry is shown.

sophisticated system for the classification of YSOs in the young embedded cluster NGC 1333, utilizing multiple IRAC color-color planes. In Figures 4.4 and 4.5 the YSO selection and classification criteria of A04 and G08 are compared to our YSO selection and Stage classification using the RW06 models. Sources plotted in Figures 4.4*a,b* and 4.5*a,b* are color-coded according to their most probable evolutionary Stage from the RW06 models: *red, orange, green*, and *lavender* for Stages 0/I, II, III, and ambiguous, respectively, while *gray* dots represent sources best fit by stellar photospheres, and *blue* dots show sources that were well-fit by YSO models but were excluded from the final sample (see §4.3.2 above). Figures 4.4*b* and 4.5*b* show only sources for which the classification using model fitting differs from the classification using the G08 color-color criteria (sources with ambiguous Stage are not plotted). In Figures 4.4*c* and 4.5*c*, sources are plotted according to their G08 color classification: protostars are *red* while Class II sources are *orange*. Like virtually all classification systems based upon colors, neither the A04 nor the G08 criteria allow ambiguity between protostars and Class II sources, but we stress that *ambiguity is an inherent property of any YSO taxonomy, whether based upon colors, spectral indices, or SEDs.*

Although the A04 disk domain contains many disk sources, it does not contain *all* candidate disk sources and selects a significant number of diskless stars with reddened photospheres. The locus of Stage II sources in Figure 4.4*a* is redder than the disk domain by $[3.6]-[4.5]\sim 0.3$ mag . The same displacement was found by Indebetouw et al. (2007) for YSOs in the Eagle Nebula (M16), another massive star formation region near the Galactic mid-plane, located ∼2.5° from M17. The discrepancy could be largely resolved by reddening the disk domain by an amount equivalent to $A_V \approx 20$ mag, a reasonable modification considering that the regions studied by A04 were not highly-reddened massive star formation regions in the Galactic plane. The G08 color classification selects 1882 Class II sources and 57 protostars that we find to be well-fit by reddened stellar photospheres (*gray* dots in Figures 4.4*b* and 4.5*b*). These sources are a striking feature of Figure 4.4*c*, where they are found predominantly to the left of the disk domain, in the locus of photospheres (A08). Largely on account of these sources, the total number of YSOs selected by the A04 criteria or especially the G08 criteria is far greater than the number of candidate YSOs in our conservative sample. Again, the fact that the G08 color criteria were derived through the study of a nearby star formation region located away from the Galactic plane would explain the large number of reddened stellar photospheres selected as YSOs. In addition, both the A04 and G08 criteria were derived from studies of regions that, unlike M17 and M16, lack many massive YSOs, which should contribute to the disparities between the color-color classifications and the model-based classifications (Whitney et al. 2004).

When compared to our evolutionary Stage classifications, the G08 classification system confuses a significant number of protostars for more evolved YSOs, and vice versa. This disagreement is evident in Figure 4.4, but it can be more readily explained by examination of Figure 4.5, in which sources are plotted using a color-color diagram that combines IRAC with MIPS [24] photometry. As shown by RW06, this color space illustrates the value of 24 μm data for distinguishing between protostars (Stage 0/I) and disk-dominated (Stage II) YSOs. Figure 4.5*a* shows a progression toward less evolved sources with increasing $[8.0]-[24]$ color, and many sources with ambiguous Stage determinations (*lavender*) lie along the boundary between the Stage 0/I and II populations. In Figure 4.5*b*, all Stage II sources (*orange* dots) plotted for $[3.6]-[5.8] > 1.5$ are protostars according to the G08 classification system (these sources are *red* dots in Figure 4.5*c*), which relies upon photometry at wavelengths $\leq$8.0 μm.

Two main classes of "false" YSOs are illustrated in the IRAC color-color plots of Figures 4.4. (1) Candidate AGB stars (open *blue* circles) are intermingled with YSOs and appear very difficult if not impossible to distinguish by IRAC colors alone. (2) The lower-right part of Figure 4.4*a*, centered on $[3.6]-[4.5]=0$ for $1 < [5.8]-[8.0] < 2.5$, contains numerous sources well-fit by YSO models (*blue* dots) that were discarded from the final sample because the IR excess emission appears at [8.0] only (see §4.3.1 above).

Spurious correlations of 24 μm sources with IRAC sources can also create artificial IR excesses (see §4.3.1), and consequently many sources discarded from our final YSO sample appear in Figure 4.5*a* as *blue* dots near $[3.6]-[5.8]=0$ for $2 < [8.0]-[24] < 4$. Candidate AGB stars are better distinguished from YSOs in Figures 4.5 than in Figures 4.4. Three candidate AGB stars (see §4.3.2 above) with $[3.6]-[5.8] \geq 1.5$ but $[8.0]-[24] < 1$ are located far from YSOs and stellar photospheres. Several other candidate AGB stars have $[8.0]-[24] \sim 2$, placing them on the blue edge of the Stage II YSO locus. This supports the interpretation that AGB stars are typically surrounded by dust shells with smaller effective radii than the disks and envelopes of YSOs (see Robitaille et al. 2008, for example).

We have experimented with the A04 and G08 color-color criteria for selecting and classifying candidate YSOs because these are among the most well-developed analysis techniques available for IRAC. It is not appropriate to apply these precise color cuts directly to the interpretation of sources in the M17 region, because they were developed through the study of relatively nearby ($d < 1$ kpc) regions that, unlike M17, are located in relatively low-density molecular clouds away from the Galactic plane. This illustrates one of the principal advantages of the model-fitting approach. *All methods for selecting populations of objects based on broadband photometric colors are based upon models.* The RW07 model fitter, with its integrated capacity to apply interstellar extinction to SED models before matching them with observed fluxes, can be employed consistently for the study of star formation in various environments without the need to empirically redraw the selection criteria. A second major advantage is the ability to use all available photometric information simultaneously to constrain the physical parameters of large numbers of sources. For more on the advantages of the model-fitting approach, see Indebetouw et al. (2007).

4.3.5 Contaminants in the YSO Sample

Even the most carefully selected sample of candidate YSOs will identify other objects that have similar IR colors. External, dusty galaxies are the most common contaminant in YSO searches using deep IRAC observations of nearby star formation regions away from the Galactic plane, such as the c2d Survey (Porras et al. 2007). GLIMPSE is a shallow survey, and employing the Porras et al. (2007) criterion for galaxy selection to our final M17 target sample of YSOs yields no galaxy candidates (the control sample contains a single source that may be a galaxy). In the Galactic plane, the objects most likely to masquerade as YSOs in significant numbers are evolved stars, specifically AGB stars with dusty winds and unresolved planetary nebulae (PNe). In addition, because we are primarily interested in analyzing the population of YSOs associated with M17, YSOs in the foreground or background must also be treated as contaminants to our sample.

A GLIMPSE 8.0 μm image of the control field is presented in Figure 4.6, with the final sample of 106 candidate YSOs and AGB stars overplotted as in Figure 4.3. Candidate YSOs are distributed throughout the search area with an average density of 140 sources deg^{-2}, or nearly 60% of the average source density in the target sample (see Table 4.1). The source density in the control sample is not uniform, decreasing with increasing Galactic latitude across the 1-degree span of the field, which implies a low Galactic scaleheight for the source population. Because of this variation, we define a box 0.5° on a side centered at $(l, b) = (15.1, 0.7)$ in the control field, to sample directly the density of contaminants at Galactic latitudes mirroring the location of M17. The source density in this control subfield is 100 deg^{-2} (Table 4.1).

The control sample represents the contamination expected to be present in the sample of candidate

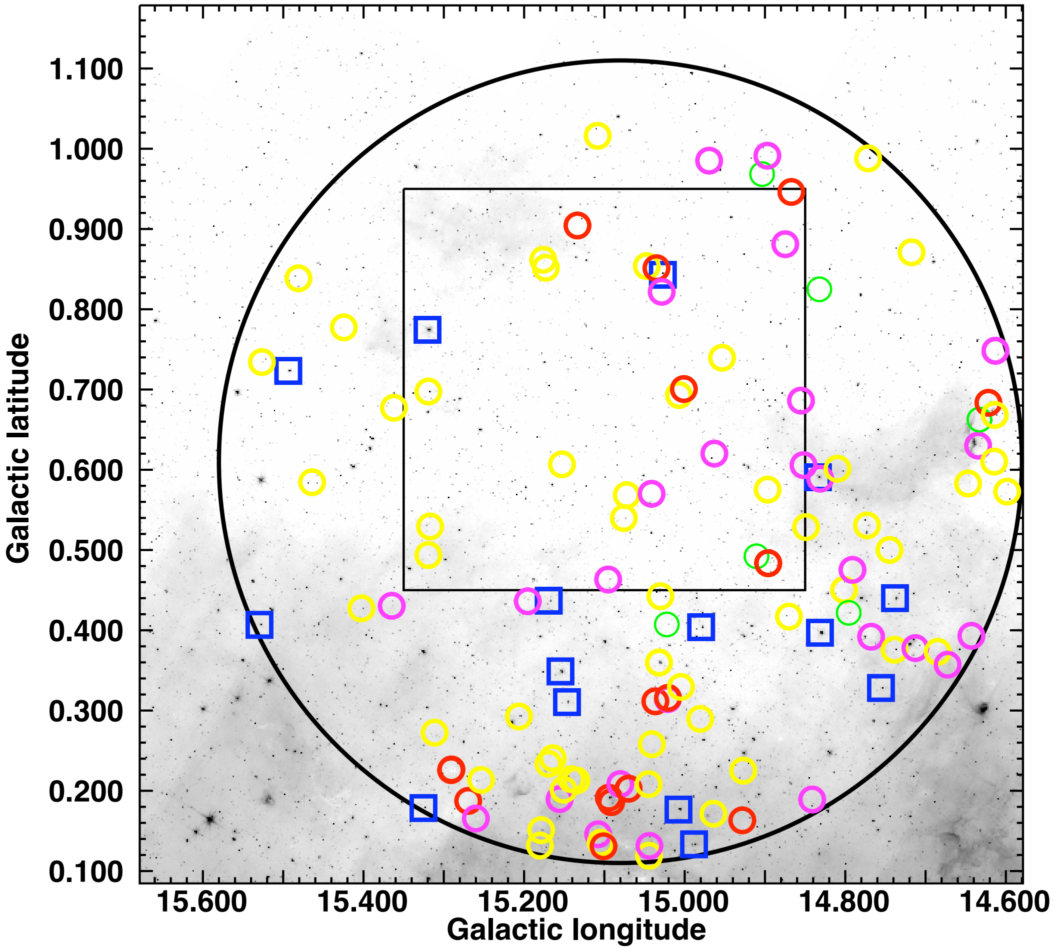

Fig. 4.6.— GLIMPSE 8.0 μm image of the control field, with the same color overlays as in Figure 4.3. The area searched for YSOs is shown by the black circle. The control subregion chosen to mirror the position of M17 about the Galactic mid-plane is the boxed area, 0.5° on a side.

YSOs in the M17 target field. To estimate the numbers of evolved stars expected in the control and target samples, we turned to a detailed model of the IR point source sky (Wainscoat et al. 1992; Cohen 1993). This Sky model incorporates 87 different source populations, including PNe and several types of AGB stars, into a geometric representation of the Galactic bulge, halo, and thin and thick disks. The model has been shown to agree well with *IRAS* observations (Wainscoat et al. 1992).

Cumulative source densities as functions of [4.5] magnitude are presented in Figure 4.7. Curves generated by the Sky model for oxygen-rich AGB stars (AGB M), optically visible/obscured carbon stars (AGB C/CI), and PNe are plotted along with YSO candidates detected in the target and control samples

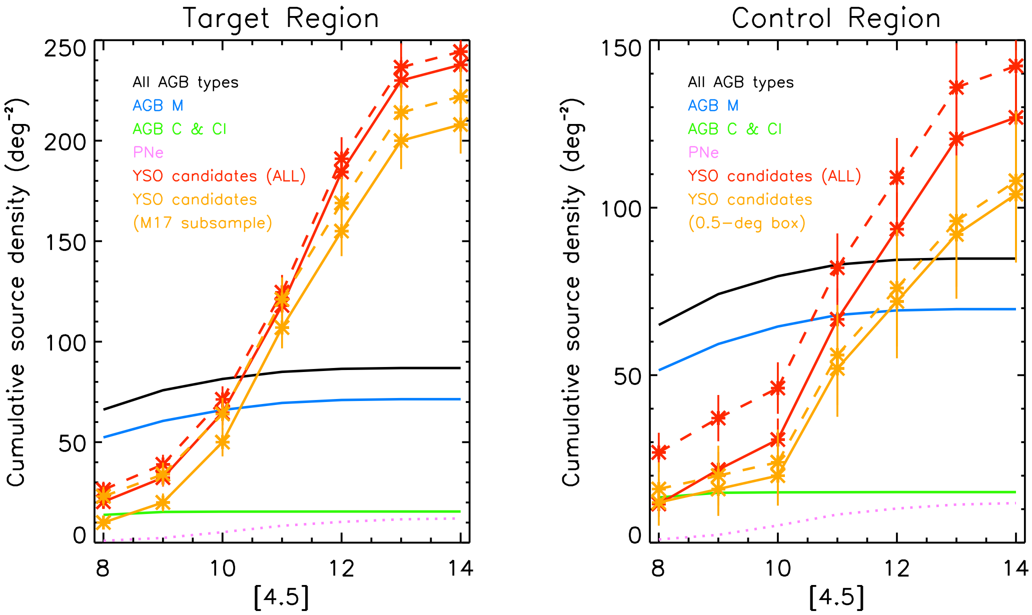

Fig. 4.7.— Cumulative densities of different types of red sources as a function of [4.5] magnitude. The curves for AGB stars (AGB M are O-rich and AGB C & CI are optically visible & obscured C-rich AGB stars, respectively) and PNe were generated by the Sky model (Wainscoat et al. 1992; Cohen 1993). The solid YSO curves represent the target and control samples and subsamples, while the dashed curves show the solid curves before bright candidate AGB stars were removed.

and subsamples (see §4.4). One striking feature of these plots is the high brightness of AGB stars in the IR. The brightest magnitude plotted in Figure 4.7 is magnitude 8, because nonlinearity begins to affect the [4.5] band for brighter sources. The source density of all AGB types brighter than magnitude 8 is more than twice the density of comparably bright sources selected for our YSO sample, even before suspected AGB candidates are removed (dashed curves in Figure 4.7). While the brightest AGB stars will saturate the IRAC detectors and hence not be extracted into the point-source Archive, there are too few such sources visible in the target and control fields to account for a significant number of the AGB stars predicted by the Sky model. While most AGB stars in the inner Galaxy will be in the GLIMPSE Archive, evidently not all types of AGB star have large IR excesses that allow them to be confused with YSOs.

Removing suspected AGB stars from the control field sample cut the cumulative source density at magnitude 8 by more than half (the difference between the dashed and solid *red* curves in the *right* panel of Figure 4.7). As the cumulative source density with magnitude plotted in Figure 4.7 shows, the Sky model predicts that $<30\% = (70\ \mathrm{deg}^{-2} - 50\ \mathrm{deg}^{-2})/70\ \mathrm{deg}^{-2}$ of O-rich AGB stars (*blue* curves) and virtually no carbon stars (*green* curves) are fainter than $[4.5] = 8$ mag. Suppose that *all* the IR excess sources remaining in the control sample brighter than [4.5] = 8 mag are O-rich AGB stars, with *no* fainter AGB stars having been removed. Scaling down the *black* curve to match the solid *red* curve at 8 mag in the control field plot of Figure 4.7 shows that the final control sample could still contain up to 15 AGB stars deg^{-2}, or ∼12% of the overall source density (∼125 deg^{-2}; value of the solid *red* curve at [4.5] = 14 mag). This represents the *maximum* possible fraction of AGB stars remaining in the control sample of candidate YSOs. The fraction of AGB stars remaining in the M17 target sample will be even lower (∼7%), because the overall source density is 1.7 times higher (Table 4.1).

There remains some potential contamination from unresolved PNe. According to the predictions of the Sky model (Figure 4.7), these represent $< 10\%$ of sources in the control sample and $< 5\%$ of sources in the target sample.

We conclude that the majority (>80%) of sources selected as candidate YSOs in the control field are actual YSOs, albeit at unknown distances. This is higher than the 60% fraction of YSOs found in the recent catalog of dusty red sources in GLIMPSE compiled by Robitaille et al. (2008). This catalog contains only sources with [8.0] > 10 mJy. Virtually all Galactic AGB stars meet this brightness criterion, but only ∼50% of the sources in our control sample do. Therefore, if we apply the [8.0] cut of Robitaille et al. (2008) to our control sample, the fraction of candidate evolved stars *doubles*, from 20% to 40%, in good agreement with the new red source catalog despite the small size of our control sample.

The density of IR excess sources drops noticeably across the 1° increase in Galactic latitude on either side of the mid-plane (Figs. 4.3 and 4.6). This suggests that star formation, in the form of isolated YSOs or small clusters, is distributed throughout the Galactic plane with a low scaleheight. The number of candidate YSOs in the M17 vicinity represents a significant enhancement over this Galactic background YSO population, as we discuss in the following section.

4.4 The Extended YSO Population and Molecular Cloud Structure of M17

A ^{13}CO zero moment map for $v = 12$–26 km s^{-1} and a ^{12}CO channel map at $v = 19$ km s^{-1} are compared to the 8 μm image of the M17 target field in Figure 4.8. The ^{12}CO and ^{13}CO maps from the HHT reveal the underlying structure of the molecular gas outlining the extended regions of M17 along with M17 EB and portions of MC G15.9-0.7. M17 EB is a coherent, albeit clumpy, kinematic structure in molecular gas at $v = 19$ km s^{-1}. The CO data thus confirm that the entire dust shell observed in the IR has a

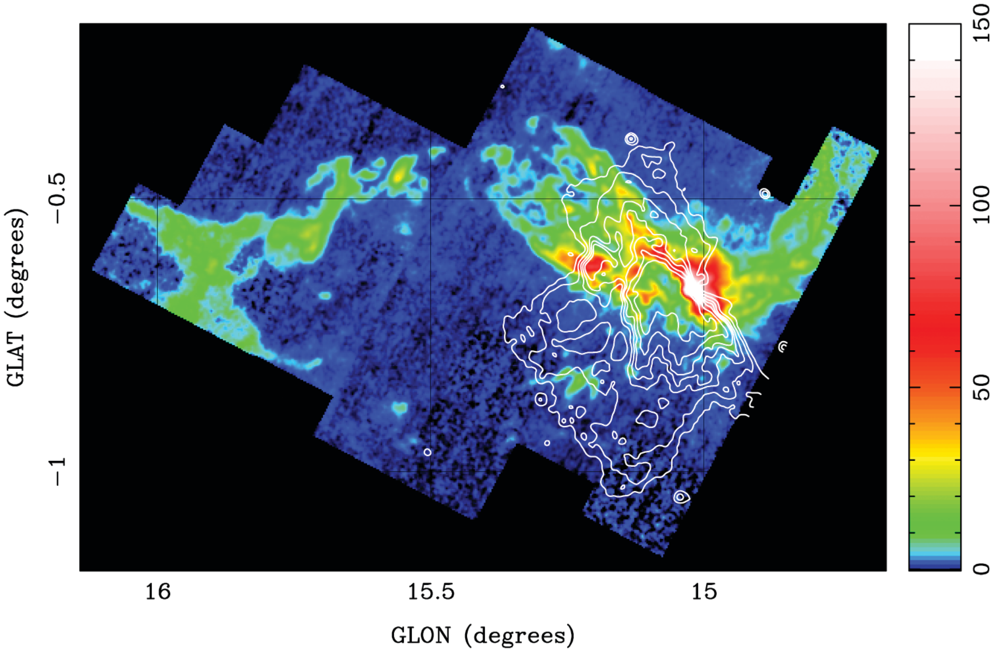

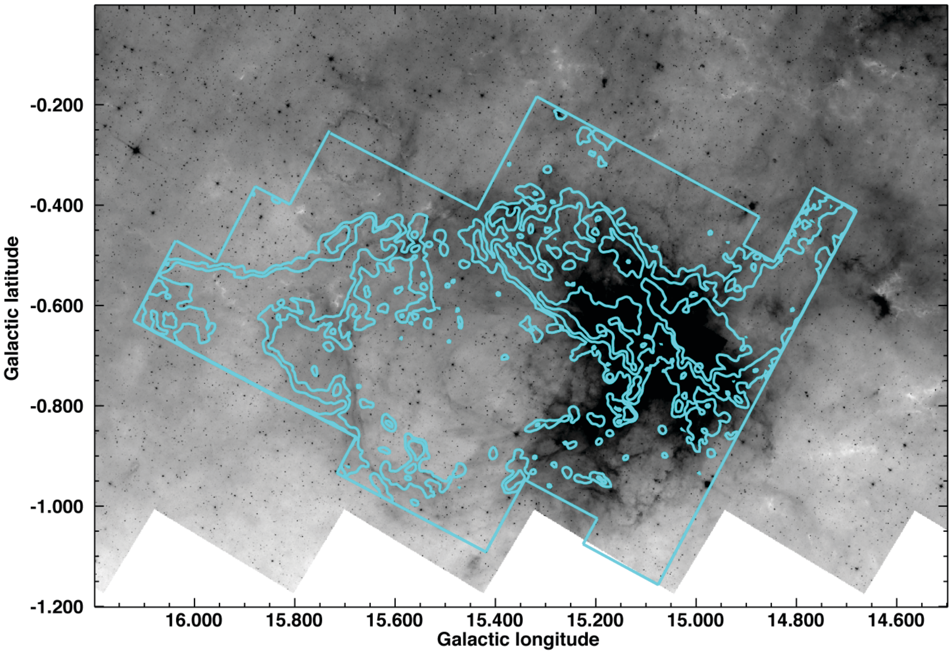

Fig. 4.8.— CO maps of extended molecular cloud structures associated with M17. (*Top*) HHT ^{13}CO moment 0 map for v = 12–26 km s^{-1}. The image colorbar is in units of K($T_A^\star$) km s^{-1}. Contours show 90 cm continuum observations from the VLA (at intervals of 5, 10, 20, 30, 40, 60, and 80% of the map peak) that trace thermal emission from ionized gas associated with the M17 H II region. (*Bottom*) GLIMPSE 8 μm image. Contours show HHT ^{12}CO emission at v = 19 km s^{-1}.

common velocity with M17, supporting our conclusion that M17, M17 EB, and MC G15.9-0.7 are all part of the same dynamical complex. M17 EB, as a bubble, should exhibit a 3-dimensional, roughly spherical structure. Many astrophysical shell structures exhibit a ring-like morphology in optically thin emission due to limb-brightening, and emission from the interior of the ring may be difficult to detect. Integrating the ^{13}CO data cube spatially over a $17' \times 11'$ box centered at $(l, b) = (15.6°, -0.7°)$, we definitively detect an emission line near $v = 20$ km s^{-1} with a peak at $\langle T_B \rangle = 0.05$ K. The line does not exhibit the double-peaked profile of an expansion signature, which means that if the bubble is still expanding, the expansion velocity is low, less than a few km s^{-1}, and the line profile is dominated by internal motions within the shell.

4.4.1 Correction for Contamination from Unassociated Sources

We have claimed that the control field sample of candidate YSOs mirrors the population of unassociated sources contaminating the M17 target field sample. We can use the control sample to remove contaminants statistically from the target sample, but first we must verify this claim. The molecular cloud complex associated with M17 contributes a significant enhancement to the gas column density in the target field with respect to the control field. This additional source of interstellar extinction could bias the source selection between our flux-limited samples.

4.4.1.1 Extinction Map

To estimate the extinction through the molecular cloud, we employ a model for CO line excitation based on an escape probability formalism for the CO line radiation (Kulesa et al. 2005). The observed ^{12}CO and ^{13}CO ($J = 2 \rightarrow 1$) line intensities, velocity widths, and peak brightness temperatures constrain the model at each map pixel to give the total CO column density, $N(\mathrm{CO})$, and the mean gas kinetic temperature, $\langle T_{kin} \rangle$. We estimate the mean H_2 density, $\langle n(\mathrm{H}_2) \rangle$ from the derived $N(^{13}\mathrm{CO})$ column density. $\langle n(\mathrm{H}_2) \rangle$ varies from 10^3 cm^{-3} in the extended cloud structures to 10^5 cm^{-3} in the M17 South core near the H II region. The derived $N(\mathrm{CO})$, $\langle n(\mathrm{H}_2) \rangle$, and $\langle T_{\mathrm{kin}} \rangle$ are then applied as constraints on a CO PDR model based on van Dishoeck & Black (1988) to estimate the far UV radiation field, G_o, incident on the molecular gas, and the total hydrogen column density $N(\mathrm{H}) = N(\mathrm{H}^0) + 2N(\mathrm{H}_2)$ (H-atoms cm^{-2}). The corresponding extinction A_V, is calculated from $N(\mathrm{H})$ using the value $N(\mathrm{H})/A_V = 1.9 \times 10^{21}$ cm^{-2} mag^{-1} (Bohlin, Savage, & Drake 1978). Our analysis thus attempts to incorporate the variations in both gas density and the far UV radiation throughout the cloud complex. The resulting distribution of extinction is

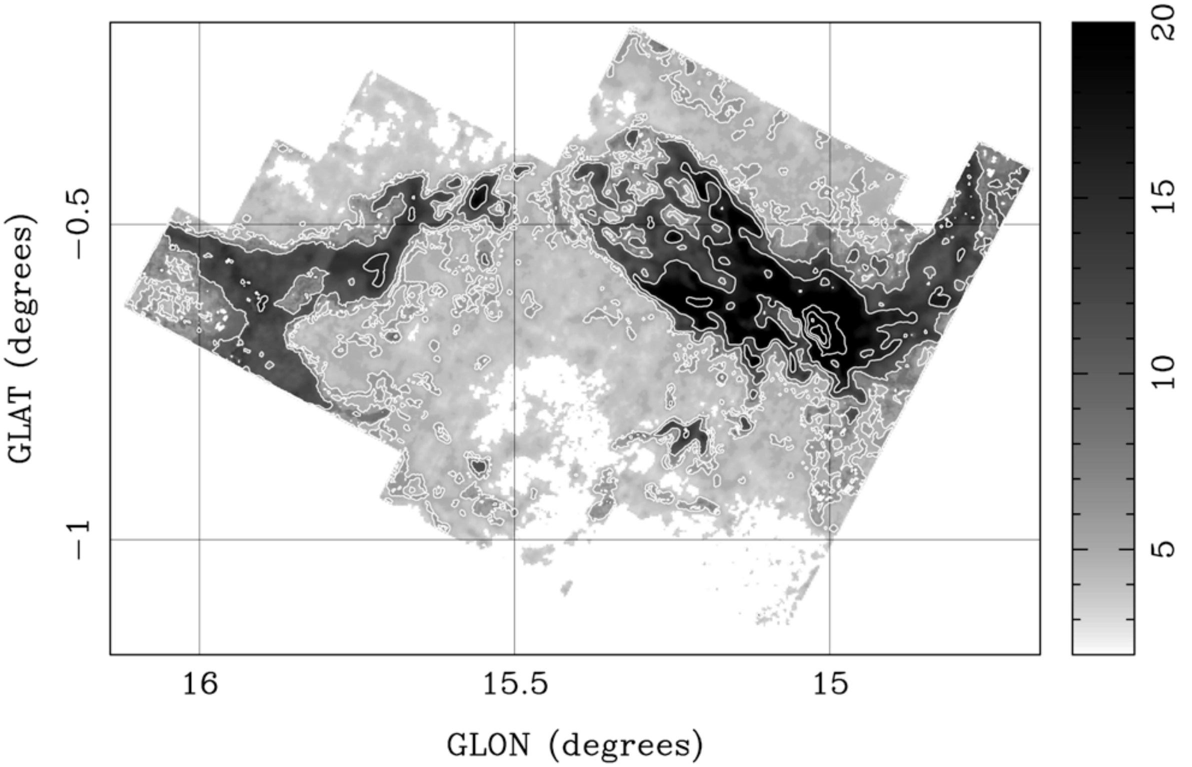

Fig. 4.9.— Extinction map produced from CO at $v = 12$–26 km s^{-1}. Grayscale is labeled in magnitudes of A_V. Contour levels are A_V of 5, 10, 15, 30, 60, and 90 mag.

shown in Figure 9, as a map of A_V over the region mapped in ^{12}CO and ^{13}CO.

The PDR model outputs the total hydrogen column density used in the extinction calculation. Abundances measured from the M17 H II region give $X = 0.698$ (Carigi & Peimbert 2008), and including unobserved He and metals the entire region mapped by HHT contains 1.35×10^5 M$_\odot$ total gas mass in the velocity range occupied by M17.

The extinction map in Figure 4.9 represents the *differential* extinction between the target and control fields due to the molecular and atomic gas associated with M17. The molecular gas occupies less than half of the image area, while candidate YSOs are found throughout (Figure 4.3). Much of the M17 molecular cloud has $A_V \gtrsim 15$ mag, reaching $A_V > 90$ mag in the dense core of M17 South. The extended outer regions of M17 and MC G15.9-0.7, however, produce $A_V < 15$ mag. This corresponds to $A_K < 2$ mag and $A_{[4.5]} < 1$ mag (Indebetouw et al. 2005) generally, and much less through the interior of M17 EB and other areas lacking high-density molecular gas. The map in Figure 4.9 represents the spatial average of A_V over each beam. Hence the extinction could be higher along localized sightlines through compact, dense clumps of molecular gas that are smaller than the $32''$ (FWHM) resolution of our map (0.33 pc at 2.1 kpc), but such clumps occupy an insignificant fraction of the mapped area. We thus do not expect the differential extinction between the target and control fields to produce a significant disparity in mid-IR point source detections, except in the M17 molecular cloud itself.

The M17 molecular cloud and PDR do create significant, spatially varying extinction and, more importantly, produce bright diffuse mid-IR emission that saturated the MIPSGAL 24 μm images and drastically reduced the point-source sensitivity of GLIMPSE. The surface density of GLIMPSE Archive sources is 14% higher in the control field than in the target field. Much of this discrepancy is due to the sharp drop in source detections near the M17 H II region and molecular cloud, which occupy ∼10% of the area in the target field. We therefore consider the control field ill-suited for comparison with the central regions of M17, but for the remaining 90% of our extended target field the control sample gives an accurate picture of the contamination to the target YSO sample.

4.4.1.2 Selection of YSOs Associated With M17

The prevalence of candidate YSOs distributed throughout the M17 target field requires that a distinction be drawn between areas that are likely dominated by sources associated with M17 and external star formation regions. Using the distribution of 8 μm emission along with the CO velocity structures revealed by our HHT data, we defined a subregion of the target field that is dominated by molecular gas associated with M17 (area bounded by *white* in Figure 4.10). The 195 candidate YSOs within this region make up the M17 target subsample (Table 4.1). This subsample is directly comparable to the control subsample found within the boxed region in Figure 4.6.

In Figure 4.10, the background contamination to the YSO sample has been statistically subtracted such that only candidate YSOs exhibiting a significant degree of clustering are plotted. This was accomplished using a simple "friends-of-friends" nearest-neighbors analysis. We first computed the median angular separation $\theta_{\rm con}$ between each source in the control field sample and its N nearest neighbors, where $3 \leq N \leq 10$. We then calculated $\theta_{\rm targ}$, the corresponding nearest-neighbors separation for each of the candidate YSOs in the target sample. The median value of $\theta_{\rm con}$ for all sources in the control sample is $\Theta_{\rm con}$. Finally, we selected the subset of sources in the target field for which $\theta_{\rm targ} < f\Theta_{\rm con}$. The factor f comes from the ratio of surface densities between the target subsample and the control subsample ($f \equiv [\Sigma_{\rm con}/\Sigma_{\rm targ}]^{0.5}$), with $f = 0.7 \pm 0.1$ using the values from the bottom row of Table 4.1 and assuming

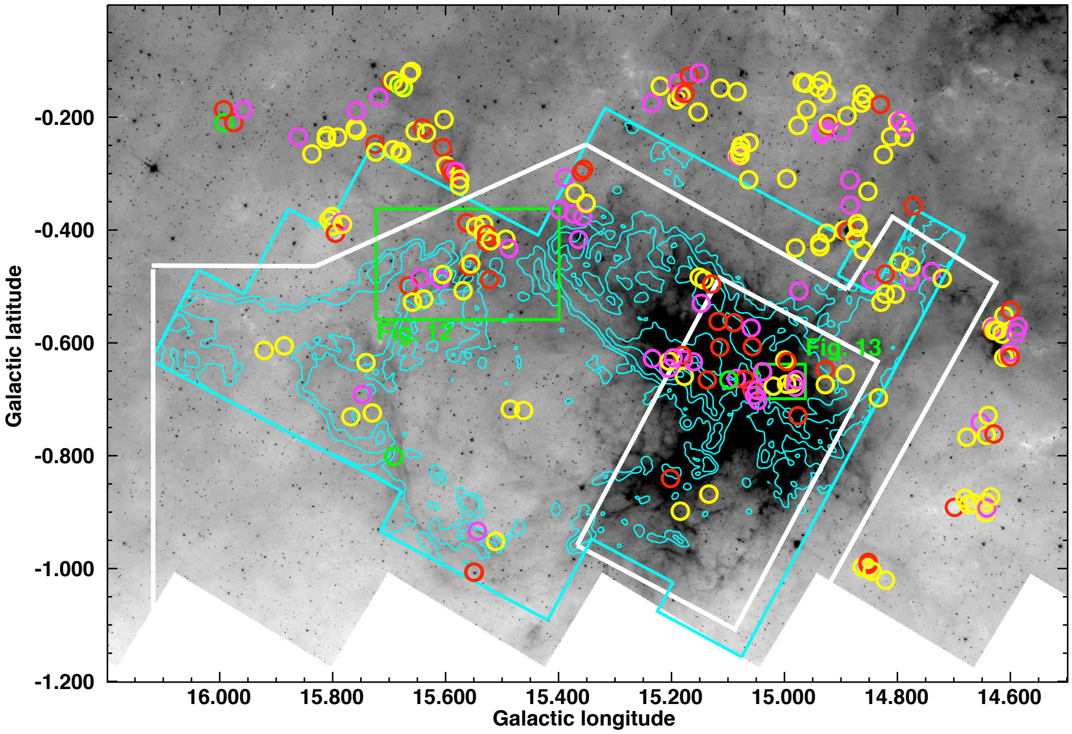

Fig. 4.10.— Candidate YSOs exhibiting significant clustering (see text). Circles mark YSO positions and are color-coded according to evolutionary Stage as in Figure 4.3. The 8 μm image and CO contours are the same as in Figure 4.8 (*bottom*). The thick *white* boundary lines enclose the CO emission and pass through breaks in the spatial distribution of YSOs. The thick *white* rectangle shows the field that has been observed by *Chandra*, within which bright diffuse mid-IR background emission severely affects the IRAC point-source sensitivity. *Green* rectangles show the fields enlarged in Figs. 4.12 & 4.13.

counting statistics. We found that the subset of candidate YSOs selected by this procedure was generally insensitive to the choice of N for $N > 3$, while the uncertainty in f creates a $\sim$20% uncertainty on the total number of sources selected. The final sample of candidate YSOs shown outside the *white* rectangle in Figure 4.10 was selected using $N = 5$, for which $\Theta_{\rm con} = 4.28'$. For the central parts of M17 we did not correct for contaminants because our control field is unsuitable, as noted above. The 34 candidate YSOs found within the *white* rectangle in Figure 4.10 are presented in Table 4.4. Excluding these 34 sources, we have discarded $197/372 = 0.47$ of the sources from the original target sample. Given that we expect a fraction $f^2 \sim 100/205 = 0.49$ of the sources in the target sample to be contaminants (Table 4.1), our cluster-finding procedure has succeeded in removing the expected contamination.

After correcting for contaminants the final M17 YSO subsample contains 96 sources (Tables 4.2 & 4.4). Two main concentrations of candidate YSOs within the final subsample are apparently associated with

Table 4.4. Candidate YSOs in the Region Observed By Chandra

Index No.	l (deg)	b (deg)	[4.5] (mag)	[8.0] (mag)	$M_\star$ ($M_\odot$) Min	Max	$\log(L_{\rm TOT}/L_\odot)$ Min	Max	Evolutionary Stage[a]
With X-ray Counterparts									
X1	14.9846	-0.6718	9.9	8.7	2	3	1.2	1.6	II
X2[b]	14.9855	0.6716	10.6	9.6	1	5	1.0	2.5	II
X3	14.9954	-0.6332	8.4	5.7	1	7	2.1	2.8	0/I
X4[c]	14.9962	-0.6733	< 3.6	···	9	10	3.7	3.9	II
X5	14.9994	-0.6304	7.3	6.9	5	6	2.6	3.2	II
X6	15.0198	-0.6768	8.6	···	4	10	2.3	3.8	II
X7[b]	15.0386	-0.6513	6.2	···	6	15	3.0	4.4	Amb.
X8	15.0470	-0.7023	9.9	8.3	1	5	1.1	2.7	Amb.
X9	15.0530	-0.6934	7.1	6.0	5	9	2.6	3.6	Amb.
X10	15.0568	-0.6068	9.9	8.1	2	5	1.5	2.0	0/I
X11	15.0699	-0.6646	9.4	6.8	1	5	1.3	2.4	0/I
X12	15.1146	-0.6079	11.4	···	1	7	1.1	2.6	0/I
X13	15.1613	-0.6335	10.4	9.5	0.5	4	0.8	1.9	Amb.
X14[b]	15.1772	-0.6593	9.0	8.2	2	5	1.5	2.3	II
Without X-ray Counterparts									
NX1[d]	14.8923	-0.6556	11.0	10.1	2	4	1.1	2.0	II
NX2[d]	14.9277	-0.6740	8.0	7.5	4	5	2.3	2.7	II
NX3[d]	14.9278	-0.6473	11.5	10.3	0.4	7	0.7	2.7	0/I
NX4	14.9761	-0.7292	11.3	···	0.4	7	0.8	3.0	0/I
NX5[e]	14.9791	-0.6651	6.6	3.3	8	11	3.5	3.9	Amb.
NX6	14.9806	-0.6787	11.0	9.9	0.5	5	1.0	2.4	Amb.
NX7	15.0494	-0.6838	7.6	···	4	10	2.2	3.8	Amb.
NX8	15.0576	-0.6830	10.8	8.7	0.6	7	1.0	2.9	0/I
NX9	15.0589	-0.5735	10.8	9.9	0.5	4	0.7	1.5	Amb.
NX10[f]	15.0848	-0.6631	7.7	6.5	2	10	2.1	3.6	Amb.
NX11	15.0895	-0.5641	11.0	9.2	0.7	5	1.0	2.6	0/I
NX12	15.0984	-0.6658	6.3	6.0	5	14	2.9	4.2	III
NX13	15.1176	-0.5618	9.2	8.3	3	7	2.0	2.7	0/I
NX14[d]	15.1337	-0.8681	10.3	8.5	0.4	6	1.0	3.0	II
NX15[d]	15.1348	-0.8683	13.0	10.7	0.2	6	0.3	2.3	0/I
NX16	15.1366	-0.6657	···	5.8	7	14	3.2	4.2	0/I
NX17	15.1784	-0.6299	10.5	9.6	0.3	3	0.7	1.6	Amb.
NX18	15.1808	-0.6222	8.2	6.7	0.5	8	1.5	2.9	0/I
NX19[d]	15.1844	-0.8984	···	5.6	5	8	2.9	3.3	II
NX20	15.2017	-0.8404	8.5	7.5	2	9	2.0	3.2	0/I

[a] The "Amb." Stage designation is the same as in Table 4.2.

[b] Selected as X-ray emitting candidate "protostars" in Table 7 of BFT07.

[c] X4 is the KW Object (see Figure 4.13).

[d] These 6 sources are located away from the bright 8 μm emission of the M17 PDR, increasing the odds that they are unassociated contaminants.

[e] NX5 is resolved by IRAC (see Figure 4.13).

[f] NX10 is located at the tip a prominent pillar structure in the M17 H II region. J02 resolve this source into two YSOs of comparable brightness in the near-IR, a Class I and a Class II/III candidate. The Class I source likely dominates the mid-IR emission.

M17 EB and the M17 H II region, respectively (Figure 4.10). The final subsample excludes 135 candidate YSOs (Table 4.3) that either are unassociated with M17 or are associated with the extended molecular cloud complex to the southwest (Elmegreen & Lada 1976; Sanders et al. 1986). YSOs in the latter group are at the same distance as M17 and are associated with the M17 complex, but they belong to an additional extended YSO population that is beyond the scope of this work.

4.4.2 Star Formation in M17 EB and MC G15.9-0.7

4.4.2.1 YSO Mass Function

We constructed a mass function for the observed YSO population following a procedure employed previously by Shepherd et al. (2007) and Whitney et al. (2008). Using Equation 4.2, we assigned a χ^2-weighted probability for the stellar mass $M_\star$ of each well-fit model to a given candidate YSO. By summing over the probabilities of all well-fit models (defined by Equation 4.1) and normalizing to unity, we derived a probability distribution of $M_\star$ for each candidate YSO. This procedure is similar to that employed to find the probability distributions of evolutionary Stage (§4.3.1), but a finer binning was used. Results of fitting models to 62 sources in the extended M17 region (within the *white* boundary lines in Figure 4.10 but excluding the *white* rectangle) are presented in Table 4.2 (at the end of this Chapter). Ranges giving 95% confidence intervals for $M_\star$ and $L_{\rm TOT}$ (total bolometric luminosity, including luminosity produced by accretion) for each candidate YSO are listed in Table 4.2. Summing the probability distributions of $M_\star$ over the 62 sources in Table 4.2 produces the YSO mass function (YMF) plotted in Figure 4.11.

The YMF in Figure 4.11 exhibits, for intermediate-mass sources, the ubiquitous Salpeter (1955) power-law slope. The turnover for $M_\star \lesssim 3$ M$_\odot$ is not a real break in the YMF but instead reflects the incompleteness of our YSO sample with respect to the detection of lower-mass sources. A completeness limit of $\sim$3 M$_\odot$ is reasonable for the detection of disk-dominated sources. The [8.0] flux density of an A0 V photosphere with $M_\star = 3.2$ M$_\odot$, $T_{\rm eff} = 10,800$ K, and $R_\star = 2.5$ R$_\odot$ (Cox 2000) at 2.1 kpc is 3.9 mJy, or $\sim$1 dex above the nominal detection limit of the point-source Archive. The extended M17 field from which the YMF has been sampled exhibits neither high source confusion nor very bright diffuse 8 μm emission, hence our YMF represents a nearly complete sample of intermediate-mass IR excess sources that will become main-sequence types A0 or earlier.

We estimated the size of the larger YSO population represented by our intermediate-mass YSO

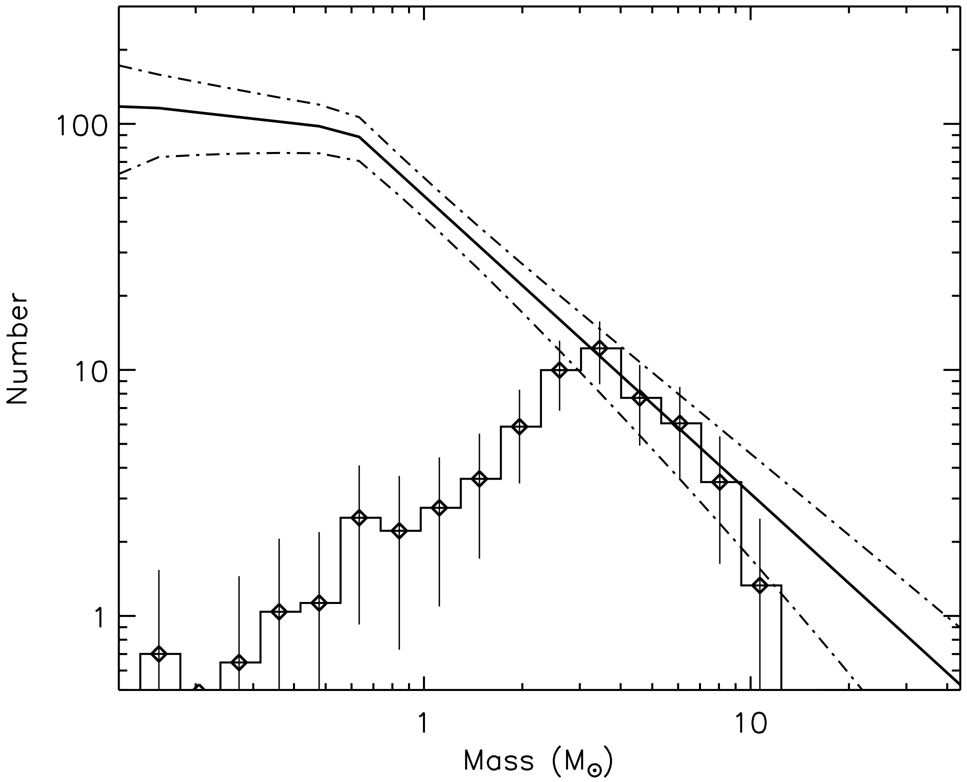

Fig. 4.11.— Mass function of the 62 candidate YSOs found inside the *white* boundary lines but outside the *white* rectangle in Figure 4.10 (histogram with error bars). The Orion Trapezium cluster IMF (Muench et al. 2002) has been scaled to match the mass function for ~3 M$_\odot$ < $M_\star$ < 8 M$_\odot$ (heavy curve with dash-dotted curves showing uncertainty envelopes).

sample by scaling the IMF of Muench et al. (2002) to fit the part of our YMF (3 $\lesssim M_\star \lesssim$ 8 M$_\odot$) where it is most complete (solid curves with dash-dotted uncertainty envelopes in Figure 4.11). This procedure generated a model IMF, $\xi(M_\star)$, for the YSO population. $\xi(M_\star)$ has a power-law slope of $\Gamma = -1.2 \pm 0.2$, as defined by

$$M_\star^\Gamma \propto \frac{d\xi(M_\star)}{d(\log M_\star)},$$

for $M_\star > 0.6$ M$_\odot$. After the break point, $\xi(M_\star)$ flattens to $\Gamma = -0.2 \pm 0.2$. Although the full Muench et al. (2002) IMF is a 4-part power law extending to brown dwarf masses, we use only $\xi(M_\star \geq 0.1$ M$_\odot)$ for consistency with the BFT07 results[6] (see §4.4.3 below). Integrating $\xi(M_\star \geq 0.1$ M$_\odot)$, we predict that the extended YSO population of M17 numbers 950 ± 90 and represents a total stellar mass of 750 ± 50

---

[6] Extrapolating down to the hydrogen-burning limit at 0.08 M$_\odot$ increases neither the total number of YSOs nor the total stellar mass by a significant amount.

$M_\odot$. *These values are lower limits.* We cannot be certain that our final YMF is 100% complete even for intermediate-mass sources. We treat any unresolved multiple sources as single YSOs, which means that we are generally sensitive only to the most luminous component of a multiple system, given that $L_{\rm TOT} \propto M_\star^\alpha$, with $\alpha > 2.5$ for PMS stars (Bernasconi & Maeder 1996). The mass determined from the YSO fits will be slightly higher than the most massive source in the beam but substantially lower than the combined mass of the sources (Whitney et al. 2008).

The YMF in Figure 4.11 contains candidate YSOs distributed throughout a large volume of space that cannot be regarded as members of any single cluster. The YMF is, however, drawn from a coeval stellar population comprising the most recent generation of star formation in the extended M17 target field (excluding YSOs associated with the central NGC 6618 cluster). Because these sources were selected on the basis of mid-IR excess emission, and a negligible fraction were fit with Stage III YSO models, the YMF population is characterized by optically-thick circumstellar disks and/or infalling envelopes. The disk destruction timescale is a decreasing function of the mass of the central star, with solar-mass YSOs losing their disks on timescales of $\lesssim$2 Myr (Haisch, Lada, & Lada 2001a). The intermediate-mass YSOs dominating our sample are expected to evolve more quickly, making them even younger.

4.4.2.2 Timescales of Evolutionary Stages and Lower Limit on Star Formation Rate

The duration of the Class I phase for YSOs in low-mass star formation regions is ~0.1 Myr (Kenyon & Hartmann 1995; Haisch, Lada, & Lada 2000). We can make an independent estimate of the duration of the Stage 0/I phase from the accretion ages of the well-fit models for each source. We define "accretion age" as $t_A = 10^{-6} M_\star/\dot{M}_{\rm env}$ [Myr]. The accretion age is a proxy for the evolutionary age t of a YSO, assuming both that $\dot{M}_{\rm env}$ is constant, on average, over t_A and that all of the accreting gas eventually reaches the central star. In reality, average accretion rates decrease with time, causing t_A to overestimate t, but accretion-driven outflows prevent 3–30% of the infalling gas from accreting (Richer et al. 2000), driving t_A in the opposite direction. Combining the probability distribution of t_A for the 25 candidate Stage 0/I YSOs in Tables 4.2 & 4.4, we find that t_A has a median value of 0.075 Myr, in good agreement with other estimates of Class I lifetimes.

Assuming a steady rate of star formation, the relative number of Stage II versus Stage 0/I YSOs gives the relative lifetime of each Stage. But we must take care to compare populations with similar mass distributions. Most YSOs fit by Stage I models have steep, Class I spectral indices, and even low-mass Stage 0/I YSOs can be bright in the mid-IR. Consequently, Stage 0/I sources disproportionately populate the YMF for $M_\star < 3$ M$_\odot$ (Figure 4.11), with the 12 Stage 0/I candidates in the YMF (Table 4.2) overrepresented at 1 M$_\odot \lesssim M_\star \lesssim 2$ M$_\odot$ compared to Stage II candidates. For $M_\star \gtrsim 3$ M$_\odot$, the YMF contains 5.6 times as many Stage II as Stage 0/I candidates, while this ratio is 2.6 for the entire mass range. The median Stage II disk lifetime in our sample is therefore $t_D = 5.6 t_A \sim 0.4$ Myr. The above calculations exclude the single Stage III candidate and 18 candidate YSOs with ambiguous Stage determinations in Table 4.2. Nearly all of the ambiguous candidates have model fits that are divided between Stage 0/I and Stage II models. In the limiting case where all ambiguous sources are treated as Stage II candidates, we have $t_D = 8.2 t_A \lesssim 0.6$ Myr. Intermediate-mass YSOs therefore lose their disks in less than half of the corresponding ∼1 Myr timescale observed for their solar-mass counterparts. This age differential tends to steepen the slope of the YMF compared to a disk-unbiased IMF, hence *the intermediate-mass YMF probably underestimates the true number of low-mass YSOs.*

The characteristic age of the source population in the YMF is $t_A + t_D \sim 0.5$ Myr. Using the stellar mass estimated from the IMF model, we arrive at a star formation rate (SFR) of 0.0016 M$_\odot$ yr^{-1} in the extended target field, which applies to M17 EB and the extended outer regions of the M17 molecular cloud. Due to the potential incompleteness and the bias against diskless sources inherent in the intermediate-mass YMF, this value must be regarded as a lower limit.

4.4.2.3 Triggered Star Formation in MC G15.9-0.7?

A concentration of star formation activity is observed in the vicinity of an IR dark cloud (IRDC) complex centered at $(l, b) = (15.55°, -0.45°)$. This region is shown in a composite GLIMPSE and MIPSGAL image in Figure 4.12. The bright, filamentary 8 μm emission slicing diagonally through this image, part of which makes up a previously identified optical reflection nebula, outlines the rim of M17 EB where it intersects MC G15.9-0.7 (Figure 4.1). Because significant concentrations of candidate YSOs are observed on the bubble rim while no group of candidate YSOs is reliably detected in the adjacent regions of MC G15.9-0.7 (Figure 4.10), the situation is strongly suggestive of star formation triggered by the expansion of M17 EB. The morphology of the IRDCs, bright 8 μm emission, and CO emission provides evidence for increased gas density resulting from the compression of the cloud.

The SED of G015.6653-00.4989, a bright 24 μm source in MC G15.9-0.7 (Figure 4.12), is very similar to the SEDs of several massive protostars associated with molecular outflows identified by Shepherd et al.

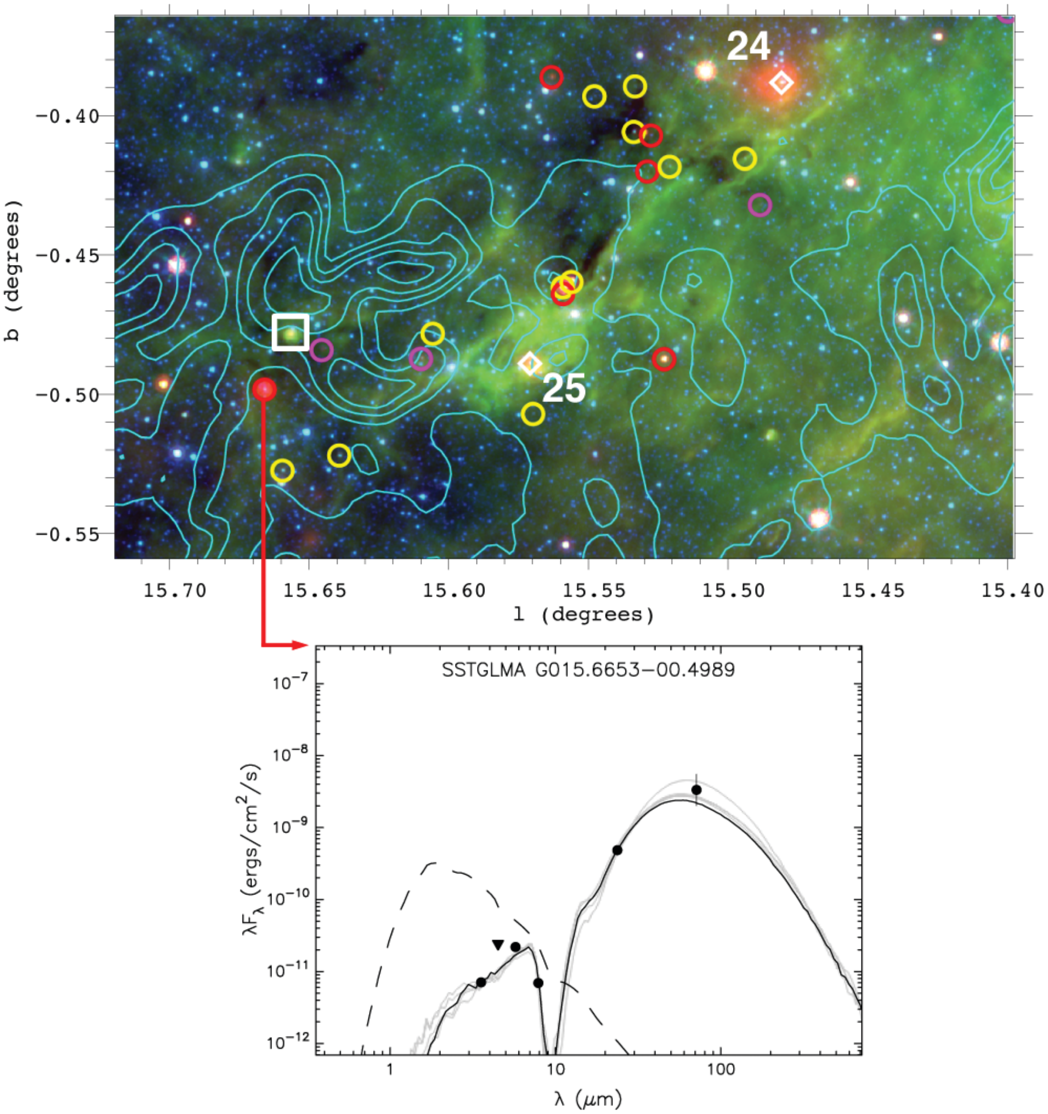

Fig. 4.12.— Image showing part of the interface between M17 EB and MC G15.9-0.7 (IRAC [4.5]=*blue*, IRAC [8.0]=*green*, MIPS [24]=*red*). The *cyan* contours are ^{12}CO emission at v = 19 km s^{-1}. The rim of the bubble M17 EB is delineated by the bright *green* filament of 8 μm emission crossing from the lower-left to the upper-right corner of the image. Candidate YSOs are overplotted as in Figure 4.10. Two candidate OB stars associated with diffuse 24 μm emission are marked by *white* diamonds and numbered as in Table 4.5. The candidate Stage 0/I YSO G015.6653-00.4989 (E55 in Table 4.2) is highlighted, and the model fits to its SED are plotted. The [4.5] flux was used as an upper limit to the fitting and is plotted as a triangle. The *dashed* curve shows the reddened photosphere of the central star as it would appear in the absence of circumstellar material.

(2007). It is characterized by excess emission at 4.5 μm (an outflow signature) and a very red IR spectral index peaking near 70 μm (this object is the brightest 70 μm point source detected in the M17 target field). The models fit to this source (E55 in Table 4.2) indicate a luminous candidate protostar with mass 7 $M_\odot \leq M_\star \leq 8\ M_\odot$ and luminosity 400 $L_\odot \leq L_{\rm TOT} \leq 10^3\ L_\odot$ accreting from its circumstellar envelope at a high rate of $2\times10^{-4}\ M_\odot\ {\rm yr}^{-1} < \dot{M}_{\rm env} < 8\times10^{-4}\ M_\odot\ {\rm yr}^{-1}$. The accretion age of this candidate protostar is $t_A < 0.04$ Myr. A nearby resolved, compact, red IR source (in the *white* box in Figure 4.12) is associated with a second 70 μm point source. The SED of this source cannot be fit well by any YSO model, and we speculate that it may be either a luminous binary YSO or a compact cluster. Both sources are apparently located in the cloud region compressed by M17 EB.

Also shown in Figure 4.12 are 2 compact, resolved sources of 24 μm emission ($30''$–$60''$ in size) that are not associated with any candidate YSO. This emission suggests a localized region of heated dust, and the most likely heat source is a massive young star or cluster. Five such 24 μm sources are observed in the M17 target field, and none are found in the control field. At the center of every 24 μm source lies a GLIMPSE Archive source with an SED consistent with a hot stellar photosphere. Following the method pioneered by Watson et al. (2008), we estimated the spectral types of these stars by employing the RW07 model fitting tool to fit Kurucz (1993) stellar atmospheres (including hot photospheres up to $T_{\rm eff} = 50,000$ K) to available $BVJHK_S$+IRAC photometry. We found that all of the stars associated with compact 24 μm emission have luminosities consistent with B or late O stars, assuming they are associated with M17 at either a distance of 1.6 kpc or 2.1 kpc (see Table 4.5). Because these stars exhibit little or no IR excess emission in the 2MASS/GLIMPSE bands, they either have already cleared out the inner regions of their circumstellar disks or have dissipated their disks entirely. The observed 24 μm emission could arise from remnant disk material or heated dust in the surrounding molecular cloud at distances of $\sim$2–5 $\times\ 10^4$ AU from the central star. This interpretation suggests that some of these stars may ionize low-luminosity compact H II regions that have not been detected by previous surveys (e.g. Wood & Churchwell 1989). None of these sources is detected by the high-resolution CORNISH survey at 6 cm (Purcell, Hoare, & Diamond 2008), indicating that any gas ionized by these B stars is diffuse enough to be resolved out by the VLA in the B configuration. This rules out the presence of hypercompact or ultracompact H II regions around the stars. The most extended of these 24 μm sources, associated with star 24 (Figure 4.12, Table 4.5), is associated with 11 cm radio emission (Reich et al. 1990) and enclosed by a partial ring of 8 μm emission at a projected distance of 0.5 pc from the star, suggesting a small H II region and PDR.

Whatever the interpretation of the physical origin of the 24 μm sources, the circumstellar environments of the associated OB stars are significantly more evolved than those of the candidate YSOs, which exhibit IR excess emission at wavelengths $<$10 μm. The comparison of star 25 with YSO E55, the candidate protostar in Figure 4.12, is particularly interesting. These two sources have comparable masses ($\sim$10 $M_{\odot}$; E55 is still gaining mass through accretion) and are apparently located within the same molecular cloud, but they occupy strikingly different phases of early massive stellar evolution, suggesting a difference in age comparable to the disk destruction timescale derived above, $t_D \sim 0.4$ Myr. This difference in age could be explained naturally by triggered star formation. The more evolved B star lies in the midst of the 8 μm emission defining the inner rim of M17 EB, while the young candidate protostar is located in a region of the molecular cloud that has only recently been overtaken by the expanding bubble. The expansion velocity of the bubble implied by this scenario is slow, a few km s^{-1} at most, which is consistent with the non-detection of an expansion signature in the CO line (§4.4 above).

4.4.3 The M17 Molecular Cloud and H II region

The contours in the top panel of Figure 4.8 show a 90-cm Very Large Array (VLA) radio image (Brogan et al. 2006) delineating the extent of the ionized gas associated with the main M17 H II region. The densest part of the M17 molecular cloud is located in M17 South (see Figure 4.1) along the interface between the H II region and the bright ^{13}CO ($J = 2 \rightarrow 1$) emission (colored *red-white* in Figure 4.8). The total gas mass (molecular and atomic) contained in the main M17 molecular cloud is $\sim 6 \times 10^4$ $M_{\odot}$, found by integrating the column density traced by the CO emission. The H II region occupies a cavity cleared of molecular gas between M17 North and M17 South. The morphology of the CO emission from M17 closely resembles the maps of the region obtained by Wilson, Howe, & Balogh (1999), but the older maps have slightly lower resolution and do not include M17 EB. The cavity in the molecular cloud has been sculpted by the winds and radiation of the O stars in NGC 6618 (Chapter 2).

4.4.3.1 Prominent Massive Stars

The spectral classifications derived from SED fits to 27 prominent OB stars in the M17 target field are presented in Table 4.5. We fit Kurucz (1993) stellar atmospheres to the broadband fluxes of 11 of the 16 known O stars in NGC 6618 that have reliable, unsaturated fluxes in the GLIMPSE Archive to estimate their

Table 4.5. Selected OB Stars Associated with M17

Index No.[a]	Name[b]	l (deg)	b (deg)	Cataloged Sp. type[c]	Spectral Type from SED $d = 1.6$ kpc	Spectral Type from SED $d = 2.1$ kpc	A_V (mag)
O Stars in NGC 6618							
1,2[d]	CEN 1a,b	15.0562	-0.6884	O4+O4 V	⋯	⋯	⋯
3	CEN 43	15.0533	-0.7045	O3–O5 V	O4–O5 V	O5+O5 V	12.3
4	CEN 2	15.0731	-0.7004	O5 V	O5.5 V	O5.5+O7 V	5.2
5	CEN 37	15.0559	-0.6883	O3–O6 V	⋯	⋯	⋯
6	OI 345	15.0110	-0.7020	O6 V	⋯	⋯	⋯
7	CEN 18	15.0812	-0.6569	O6–O8 V	O6 V	O6+O7.5 V	7.6
8	M17-S3	15.1032	-0.6487	⋯	O7 V	O5 V	11.2
9	CEN 25	15.0673	-0.6879	O7–O8 V	O9 V	O6.5 V	8.0
10	OI 352	14.9945	-0.7486	O8 V	O5.5+O5.5 V	multiple[e]	∼7
11	OI 174	15.1325	-0.5257	O9 V	O6 V	O4 V or O6+O7 V	7.0
12	CEN 3	15.0658	-0.7084	O9 V	O7 V	O5 V or O7+O7 V	3.7
13	CEN 16	15.0748	-0.6460	O9–B2 V	O9.5–B0.5 V	O8 V or B0+B0 V	5.9
14	CEN 61	15.0594	-0.6884	O9–B2 V	O9 V	O6.5 V or O9.5+O9.5 V	9.9
15	CEN 27	15.0433	-0.6950	O9 V	B1 V	O9 V	∼9.5
16	CEN 31	15.0759	-0.6534	O9.5 V	⋯	⋯	⋯
Candidate OB Stars in NGC 6618PG							
17	BD-16 4831	15.3213	-0.7758	O+	O5.5 V or O9 III	O4 V or O7 III	4.4
18[f]	BD-16 4826	15.2604	-0.7263	O5	O5.5 V or O9 III	O5 V or O6.5 III	3.9
19	BD-16 4822	15.2244	-0.6796	B...	O8.5 V	O6.5 V	2.9
20	TYC 6265-1174-1	15.1882	-0.7598	B0	B1 V	O9 V	3
21	HD 168585	15.2855	-0.7498	B7–B8 II	B1 V	O9 V	1.6
Candidate OB Stars Associated with 24 μm Emission in M17 EB							
22[g]	ISOGAL YSO	15.3320	-0.7174	⋯	late B V	B1.5 V	2.1
23[h]	TYC 6265-347-1	15.3583	-0.6543	O...	B2 V	B1 V	2.6
24	BD-15 4928	15.4801	-0.3889	B	B0.5 V	O8 V	2.8
25		15.5702	-0.4895	⋯	B1 V	B0.5 V	∼4.8
26	TYC 6265-2079-1	15.5900	-0.8268	O...	B4 V	B2 V	1.7

Note. — All O stars in NGC 6618 are *Chandra* point sources (BFT07). The only star in NGC 6618PG that has been observed by *Chandra*, No. 20, is also an X-ray point source.

[a] OB stars in each of the first two groups are listed in order of decreasing luminosity, while the candidate B stars in the final group are listed in order of increasing Galactic longitude.

[b] CEN is Chini, Elsässer, & Neckel (1980), and OI is Ogura & Ishida (1976). SWB M17-3 is a recently-discovered O star driving a stellar wind bow shock (Chapter 3). Other identifiers are from SIMBAD.

[c] Spectral types for NGC 6618 are from OI, CEN, Hanson, Howarth, & Conti (1997), and H08; others are from SIMBAD.

[d] CEN 1a,b refer to the main components of an apparent O4+O4 visual binary that are saturated and marginally resolved by IRAC. CEN 1a,b each are spectroscopic binary systems with nearly equal-luminosity components (H08).

[e] At 2.1 kpc, the SED fits to OI 352 return a radius larger than that of an O supergiant. It may be an unresolved multiple O system (see text).

[f] BD-16 4826 is a *ROSAT* point source (Dunne et al. 2003).

[g] This source, ISOGAL-P J182108.8-155658 from the catalog of Felli et al. (2002), exhibits a marginal IR excess at 5.8 μm and is not detected as a point source at 8.0 μm.

[h] This source exhibits an IR excess at 8 μm.

spectral types. Although all known O stars in NGC 6618 except No. 8 have previously reported spectral types from optical and near-IR spectroscopy and photometry (Ogura & Ishida 1976; Chini, Elsässer, & Neckel 1980; Hanson, Howarth, & Conti 1997; H08), mid-IR photometry offers the advantage of a relatively extinction-independent determination of the luminosity in the Rayleigh-Jeans regime of the stellar SED. We incorporated available B, V photometry (Ogura & Ishida 1976; H08) into each SED to obtain more reliable estimates of A_V toward each star than would be possible from the 2MASS photometry alone. Because the optical-IR SED shape does not vary significantly for stars earlier than B3, the A_V derived from our SED fitting is independent of adopted distance. As shown in Table 4.5, our SED-based luminosity classification at 1.6 kpc agrees with previously reported spectral types to within 2 subclasses for 8 of the O stars analyzed in NGC 6618. This might seem surprising, given that the most recent distance determination found that M17 cannot be significantly nearer than 2 kpc (H08). However, previous photometric determinations of spectral type assumed that each source was a single star, and our method shares the same systematic bias with respect to distance. Even spectroscopic determinations have generally neglected multiplicity, and the resulting spectrophotometric distance estimates contributed to the wide adoption of the 1.6 kpc distance.

Revising the distance from 1.6 to 2.1 kpc multiplies the luminosity of every star in Table 4.5 by 1.7. This factor of $\sim$2 is suggestive. The majority of O stars in clusters have been observed to be in near-equal-mass binary systems (Sana et al. 2008; Mason et al. 2009). H08 found that each component of the historical O4+O4 binary CEN 1, the most luminous star system in M17, is itself a spectroscopic binary with approximately equal-luminosity components and suggested that several other known O stars in NGC 6618 could also be unresolved binaries. Assuming the stars in Table 4.5 are at 2.1 kpc, we find that the majority of O stars in NGC 6618 are far more luminous in the mid-IR than expected from the cataloged main-sequence spectral types. Three of these stars, CEN 43, CEN 2, and CEN 18, each have mid-IR luminosities exceeding an O3 V star. Three others, OI 174, CEN 3, and CEN 61, are unlikely to be single main-sequence stars because their SED-derived spectral types are > 2 subclasses earlier than their cataloged spectral types (Table 4.5). Because NGC 6618 is very young and even O4 V stars take $\sim$4 Myr to evolve off the main sequence (Bressan et al. 1993), it is unlikely that the massive stars in NGC 6618 are giants. We therefore give binary classifications for the over-luminous stars in Table 4.5, with spectral types estimated for each component assuming (1) that the components have nearly equal masses and (2) that their combined light yields the cataloged or SED-derived spectral type for a single star at 1.6 kpc.

We stress that our spectral typing for each component of the binary systems is not definitive, but the high fraction of candidate binary systems is a robust result.

At 2.1 kpc, one source, OI 352, has mid-IR luminosity equivalent to a binary O3+O3 V system. If this were the true classification, then OI 352 would compete with CEN 1a,b for domination of the H II region, but in fact OI 352 is located in an unremarkable part of the nebula, outside the central wind-dominated cavity (Townsley et al. 2003, Chapter 2). We therefore speculate that this star, like CEN 1, could be a multiple system of 3 or more later-type O-dwarfs. BFT07 report an unusually hard (4.4 keV) thermal component from their plasma fits to the X-ray spectrum of OI 352. Strong shocks produced by colliding-wind binaries are the most promising explanation for O stars with >1 keV hard X-ray emission. CEN 1a,b, CEN 43, CEN 2, and CEN 18 all produce hard X-ray emission (BFT07), and all are identified as candidate binaries by H08 and/or by our SED fitting, with primaries of type O6 V or earlier. CEN 25, a solitary O6.5 V star, lacks hard X-ray emission. In contrast, OI 174, CEN 3, and CEN 61 are likely binary systems with primaries of type O6 V or later, and these systems have only soft-component X-ray spectra. Evidentally hard X-ray emission is not a ubiquitous property of massive binary systems, but this phenomenon may be more common in earlier-type binaries. CEN 16 seems anomalous, for although it boasts a very hard X-ray spectrum (3.5 keV), it is among the least luminous candidate O stars, equivalent to an early B binary system (Table 4.5).

4.4.3.2 Comparison of X-ray Sources with GLIMPSE YSOs

The *white* box in the bottom panel of Figure 4.10 outlines the field observed to date by *Chandra* (Townsley et al. in prep., Broos et al. in prep.). BFT07 presented 886 X-ray point sources extracted from the first *Chandra* Advanced CCD Imaging Spectrometer (ACIS) observation of M17. By scaling the X-ray luminosity function (XLF) of the Orion Trapezium Cluster to match the XLF of the M17 sources, BFT07 estimated a total young stellar population of 8,000–10,000 members (to a limiting mass of 0.1 $M_\odot$) in the NGC 6618 cluster and its immediate vicinity in M17. BFT07 assumed a distance of 1.6 kpc, and scaling their XLF to 2.1 kpc increases the total population to 11,000–14,000 stars and YSOs.

Of the 195 candidate YSOs in our M17 subsample (Table 4.1), only 34 fall within the $17' \times 17'$ field of the ACIS observations. This number would be many times higher if not for the presence of extremely bright diffuse mid-IR emission from the H II region and PDR that drastically reduces the point-source sensitivity in all IRAC bands. The source density in the GLIMPSE Archive within the ACIS field analyzed by BFT07 is 107,000 deg^{-2}. This is only ∼50% of the average density of Archive sources in the larger M17 target field (see Table 4.1), *despite* the fact that the ACIS field contains the dense center of the NGC 6618 cluster. Because of this incompleteness, we cannot attempt any meaningful quantification of the YSO population most directly associated with NGC 6618. X-ray observations, by contrast, do not suffer from the deleterious effects of bright backgrounds, and moreover the (near-axis) spatial resolution of ACIS is higher than that of IRAC. Because very different physical mechanisms are responsible for X-ray versus IR emission from young stars, we are interested in learning whether the IR-excess sources selected for our YSO sample represent a subsample of the X-ray-selected population or a distinct population.

Preibisch et al. (2005) performed a detailed analysis of the X-ray source population observed as part of the *Chandra* Orion Ultradeep Project (COUP). They found that the 838.1-ks COUP observation detected 100% of the known young F- and G-type young stars and YSOs in Orion but only ∼50% of A-type stars. Preibisch et al. (2005) concluded that the X-ray emission observed in the low-mass stars in the COUP sample is consistent with an origin in stellar coronae analogous to the solar corona, but at a considerably higher level of activity. The disappearance of solar-type convective envelopes in more massive stars on the main sequence could explain the drop in the COUP completeness for intermediate-mass stars.[7] Preibisch et al. (2005) also observed that X-ray emission in T Tauri stars is partially suppressed by accretion. As we have shown, our IR-selected sample of candidate YSOs is highly sensitive to intermediate- to high-mass objects that are still accreting via circumstellar disks and/or envelopes. We therefore expect that our YSO sample complements the (much larger) X-ray-selected sample, as we preferentially select the YSOs that are the most likely to be missed by *Chandra*.

We have correlated our final YSO sample with an updated X-ray source catalog covering the entire area observed to date by *Chandra*/ACIS, with 400 ks total integration time (Broos et al. in prep). Out of the 34 candidate YSOs in the overlap region, 14 have X-ray counterparts. The 95% confidence intervals for $M_\star$ and $L_{\rm TOT}$, along with the evolutionary Stage derived from the well-fit (Equation 4.1) YSO models, are given in Table 4.4 for each source. The sources in Table 4.4 exhibit no obvious trends in mass, luminosity, or evolutionary Stage with which to distinguish candidate YSOs with X-ray counterparts from those without. The majority of the candidate YSOs in Table 4.4 are fit with models of intermediate to high stellar mass

---

[7] Microshocks in OB stellar winds are believed to be the primary source of soft X-ray emission from massive stars; this very different from the emission mechanism operating in low-mass stars.

corresponding to spectral types A and B on the main sequence. There may be a slight preference for less-evolved sources with higher accretion rates in the X-ray quiet population in Table 4.4, but this is not significant, given the small sample size. Intrinsic X-ray variability may play a role in determining which YSOs are detected. It is also possible that some of the luminous YSOs with ACIS detections are themselves X-ray quiet but possess binary companions that are X-ray bright. *There is no evidence that the 34 candidate YSOs listed in Table 4.4 represent a distinct population from the X-ray-selected sources.*

Two interesting candidate massive YSOs are located near the peak molecular gas density of M17 South and the interface with the H II region, shown in Figure 4.13. One, the KW Object, is a binary system. A candidate Herbig Be star is the more luminous component (KW-1) and dominates the IR emission (J02; Chini et al. 2004a). The lower-luminosity component (KW-2) is X-ray bright (BFT07) but unresolved in our IR survey data, hence the KW Object is considered an X-ray detected source (X4) in Table 4.4. KW-1 is saturated in the GLIMPSE and MIPSGAL images, so models were fit to its 2MASS and *MSX* fluxes only. The model fits indicate a central star of $M_\star \sim 10$ M$_\odot$ and $T_{\rm eff} \sim 26,000$ K, consistent with an early B star and in good agreement with the findings of Chini et al. (2004a). The models indicate that the star may have a substantial circumstellar disk (0.01 M$_\odot \leq M_{\rm disk} \leq 0.3$ M$_\odot$) with a large inner hole of radius ∼40 AU (∼10 times the dust sublimation radius). The inner hole is responsible for the precipitous rise in the near- through mid-IR SED (Figure 4.13) and indicates that the central star has ceased accreting material from the disk. Our model SEDs produce a broad 9.7 μm silicate feature in emission, but ISOCAM spectra presented by Chini et al. (2004a) show that the "bumps" in the SED near 8 and 11 μm are actually due to PAH emission features excited by the hot, central star. We have therefore used the *MSX* A and C bands as upper limits to the SED fitting, since these bands contain PAH features that increase their flux with respect to the continuum provided by the YSO models. The 1-D envelope model employed by Chini et al. (2004a) predicts the silicate feature in absorption and does not explicitly include a disk. These authors report a total circumstellar mass of 10 M$_\odot$ within 0.1 pc from the star. The total mass and envelope radius are very difficult to constrain in the absence of mm/sub-mm data, hence we cannot confirm these reported values.

The other prominent candidate YSO highlighted in Figure 4.13, G014.9791-00.6651, is resolved by IRAC. This source, NX5 in Table 4.4, is not detected in X-rays. Like KW-1, NX5 is massive ($M_\star \sim 10$ M$_\odot$), but it may be somewhat less evolved. The parameters of the 47 well-fit models poorly constrain the

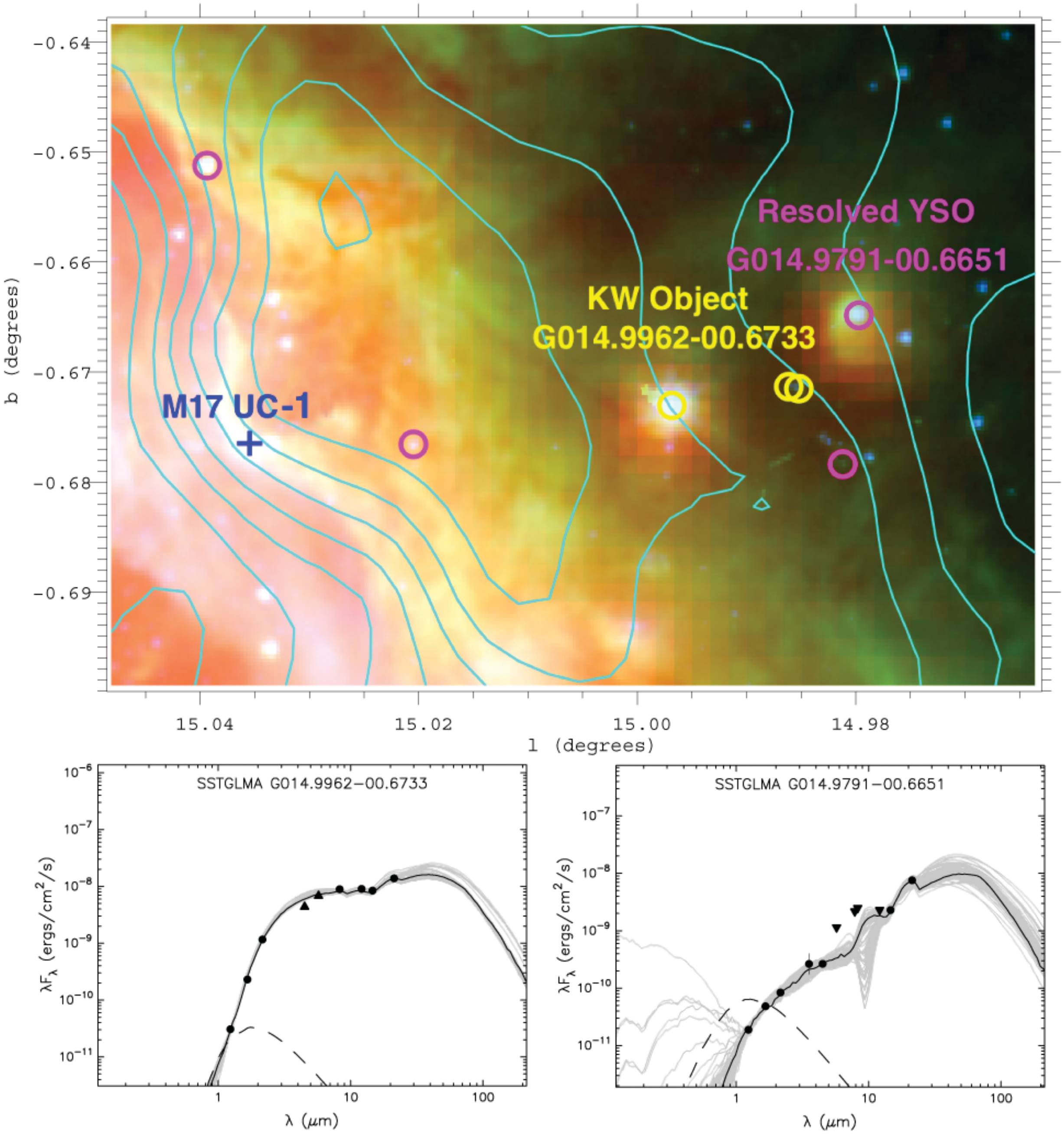

Fig. 4.13.— Region containing the peak molecular gas density in M17, near the H II region–PDR interface. The image combines IRAC [4.5] (*blue*) and [5.8] (*green*) with *MSX* E (21.3 μm; *red*). The *cyan* contours are the HHT ^{13}CO moment 0 map from the *top* panel of Figure 4.8. Candidate YSOs are overplotted as circles using the color scheme of Figure 4.3. The ultracompact H II region M17 UC-1 is marked. The KW Object (*left*) and neighboring resolved YSO (*right*) are also highlighted, and the model fits to their SEDs are plotted as in Figure 4.12. Fluxes used as upper or lower limits for the model fitting are plotted as downward- and upward-pointing triangles, respectively.

circumstellar environment of NX5, allowing for a wide range of both $M_{\rm disk}$ and $\dot{M}_{\rm env}$, so the evolutionary Stage is ambiguous, split between 60% Stage II and 40% Stage 0/I models. The resolved outer envelope of this star is large, with radius $\sim10^5$ AU, and the SED exhibits the signatures of a PAH spectrum. As with our modeling of KW-1, we set the bands most affected by PAHs as upper limits for the model fitting, and the majority of well-fit models cluster around $T_{\rm eff} \sim 23,000$ K, hot enough for the star to produce sufficient UV radiation to excite PAHs in its circumstellar material. Together with M17 UC-1, the nearby hypercompact H II region that is excited by a B0 star (Sewilo et al. 2004), KW-1 and NX5 are 3 very luminous YSOs with very similar stellar masses but with very different circumstellar environments. This demonstrates that, in spite of their close proximity to each other, these 3 sources are not precisely coeval.

4.4.3.3 Challenges of Identifying Cluster Members and Determining the Age of NGC 6618

The fraction of stars exhibiting IR excess emission due to circumstellar disks is a diagnostic of the age of embedded clusters (Haisch, Lada, & Lada 2001b). BFT07 find that only ~10% of the sources in their X-ray selected sample exhibit IR excesses. This fraction is very low in comparison to recent results using IR-selected source samples. J02 found a JHK excess fraction of 53% in the central regions of the NGC 6618 cluster, and H08 reported a 74% excess fraction from deeper $JHKL$ observations of a similar field. Some variation in excess fraction is inevitable due to differences in sample selection, and excess fractions measured in the $JHKL$ color plane are expected to be higher than those in the JHK color plane. The low excess fraction reported by BFT07 is partially explained by selection biases against embedded sources and against low-mass sources, both of which are fainter in X-rays. To gain depth beyond the 2MASS and GLIMPSE catalogs, BFT07 correlated their X-ray sample with SIRIUS JHK_S photometry presented by J02, hence the difference between the excess fractions reported by these two works reflects the different selection criteria and analysis techniques rather than differences in IR photometry.

The large discrepancy between reported IR excess fractions reflects a more basic issue: The M17 H II region is a difficult place to search for YSOs. The diffuse IR emission is bright at all wavelengths with a steep red spectral index and exhibits complex morphological structure on multiple spatial scales (Chapter 2). This makes reliable mid-IR photometry difficult even for bright sources and impossible for faint ones. Nebular structures can be mistaken for IR excess emission associated with stars. As noted in Chapter 3, two of the high-mass Class I sources identified by Nielbock et al. (2001) are actually mid-IR emission from stellar-wind bow shocks that could be mistaken for circumstellar disks. Lada et al. (1991) claimed that the majority of high-mass stars in NGC 6618 display JHK excess, but this was disputed by H08. Among the O stars in NGC 6618 detected by GLIMPSE, all are detected at wavelengths as long as 4.5 μm and many are detected at 8.0 μm, but we can state with high confidence that none displays an IR excess, with the possible exception of star No. 8 in Table 4.5, which is associated with a third mid-IR bow shock (Chapter 3).

Near-IR photometry can be more reliable, because the diffuse emission is less bright. But $JHKL$ observations are challenged by the large spatial variations in interstellar extinction across the M17 cloud (see the A_V values in Table 4.5, for example). While the extinction due to molecular gas in the M17 North and South cloud components is generally $A_V > 15$ mag, and the dense core of M17 South produces $A_V > 90$ mag, the average extinction through the central cavity is $A_V < 15$ mag (Figure 4.9). The average extinction observed toward the ionizing stars of the M17 H II region is $A_V \sim 8$ mag (Table 4.5; Chini, Elsässer, & Neckel 1980; Hanson, Howarth, & Conti 1997; H08). The foreground extinction to the cloud is $A_V \sim 2$ mag (Pellegrini et al. 2007; H08). We thus deduce that the column density of the M17 cloud is divided into approximately equal halves behind ($A_V \sim 7$ mag) and in front ($A_V \sim 6$ mag) of the H II region. Including foreground extinction, the total extinction along a typical line-of-sight through the cavity is $A_V < 17$ mag, or $A_K < 2$ mag. Hence background stars are detectable even in relatively shallow near- and mid-IR observations along the line of sight through the central cavity and the ionizing cluster. In contrast, adjacent dense regions of the M17 North and South cloud components produce sufficient extinction to screen out background stars against even deep near-IR observations. Because of this complex extinction morphology, there is no comparable nearby field that can be used to estimate the background contamination in observations of NGC 6618. Any attempt to measure accurately the disk fraction or low-mass IMF in NGC 6618 must overcome this significant challenge.

A major strength of X-ray observations is the ability to separate young cluster members, which are 2–3 orders of magnitude brighter in X-rays than older main-sequence or evolved stars, from the field star population (BFT07 and references therein). The contamination from unassociated sources in the X-ray sample of the M17 young stellar population is therefore very low, <5% (BFT07). J02 recognized the difficulty in using their off-cluster field to correct for source contamination and instead used a Galactic disk population synthesis model. While we are not in a position to verify their results, the conservative upper limit of 3 Myr on the cluster age derived by J02 is reasonable. H08 assumed that all stars with IR excess, and by extension all sources with reddening equivalent to $A_V \gtrsim 10$ mag, were cluster members. H08 therefore concluded that the M17 molecular cloud behind NGC 6618 was opaque. Both the assumption and the conclusion were not valid. The extinction through the central cavity is relatively low ($A_K < 2$ mag) and the deep observations used by H08 detected stars as faint as $K = 20.1$ mag and $L = 15.6$ mag. The sample of H08 therefore contains a potentially large fraction of background stars, casting doubt upon the reported disk fractions and the correspondingly young age of 0.5 Myr claimed for the M17 stellar population.

It is tempting to conclude that the inclusion of diskless field stars in a magnitude-limited sample of the M17 young stellar population would decrease the measured IR excess fraction. But stars with disks are not well-separated from reddened stellar photospheres in the JHK or even in the $JHKL$ color-color diagrams (Whitney et al. 2003b; Robitaille et al. 2006). Color-color spaces or SEDs that include photometry at 4.5 μm and longer wavelengths provide a significantly more reliable means for distinguishing circumstellar extinction from interstellar extinction. Of the 64 candidate X-ray emitting protostars identified by BFT07 (their Table 7) most of them on the basis of the $K - [3.6]$ color (analogous to $K - L$), only 3 were selected as YSOs by our more conservative multiband SED fitting (see Table 4.4), but 16 were well-fit by reddened stellar photospheres (the remaining sources are detected in too few 2MASS/GLIMPSE bands to be fit reliably with SED models). Highly-reddened contaminating sources that are intrinsically red, such as the numerous red giants in the Galactic plane behind the M17 H II region, are the most difficult to separate from YSOs on the basis of $JHKL$ colors alone. If correction for contamination is not done, then highly-reddened, background red giants may provide a significant number of *false* IR excess sources. This would artificially increase the derived disk fraction, leading to an underestimate of the cluster age.

We are left without a strong constraint on the age of the M17 young stellar population. There is a population of PMS stars lacking inner disks (BFT07), and there is also ample evidence for ongoing star formation (Nielbock et al. 2001, J02, this work). The preponderance of observational evidence indicates that M17 has not formed all of its stars simultaneously, but has experienced continuous or episodic star formation over a period of <3 Myr. Sources like the candidate massive YSOs and M17 UC-1 shown in Figure 4.13 are almost certainly younger than 0.5 Myr, the average age of the extended YSO population (§4.4.2 above). To minimize the impact of the lingering age uncertainty, we adopt a mean age of ∼1 Myr for the young stars and YSOs in NGC 6618 and the surrounding molecular cloud.

We can use the BFT07 results to make an estimate of the star formation rate (SFR) that has produced the ionizing cluster of M17 and its entourage of YSOs. Scaling the stellar initial mass function (IMF) measured by Muench et al. (2002) for the Orion Trapezium Cluster to the 11,000–14,000 stars in M17, we arrive at a total mass in stars of 8,000–10,000 $M_\odot$. Stars have been forming in M17 at an average rate of 0.008–0.01 $M_\odot$ yr^{-1}.

4.5 A History of Propagating Massive Star Formation

We have shown that the major sites of star formation in the extended M17 region are located around the rim of the large bubble M17 EB. We will now examine the structure and possible origins of M17 EB and show that the beginnings of a plausible star formation history of M17 are found within this bubble.

4.5.1 The Origin of M17 EB

The most likely production mechanisms for a bubble the size of M17 EB are the expansion of an H II region or a supernova explosion, both of which are expected to occur in regions of massive star formation. We favor the H II region interpretation. The morphology of the mid-IR emission outlining M17 EB is similar to that of other 8 μm bubbles outlining the PDRs of H II regions (Churchwell et al. 2006; Watson et al. 2008). One of the best ways to discriminate between H II regions and supernova remnants (SNRs) is by the radio continuum spectral index. H II regions are filled with thermal emission from ionized gas and exhibit a flat spectral index for optically thin radio emission, while SNRs are often characterized by steep, non-thermal spectral indices from synchrotron emission (e.g. Brogan et al. 2006). M17 EB is included in two single-dish radio Galactic plane surveys of comparable spatial resolution. Images at 3 cm from the Nobeyama 45-m telescope (HPBW=2.7′; Handa et al. 1987) and at 11 cm from the Effelsberg 100-m telescope (HPBW=4.3′; Reich et al. 1990)[8] show a plateau of radio continuum emission that fills the half of M17 EB farthest from M17 (other half is dominated by emission from the M17 H II region itself) and drops sharply at the location of the 8 μm emission outlining M17 EB. Comparison of the 3 cm and 11 cm surface brightnesses at various points in the interior of M17 EB shows that the radio continuum flux density is approximately constant (with a typical value of ~50 mJy) over this wavelength range, consistent with a flat, thermal emission spectral index.

One caveat regarding the interpretation of the radio emission within M17 EB should be kept in mind. The non-thermal emission from SNRs eventually fades (on the order of a few 10^5 yr) to the point

---

[8] See http://www.mpifr-bonn.mpg.de/survey.html.

of becoming indistinguishable from the background. The residual thermal emission from the parent H II region lasts much longer. Hence, we cannot rule out the possibility that a supernova has occurred within M17 EB. But because the observed thermal radio emission completely fills the bubble, there is no need to invoke a supernova explosion to explain its origin.

A search of SIMBAD objects with coordinates inside M17 EB reveals a group of 5 stars with OB spectral classifications. Although a few of these stars have proper motion estimates (Høg et al. 2000), none have parallax distances. The spectral types of these sources listed in the SIMBAD database are of unknown provenance and questionable quality, so while we list the catalogued spectral types for reference in the lower 2 sections of Table 4.5, we trust the classifications only to the extent that they identify hot stars. Again following Watson et al. (2008), we fit SEDs generated from Kurucz (1993) stellar atmospheres to available B, V, 2MASS, and GLIMPSE fluxes of these stars, and we find that their IR luminosities are consistent with very early spectral types at either 1.6 kpc or 2.1 kpc (Table 4.5). If the stars were at a significantly different distance, their SEDs would be inconsistent with early-type stars. We therefore suggest that these stars are the 5 most massive members of NGC 6618PG, the ionizing cluster driving M17 EB (Figs. 4.14 and 4.15).

The OB stars of NGC 6618PG are significantly less reddened ($A_V \leq 5$ mag) than the O stars in NGC 6618, as expected since NGC 6618PG is located in a much more diffuse H II region. NGC 6618PG is associated with both Hα emission and *ROSAT* soft X-ray emission (Dunne et al. 2003). The soft X-ray emission is also apparent in an archival *Einstein* observation taken 13 years earlier than the *ROSAT* survey. Significant differences in morphology between these 2 images show that the X-ray emission is variable on $\lesssim$10-yr timescales. We therefore infer that the emission is dominated by unresolved X-ray-bright point sources; these are the young stars of the NGC 6618PG cluster. High-resolution X-ray observations of the interior of M17 EB with *Chandra* or *XMM-Newton* are needed to separate individual cluster members from field stars and to detect any truly diffuse X-ray emission.

The NGC 6618PG cluster must be significantly more evolved than NGC 6618 because, even in the absence of bright diffuse mid-IR emission from the interior of M17 EB, we do not detect *any* candidate YSOs above the background level in the vicinity of the candidate ionizing stars and X-ray emission. Given that elsewhere in the target field we detect at least a few solar-mass stars with optically thick disks, the absence of candidate YSOs means that the age of NGC 6618PG is >2 Myr (Haisch, Lada, & Lada 2001a).

We therefore consider the possibility that the OB stars have evolved off the main sequence, and list possible spectral types of luminosity class III for the most luminous stars, BD-16 4831 and BD-16 4826 (Nos. 17 and 18 in Table 4.5). These stars place an upper limit on the age of NGC 6618PG. Assuming negligible mass loss, an O6.5 III star spent ∼4.5 Myr as an O5 V star followed by $\lesssim$0.5 Myr of post-main-sequence evolution (Bressan et al. 1993; Martins, Schaerer, & Hillier 2005), for a maximum age of ∼5 Myr. Stars 17 and 18 are the best candidates for ionizing the H II region inside M17 EB, although we cannot rule out the possibility that other luminous stars once contributed to the ionization and have since gone supernova.

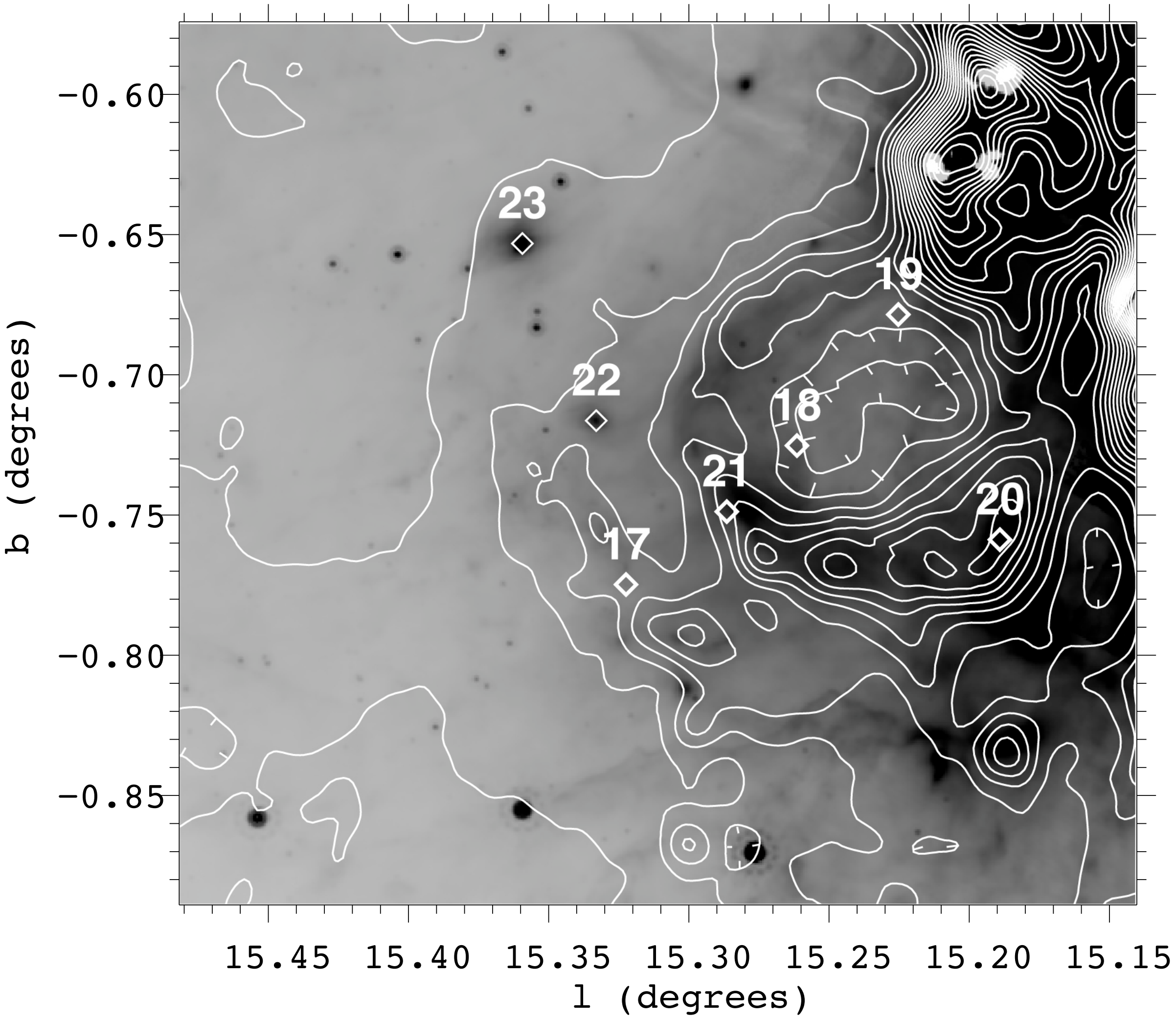

Fig. 4.14.— MIPS 24 μm image highlighting the OB stars of NGC 6618PG (heavy diamonds) and the 90 cm radio ring (contours). Two candidate B stars associated with 24 μm emission are indicated by thin diamonds. Source numbers are from Table 4.5.

Locations of all 5 candidate ionizing stars in NGC 6618PG and the surrounding interior of M17 EB are marked on a MIPSGAL 24 μm image in Figure 4.14. Also shown are contours of 90 cm radio continuum from VLA observations (Brogan et al. 2006). An obvious feature of this image is a ring-shaped structure, centered at $(l, b) = (15.23°, -0.72°)$ and $\sim 6'$ in diameter, that is apparent in both the IR and radio continuum. While this structure is superficially suggestive of a SNR, careful analysis of available VLA data at 20 cm and 90 cm combined with 3.6 cm observations from the commissioning of the 100-m Robert C. Byrd Green Bank Telescope[9] reveals that the radio spectral index is consistent with thermal emission. There is no significant difference between the spectral index of the radio ring and the rest of the M17 H II region. The 24 μm morphology is reminiscent of a stellar-wind bubble produced by a luminous star (like bubble N49 in Watson et al. 2008), but there is only a faint hint of a PDR in the GLIMPSE 8.0 μm images, and this structure is not detected in the HHT CO maps. We have fit SEDs to every Archive source located within the ring, and we find no candidate early-type star apart from those included in Figure 4.14 and Table 4.5. Star 17 is the closest O star to the center of the ring, but it is not central enough to explain the ring geometry. The origin of the ring is therefore puzzling. Recent structural models of the M17 H II region suggest that the blister has broken to the North (Pellegrini et al. 2007, Chapter 2) and hence could vent energy into the interior of M17 EB. The ring structure may be material blown from the side of the M17 H II region by such venting. This raises the possibility that NGC 6618 contributes energy to M17 EB.

4.5.2 Constraints on the Expansion Timescale of M17 EB

M17 EB is a PDR around a faint, diffuse H II region. In the classical model for an expanding H II region (neglecting stellar winds), the timescale for expansion to a radius R is given by

$$t_{\text{phot}}[\text{Myr}] = (3.175 \times 10^{-14}) \times \frac{4R_S}{C_{\text{II}}} \left[\left(\frac{R}{R_S} \right)^{\frac{7}{4}} - 1 \right], \tag{4.3}$$

from Equation 12-20 of Spitzer (1978). We assume typical properties of ionized gas at $T_e = 8,000$ K: Isothermal sound speed $C_{\text{II}} = 10$ km s^{-1} and recombination coefficient $\alpha^{(2)} = 3.09 \times 10^{-13}$ cm^3 s^{-1}. The Strömgren radius R_S depends upon the ambient ISM gas density n_0. We can make a rough estimate of n_0 from the column density of molecular gas swept up by the expansion of the bubble. Using the column density of molecular and atomic gas at $v = 12$–26 km s^{-1} derived from the CO emission (see §4.4.1), the total gas mass in M17 EB (including M17 North and part of MC G15.9-0.7) is $\sim 50,000$ M$_\odot$. If we model

---

[9] See http://wiki.gb.nrao.edu/bin/view/Observing/M17publicImage.

M17 EB as a thin spherical shell with diameter $2R = 20$ pc, then redistributing the gas throughout the shell interior yields a mean ambient density of $n_0 \sim 350$ cm^{-3}, consistent with an inhomogeneous molecular cloud environment. Photoionzed expansion driven by stars 17 and 18 in NGC 6618PG cannot produce an H II region the size of M17 EB within the stellar lifetimes ($t_{\rm phot} > 5$ Myr).

The expansion of M17 EB could instead be dominated by stellar winds. According to the analytical model of Weaver et al. (1977), the timescale for expansion of a windblown bubble to radius R is

$$t_{\rm wind}[\rm Myr] = \left[n_0 \left(\frac{R(\rm pc)}{27}\right)^5 \left(\frac{L_{\rm wind}}{10^{36}}\right)^{-1} \right]^{\frac{1}{3}} . \qquad (4.4)$$

Typical wind luminosities for massive stars are $L_{\rm wind}/L_{\rm bol} = 2.5\times10^{-3}$ for dwarfs and $L_{\rm wind}/L_{\rm bol} \sim 5\times10^{-3}$ for giants (Vink, de Koder, & Lamers 2001). For a given n_0, wind-driven expansion produces a large bubble much more quickly than photoionized expansion. The Weaver et al. (1977) model with $n_0 \sim 350$ cm^{-3} and the same 2 driving stars produces M17 EB in $t_{\rm wind} < 1$ Myr.

The analytical models for both photoionized expansion and wind-driven expansion are oversimplifications of the physics governing the structure of H II regions. Both models underestimate the expansion timescales because they neglect radiative cooling by dust and, in the case of expansion driven by gas pressure (Equation 4.3), depressurization caused by breaks in the bubble. Given the above caveats, the ideal case of photoionized expansion gives a lower limit on $t_{\rm phot}$ that exceeds the stellar lifetimes. In the wind-driven case, unless radiative cooling increases $t_{\rm wind}$ by a factor >10, expansion driven by wind momentum (Equation 4.4) from the 2 most luminous stars in NGC 6618 PG can produce the bubble in $t_{\rm wind} < 5$ Myr. In the other limiting case of $t_{\rm wind} > 2$ Myr (see §4.5.1 above), the average expansion velocity of the bubble is 4.5 km s^{-1}, and the current velocity is lower because the expansion slows with time. The signature of such slow expansion would be undetectable in our spatially-integrated CO line profiles (§4.4).

4.5.3 Sequence of Events

We now reconstruct a plausible star formation history for M17 based upon the wealth of observational data presented in this work.

Initially, the area shown within the *white* boundaries in Figure 4.15 was spanned by a large GMC complex that included the gas now observed in the M17 molecular cloud and MC G15.9-0.7. Between 2 and 5 Myr ago, a massive cloud subcomponent in the center of the complex underwent gravitational collapse, forming the first cluster of perhaps 2,000–3,000 stars, NGC 6618PG, the predecessor and possible progenitor of subsequent star formation in the complex. The OB stars in NGC 6618PG (*blue* diamonds in Figure 4.15) ionized an H II region that expanded, sweeping ambient ISM gas and dust into a bubble, M17 EB.

The M17 molecular cloud, with initial mass $>7 \times 10^4$ $M_\odot$, lay to the south of NGC 6618PG, in the path of the expanding M17 EB. What happened next is debatable. The onset of star formation in M17 may have been triggered when M17 EB collided with the M17 molecular cloud. But triggered star formation is impossible to prove, because we cannot prove that the molecular cloud would *not* have collapsed on its own, independent of the existence of NGC 6618PG. Indeed, it is curious that NGC 6618, the more massive cluster, formed later than NGC 6618PG. Measurements of the magnetic field strength in the PDR interface between the H II region and M17 South (see Figure 4.13) indicate that M17 South is in

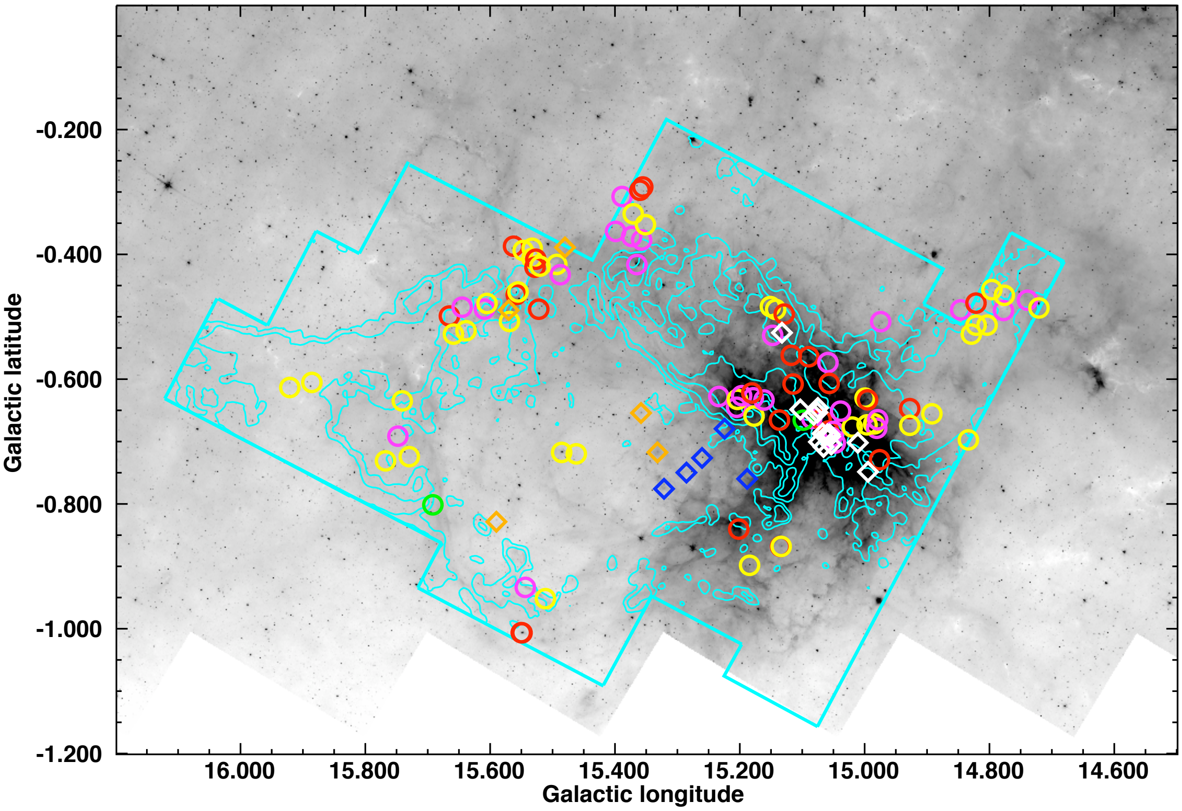

Fig. 4.15.— Overview of the extended massive young stellar population associated with M17 described in this Chapter. *Cyan* contours of ^{12}CO emission at $v = 19$ km s^{-1} are overlaid on a GLIMPSE 8 μm image. Candidate YSOs associated with the extended M17 molecular cloud and M17 EB are marked by colored circles as in Figure 4.10. Diamonds mark the known O stars of NGC 6618 (*white*), the 5 most massive OB stars detected in NGC 6618 (*blue*), and the 5 candidate OB stars identified by associated diffuse 24 μm emission (*orange*).

approximate dynamic equilibrium, with thermal, turbulent, and magnetic pressure combined supporting the cloud (Brogan & Troland 2001; Pellegrini et al. 2007). These support mechanisms might have allowed M17 initially to resist gravitational collapse.

The M17 molecular cloud began to collapse and form stars not more than 2 Myr ago. We know that NGC 6618 is younger than NGC 6618PG, because: (1) Despite being a more luminous cluster exhibiting many signs of strong stellar winds (Townsley et al. 2003, and Chapters 2 and 3), NGC 6618, unlike NGC 6618PG, has not yet dispersed its natal cloud; and (2) NGC 6618 has numerous highly-embedded intermediate- to high-mass stars (ongoing massive star formation), while NGC 6618PG has no intermediate-mass stars with optically thick disks (massive star formation has ceased). The burst of star formation that created the most massive members of NGC 6618 was probably very rapid. The time-averaged SFR in the central regions of M17 has been 0.008–0.01 $M_\odot$ yr^{-1}.

The presence of NGC 6618PG explains some puzzling features of the classic "blister" structure of the M17 H II region. Why should a blister H II region form in the first place? This question has received its share of theoretical attention in recent years. Two-dimensional models of molecular clouds with uniform density show that gravitational acceleration peaks at the edges of clouds, sweeping material inward (Burkert & Hartmann 2004). Heitsch et al. (2008) present 3-dimensional numerical simulations that lead to the formation of massive protostellar cores on the edges of molecular clouds facilitated by gravitational instabilities that focus large-scale colliding flows. M17 could be a good example of the end-product of such a process, with its cluster of very massive young stars forming on the northern side of the massive M17 South cloud. The CO maps show a narrow molecular ridge tracing M17 North that appears to be pressure-bounded on 2 sides. The ridge lies between NGC 6618 and NGC 6618PG (contours between NGC 6618 and NGC 6618PG in Figure 4.15). The source of outward pressure from the stars ionizing the M17 H II region is well-known, and we have now identified a potential source of counteracting pressure from the expansion of M17 EB. This provides a natural explanation for the morphology of the M17 North cloud and the associated northern half of the M17 H II region and PDR.

As the M17 H II region pushes outward from M17 South, M17 North is eroded. Once this barrier is breached, the built-up pressure in the H II region can be released into the diffuse interior of M17 EB. There are observational clues that this may already have occurred. The diffuse X-ray emission identified by Townsley et al. (2003) traces hot plasma filling the interior cavity of the M17 H II region. This plasma appears to spill out of the H II region to the East and North (Townsley et al. in prep.). The thermal radio/IR ring shown in Figure 4.14 may also be evidence of a blowout from the northern side of the H II region. In this scenario, it is possible that NGC 6618 now pumps energy into M17 EB, even though the bubble was originally driven by NGC 6618PG. Additional observations in X-rays and optical recombination lines are needed to reveal the detailed structure of M17 EB.

The expansion of M17 EB is asymmetric, with NGC 6618PG offset from the center of the bubble toward its southern rim, near M17 itself. This is reasonable given that the presence of the large molecular mass in M17 indicates a strong density gradient across the bubble. Any energy input from NGC 6618 into M17 EB would provide an additional push to expand the bubble preferentially away from the M17 H II region.

The northward expansion of M17 EB overtook another molecular cloud, MC 15.9-0.7. The central regions of MC G15.9-0.7 lack IR signatures of star formation. As Figure 4.15 shows, only the side of this cloud that intersects the 8 μm emission from M17 EB exhibits a significant concentration of candidate YSOs after the removal of background contaminants. Hence the circumstantial evidence for triggered star formation is stronger here than in the case of NGC 6618. Outside of M17 itself, the bubble-cloud interface produces the brightest CO ($J = 2 \rightarrow 1$) emission at $v = 20$ km s^{-1}. The current SFR in the molecular gas swept up by M17 EB and in the extended outer regions of M17 is >16% of the SFR that produced the well-studied young stellar population of the M17 H II region.

4.6 Conclusions

We have used IR, radio, and X-ray survey data combined with targeted millimeter observations to show that star formation in the M17 complex extends ∼0.5° farther to the north than previously thought. Our ^{12}CO and ^{13}CO line maps cover a 0.72 deg^2 area that contains 1.35×10^5 M$_\odot$ in gas at $v = 12$–26 km s^{-1}. The morphology of the CO map (Figure 4.15) is dominated by an extended bubble, M17 EB, occupying the space between the well-studied M17 molecular cloud and a neighboring molecular cloud to the north, MC G15.9-0.7.

We have found 406 candidate YSOs in a $1.5° \times 1°$ target field centered on M17 EB by fitting model SEDs to fluxes of sources in the GLIMPSE Archive supplemented by MIPSGAL and *MSX* photometry. We characterized the contamination from unassociated sources in our YSO sample by analyzing a control field exhibiting no obvious signs of massive star formation. We were able to identify and remove the brightest $\gtrsim$50% of dust-rich AGB stars from our sample. We conclude that >80% of sources in the control field sample are candidate YSOs distributed at unknown distances along the long sightline through the inner Galactic plane.

We created a map of the extinction produced by the molecular cloud structures associated with M17. Outside of a few small regions of high gas column density, across ∼90% of our target field the extinction is too low to significantly reduce mid-IR detections of background sources. The complex, spatially varying extinction in the M17 molecular cloud itself creates special challenges for observations of the young stellar population associated with NGC 6618. The average extinction through the cloud cavity occupied by the central M17 H II region is $A_V < 17$ mag, too low to prevent the detection of a significant fraction of background stars even for relatively shallow near-IR observations. Recent results reported by H08, in particular the high IR excess fraction and young age of 0.5 Myr for the young stellar population in M17, appear to have been compromised by the use of an IR-selected sample that was not corrected for background contamination.

Approximately half of the candidate YSOs in our target field are unassociated contaminants. In studies of massive young clusters, IR excess sources are commonly assumed to be associated by virtue of their apparent youth, but this assumption is not valid in the case of star-formation regions near the inner Galactic mid-plane. By selecting candidate YSOs exhibiting a significant degree of clustering with respect to the control sample, we successfully removed the predicted level of contamination.

Among 195 candidate YSOs overlapping the area occupied by the extended M17 complex, 96 have high statistical likelihood of association with M17 once the contribution from unassociated foreground and background sources is removed. Modeling the YSO population, we find that our sample consists primarily of intermediate-mass YSOs with disks (Stage II; Robitaille et al. 2006) and highly embedded (Stage 0/I) YSOs. We model the accretion rates for the Stage 0/I sources and find that their median age is $\lesssim$0.075 Myr, leading us to derive a circumstellar disk lifetime of ∼0.5 Myr for sources with $M_\star \gtrsim 3$ M$_\odot$ (corresponding to B-type stars on the main sequence). Candidate YSOs distributed around the rim of M17 EB and the extended outer regions of M17 represent a >16% addition to the star formation rate that has produced the young stellar population in the central regions of M17, as observed by *Chandra* (BFT07). The concentration of star formation activity tracing the interface between M17 EB and MC G15.9-0.7 appears to have been triggered by the expansion of the bubble.

We have identified 5 candidate ionizing stars inside M17 EB. By fitting stellar atmosphere models to their IR SEDs we constrained the luminosity distance of these 5 sources, showing that their IR luminosities give OB spectral types at the M17 distance. An associated lower-mass population of young stars is suggested by X-ray survey observations by the *Einstein* and *ROSAT* satellites, leading us to deduce the presence of a young cluster, NGC 6618PG. The two earliest-type stars in NGC 6618PG, BD-16 4831 and BD-16 4826 (stars 17 and 18 in Table 4.5), have luminosities equivalent to main-sequence spectral types O4–O5, but the stars may be evolved. The stellar winds from these two stars carry sufficient momentum to produce an H II region the size of M17 EB in <5 Myr. The current expansion velocity of M17 EB is low, a few km s^{-1} maximum.

We also fit stellar atmosphere SEDs to 11 of the principal ionizing stars in NGC 6618. At the newly-revised 2.1 kpc distance (H08), we find that a high fraction of the O stars in NGC 6618 are too luminous in the mid-IR to be single stars on the main sequence, yet the stars are too young to have evolved off the main sequence. This finding supports the hypothesis of H08 that most of the O stars in M17 are in binary systems with approximately equal-mass components.

The wealth of observational data paints a picture of propagating star formation in this region. Three main waves of star formation can be identified: (1) The formation of the NGC 6618PG cluster (2,000–3,000 stars), 2–5 Myr in the past, followed by the expansion of an H II region delineated by M17 EB; (2) The rapid collapse of the M17 molecular cloud (current mass $>6 \times 10^4$ $M_\odot$) within the last 2 Myr, producing the massive NGC 6618 cluster and associated massive star formation that continues to the present day (11,000–14,000 stars); and (3) The onset of star formation in MC G15.9-0.7 and the extended outer regions of M17 ($>1,000$ stars). The possibility that the later waves of star formation were triggered by the first raises a tantalizing question: Can a massive progenitor cluster trigger the formation of an even more massive daughter cluster?

Because they are beacons observable at large distances across the local universe, H II regions are commonly used as SFR tracers in external galaxies, and have been used to estimate the SFR of the Milky Way as well (Smith, Biermann, & Mezger 1978). The canonical Galactic SFR of a few $M_\odot$ yr^{-1} is equivalent to several hundred H II regions the size of M17. Observational tracers tied to H II regions are sensitive only to the most massive <1% of stars, and the uncertainty involved in extrapolating over the IMF to the low-mass stars that make up the bulk of the stellar mass is enormous. Star formation distributed at lower densities but over large spatial volumes is increasingly observed in prominent Galactic molecular cloud complexes, including Orion (Megeath et al. 2005), W5 (Koenig et al. 2008), and now M17. It is not yet clear if low-density star formation outside of bright H II regions or dense GMCs significantly increases the galactic SFRs derived from observational tracers of ionized or molecular gas.

We are indebted to Leisa Townsley for keen insights and suggestions that helped guide this work and for sharing early results from *Chandra*. We thank the anonymous referee for numerous comments that helped to substantially improve this work. Frank D. Ghigo, Ronald J. Maddalena, and Dana S. Balser provided the GBT 3 cm image used in our analysis. We thank Steve Bracker for IR color analysis of candidate AGB stars, David Pooley for finding the *Einstein* image, and Cormac Purcell for inspecting the CORNISH survey images on our behalf. Conversations with Debra Shepherd, Fabian Heitsch, and Kyle Westfall helped improve this work. We thank Dr. A. R. Kerr of the National Radio Astronomy Observatory for providing the single-sideband ALMA Band 6 prototype mixers used in this study. The Heinrich Hertz Telescope is operated by the Arizona Radio Observatory, a part of Steward Observatory at The University of Arizona. This work was supported by NASA/JPL contract 1275394 and NSF grant AST-0303689 to the University of Wisconsin. Additional support was provided by the *Spitzer* Theoretical Research Program (1290701 & 1310231; B. A. W., T. P. R.), the NASA Theory Program (NNG05GH35G; B. A. W.), and NSF grant AST-0708131 to The University of Arizona (M. K., J. H. B.). M. K. gratefully acknowledges support from a Korea Research Foundation Grant (KRF-2007-612-C00050). Additional support was provided by NASA through the *Spitzer Space Telecopse* Fellowship Program (T. P. R.). This work relies on observations made the the *Spitzer Space Telescope*, operated by the Jet Propulsion Laboratory under a contract with NASA. This research has made use of the SIMBAD database, operated at CDS, Strasbourg, France. This work has also made use of data obtained from the High Energy Astrophysics Science Archive Research Center (HEASARC), provided by NASA's Goddard Space Flight Center.

Table 4.2. Candidate YSOs in the Extended Environment of M17

Index No.	l (deg)	b (deg)	[4.5] (mag)	[8.0] (mag)	[24] (mag)	$M_\star$ ($M_\odot$) Min	Max	$\log(L_{\rm TOT}/L_\odot)$ Min	Max	Evolutionary Stage[a]
The Bridge										
E1	14.7207	-0.4859	6.4	6.0	3.3	6	6	3.1	3.2	II
E2	14.7392	-0.4736	12.0	10.4	5.7	0.3	4	0.1	2.2	Amb.
E3	14.7762	-0.4657	7.4	6.8	3.9	6	6	3.1	3.2	II
E4	14.7776	-0.4900	9.7	9.5	5.8	1	4	1.3	2.1	Amb.
E5	14.7963	-0.4565	12.3	11.2	6.9	1	4	1.3	2.5	II
E6	14.8039	-0.5135	7.4	7.0	4.3	3	6	2.1	2.9	II
E7	14.8214	-0.5136	7.5	6.5	2.8	4	8	2.4	3.4	II
E8	14.8217	-0.4782	11.3	11.1	6.8	0.6	4	0.6	1.7	0/I
E9	14.8291	-0.5279	9.2	8.4	4.8	3	5	1.8	2.6	II
E10	14.8462	-0.4890	12.7	11.9	7.0	0.2	4	0.1	1.7	Amb.
The Outer Regions of the M17 GMC										
E11	14.8338	-0.6974	9.6	8.8	6.0	3	5	1.7	2.6	II
E12	14.9743	-0.5079	11.7	9.8	> 3.3	0.3	4	0.4	2.3	Amb.
E13	15.1289	-0.4958	11.5	9.0	3.2	0.2	5	1.0	2.7	0/I
E14	15.1426	-0.4883	11.4	9.8	> 4.1	0.2	5	0.5	2.8	II
E15	15.1473	-0.5299	9.2	8.3	3.5	1	5	1.5	2.5	Amb.
E16	15.1511	-0.4837	10.2	9.2	5.8	2	4	1.3	2.3	II
E17	15.1971	-0.6266	7.0	5.7	···	5	10	2.6	3.5	Amb.
E18	15.2039	-0.6325	8.2	7.3	···	3	6	2.1	2.7	II
E19	15.2052	-0.6451	9.2	···	···	3	9	2.1	3.7	Amb.
E20	15.2336	-0.6279	9.2	7.8	3.2	0.2	5	0.9	2.5	Amb.
M17 EB										
E21	15.3512	-0.3525	10.7	10.1	6.8	2	4	1.0	2.0	II
E22	15.3555	-0.2921	9.8	8.7	2.5	0.9	6	1.3	2.4	0/I
E23	15.3572	-0.3770	10.3	9.4	4.7	0.9	4	1.0	2.4	Amb.
E24	15.3599	-0.2973	11.4	10.5	5.2	0.2	4	0.2	2.1	0/I
E25[b]	15.3649	-0.4164	7.2	3.4	< -0.4	6	10	2.9	3.4	Amb.
E26	15.3708	-0.3350	7.1	6.4	2.4	5	6	2.6	3.0	II
E27	15.3733	-0.3714	12.9	12.5	7.7	0.2	3	-0.2	1.6	Amb.
E28	15.3886	-0.3073	10.9	10.1	5.9	0.8	4	0.8	2.0	Amb.
E29	15.3990	-0.3633	12.9	10.7	7.1	1	5	0.5	2.7	Amb.
E30	15.4620	-0.7198	10.3	9.5	6.2	2	4	1.3	2.2	II
E31	15.4854	-0.7175	4.6	3.7	1.7	9	10	3.6	3.7	II
E32	15.4878	-0.4327	12.8	11.8	6.9	0.1	4	-0.1	1.8	Amb.
E33	15.4932	-0.4162	11.7	10.1	5.9	0.4	4	0.6	2.4	II
E34	15.5115	-0.9519	9.9	8.8	6.7	2	7	1.3	3.3	II
E35	15.5202	-0.4190	10.9	10.0	> 5.4	0.7	4	0.8	1.7	II
E36	15.5221	-0.4880	8.2	7.0	2.4	0.2	1	1.3	1.6	0/I
E37	15.5268	-0.4078	11.1	11.3	> 6.1	0.9	1	1.0	1.1	0/I
E38	15.5281	-0.4207	12.5	11.9	> 4.6	0.2	4	0.3	1.7	0/I
E39	15.5326	-0.3903	12.5	11.2	8.0	0.4	4	0.1	2.2	II
E40	15.5330	-0.4066	10.6	9.4	> 5.3	3	6	1.8	2.9	II
E41	15.5437	-0.9338	9.0	7.3	4.0	3	8	2.1	3.4	Amb.
E42	15.5471	-0.3938	11.9	11.5	7.5	0.3	4	0.1	1.7	II
E43	15.5489	-1.0066	8.3	> 5.6	< 0.2	2	7	2.2	2.7	0/I
E44	15.5502	-1.0063	10.1	8.0	> 0.2	1	5	1.4	2.0	0/I
E45	15.5553	-0.4603	7.1	6.2	2.5	5	8	2.9	3.4	II
E46	15.5583	-0.4646	12.6	11.0	> 1.1	0.2	5	0.4	2.2	0/I
E47	15.5584	-0.4622	6.5	< 5.0	1.1	5	10	2.8	3.8	II
E48	15.5625	-0.3870	13.3	11.0	4.9	0.1	5	0.4	2.0	0/I
E49	15.5691	-0.5076	12.0	11.2	7.4	0.9	3	0.4	1.4	II
E50	15.6050	-0.4788	11.4	10.4	6.7	0.6	4	0.5	2.1	II
E51	15.6092	-0.4878	12.0	10.5	5.4	0.1	4	0.0	2.3	Amb.
E52	15.6385	-0.5225	10.1	9.0	6.0	2	3	1.2	1.7	II
E53	15.6448	-0.4847	13.0	···	6.1	0.1	4	-0.0	2.4	Amb.
E54	15.6588	-0.5279	10.2	9.4	5.8	3	4	1.7	2.5	II
E55[c]	15.6653	-0.4989	9.2	9.5	0.7	7	8	2.6	3.0	0/I
E56	15.6918	-0.8014	11.2	10.7	8.3	2	3	0.8	1.5	III
E57	15.7296	-0.7243	13.5	11.4	7.0	0.2	4	0.0	2.0	II
E58	15.7408	-0.6349	12.0	11.2	8.1	0.5	3	0.3	1.7	II

Table 4.2 (continued)

Index No.	l (deg)	b (deg)	[4.5] (mag)	[8.0] (mag)	[24] (mag)	$M_\star$ ($M_\odot$) Min	Max	$\log(L_{\rm TOT}/L_\odot)$ Min	Max	Evolutionary Stage[a]
E59	15.7478	-0.6914	13.1	10.7	5.5	0.1	4	0.2	2.1	Amb.
E60	15.7677	-0.7310	10.6	9.4	5.4	1	4	1.1	2.4	II
MC G15.9-0.7 (Likely Unassociated)										
E61	15.8856	-0.6053	9.0	8.7	6.0	3	4	1.7	2.2	II
E62	15.9210	-0.6134	12.6	11.9	8.4	0.3	3	-0.1	1.6	II

Note. — The sources presented in this table are found within the *white* boundary lines but outside the rectangle in Figure 4.10. While the association of any given source with M17 is uncertain, the groupings of candidate YSOs are significant. The "Bridge" is a molecular gas structure connecting the M17 molecular cloud with the GMC complex extending 85 pc to the southwest. Although our cluster-finding algorithm selects 2 candidate YSOs apparently located in MC 15.9-0.7, these sources are likely unassociated.

[a] "Amb." means that the well-fit models are divided between different evolutionary Stages

[b] Source E25 is resolved by IRAC and is also an *MSX* point source. Its SED exhibits PAH emission.

[c] Source E55 is the candidate protostar shown in Figure 4.12.

Table 4.3. Other Candidate Clustered YSOs in the M17 Target Field

Index No.	l (deg)	b (deg)	[4.5] (mag)	[8.0] (mag)	[24] (mag)	Group[a]
F1	14.5865	-0.5708	10.6	9.1	4.9	SW
F2	14.5898	-0.5822	12.8	11.6	7.3	SW
F3	14.5999	-0.5422	10.2	9.7	6.3	SW
F4	14.6005	-0.6248	9.9	9.9	5.6	SW
F5	14.6017	-0.6177	10.9	10.1	5.3	SW
F6	14.6043	-0.6229	10.3	9.7	6.4	SW
F7	14.6116	-0.5520	11.2	9.9	5.7	SW
F8	14.6117	-0.6259	9.7	9.3	6.4	SW
F9	14.6148	-0.5843	11.4	10.4	> 5.7	SW
F10	14.6235	-0.5775	10.7	9.9	> 5.5	SW
F11	14.6285	-0.5781	9.5	8.6	> 4.6	SW
F12	14.6290	-0.7614	12.5	···	5.3	SW
F13	14.6297	-0.5724	11.1	10.1	> 5.4	SW
F14	14.6311	-0.5784	10.6	9.3	> 2.1	SW
F15	14.6314	-0.5774	11.7	10.2	2.1	SW
F16	14.6327	-0.5719	10.9	10.2	> 6.4	SW
F17	14.6348	-0.8730	13.1	12.1	8.1	SW
F18	14.6395	-0.7286	11.6	11.3	8.3	SW
F19	14.6416	-0.8928	13.1	11.8	6.1	SW
F20	14.6426	-0.7639	11.2	9.7	5.3	SW
F21	14.6428	-0.8833	12.3	11.5	7.2	SW
F22	14.6437	-0.9011	10.9	10.3	6.8	SW
F23	14.6533	-0.7411	12.6	11.5	8.2	SW
F24	14.6660	-0.8838	12.6	11.9	8.0	SW
F25	14.6745	-0.8863	10.9	10.6	7.0	SW
F26	14.6771	-0.7672	9.7	9.0	5.1	SW
F27	14.6802	-0.8755	11.8	10.6	6.0	SW
F28	14.6990	-0.8916	12.3	11.9	6.9	SW
F29	14.7720	-0.3570	···	8.6	3.1	
F30	14.7868	-0.2176	11.9	10.2	> 6.4	
F31	14.7878	-0.2353	10.9	10.5	7.3	
F32	14.7952	-0.2062	12.0	11.7	7.7	
F33	14.7999	-0.2072	12.6	11.1	7.7	
F34	14.8122	-0.2346	9.9	9.3	6.4	
F35	14.8209	-1.0206	8.0	7.4	4.7	SW
F36	14.8247	-0.2663	11.7	10.2	5.9	
F37	14.8302	-0.1774	11.1	10.7	2.2	
F38	14.8443	-1.0049	6.9	6.4	3.3	SW
F39	14.8516	-0.9890	> 10.7	10.1	3.2	SW
F40	14.8519	-0.9927	> 10.8	10.0	3.2	SW
F41	14.8521	-1.0007	11.4	10.7	7.7	SW
F42	14.8522	-0.3314	11.5	11.0	7.8	
F43	14.8566	-0.1674	13.0	12.1	> 7.0	
F44	14.8607	-0.4358	10.1	9.4	6.8	MC G14.9
F45	14.8621	-0.1594	13.8	12.1	7.6	
F46	14.8624	-0.9974	12.8	11.8	8.0	SW
F47	14.8637	-0.1750	11.0	10.7	7.0	
F48	14.8695	-0.3952	11.3	9.9	5.9	MC G14.9
F49	14.8709	-0.3886	11.9	···	5.5	MC G14.9
F50	14.8747	-0.4154	10.8	9.2	5.7	MC G14.9
F51	14.8840	-0.3558	12.4	···	7.0	
F52	14.8844	-0.3114	11.7	···	6.3	
F53[b]	14.8891	-0.4018	6.1	2.5	< -1.0	MC G14.9
F54	14.8892	-0.1977	11.8	11.1	7.4	
F55	14.8951	-0.4004	11.2	7.6	> 2.9	MC G14.9
F56	14.8993	-0.2249	10.0	9.7	5.2	
F57	14.9224	-0.2113	12.9	12.0	8.1	
F58	14.9234	-0.2147	12.3	···	5.4	
F59	14.9251	-0.4058	9.2	8.9	5.8	MC G14.9
F60	14.9261	-0.1578	12.4	···	7.9	
F61	14.9314	-0.2239	12.4	···	8.0	

Table 4.3 (continued)

Index No.	l (deg)	b (deg)	[4.5] (mag)	[8.0] (mag)	[24] (mag)	Group[a]
F62	14.9340	-0.1358	11.1	10.3	7.0	
F63	14.9346	-0.2295	12.0	11.7	7.7	
F64	14.9372	-0.4296	10.5	9.8	6.2	MC G14.9
F65	14.9378	-0.4229	11.8	···	7.9	MC G14.9
F66	14.9402	-0.1474	11.7	11.1	7.8	
F67	14.9607	-0.1868	6.8	6.1	3.3	
F68	14.9622	-0.1400	9.7	9.4	6.6	
F69	14.9685	-0.1384	11.6	10.8	7.8	
F70	14.9764	-0.2147	12.0	10.5	6.3	
F71	14.9804	-0.4319	10.0	9.2	6.2	
F72	14.9960	-0.3090	11.2	10.8	7.8	
F73	15.0626	-0.2450	10.7	10.2	7.2	
F74	15.0634	-0.3109	10.8	10.2	7.4	
F75	15.0768	-0.2528	11.4	10.7	6.7	
F76	15.0773	-0.2511	11.1	10.2	7.1	
F77	15.0784	-0.2678	12.4	11.6	7.1	
F78	15.0795	-0.2609	9.2	8.3	4.2	
F79	15.0817	-0.2699	13.0	11.7	> 5.2	
F80	15.0832	-0.2686	10.1	9.2	5.2	
F81	15.0841	-0.1548	10.8	10.0	6.5	
F82	15.1135	-0.1485	9.6	7.8	4.7	
F83	15.1512	-0.1216	11.9	11.2	6.5	
F84	15.1530	-0.1909	12.4	9.7	4.9	
F85	15.1684	-0.1267	11.2	11.4	4.1	
F86[b]	15.1761	-0.1585	12.0	9.4	3.7	
F87[b]	15.1831	-0.1625	7.8	4.7	< -0.5	
F88	15.1841	-0.1589	8.9	6.6	> 1.2	
F89[b]	15.1850	-0.1561	9.7	6.1	> 2.3	
F90	15.1898	-0.1400	12.2	11.6	7.1	
F91	15.1904	-0.1692	12.6	9.9	> 5.9	
F92	15.2199	-0.1451	10.8	9.7	> 4.1	
F93	15.2354	-0.1750	9.1	8.3	5.7	
F94	15.5750	-0.3101	11.0	10.4	> 6.5	Bu G15.7
F95	15.5754	-0.3218	12.3	11.1	7.2	Bu G15.7
F96	15.5815	-0.2963	11.1	9.9	> 6.3	Bu G15.7
F97	15.5869	-0.3003	9.1	8.3	3.7	Bu G15.7
F98	15.5920	-0.2923	13.4	10.9	6.6	Bu G15.7
F99	15.5998	-0.2861	10.8	10.3	6.6	Bu G15.7
F100	15.6028	-0.2040	9.5	8.6	5.0	Bu G15.7
F101	15.6051	-0.2537	11.3	10.6	6.6	Bu G15.7
F102	15.6337	-0.2282	10.3	9.7	> 6.0	Bu G15.7
F103	15.6408	-0.2189	7.9	> 6.2	1.0	Bu G15.7
F104	15.6541	-0.2249	11.6	7.9	2.1	Bu G15.7
F105	15.6603	-0.1189	11.4	9.1	5.6	
F106	15.6638	-0.1231	9.9	9.1	5.7	
F107	15.6747	-0.1476	10.5	···	5.4	
F108	15.6768	-0.1465	11.9	8.2	4.6	
F109	15.6781	-0.2651	10.3	9.9	6.2	Bu G15.7
F110	15.6807	-0.2613	10.7	8.9	5.2	Bu G15.7
F111	15.6829	-0.1424	10.3	9.3	5.6	
F112	15.6929	-0.2576	11.4	11.1	7.6	Bu G15.7
F113	15.6929	-0.1355	10.5	7.0	2.2	
F114	15.6956	-0.1367	10.8	10.5	> 2.2	
F115	15.7181	-0.1648	10.6	9.3	> 3.0	
F116	15.7237	-0.2617	11.5	10.5	7.3	Bu G15.7
F117	15.7250	-0.2480	11.9	11.5	5.0	Bu G15.7
F118	15.7574	-0.2234	12.2	8.8	4.7	
F119	15.7580	-0.1887	8.9	8.2	5.8	
F120	15.7600	-0.2195	9.3	8.6	6.1	
F121	15.7826	-0.3897	12.1	10.5	6.5	
F122	15.7848	-0.3864	12.8	···	7.4	

Table 4.3 (continued)

Index No.	l (deg)	b (deg)	[4.5] (mag)	[8.0] (mag)	[24] (mag)	Group[a]
F123	15.7911	-0.2355	11.3	10.3	6.0	
F124	15.7951	-0.4058	> 11.8	12.1	7.0	
F125	15.7991	-0.3927	9.9	8.8	5.5	
F126	15.8012	-0.3760	8.8	8.4	5.6	
F127	15.8067	-0.3818	12.0	11.2	7.5	
F128	15.8108	-0.2328	11.7	10.5	8.0	
F129	15.8113	-0.2394	12.6	11.1	6.8	
F130	15.8367	-0.2653	10.9	9.9	6.3	
F131	15.8612	-0.2350	11.1	···	5.7	
F132	15.9580	-0.1866	11.8	10.7	6.3	
F133	15.9750	-0.2097	9.5	8.3	3.9	
F134	15.9920	-0.2097	12.1	10.6	4.6	
F135	15.9930	-0.1868	10.9	10.7	6.4	

Note. — The sources presented in this table are found outside the *white* boundary lines in Figure 4.10. The majority of these sources are at unknown distances.

[a] Groups of these candidate YSOs are apparently associated with prominent molecular cloud structures: “SW” refers to the near end of the large GMC complex at $v = 20$ km s^{-1} extending southwest from M17; “MC G14.9” refers to the molecular cloud G14.9-0.4 at $v = 60$ km s^{-1} (see Figure 4.1); and “Bu G15.7” refers to an IR/CO shell structure, 4$'$ in diameter, centered at $(l, b) = (15.67^\circ, -0.29^\circ)$ and $v \approx 45$ km s^{-1}.

[b] These 4 sources are resolved by IRAC. F53, F87, and F89 are detected by *MSX* and may be compact H II regions ionized by young clusters rather than single YSOs.

References

Allen, L. et al. 2004, ApJS, 154, 363 (A04)

Benjamin, R. A. et al. 2003, PASP, 115, 953

Bernasconi, P. A. & Maeder, A. 1996, A&A, 307, 829

Bohlin, R. C., Savage, B. D., & Drake, J. F. 1978, ApJ, 224, 132.

Bressan, A., Fagotto, F., Bertelli, G., & Chiosi, C. 1993, A&AS, 100, 647

Brogan, C. L. & Troland, T. H. 2001, ApJ, 560, 821

Brogan, C. L., Gelfand, J. D., Gaensler, B. M., Kassim, N. E., & Lazio, T. J. W. 2006, ApJ, 639, L25

Broos, P. S. et al. 2007, ApJS, 169, 353 (BFT07)

Brott, I. & Hauschildt, P. H. 2005, in The Three-dimensional Universe with *Gaia*, eds. C. Turon, K. S. O'Flaherty, & M. A. C. Perryman (ESA Sp-576; noordwijk: ESA), 565

Burkert, A. & Hartmann, L. 2004, ApJ, 612, 88

Carey, S. J. et al. 2009, PASP, 121, 76

Carigi, L. & Peimbert, M. 2008, RMxAA, 44, 341

Cesarsky, C. J., Cesarsky, D. A., Lequeux, J., & Churchwell, E. 1978, A&A, 68, 33

Cesarsky, D., Lequeux, J., Abergel, A., Perault, M. Palazzi, E., Madden, S., & Tran, D. 1996, A&A, 315L, 309

Chini, R., Elsässer, H., & Neckel, T. 1980, A&A, 91, 186 (CEN)

Chini, R. & Wargau, W. F. 1998, A&A, 329, 161

Chini, R., Hoffmeister, V. H., Kämpgen, K., Kimeswenger, S., Nielbock, M., & Siebenmorgen, R. 2004a, A&A, 427, 849

Chini, R., Hoffmeister, V., Kimeswenger, S,. Nielbock, M. Nürnberger, D., Schmidtobreick, L,. & Sterzik, M. 2004b, Nature, 429, 155

Churchwell, E., Povich, M. S., et al. 2006, ApJ, 649, 759

Cohen, M. 1993, AJ, 105, 1860

Cox, A. N. ed. 2000, Allen's Astrophysical Quantities, 4th ed. Springer

Cyganowski, C. J. et al. 2008, AJ, 136, 2391

Davis, C. J., Kumar, M. S. N., Sandell, G., Froebrich, D., Smith, M. D., & Currie, M. J. 2007, MNRAS, 374, 29

Dunne, B. C., Chu, Y.-H., Chen, C.-H. R., Lowry, J. D., Townsley, L., Gruendl, R. A., Guerrero, M. A., & Rosado, M. 2003, ApJ, 590, 306

Elmegreen, B. G. & Lada, C. J. 1976, AJ, 81, 12

Fazio, G. G. et al. 2004, ApJS, 154, 10

Felli, M., Churchwell, E., & Massi, M. 1984, A&A, 136, 53 (FCM84)

Felli, M., Testi, L., Schuller, F., & Omont, A. 2002, A&A, 392, 971

Guandalini, R., Busso, M., Ciprini, S., Silvestro, G., & Persi, P. 2006, A&A, 445, 1069

Gutermuth, R. A., Myers, P. C., Megeath, S. T., Allen, L. E., Pipher, J. L., Muzerolle, J., Porras, A., Winston, E., & Fazio, G. 2008, ApJ, 674, 336 (G08)

Haisch, K. E., Lada, E. A., & Lada, C. J. 2000, AJ, 120, 1396

Haisch, K. E., Lada, E. A., & Lada, C. J. 2001a, AJ, 121, 2065

Haisch, K. E., Lada, E. A., & Lada, C. J. 2001b, ApJ, 553, L153

Handa, T., Sofue, Y., Nakai, N., Hirabayashi, H., & Inoue, M. 1987, PASJ, 39, 709

Hanson, M. M., Howarth, I. D., & Conti, P. S. 1997, ApJ, 489, 698

Heitsch, F., Hartmann, L. W., Slyz, A. D., Devriendt, J. E. G., & Burkert, A. 2008, ApJ, 674, 316

Hoffmeister, V. H., Chini, R., Scheyda, C. M., Schulze, D., Watermann, R., Nürnberger, D., Vogt, N., & Nielbock, M. 2008, ApJ, 686, 310 (H08)

Høg, E., Fabricius, C., Makarov, V. V., Urban, S., Corbin, T., Wycoff, G., Bastian, U., Schwekendiek, P., & Wicenec, A. 2000, A&A, 355, 27L

Hony, S., Waters, L. B. F. M., & Tielens, A. G. G. M. 2002, A&A, 390, 533

Indebetouw, R. et al. 2005, ApJ, 619, 931

Indebetouw, R., Robitaille, T. P., Whitney, B. A., Churchwell, E., Babler, B., Meade, M., Watson, C., & Wolfire, M. 2007, ApJ, 666, 321

Jaffe, D. T. & Fazio, G. G. 1982, ApJ, 257, L77

Jiang, Z. et al. 2002, ApJ, 577, 245 (J02)

Kenyon, S. J. & Hartmann, L. 1995, ApJS, 101, 117

Kleinmann, D. E. & Wright, E. L. 1973, ApJ, 185, L131

Koenig, X. P., Allen, L. E., Gutermuth, R. A., Hora, J. L., Brunt, C. M., & Muzerolle, J. 2008, ApJ, 688, 1142

Kulesa, C. A., Hungerford, A. L., Walker, C. K., Zhang, X., & Lane, A. P. 2005, ApJ, 625, 194

Kurucz, R. 1993, ATLAS9 Stellar Atmosphere Programs and 2 km/s grid. Kurucz CD-ROM No. 13. Cambridge, MA: Smithsonian Astrophysical Observatory

Kutner, M. L. & Ulich, B. L. 1981, ApJ, 250, 341

Lada, C. 1976, ApJS, 32, 603

Lada, C. J. 1987, in IAU Symp. 115: Star Forming Regions, eds. M. Peimbert & J. Jugaku (Dordrecht: Kluwer), 1

Lada, C. J., DePoy, D. L., Merrill, K. M., & Gatley, I. 1991, ApJ, 374, 533

Martins, F., Schaerer, D. & Hillier, D. J. 2005, A&A, 436, 1049

Mason, B. D., Hartkopf, W. I., Greis, D. R., Henry, T. I., & Helsel, J. G. 2009, AJ, in press (astro-ph/0811.0492)

McClure-Griffiths, N. M., Dickey, J. M., Gaensler, B. M., Green, A. J., Haverkorn, M., & Strasser, S. 2005, ApJS, 158, 178

Megeath, S. T. et al. 2005, in IAU Symp. 227: Massive Star Birth: A Crossroads of Astrophysics, eds. R. Cesaroni, M. Felli, E. Churchwell, & C. M. Walmsley, 383

Mizuno, A. & Fukui, Y. 2004, ASPC, 317, 59

Muench, A. A., Lada, E. A., Lada, C. J. & Alves, J. 2002, ApJ, 573, 366

Nielbock, M., Chini, R., Jütte, M., & Manthey, E. 2001, A&A, 273, 284

Ogura, K. & Ishida, K. 1976, PASJ, 28, 35 (OI)

Pellegrini, E. W., Baldwin, J. A., Brogan, C. L., Hanson, M. M., Abel, N. P., Ferland, G. J., Nemala, H. B., Shaw, G., & Troland, T. H. 2007, ApJ, 658, 1119

Porras, A. et al. 2007, ApJ, 656, 493

Purcell, C. R., Hoare, M. G., & Diamond, P. 2008, ASPC, 387, 389

Preibisch, T. et al. 2005, ApJS, 160, 401

Price, S. D., Egan, M. P., Carey, S. J., Mizuno, D. R., and Kuchar, T. A. 2001, AJ, 121, 2842

Reich, W., Fuerst, E., Reich, P., & Reif, K., 1990, A&AS, 85, 633

Richer, J. S., Shepherd, D. S., Cabrit, S., Bachiller, R., & Churchwell, E. 2000, in Protostars and Planets IV, eds. V. Mannings, A. Boss, & S. Russell (Tucson: Univ. Arizona Press), 867

Robitaille, T. P., Whitney, B. A., Indebetouw, R., Wood, K., & Denzmore, P. 2006, ApJS, 167, 256 (RW06)

Robitaille, T. P., Whitney, B. A., Indebetouw, R., & Wood, K. 2007, ApJS, 169, 328 (RW07)

Robitaille, T. P. et al. 2008, AJ, 136, 2413

Sanders, D. B., Clemens, D. P., Scoville, N. Z. & Solomon, P. M. 1986, ApJS, 60, 1

Salpeter, E. E. 1955, ApJ, 121, 161

Sana, H., Gosset, E., Nazé, Y., Rauw, G., & Linder, N. 2008, MNRAS, 386, 447

Sault, R. J., Teuben, P. J., & Wright, M. C. H. 1995, in Astronomical Data Analysis Software and Systems IV, eds. R. Shaw, H. E. Payne, & J. J. E. Hayes (ASP Conf. Ser., Vol. 77), p. 433

Sewilo, M., Churchwell, E., Kurtz, S., Goss, W. M., & Hofner, P. 2004, ApJ, 605, 285

Shepherd, D. S., Povich, M. S., et al. 2007, ApJ, 669, 464

Siess, L., Dufour, E., & Forestini, M. 2000, A&A, 358, 593

Skrutskie, M. F. et al. 2006, AJ, 131, 1163

Smith, L. F., Biermann, P., & Mezger, P. G. 1978, A&A, 66, 65

Smith, H. A., Hora, J. L., Marengo, M., & Pipher, J. L. 2006, ApJ, 645, 1264

Spitzer, L. 1978, Physical Processes in the Interstellar Medium (New York: Wiley)

Stetson, P. 1987, PASP, 99, 191

Sylvester, R. J., Kemper, F., Barlow, M. J., de Jong, T., Waters, L. B. F. M., Tielens, A. G. G. M., & Omont, A. 1999, A&A, 352, 587

Townsley, L. K., Feigelson, E. D., Montmerle, T., Broos, P. S., Chu, Y.-H., & Garmire, G. P. 2003, ApJ, 593, 874

van Dishoeck, E. & Black, J. H. 1988, ApJ, 334, 771

Verstraete, L., Puget, J. L., Falgarone, E. Drapatz, S., Wright, C. M., & Timmermann, R. 1996, A&A, 315L, 337

Vink, J. S., de Koter, A., & Lamers, H. J. G. L. M. 2001, A&A, 369, 574

Wainscoat, R. J., Cohen, M., Volk, K., Walker, H. J., & Schwartz, D. E. 1992, ApJS, 83, 111

Wallerstein, G. & Knapp, G. R. 1998, ARA&A, 36, 369

Watson, C., Povich, M. S., Churchwell, E. B., Babler, B L., Chunev, G., Hoare, M., Indebetouw, R., Meade, M. R., Robitaille, T. P. & Whitney, B. A. 2008, ApJ, 681, 1341

Weaver, R., McCray, R., Castor, J., Shapiro, P., & Moore, R. 1977, ApJ, 218, 377

Weingartner, J. C. & Draine, B. T. 2001, ApJ, 548, 296

Whitney, B. A., Wood, K., Bjorkman, J. E., & Wolff, M. J. 2003a, ApJ, 591, 1049

Whitney, B. A., Wood, K., Bjorkman, J. E., & Cohen, M. 2003b, ApJ, 598, 1079

Whitney, B. A., Indebetouw, R., Bjorkman, J. E., & Wood, K. 2004, ApJ, 617, 1177

Whitney, B. A. et al. 2008, ApJ, 136, 18

Wilson, C. D., Howe, J. E., & Balogh, M. L. 1999, ApJ, 517, 174

Wood, D. O. S. & Churchwell, E. 1989, ApJ, 340, 265

Chapter 5

Synthesis:
Star Formation Rate Diagnostics Applied to M17

More tuna and less mayonnaise.

— *Hobbes*
Calvin & Hobbes
by Bill Watterson

5.1 The Star Formation Rate in M17 Predicted By Diffuse Emission Tracers of the Massive Stellar Population

In Chapter 4, I reported a star formation rate $\mathrm{SFR}_X = 0.008$–$0.01\ \mathrm{M}_\odot\ \mathrm{yr}^{-1}$ in NGC 6618, the massive cluster ionizing the M17 H II region. This and all other values for SFRs and luminosities used in this chapter assume a distance of 2.1 kpc to M17 (Hoffmeister et al. 2008). SFR_X is based upon the X-ray luminosity function (XLF) of 886 sources detected by *Chandra*/ACIS (Broos et al. 2007). The XLF is a reliable statistical measure of the stellar initial mass function (IMF) in young massive clusters (Getman et al. 2006; Wang et al. 2007). Young low- and intermediate-mass stars exhibit powerful convectively-driven magnetic reconnection flaring activity, hence they are 10^2–10^3 times brighter in X-rays than older Galactic field stars (Preibisch & Feigelson 2005). X-ray detections of cluster members suffer relatively little absorption and are generally free of the contamination from unassociated stellar and extragalactic sources that plagues IR photometric catalogs (Chapter 4). In addition, X-ray observations are unaffected by the bright diffuse emission from H II regions and photodissociation regions (Chapter 2) that drastically reduces infrared (IR) point-source sensitivity. While there does appear to be a population of embedded intermediate-mass young stellar objects (YSOs) corresponding to late B stars on the main sequence that are not detected in X-rays (Chapter 4), the XLF of Broos et al. (2007) is complete for O stars and lower-mass stars (to a limiting mass of $\sim$2 $\mathrm{M}_\odot$) and unbiased by the presence or absence of circumstellar disks.

The approximate range of masses sampled by XLFs of various massive clusters observed with ACIS is indicated on a plot of the Kroupa (2001) IMF in Figure 5.1. Also shown in Figure 5.1 are the approximate mass ranges of completeness for GLIMPSE (including MIPSGAL) detections of YSOs (at the 2–3 kpc distances of nearby giant H II regions like M17; see Figure 4.11) and OB stars ionizing H II regions (spectral types B3 and earlier). While the general, multi-power-law form of the observed IMF is remarkably consistent among clusters and field star populations, there are variations both in reported power-law slopes and in locations of the break points where the slopes change (Kroupa 2001). Alternate IMFs with maximally deviant slopes are plotted along with the Kroupa (2001) IMF as *dash-dotted* curves in Figure 5.1; all three IMF curves are normalized to give the same relative number of ionizing stars. In principle, any true variation in the IMF lies in between these curves. But the center-of-mass of the IMF is at $\sim$1 $\mathrm{M}_\odot$, meaning

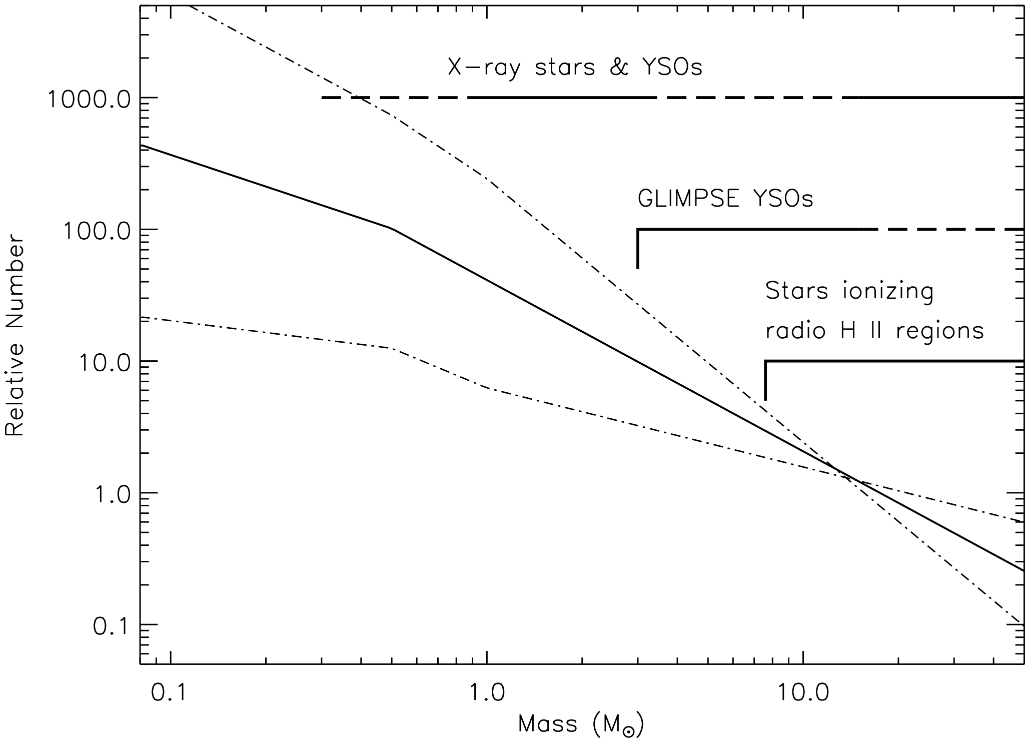

Fig. 5.1.— Plot of a simulated Galactic field IMF (Kroupa 2001) normalized to the integral of the distribution for $M > 7.6$ M$_\odot$. Dash-dotted curves represent 99% confidence intervals. Three mass ranges probed by different observational tracers are indicated: massive stars that ionize H II regions (spectral type B3 or earlier, $M_\star > 7.6$ M$_\odot$); completeness of GLIMPSE detections of YSOs ($M_\star > 3$ M$_\odot$, objects with $M_\star \gtrsim 17$ M$_\odot$ that will become O stars on the main sequence may evolve too quickly to be observed frequently as embedded YSOs); and completeness of *Chandra*/ACIS detections of young stars and YSOs (detection of stars with $M_\star < 1$ M$_\odot$ depends upon observation depth, and ∼20% of A through late B stars are X-ray quiet).

the integrated stellar mass is divided equally between higher and lower masses (Kroupa 2001). Hence, the impact of any IMF variation is largest on cluster masses and SFRs derived through extrapolations over the IMF that are pinned to massive stars only, because such stars are far from the center-of-mass. Sampling the IMF in the intermediate-mass range, as the XLF does, avoids this problem. The adoption of the IMF of the Orion Nebula Cluster (Muench et al. 2002), a similar, though smaller, young stellar population to that of M17, minimizes any lingering uncertainties on the total stellar mass due to IMF variations. The dominant source of uncertainty on SFR$_X$ is the adopted age of ∼1 Myr, which is uncertain by ∼50% (see discussion in Chapter 4).

YSOs identified on the basis of IR excess emission in the GLIMPSE and MIPSGAL surveys provide an excellent means of quantifying very recent star formation activity, especially in the extended molecular clouds associated with H II regions. GLIMPSE and MIPSGAL provide a highly complete sample of YSOs with ages <0.5 Myr and $M_\star \gtrsim 3$ M$_\odot$ at the M17 distance (Figures 4.11 and 5.1, and discussion in Chapter 4). The major caveat to the preceding statement is that mid-IR detections of YSOs are *very* incomplete in bright H II regions such as M17 due to masking by diffuse emission. The YSO sample from the extended M17 environment outside the area of the ACIS observations represents a >16% addition to the SFR in the central ionizing cluster, but given the uncertainties, this increase is not significant. The area analyzed in Chapter 4 is not the whole story of star formation in the M17 giant molecular cloud (GMC) complex, however, and I will further address this issue in §5.3.

In the following two subsections, I estimate the M17 SFR using independent tracers of the massive stellar population and compare the results to SFR$_X \sim 0.01$ M$_\odot$ yr^{-1} derived from the XLF. In §5.2 I will discuss the often overlooked systematic uncertainties involved in SFR determinations.

5.1.1 M17 As a Galactic H II Region: The Thermal Radio Continuum SFR Diagnostic

Smith, Biermann, & Mezger (1978, hereafter SBM78) reported a thermal radio flux density emitted by the M17 H II region of $S_{5\mathrm{GHz}} = 478.3$ Jy, corresponding to a Lyman continuum photon rate $N_c' = 2.26{\times}10^{50}$ s^{-1}. Correcting for absorption of ionizing photons by dust, SBM78 arrived at $N_c = 5.37{\times}10^{50}$ s^{-1} as the contribution of M17 to the Galactic production of Lyman continuum photons. Putting this number into Equation 1.7 yields SFR$_{ff} = 0.05$ M$_\odot$ yr^{-1}, $\gtrsim 5 \times$ SFR$_X$ and ∼1% of the 5 M$_\odot$ yr^{-1} Galactic SFR calculated by SBM78.

If the single case of M17 were taken to be a representative example of the Galactic SFR calibration, then the Galactic SFR reported by SBM78 would appear to be too large by a factor of 5, which is in line with the level of uncertainty acknowledged by the authors themselves. A factor of 2 is explained by the difference in ages; SBM78 assumed a typical age of ∼0.5 Myr for radio H II regions, while I used an age of ∼1 Myr for the calculation of SFR$_X$ (Chapter 4). SBM78 based their adoption of 0.5 Myr on the ratio of O stars found inside versus outside H II regions within ∼2 kpc of the Sun, which gives the H II region lifetime as a fraction of the main-sequence stellar lifetimes. This calculation assumed that the massive stellar population in the solar neighborhood is typical of the Galaxy as a whole and neglected runaway O stars. In addition, SBM78 most likely underestimated the number of O stars in radio H II regions, because the Salpeter IMF does not account for the very high binary fraction among O stars (the consequences of binarity are discussed in §5.2).

As I discussed in Chapter 2, historically there has been significant disagreement between different measurements of the M17 radio continuum flux density. The value used by SBM78 falls at the extreme low end of the range. Adopting instead $S_{5\text{Ghz}} = 784$ Jy and $S_{15\text{Ghz}} = 609$ Jy from Table 2.2 and using the same conversion from thermal continuum to ionizing photon rate as SBM78 (Equation 2 of Mezger, Smith, & Churchwell 1974), I calculate $N_c' = 3.4 \times 10^{50}$ s^{-1} and 2.9×10^{50} s^{-1}, at 5 GHz and 15 Ghz, respectively. The difference suggests a ∼15% uncertainty on N_c'.

Summing over the known O stars in NGC 6618, including all known or suspected binary stars ($d = 2.1$ kpc column in Table 4.5), and using the models of Martins, Schaerer, & Hillier (2005) to obtain the ionizing photon rates for each spectral type, the rate of ionizing photons *emitted* is $N_c \sim 3 \times 10^{50}$ s^{-1}. This is in surprisingly good agreement with N_c' derived above, given that some fraction of the Lyman continuum photons are absorbed by dust before contributing to the ionization of the H II region and some fraction of the ionizing flux may escape from nebula altogether (Chapter 2). According to SBM78, $N_c'/N_c = 0.42$ for M17. My calculation of N_c largely neglected the contribution of stars later than O8 to the ionization, but the inclusion of O8–B3 stars would only increase N_c by a few percent. There may yet be new major ionizing stars waiting to be discovered in M17, (I reported the discovery of a new candidate O5 V star in Chapter 3), but it strains credulity to imagine that >1/2 of the ionizing stellar population in M17 has been missed. I have accounted for binarity of the majority of the principal ionizing stars (types O6 and earlier) in my calculation of N_c. The total bolometric luminosity of the known O stars is $L_{\text{OB}} \sim 5.8 \times 10^6$ L$_\odot$. When compared to the luminosity in the global spectral energy distribution (SED), it is clear that the energy budget of the nebula cannot accommodate any significant increase in the ionizing stellar population, unless the distance were significantly greater than 2.1 kpc (Table 2.4).

I conclude that absorption of Lyman continuum photons by dust has a negligible impact upon the ionization of M17. More important is the escape of ionizing photons into the diffuse interstellar medium (ISM) through the blow-out in the H II region (Chapter 2); $N_c'/N_c = f$. In the most probable nebular geometries, $f \gtrsim 0.9$ (Table 2.4 and related discussion in Chapter 2). SBM78 generally assumed $N_c'/N_c \approx 0.5$ for giant H II regions, and consequently their values of $\langle N_c \rangle$ and corresponding SFR determinations (Equation 1.7), were likely overestimated by a factor of ∼2.

Thus far I have discussed aspects of the SBM78 SFR calibration that are *extrinsic,* based on the assumptions and uncertainties involved in tracing the ionizing photon rate from thermal radio continuum observations. Together, a factor of ∼2 from an over-correction for dust absorption and another factor of ∼2 from the adoption of a younger cluster age account for much of the deviation of SFR_{ff} compared to SFR_X. The heart of the SBM78 calibration, the $\langle M\rangle/\langle N_c\rangle$ relation of Equation 1.6, appears more robust. Taking $\langle N_c'\rangle = 3.2 \times 10^{50}\ \mathrm{s}^{-1}$, averaged from the measurements of $S_{5\mathrm{GHz}}$ and $S_{15\mathrm{GHz}}$, the Lyman continuum photon rate is $\langle N_c\rangle \sim \langle N_c'\rangle/0.9 = 3.5 \times 10^{50}\ \mathrm{s}^{-1}$. The total stellar mass from Equation 1.6 is thus $\langle M\rangle \sim 16,000\ \mathrm{M}_\odot$, higher than the stellar mass traced by the XLF (Chapter 4) by a factor of 1.6–2. Assuming a cluster age of 1 Myr, I arrive at a new $\mathrm{SFR}_{ff}' \sim 0.016\ \mathrm{M}_\odot\ \mathrm{yr}^{-1}$, which is, of course, higher than SFR_X by the same factor of 1.6–2. This residual discrepancy is rooted in systematic uncertainties on the IMF and the properties of massive stars, hence it is *intrinsic* to the SFR calibration. I will further discuss such intrinsic, systematic discrepancies in §5.2.

5.1.2 M17 As an Extragalactic H II Region: The 24 μm Mid-IR SFR Diagnostic

According to Calzetti et al. (2007, hereafter CK07), their 24 μm SFR calibration "is appropriate for metal-rich H II regions or starbursts" where the radiation field is dominated by young, massive stars. M17 is a highly embedded Galactic H II region that radiates $\gtrsim$90% of its energy in the mid-IR (Chapter 2), so it certainly fits these criteria. In fact, the environmental conditions in its central regions qualify M17 as a miniature starburst. Starburst conditions prevail in regions where $\Sigma_{\mathrm{SFR}} \gtrsim 10\ \mathrm{M}_\odot\ \mathrm{yr}^{-1}\ \mathrm{kpc}^{-2}$ (Kennicutt 1998a,b), whether applied to an entire galaxy or an individual super star cluster, such as R136 in the 30 Doradus region of the Large Magellanic Cloud (Massey & Hunter 1998). In M17, $\mathrm{SFR}_X \sim 0.01\ \mathrm{M}_\odot\ \mathrm{yr}^{-1}$ was measured within a single $17' \times 17'$ ACIS field (Broos et al. 2007), an area $10^{-4}\ \mathrm{kpc}^2$ at $d = 2.1$ kpc, hence $\Sigma_{\mathrm{SFR}} \sim 100\ \mathrm{M}_\odot\ \mathrm{yr}^{-1}\ \mathrm{kpc}^{-2}$.

Because the M17 H II region is bright enough to completely saturate even the short MIPSGAL exposures at 24 μm, there is no direct measurement of L_{24} that can be used to calculate the SFR according to the CK07 relation (Equation 1.4). Fortunately, the global SED presented in Figure 2.3 provides the 24 μm flux, $\nu F_\nu(24) = \lambda F_\lambda(24)$, interpolated between the *MSX* and *IRAS* fluxes at 20–60 μm. Thus

$$L_{24} \equiv \nu L_\nu(24) = 4\pi d^2 \nu F_\nu(24) = 8.4 \times 10^{39}\ \mathrm{erg\ s}^{-1},$$

(<10% uncertainty) and, from Equation 1.4, $\mathrm{SFR}_{24} = 0.0027\ \mathrm{M}_\odot\ \mathrm{yr}^{-1}$. This result is significantly different from SFR_X. Apparently, if M17 were located in a nearby galaxy and observed by *Spitzer*/MIPS, the L_{24}

diagnostic would underestimate its SFR by a factor of ∼3.

The L_{24} SFR diagnostic is a statistical relation based on 179 observed H II region "knots" in 23 different high-metallicity galaxies with $[12 + \log(\mathrm{O/H}) > 8.35]$ (Figure 5.2), and its failure to predict the SFR of a single, Galactic H II region is hardly a scathing indictment. Perhaps M17 is simply an outlier from the trend, or perhaps it is too different from the extragalactic H II regions analyzed by CK07 to draw useful comparisons. I have measured the mid-IR luminosity of M17 using a large aperture chosen to match the linear extent of the H II region and photodissociation region (Figure 2.1), while H II knots in distant galaxies are generally smaller than the small apertures used by CK07 to extract their fluxes. Hence, there could be a systematic offset between the mid-IR luminosity measured for M17 and the luminosities of the extragalactic H II knots due to the drastically different filling factors and background subtractions involved. The impact of such potential biases can be evaluated by hypothetically locating M17 among the CK07 extragalactic sample (Figure 5.2). CK07 measured the fluxes $S_{\mathrm{P}\alpha}$ and S_{24}, which they called luminosity surface densities (LSDs; units of erg s^{-1} kpc^{-2}), for each H II knot using a fixed photometric aperture matched to the MIPS 24 μm resolution. The aperture size corresponded to a linear size of ∼300 pc at $d = 5$ Mpc. A bilinear least-squares fit to the LSDs of the high-metallicity sample yielded (CK07)

$$\log S_{24} = (1.23 \pm 0.03) \log S_{\mathrm{P}\alpha,\mathrm{corr}} - (6.88 \pm 0.97), \tag{5.1}$$

(*solid* line in Figure 5.2), which is an alternate version of Equation 1.4, with S_{24} substituted for L_{24} and $S_{\mathrm{P}\alpha,\mathrm{corr}}$ (corrected for dust extinction) representing the SFR surface density, Σ_{SFR}, in place of the absolute SFR. Among the high-metallicity H II knots, the range of observed LSDs was $38 \lesssim \log S_{\mathrm{P}\alpha,\mathrm{corr}} \lesssim 40$ and $40.5 \lesssim \log S_{24} \lesssim 42.5$. An H II region with the same L_{24} as M17, located in a galaxy at 5 Mpc, would have an observed LSD of $\log S_{24} = 41.07$, in the middle of the range. M17 would be easily observable at 24 μm as an H II knot in a nearby galaxy.

But what if $S_{\mathrm{P}\alpha}$ causes M17 to depart from the trend of Equation 5.1? To facilitate the comparison between SFR$_{24}$ and SFR$'_{ff}$ from §5.1.1 above, I calculate the luminosity $L_{\mathrm{P}\alpha}$ in the Pα line from the thermal radio continuum (Chapter 2). The emissivity of the Pα line can be calculated as $j(\mathrm{P}\alpha)/j_\nu(ff)$; given $j(\mathrm{P}\alpha)/j(\mathrm{Br}\alpha) = 4.430$ (Osterbrock 1974; Giles 1977), the coefficient in Equation 2.4 becomes 1.355×10^{13}. Then a slightly modified form of Equation 2.5 gives

$$L_{\mathrm{P}\alpha} = 4\pi d^2 \frac{j(\mathrm{P}\alpha)}{j_\nu(ff)} F_\nu(\nu). \tag{5.2}$$

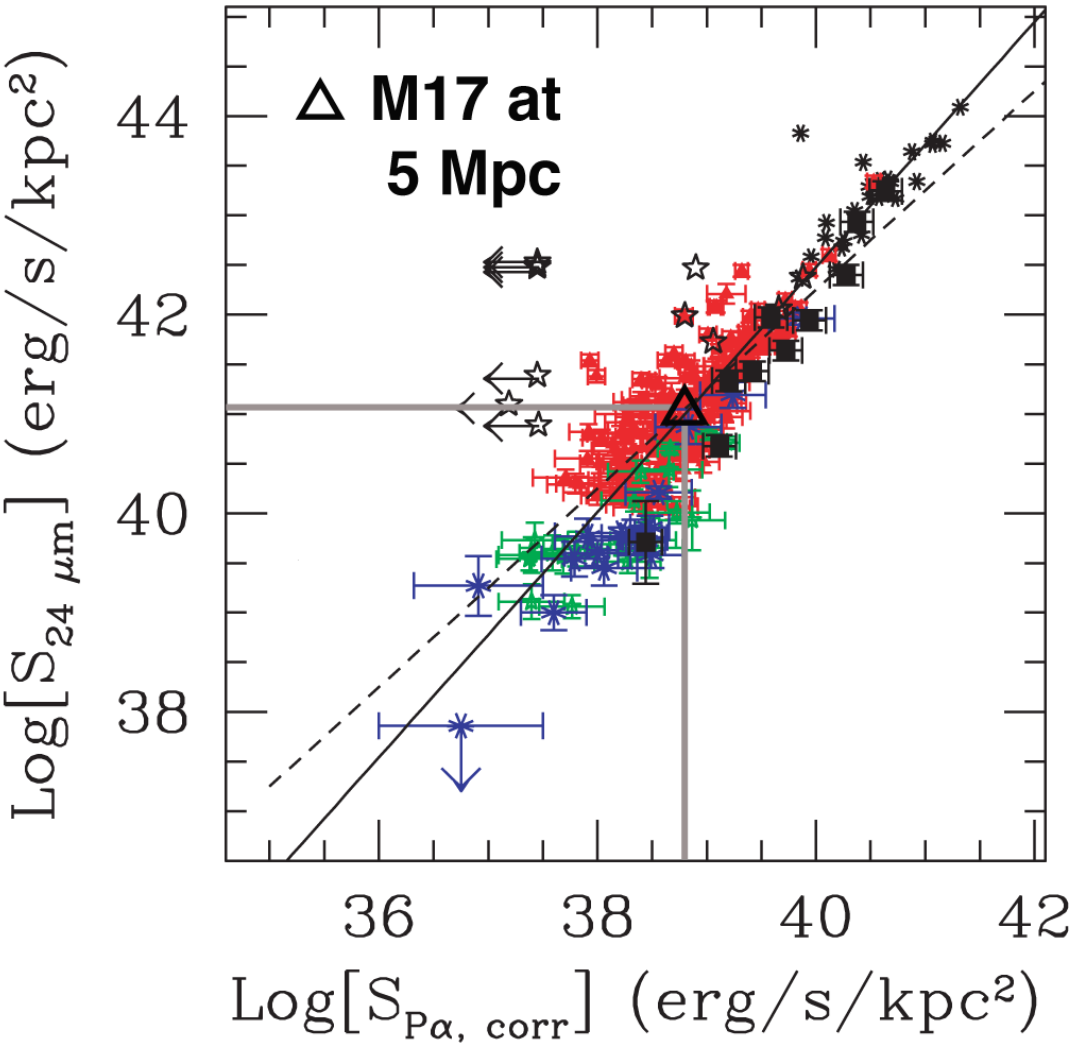

Fig. 5.2.— LSD at 24 μm, S_{24}, as a function of the extinction-corrected LSD at Pα, $S_{\mathrm{P}\alpha,\mathrm{corr}}$, for 220 H II region knots in 33 galaxies, reproduced from CK07. H II knots are divided into three metallicity bins: high (*red triangles*), intermediate (*green stars*), and low (*blue asterisks*) oxygen abundance. *Filled black squares* and *asterisks* are starburst galaxies. Error bars are 3σ. *Black stars* show the locations of active galactic nuclei. The *solid* line is the best fit to the high-metallicity (*red*) H II knots, while the *dashed* line is the fit to the same data points with a fixed slope of 1. The LSDs of M17 observed as an H II knot in a galaxy at 5 Mpc are plotted as the *open black triangle* and *solid gray* lines.

From the values of $F_\nu(\nu)$, the free-free radio continuum flux density at frequency ν, in Table 2.2, I find $L_{\mathrm{P}\alpha} = 4.1 \times 10^{37}$ erg s^{-1} (<15% uncertainty). Assuming again a 300 pc test aperture, $\log S_{\mathrm{P}\alpha} = 38.76$ (since it is based on radio observations, there is no need to correct the LSD for extinction).

There is nothing unusual about the LSDs of M17 compared to the extragalactic sample; observed as an H II knot in a galaxy 5 Mpc distant, M17 would be found near the center of the high-metallicity distribution plotted in Figure 5.2. Of course, 5 Mpc is completely arbitrary. Assuming any other distance simply displaces M17 in the LSD plot, parallel to a line with slope 1 (the *dashed* line in Figure 5.2). This displacement is mostly parallel to the best-fit line of Equation 5.1, hence the impact on the derived SFR$_{24}$ must be small. As with the calibration of the Galactic SFR from thermal radio continuum (SBM78), it appears that there is an intrinsic systematic uncertainty affecting the L_{24} SFR diagnostic, at the factor of ~3 level, that cannot be readily explained by biases in the empirical determination of ionizing photon rates.

5.2 Discrepancies Between Various SFR Diagnostics

From the analysis in the previous section, I conclude that *even if ionizing photon rates in H II regions were known to arbitrarily high precision, there would remain an intrinsic uncertainty in the derived SFRs.* This is the uncertainty on the calibration of $\langle M \rangle / \langle N_c \rangle$ formulated explicitly by SBM78 (Equation 1.6), which is also present implicitly in the population synthesis models used by CK07.[1] The magnitude of the uncertainty can be estimated from the discrepant results given by the 3 different diagnostics of the M17 SFR explored in this Chapter. Among the 3, only SFR$_X$ does not depend on $\langle N_c \rangle$, because the XLF traces primarily the intermediate-mass stellar population. SFR$_X$ ~ 0.01 M$_\odot$ yr^{-1} is therefore the baseline measurement. Given SFR$'_{ff}$ $\sim 2\times$SFR$_X$ and SFR$_X$ $\sim 3\times$SFR$_{24}$, the intrinsic uncertainty is a factor of ~2–3. Several systematic effects are likely to be important:

Uncertain ionizing photon production rates for O stars. Fundamentally, $\langle M \rangle / \langle N_c \rangle$ is tied to $M_\star / N_c$, the ratio of stellar mass to Lyman continuum photon production for individual O stars, as a function of spectral type. This relation must be obtained from models of the stellar parameters of O stars. SBM78 relied on the best models available at the time, from Panagia (1973). The STARBURST99 grid of population synthesis models (Vazquez & Leitherer 2005) used by CK07 incorporated the modern O star calibrations

---

[1] In population synthesis models (e.g. Vazquez & Leitherer 2005), $\langle M \rangle / \langle N_c \rangle$ is a function of age, adding another dimension of uncertainty.

and synthetic atmospheres of Smith, Norris, & Crowther (2002). Currently, O star calibrations employ sophisticated non-LTE stellar atmosphere models that include the effects of line-blanketed winds (Smith, Norris, & Crowther 2002; Martins, Schaerer, & Hillier 2005). These calibrations predict cooler effective temperatures by as much as ∼5000 K for the earliest spectral types, resulting in ∼40% reductions of N_c for a given spectral type compared to earlier models (Panagia 1973; Vacca, Garmany, & Shull 1996). This would tend to increase $M_\star/N_c$, resulting in higher SFRs derived from ionizing photon rates, but this trend moves in the *opposite* direction from the observed discrepencies, predicting that SFR'_{ff}, as I have derived it, should be ∼40% *lower* than SFR_X instead of a factor of ∼2 higher. Thus the *model-dependent* ionizing photon rates of O stars do not appear to be the dominant source of uncertainty for SFR calibrations, however Martins, Schaerer, & Hillier (2005) caution that N_c is uncertain by a factor of ∼2 *in any model*, hence its impact cannot be ignored.

The O star mass discrepancy. The uncertainty in the numerator of $M_\star/N_c$ also turns out to be significant. Model-based calibrations of O star parameters predict the stellar mass as a function of spectral type in two different ways. The emergent spectrum gives values for stellar luminosity L, effective temperature T_{eff}, and effective surface gravity g_{eff}, giving

$$M_{\mathrm{spec}} = \frac{g_{\mathrm{eff}} L}{4\pi G \sigma T_{\mathrm{eff}}^4}, \tag{5.3}$$

(Vacca, Garmany, & Shull 1996; Martins, Schaerer, & Hillier 2005) where σ is the Stefan-Boltzmann constant and G is the gravitational constant. Alternatively, L, T_{eff} from stellar evolutionary tracks can be used to determine an evolutionary mass M_{evol}, which is associated with a stellar gravity g_{evol} (Vacca, Garmany, & Shull 1996). In general, $g_{\mathrm{eff}} < g_{\mathrm{evol}}$, because a strong stellar wind lifts the surface layers of a star, reducing the gravity probed by spectral lines formed in the photosphere. Consequently, there is a discrepancy in the derived masses of up to a factor of ∼2, a systematic effect with $M_{\mathrm{spec}} < M_{\mathrm{evol}}$. O star masses are thus poorly determined in stellar models, particularly for the earliest spectral types, a fact that must be borne in mind when considering claims that the Salpeter IMF extends without variation to the very highest stellar masses (e.g. Massey & Hunter 1998). The O3 spectral class is highly degenerate in this regard, since it is essentially open-ended in mass.

Binarity of O stars. As I discussed in Chapter 4, the majority of O stars are thought to form in binary systems with nearly equal-mass components, and the most massive stars in M17 seem to follow this rule. Maíz Apellániz (2008) performed numerical experiments testing the consequences of neglecting unresolved, massive binaries on observational IMF determinations. Maíz Apellániz (2008) found that the neglect of stellar multiplicity has a neglible effect on the derived IMF slope, but the masses of the most massive stars determined from spectroscopic or photometric observations of a distant cluster will be systematically *overestimated*. For example, a high-mass binary system in NGC 3603 has component masses of 114 $\mathrm{M}_{\odot}$ and 84 $\mathrm{M}_{\odot}$, measured directly from periodic radial velocity variations in the stellar spectra. If this system were mistaken for a single star, its observed M_{evol} would range from 159 $\mathrm{M}_{\odot}$ to 217 $\mathrm{M}_{\odot}$ (Maíz Apellániz 2008). Assuming, very approximately, $N_c(M_\star) \propto M_\star^{3.5}$, then

$$\frac{N_c(114\ \mathrm{M}_\odot + 84\ \mathrm{M}_\odot)}{N_c({>}159\ \mathrm{M}_\odot)} < 0.4.$$

For every massive binary system treated as a single star in the adopted IMF, $M_\star/N_c$ increases by >40%. This correspondingly increases the derived SFRs. Such a correction reduces the discrepancy between SFR_{24} and SFR_X for M17, but the discrepancy between SFR'_{ff} and SFR_X actually increases.

The factors of ~2 uncertainties on each of N_c and $M_\star$, combined with a ~40% correction for binarity, yield a factor of ~2–3 uncertainty on $\langle M\rangle/\langle N_c\rangle$. Hence systematic uncertainties in the calibration of ionizing photon rate to the IMF can explain why various diagnostic methods produced discrepant results for the M17 SFR.

Nowhere in this analysis have I invoked a variable IMF. While systematic differences in the IMF between galaxies would have significant consequences for SFR determinations, scatter about the standard IMF (Kroupa 2001) among different regions in an individual galaxy may cancel out when averaged among a large sample of regions. Indeed, if M17 itself possessed a deviant IMF, then doubt would be cast upon the generality of the discussion in this Chapter, but there is no evidence that this is the case. The main challenge for accurate SFR determinations is the assignment of accurate masses to the ionizing stars, which is the starting point for the IMF extrapolations used to obtain an integrated mass for the entire young stellar population. Put another way, a well-defined value of $\langle M\rangle/\langle N_c\rangle$ could exist, but thus far the measured values have been affected by large, systematic uncertainties on O star parameters. Measurements of $\langle M\rangle$ directly from the intermediate-mass stellar population, using XLFs in Galactic H II regions, for instance, hold the potential for new, more robust calibrations of SFR against observational tracers of ionized gas.

5.3 Sequential Star Formation and the Schmidt Law

Comparing the SBM78 calibration of the Galactic SFR directly to the CK07 extragalactic calibration gives

$$\frac{\mathrm{SFR}_{ff}}{\mathrm{SFR}_{24}} \sim \frac{5\times 10^{-2}}{2.7\times 10^{-3}} = 18.5.$$

This result seems to imply that 5 $\mathrm{M}_{\odot}\ \mathrm{yr}^{-1}$ (SBM78) is a severe overestimate of the Galactic SFR. Calibrated against the SFRs in other galaxies (Kennicutt 1998a,b; CK07), the Galactic SFR may only be a fraction of a solar mass per year. Yet paradoxically, the SBM78 result should be an *underestimate* of the actual Galactic SFR, because only giant, radio H II regions were included in the accounting. The mass function of young open clusters in the Milky Way and other galaxies has been observed to obey a power law $\psi(M) \propto M^{\alpha}$, with $\alpha \sim -2$, similar to the stellar IMF and the mass function of molecular clouds (Zhang & Fall 1999; Dowell, Buckalew, & Tan 2008, and references therein). Just as the IMF predicts that the bulk of the stellar mass is contained in low-mass stars, much of the cluster mass, and hence the SFR, may be contained in numerous lower-mass clusters that do not produce bright H II regions. The omission of this more distributed component of star formation in the SBM78 SFR calculation is at least partially compensated by the young age adopted by SBM78 for radio H II regions, which inflates the total SFR in massive clusters. It is difficult to escape the conclusion that the Galactic SFR is barely constrained at all, save for the fact that the Galaxy appears to obey an internal Schmidt Law (Misiriotis et al. 2006) that is consistent with the global relation observed for other normal spiral galaxies (Figure 1.2).

When considering global SFR diagnostics like the Schmidt–Kennicutt Law (Chapter 1), it is easy to overlook the complexity of the star formation process on the scale of individual molecular clouds. A prime example of this complexity is illustrated in Figure 5.3, which shows a combined GLIMPSE and MIPSGAL image of the large GMC complex extending ∼85 pc southwest (equatorial) from M17 (Elmegreen & Lada 1976). A very prominent system of IR dark clouds criss-crosses the complex, revealing the highest-density regions of the GMC. Interspersed among the IR dark clouds in Figure 5.3 are numerous bright *yellow* and *red* diffuse emission sources; these are compact, ultracompact, and even hypercompact H II regions. Also evident are numerous 24 μm (*red*) point sources, mostly located along the IR dark cloud lanes. These sources are candidate intermediate- and high-mass YSOs in early stages of evolution, when the SED is dominated by mid-IR emission from the circumstellar envelope. SED plots of 2 such sources are also presented in Figure 5.3; these are qualitatively similar to the SED of the very young, intermediate-mass

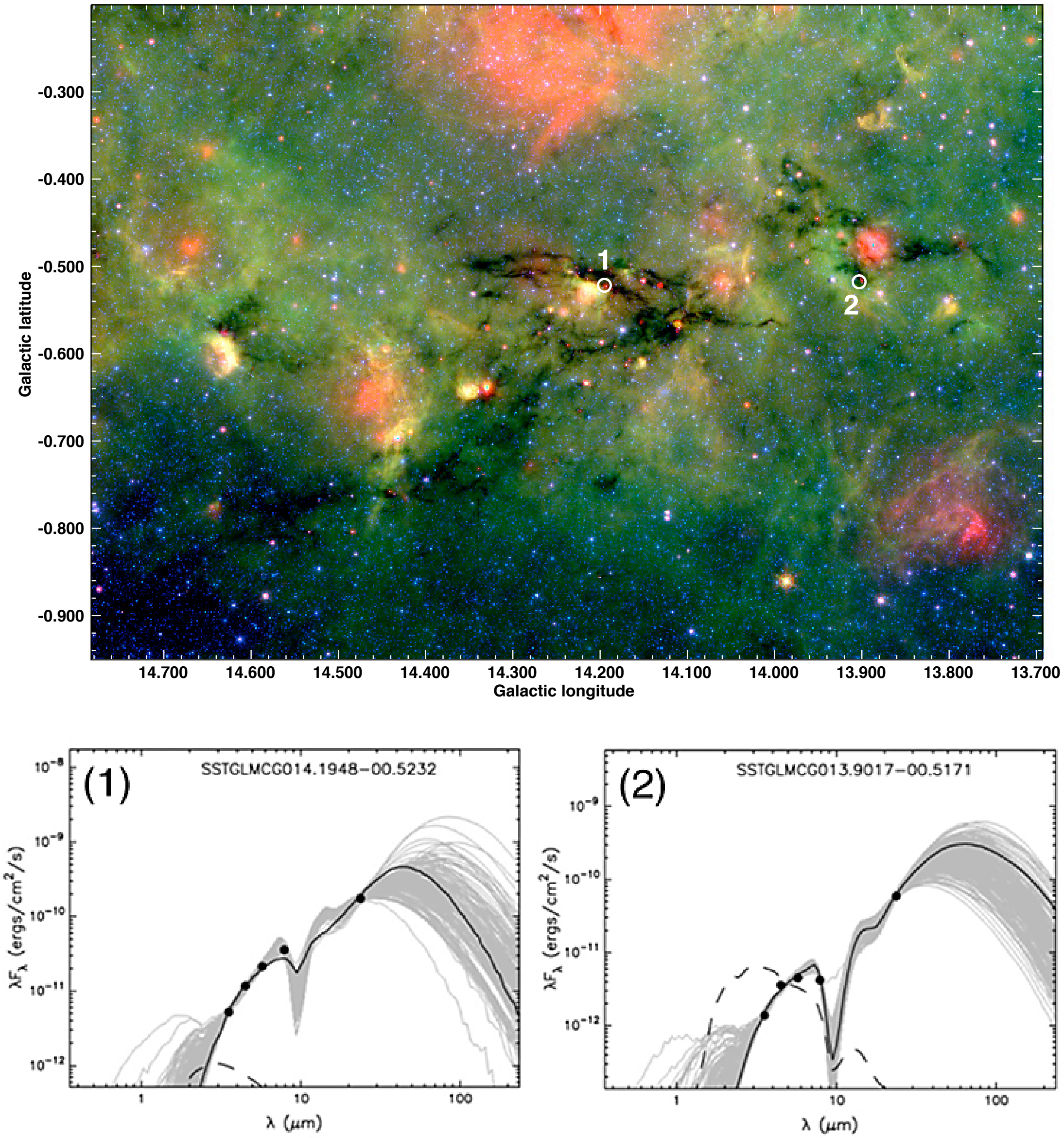

Fig. 5.3.— GLIMPSE/MIPSGAL image of the large GMC complex adjacent to M17 (*red:* 24 μm, *green:* 8.0 μm, *blue:* 4.5 μm). The compact region of bright diffuse emission at the far left of this image $[(l, b) = (14.64^\circ, -0.60^\circ)]$ appears at the far right of the GLIMPSE image shown in Figure 4.1. The SEDs of two heavily embedded candidate YSOs marked in the image are plotted. The IRAC and MIPS fluxes (*dots*) are fit by model SEDs of heavily embedded YSOs (*black* and *gray* curves). The dashed curves show the reddened spectra of the central stars.

YSO E55 plotted in Figure 4.12.

In Chapter 4, I presented a complex star formation history for the extended M17 environment, which began with the formation of the progenitor cluster NGC 6618PG some $\sim$5 Myr ago. NGC 6618PG ionized a large H II region, producing a wind-blown bubble, called M17 EB, that very likely triggered subsequent star formation, and possibly even the birth of M17 itself, as it expanded. The diffuse H II region inside M17 EB is now too faint to be easily detectable in thermal radio or even 24 μm emission, hence it has been completely ignored in my calculations of the M17 SFR *even though* star formation events lasting longer than 5 Myr are routinely included in the population synthesis models for extragalactic SFR diagnostics (Kennicutt 1998a). It is practically impossible to include such evolved H II regions in an estimate of the Galactic SFR, because the Hα SFR diagnostic is unavailable. Recent events in the M17 star formation history are playing out around the rim of M17 EB, but this is by no means the full extent of current star formation activity in the region. The star formation activity in the GMC complex shown in Figure 5.3, while still in its earliest stages, almost certainly represents a significant enhancement to the SFR of the entire complex, including M17 itself.

Elmegreen & Lada (1976) report a molecular gas mass of $\sim 10^6$ $M_\odot$ from CO observations of the 22×85 pc GMC area. This corresponds to a gas surface density $\Sigma_{\rm gas} \sim 535$ $M_\odot$ pc^{-2}, a lower limit on the total gas surface density, which would include atomic gas. The gas surface density in the more compact M17 molecular cloud itself, based on a total gas mass $\sim 6 \times 10^4$ (Chapter 4), is $\Sigma_{\rm gas} \sim 550$ $M_\odot$ pc^{-2}. Even accounting for $\sim 10^4$ $M_\odot$, or $\sim$14% of the original mass of the M17 molecular cloud converted into stars in the ionizing cluster, it is clear that the gas surface density in the extended GMC complex is comparable to that of the M17 molecular cloud. The Schmidt Law (Equation 1.1) predicts that the SFR surface densities ($\Sigma_{\rm SFR}$) are also comparable. Given its larger spatial exent, the GMC complex in Figure 5.3 would therefore be expected to produce a SFR equivalent to several M17s. This is indeed a major enhancement of star formation activity in the region, and it, rather than M17 itself, may even dominate the total SFR. Elmegreen & Lada (1976) reached the same conclusion and suggested that the entire M17 GMC complex will eventually form an extended OB association. Yet at present the M17 H II region alone still dominates the IR emission. Herein lies a central mystery of the Schmidt–Kennicutt Law.

The Schmidt–Kennicutt Law (Figure 1.1) derives $\Sigma_{\rm SFR}$ from ionized gas tracers. $\Sigma_{\rm gas}$, averaged over entire galaxies, includes the full range of ISM environments, from GMCs harboring giant H II regions to GMCs that have yet to produce bright H II regions to the diffuse ISM and smaller molecular clouds between GMC complexes that will never produce bright H II regions. The relation encompasses multiple generations of sequential star formation that may or may not be causally connected by local triggering from stellar-wind bubbles and supernovae. It is far from clear that any unified physical process as simple as self-gravitational collapse on a dynamical timescale, for example (Equation 1.5), can explain why the global Schmidt–Kennicutt Law actually holds. On the scale of GMC complexes such as M17, measurements of $\Sigma_{\rm gas}$ depend critically on the area chosen for the integration, to the point that no generally applicable Schmidt Law can be derived. Given that my prediction of the SFR in the extended M17 GMC complex was based on an argument from the Schmidt Law, might it be in error? A future in-depth study of the YSO population present in Figure 5.3, along the lines of the analysis presented in Chapter 4, will hopefully answer this question.

References

Broos, P. S. et al. 2007, ApJS, 169, 353

Calzetti, D. et al. 2007, ApJ, 666, 870 (CK07)

Dow, J. D., Buckalew, B. A., & Tan, J. C. 2008, AJ, 135, 823

Elmegreen, B. G. & Lada, C. J. 1976, AJ, 81, 12

Getman, K., Feigelson, E. D., Townsley, L., Broos, P., Garmire, G., & Tsujimoto, M. 2006, ApJS, 163, 306

Giles, K. 1977, MNRAS, 180, 57P

Hoffmeister, V. H., Chini, R., Scheyda, C. M., Schulze, D., Watermann, R., Nürnberger, D., Vogt, N., & Nielbock, M. 2008, ApJ, 686, 310

Kennicutt, R. C., Jr. 1998, ARA&A, 36, 189

Kennicutt, R. C., Jr. 1998, ApJ, 498, 541

Kroupa, P. 2001, MNRAS, 322, 231

Maíz Apellániz, J. 2008, ApJ, 677, 1278

Martins, F., Schaerer, D. & Hillier, D. J. 2005, A&A, 436, 1049

Massey, P. & Hunter, D. A. 1998, ApJ, 493, 180

Mezger, P. G., Smith, L. F., & Churchwell, E. 1974, A&A, 32, 269

Misiriotis, A., Xilouris, E. M., Papamastorakis, J., Boumis, P. & Goudis, C. D. 2006, A&A, 459, 113

Muench, A. A., Lada, E. A., Lada, C. J. & Alves, J. 2002, ApJ, 573, 366

Osterbrock, D. E. 1974, Astrophysics of Gaseous Nebulae (San Fransisco: W. H. Freeman and Co.)

Panagia, N. 1973, AJ, 78, 929

Preibisch, T. & Feigelson, E. D. 2005, ApJS, 160, 390

Smith, L. F., Biermann, P., & Mezger, P. G. 1978, A&A, 66, 655

Smith, L. J., Norris, R. P. F., & Crowther, P. A. 2002, MNRAS, 337, 1309

Vacca, W. D., Garmany, C. D., & Shull, J. M. 1996, ApJ, 460, 914

Vázquez, G. A. & Leitherer, C. 2005, ApJ, 621, 695

Wang, J., Townsley, L. K., Feigelson, E. D., Getman, K. V., Broos, P. S., Garmire, G. P., & Tsujimoto, M. 2007, ApJS, 168, 100

Zhang, Q. & Fall, M. S. 1999, ApJ, 527, L81

Chapter 6

Conclusions and Future Work

[Our remote descendants] will gaze up and strain to find the blue dot in their skies.
They will love it no less for its obscurity and fragility.
They will marvel at how vulnerable the repository of all our potential once was,
how perilous our infancy, how humble our beginnings,
how many rivers we had to cross before we found our way.

— *Carl Sagan*
Pale Blue Dot

I have presented an in-depth analysis of the Galactic H II region M17 based upon a wealth of available multiwavelength observational data. I have demonstrated (Chapter 4) that it is possible to reconstruct a detailed star formation history in the extended molecular cloud complex associated with M17 from the combination of infrared (IR) and X-ray detections of individual young stars and young stellar objects (YSOs). X-ray luminosity functions (XLFs) and YSO mass functions (YMFs) are reliable tracers of the star formation rates (SFRs) in young massive clusters and extended molecular cloud regions, respectively. Both the XLF and the YMF sample the stellar initial mass function (IMF) where it is the most reliably constrained, at intermediate masses (Scalo 1998). The dominant source of uncertainty on SFR_X, derived from the XLF in M17, is the ∼50% uncertainty on the cluster age. SFRs for M17 predicted by the thermal radio continuum (Galactic SFR diagnostic; Smith, Biermann, & Mezger 1978) and the 24 μm luminosity (extragalactic SFR diagnostic; Calzetti et al. 2007) disagree with SFR_X by factors of ∼2–3 (Chapter 5). These large discrepancies are due chiefly to large uncertainties in the masses and ionizing photon production rates of O stars and the need to correct for the high binary fractions observed among massive stars.

A new Galactic SFR calibration using XLFs and YMFs would avoid the problematic dependence on the stellar parameters of O stars. Assuming that the average IMF is invariant across the full mass range, at least when considering a statistically large sample of clusters, both the exact behavior of the IMF at the high-mass tail and the parameters of O stars as functions of spectral type are irrelevant to a calibration of SFR_X against 24 μm luminosity, for example. This works because it produces a more robust conversion between cluster mass and Lyman continuum photon production rate, $\langle M\rangle/\langle N_c\rangle$ (Equation 1.6), with $\langle M\rangle$ determined from *direct* constraints on the IMF based on the detection of individual stars. Such a calibration is within reach using currently available data, and the analysis in Chapter 5 points the way. But the isolated analysis of a single H II region does not produce a calibration.

The logical outgrowth of this research would begin with the more than 20 young massive clusters that have been observed to date in X-rays using *Chandra*/ACIS, M17 and RCW 49 among them (Broos et al. 2007; Tsujimoto et al. 2007). The majority of these clusters are found in H II regions near the Galactic plane, hence their 24 μm luminosities can be measured from the *MSX* survey (like M17, many of these H II regions will be too bright for MIPSGAL, which missed the outer Galactic plane in any case). Once a good correlation can be established between SFR_X and mid-IR emission, as I expect is possible, then the implications of the SFR discrepancies discussed in Chapter 5 can be explored in full. Subsequently, thanks to the MIPSGAL 24 μm survey images, the correlation could be used to determine SFRs for distant or faint Galactic H II regions where individual stars cannot be easily resolved or detected. With this Thesis, I have demonstrated that modern survey data hold the potential for making a new determination of the Galactic SFR and providing an alternate SFR calibration against which extragalactic SFR diagnostics (Kennicutt 1998a; Calzetti et al. 2007) may be tested.

This research has produced the first *direct* comparison of the SFR in a Galactic H II region with global SFR tracers applied to the Milky Way and other galaxies. Thus the primary goal of this Thesis has been attained, and numerous other notable results have been presented along the way, including:

- The emergent luminosity in the IR peak of the global M17 SED balances the bolometric luminosity produced by the known massive stars in the ionizing cluster (Chapter 2), while the thermal radio plateau generally agrees with model predictions of the Lyman continuum photon rate from the ionizing stars.

- Bright emission features from polycyclic aromatic hydrocarbons (PAHs) dominate the mid-IR emission from photodissociation regions (PDRs) at wavelengths $\lesssim$10 μm. PAH emission abruptly disappears interior to the ionization front, probably because PAH molecules are destroyed by the extreme ultraviolet photons that dominate the radiation field within the ionized gas (Chapter 2). PDRs are hence easily recognized in the GLIMPSE images of the Galactic plane (Churchwell et al. 2006, 2007).

- Stellar winds from O stars dominate the structure and dynamics of giant H II regions, as evidenced by the presence of evacuated cavities in the central regions of M17 and RCW 49 (Chapters 2 and 3). Stellar-wind bow shocks driven by the interaction of OB star winds with large-scale gas flows may be a common feature of such H II regions, and they offer an independent *in situ* probe of the local ISM conditions (Chapter 3).

- Because of severe contamination problems for inner Galactic plane IR catalogs, IR excess emission alone is an unreliable indicator of membership in young embedded clusters. The most significant contaminants are dust-rich asymptotic giant branch stars and YSOs located at unknown distances along the line of sight (Chapter 4).

- Ongoing star formation is distributed over far larger cloud volumes associated with bright H II regions than previously thought. Contamination from unassociated sources is severe for lower-density, extended YSO populations. Employing a cluster-finding technique statistically removes the contaminating sources, while selecting significant groupings of candidate YSOs that coincide spatially with observed extended molecular cloud structures (Chapter 4).

- The identification and characterization of candidate YSOs through fitting model SEDs to broadband IR survey data (Robitaille et al. 2006, 2007) has been successful so far. YMFs and evolutionary ages supplied by the models provide a self-consistent picture of the ensemble properties of observed YSOs (Chapter 4).
- The extended bubble M17 EB provides a compelling case for massive star formation triggered by collect-and-collapse of molecular gas in the path of expanding, wind-driven bubbles. The relative importance of this mode of star formation remains unclear; if it can be proved that M17 was triggered by the older, likely less massive NGC 6618PG cluster (Chapter 4), this would constitute concrete evidence for self-propagating cluster formation driven by massive star feedback.
- The majority of O stars in NGC 6618, the M17 ionizing cluster, including virtually all known O stars earlier than type O6, appear to be members of unresolved near-equal-mass binary systems (Chapter 4). These stars are too luminous in the mid-IR to be single O stars on the main sequence, and many are anomalous hard X-ray emitters (Broos et al. 2007).

GLIMPSE, MIPSGAL, and complementary IR and radio Galactic plane surveys will remain an invaluable resource for star formation research for the foreseeable future. Currently, the trajectory of innovation in the area of astronomical innovation primarily produces facilities with ever-increasing resolution (spatial and spectral) and sensitivity, but often at the expense of a wide field-of-view. The next generation of IR and mm telescopes, led by flagships the *Stratospheric Observatory for Infrared Astronomy*, the *James Webb Space Telescope*, and the *Atacama Large Millimeter Array*, will likely revolutionize our understanding of the microphysics of star and planet formation, yet the march to observe ever smaller size scales and ever more distant objects, tends to produce a collection of postage-stamp views of the universe. The legacy of *Spitzer* is the big picture, the global perspective that helps tie together every other good idea.

References

Broos, P. S. et al. 2007, ApJS, 169, 353

Calzetti, D. et al. 2007, ApJ, 666, 870

Churchwell, E., Povich, M. S., et al. 2006, ApJ, 649, 759

Churchwell, E., Watson, D. F., Povich, M. S., et al. 2007, ApJ, 670, 428

Kennicutt, R. C., Jr. 1998, ARA&A, 36, 189

Robitaille, T. P., Whitney, B. A., Indebetouw, R., Wood, K., & Denzmore, P. 2006, ApJS, 167, 256

Robitaille, T. P., Whitney, B. A., Indebetouw, R., & Wood, K. 2007, ApJS, 169, 328

Scalo, J. 1998, ASPC, 142, 201

Smith, L. F., Biermann, P., & Mezger, P. G. 1978, A&A, 66, 655

Tsujimoto, M. et al. 2007, ApJ, 665, 719